*David Virant*

DISSERTATION

---

# *Studying Large Multi-Protein Complexes Using Single Molecule Localization Microscopy*

---

Max Planck Institute for Terrestrial Microbiology

Department of Systems and Synthetic Microbiology

**01.03.2015 - 30.04.2019**

written by David Virant

born 09.05.1991 in Ljubljana (Slovenia)

Die Untersuchungen zur vorliegenden Arbeit wurden von März 2015 bis April 2019 in der Abteilung System- und Synthetische Mikrobiologie des Max-Planck-Institutes für terrestrische Mikrobiologie in Marburg in der Arbeitsgruppe von Dr. Ulrike Endesfelder durchgeführt.

Vom Fachbereich Biologie der Philipps-Universität Marburg als Dissertation angenommen am:

Gutachter dieser Arbeit waren:

Erstgutachter: Dr. Ulrike Endesfelder

Zweitgutachter: Prof. Dr. Victor Sourjik

# Erklärung

Ich versichere, dass ich meine Dissertation mit dem Titel "Studying Large Multi-Protein Complexes Using Single Molecule Localization Microscopy" selbstständig, ohne unerlaubte Hilfe angefertigt und mich dabei keiner anderen als der von mir ausdrücklich bezeichneten Quellen und Hilfsmittel bedient habe.

Diese Dissertation wurde in der jetzigen oder einer ähnlichen Form noch bei keiner anderen Hochschule eingereicht und hat noch keinen sonstigen Prüfungszwecken gedient.

David Virant

Ljubljana, den 05.10.2019

# Contents

# 1 List of Acronyms

**AF647** Alexa Fluor 647

**SAC** Spindle Assembly Checkpoint

**SRM** Super Resolution Microscopy

**NMR** Nuclear Magnetic Resonance

**SMLM** Single-Molecule Localization Microscopy

**STORM** Stochastic Optical Reconstruction Microscopy

**dSTORM** direct Stochastic Optical Reconstruction Microscopy

**PALM** Photoactivated Localization Microscopy

**Cryo-EM** Cryogenic Electron Microscopy

**Nb** Nanobody, a small single-chain antibody fragment consisting of one variable domain with a diameter of roughly 3nm

**FP** Fluorescent Protein

**GFP** Green Fluorescent Protein

**paGFP** Photo-Activatable Green Fluorescent Protein

**PC** Primed Conversion

**psFP** Photo-Switchable Fluorescent Protein

**paFP** Photo-Activatable Fluorescent Protein

**pcFP** Photo-Convertible Fluorescent Protein

**pc-pcFP** Primed Convertible Photo-Convertible Fluorescent Protein

**PAmCherry** Photo-Activatable Monomeric Cherry Fluorescent Protein

**PAmKate** Photo-Activatable Monomeric Kate Fluorescent Protein

**mEos3.2** Monomeric Photoconvertible Eos Fluorescent Protein Version 3.2

**mEos3.2-A69T** Monomeric Photoconvertible Eos Fluorescent Protein Version with a threonine substitition at position 69

| | |
|---|---|
| **mScarlet-I** | monomeric Scarlet Fluorescent Protein with a a threonine to isoleucine mutation at position 74 |
| **UV** | Ultra-Violet light |
| **IR** | Infrared light |
| **CenH3** | Centromeric H3 |
| **CCAN** | Constititive Centromere Associated Network |
| **SPB** | Spindle Pole Body - yeast microtubule organizing element |
| **POI** | Protein Of Interest |
| **OPTICS** | Ordering Points To Identify the Cluster Structure |
| **PSF** | Point Spread Function |
| **FWHM** | Full Width at Half Maximum of a normal distribution |
| **MLE** | Maximum Likelihood Estimation |

# 2 Summary

Biology would not be where it is today without fluorescence microscopy. It is arguably one of the most commonly used tools in the biologists toolbox and it has helped scientists study the localization of cellular proteins and other small things for decades, but it is not without its limitations. Due to the diffraction limit, conventional fluorescence microscopy is limited to micrometer-range structures. Science has long relied upon electron microscopy and X-ray crystallography to study phenomena that occur below this limit. However, many of lifes processes occur between these two spatial domains.

Super-resolution microscopy, the next stage of evolution of fluorescence microscopy, has the potential to bridge this gap between micro and nano. It combines superior resolutions of down to a few nanometers with the ability to view objects in their natural environments. It is the ideal tool for studying the large, multi-protein complexes that carry out most of lifes functions, but are too complex and fragile to put on an electron microscope or into a synchrotron.

A form of super-resolution microscopy called SMLM Microscopy shows especially high promise in this regard. With its ability to detect individual molecules, it combines the high resolution needed for structural studies with the quantitative readout required for obtaining data on the stoichiometry of multi-protein complexes. This thesis describes new tools which expand the toolbox of SMLM with the specific aim of studying multi-protein complexes.

First, the development of a novel fluorescent tagging system that is a mix of genetic tagging and immuno-staining. The system, termed BC2, consists of a short, genetically encodable peptide that is targeted by a nanobody (BC2 nanobody). The system brings several advantages. The small tag is not disruptive to the protein it is attached to and the small nanobody can get into tight spaces, making it an excellent tag for dense multi-protein structures.

Next, several new variants of some commonly used green-to-red fluorescent proteins. The novel variants, which can be converted with a combination of blue and infrared light are especially useful for live-cell imaging. The developed fluorescent proteins can also be combined with photo-activatable fluorescent proteins to enable imaging of several targets with the same color protein.

Finally, an application of the latter technique to study the multi-protein kinetochore complex and gain first glimpses into its spatial organization and the stoichiometry of its subunits.

# 3 | Zusammenfassung

Die Biologie wäre heute nicht, wo sie ist, ohne die Fluoreszenzmikroskopie. Sie ist unbestreitbar eines der am häufigsten verwendeten Werkzeuge im Repertoire des Biologen und es hilft Wissenschaftlern seit Jahrzehnten, die Lokalisation von Zellproteinen und anderen kleinen Strukturen zu untersuchen. Sie ist aber nicht ohne Limitationen. Aufgrund des Abbe-Limits ist die Fluoreszenzmikroskopie beschränkt auf Strukturen im Mikrometerbereich. Die Naturwissenschaften haben sich lange auf die Elektronenmikroskopie und Röntgenkristallographie verlassen, um Phänomene unterhalb dieses Limits zu studieren. Allerdings gibt es viele Prozesse, welche sich zwischen diesen beiden räumlichen Domänen ereignen.

Superauflösende Mikroskopie, der nächste Schritt in der Evolution der Fluoreszenzmikroskopie, hat das Potential, den Bereich zwischen mikro und nano zu überbrücken. Sie kombiniert höhere Auflösungen von bis zu wenigen Nanometern mit der Fähigkeit, Objekte in ihrer natürlichen Umgebung zu beobachten. Sie ist das ideale Werkzeug, um grosse Multiproteinkomplexe zu untersuchen, welche die meisten Funktionen des Lebens ausführen, aber zu komplex und fragil für die Elektronenmikroskopie oder Kristallographie sind.

Eine Form der superauflösenden Mikroskopie, genannt SMLM, ist diesbezüglich sehr vielversprechend. Mit ihrer Fähigkeit, individuelle Moleküle zu detektieren, kombiniert sie die hohe Auflösung für strukturelle Studien mit der quantitativen Auslesung für den Erhalt von Stöchiometrien von Multiproteinkomplexen. Diese Thesis beschreibt neue Werkzeuge, welche das Repertoire von SMLM erweitert mit dem spezifischen Ziel, Multiproteinkomplexe zu untersuchen.

Als erstes, die Entwicklung eines neuen fluoreszierenden tagging Systems, das eine Mischung ist aus genetischem Tagging und Immunofärbung. Das System, bezeichnet als BC2, besteht aus einem kurzen, genetisch codierbaren Peptid, das von einem Nanobody (BC2 nanobody) anvisiert werden kann. Dieses System bring mehrere Vorteile. Das kleine Tag stört das Protein, an welches es befestigt ist, nicht und der kleine Nanobody kommt in enge Räume rein, was es zu einem exzellenten Tag für dichte Multiproteinstrukturen macht.

Als nächstes, mehrere neue Varianten von oft verwendeten grün-zu-rot fluoreszierenden Proteinen. Diese neuen Varianten, welche mit einer Kombination von blauem und infrarotem Licht konvertiert werden können, sind besonders nützlich für Lebendzellmikroskopie. Die entwickelten fluoreszierenden Proteine können auch mit photo-aktivierbaren fluoreszierenden Proteinen kombiniert werden, um das Mikroskopieren von mehreren Zielstrukturen mit derselben Farbe zu ermöglichen.

Zuletzt, eine Applikation dieser letztgenannten Technik, um den Multiproteinkomplex des Kinetochors zu untersuchen und erste Einsichten in seine Architektur und räumliche Organisation zu erhalten, ebenso wie zur Stöchiometrie seiner Untereinheiten.

# 4 | Introduction

## 4.1 Introduction to Single Molecule Localization Microscopy Techniques

### From single molecules to life: microscopy at the nanoscale

Bartosz Turkowyd, David Virant, Ulrike Endesfelder

This part of the thesis is written in the style of a manuscript and was published in Analytical and Bioanalytical Chemistry. Bartosz Turkowyd and me contributed equally to this work and share the first author position. My roles in this publication included literature research, preparing figures and writing the text for certain sections of the manuscript. This section serves as an introduction to the techniques of SMLM and Super Resolution Microscopy (SRM) as a whole, as well as their uses, advantages and limitations. All the microscopy techniques applied in this work are described and put into context. [1]

Anal Bioanal Chem (2016) 408:6885–6911
DOI 10.1007/s00216-016-9781-8

REVIEW

# From single molecules to life: microscopy at the nanoscale

**Bartosz Turkowyd**[1] · **David Virant**[1] · **Ulrike Endesfelder**[1]

Received: 31 March 2016 / Revised: 30 June 2016 / Accepted: 7 July 2016 / Published online: 9 September 2016

**Abstract** Super-resolution microscopy is the term commonly given to fluorescence microscopy techniques with resolutions that are not limited by the diffraction of light. Since their conception a little over a decade ago, these techniques have quickly become the method of choice for many biologists studying structures and processes of single cells at the nanoscale. In this review, we present the three main approaches used to tackle the diffraction barrier of ~200 nm: stimulated-emission depletion (STED) microscopy, structured illumination microscopy (SIM), and single-molecule localization microscopy (SMLM). We first present a theoretical overview of the techniques and underlying physics, followed by a practical guide to all of the facets involved in designing a super-resolution experiment, including an approachable explanation of the photochemistry involved, labeling methods available, and sample preparation procedures. Finally, we highlight some of the most exciting recent applications of and developments in these techniques, and discuss the outlook for this field.

**Keywords** Super-resolution microscopy · Photophysics and photochemistry of fluorophores · Live cell imaging · Quantitative cell biology

## Spatial and temporal scales in the life sciences and microscopy

The timescales and spatial scales of the processes and molecules associated with life span extremely broad ranges, covering many orders of magnitude (Fig. 1). For instance, intracellular regulation (e.g., conformational changes or biochemical reactions within molecules) takes place at submillisecond timescales, nanosized molecules such as ATP (which serves the energy demands of cells) diffuse in milliseconds through cell volumes ranging from several micrometers up to millimeters, while (clustered) membrane receptors move at speeds that are about a magnitude slower. Large multicomponent machineries realize and control complex multilayered cellular functions that occur in seconds to hours. The ribosome, a large macromolecule which consists of two functional subunits of several dozen proteins on nucleic acid chain scaffolds, takes a matter of seconds to synthesize new peptide chains comprising hundreds of amino acids, which then quickly fold up into functional proteins. On the other hand, the replication of a full genome requires at least about 40 min for the 4.6 million nucleic acid base pairs of the bacterium *Escherichia coli*, and the cellular division cycle ranges from tens of minutes for *E. coli* to several hours for mammalian cells.

Observing and understanding all of these components of life requires us to be, at best, passive witnesses of undisturbed processes, but also to demand hard observational data that can allow us to quantitatively measure and trace all of the players involved—ranging from small molecules up to the interactions of whole cells in cellular communities—with the highest specificity and precision.

To achieve this, instrumentation is needed that permits a wide three-dimensional view but also allows details to be

---

Bartosz Turkowyd and David Virant contributed equally to this work.

✉ Ulrike Endesfelder
ulrike.endesfelder@synmikro.mpi-marburg.mpg.de

[1] Department of Systems and Synthetic Microbiology, Max Planck Institute for Terrestrial Microbiology and LOEWE Center for Synthetic Microbiology (SYNMIKRO), Karl-von-Frisch-Str. 16, 35043 Marburg, Germany

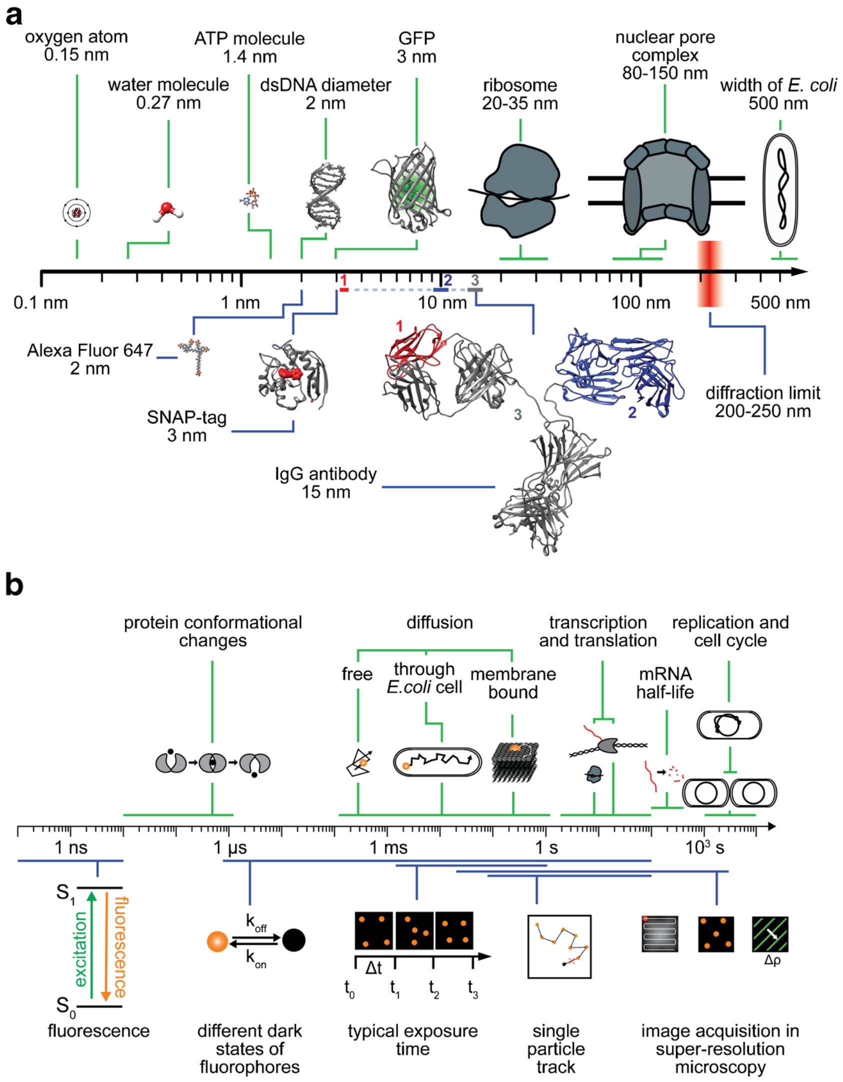

**Fig. 1a–b** Spatial and temporal scales in the life sciences and microscopy. **a** Selected characteristic submicrometer objects are separated on the basis of biological (*above the axis*, *green*) and technical (*below the axis*, *blue*) significance. The IgG antibody structure (15 nm) contains two other notable structures: the antigen-binding region, called the Fab fragment (10 nm, *blue*) and the single-variable domain (3 nm, *red*), from which so-called nanobodies from cameloids are derived. Structures are taken from the PDB [GFP 1KYS, IgG 1IGT, SNAP 3KZZ, DNA 4LEY] and PubChem [ATP CID 5957, Alexa Fluor 647 CID 102227060]. **b** Timescales of various important biological processes (*above the axis*, *green*) and physical events, as well as typical timescales associated with microscopy procedures (*below the axis*, *blue*)

explored in high resolution, is noninvasive but can tell different cellular components apart, and offers detection that is rapid enough to be able to probe the processes of interest.

Today, the use of modern super-resolution fluorescence microscopes allows us to zoom into the intracellular structures of live cells [1, 2]. It is not only possible to resolve specimens in greater detail than naturally possible using the discriminating power of the human eye through the application of conventional light microscopes, but we are also able to circumvent the diffraction limit of light and study structures at near-molecular scale. This significant gain in resolution (which has revealed the heterogeneous nature of the lives of single cells), the inherent specific contrast of single fluorescent labels, and the ability to live-cell image single cells and large multicellular organisms have made fluorescence super-resolution microscopy one of the most powerful tools applied in the life sciences.

Nevertheless, there are limitations: the maximal photon flux of a fluorophore—which is mainly determined by its fluorescence lifetime—yields a lower bound for the detection range when observing molecular dynamics, and its maximum photon budget (above which it is irreversibly destroyed, i.e., photobleached) marks the upper bound for studying individual molecules. Technology-wise, minimal exposure times in the millisecond range limit the maximum observation rate of a planar live image array [3], and (for example) the sizes of labeling molecules such as dyes, protein tags, and antibodies yield steric resolution limits [4, 5]. Typical sizes of labeling molecules and the range of timescales of various life processes and imaging procedures are visualized in the lower panels of Fig. 1a and b.

It is important to point out that none of the advanced super-resolution microscopy techniques are routine methods as yet. They work close to current technological limits, and thus improve with each new implementation. Behind their stunning results and attractive images hide highly complex and tailored experimental designs. It is thus advisable to define the particular biological question to be answered as precisely as possible, and to plan biological experiments such that they suit the techniques well. Therefore, here, we will briefly review the basic principles of the three most widely used super-resolution microscopy techniques: stimulated-emission depletion (STED) microscopy [6], structured illumination microscopy (SIM) [7], and single-molecule localization microscopy (SMLM) [8–10], as depicted in Fig. 2 and summarized in Table 1. We explain, in detail, the essential characteristics of currently used reporter fluorophores, from their individual photophysics to general labeling strategies. Finally, we highlight the recent advances of the last few years, which have not only allowed the molecular compositions and structures of individual cellular components to be elucidated, but have also enabled us to place them into their native environmental context of large-scale spatial organization and to follow their dynamics. At the end of the paper, we emphasize the main challenges we currently face in order to achieve further improvements in these techniques and we introduce promising correlative schemes and sophisticated algorithmic and analytic tools which facilitate large-data and computational systems biology approaches.

## Principles of super-resolution microscopy

The resolution of light microscopy is often introduced via the Rayleigh criterion. Light from point-like sources is convolved by the so-called point-spread function (PSF) of an optical system when transmitted through a diffraction-limited microscope (Fig. 2a). In 1896, Lord Rayleigh defined the maximum resolution of an optical system as the minimum distance between two point-like objects which can be separated as individual sources. He regarded two point sources of equal strength as just discernible when the main diffraction maximum of one image coincides with the first minimum of the other. For an epifluorescence microscope with a circular aperture where the light is collected with the same objective, this yields

$$d = \frac{0.61\lambda}{\mathrm{NA}},$$

where $\lambda$ is the wavelength of light and NA is the numerical aperture [16].

Nevertheless, as already demonstrated by Zsigmondy using his ultramicroscope in 1902 [17], particles with dimensions below the resolution limit of visible light can be resolved. Also, confocal or multiphoton fluorescence approaches possess higher resolution than epifluorescence microscopes, as these techniques repress out-of-focus fluorescence, permitting straightforward three-dimensional imaging [18]. The resolution of near-field scanning microscopy (NSOM) is not limited by diffraction, as the diffraction limit applies only to light that has propagated a distance that is sufficiently larger than its wavelength. NSOM is therefore only limited by the aperture of the nanometer-sized excitation and detection tip placed near the sample [19].

Since the development of STED, the first far-field super-resolution fluorescence microscopy technique, many new methods that spatially or temporally confine fluorescence (which allows them to circumvent the diffraction barrier) have evolved. They can be categorized into two types of super-resolved far-field methods, with the first group concentrating on particular incident excitation light patterns and the second focusing on the modulation of the detected emission light over time. To be more specific, the first group, including techniques such as STED and SIM, make use of structured illumination schemes which spatially modulate the fluorescence of molecules such that not all of them simultaneously emit light. The second group, namely SMLM, rely on single-molecule imaging, and uses stochastic photomodulation of individual fluorophores. The number of photoswitchable fluorophores in their active fluorescent state can be controlled by irradiating the fluorophores with specific wavelengths of light. Thus, the stochastic activation of fluorescence at low rates allows the fluorescence emissions of single fluorophores to be spatially and temporally separated.

### Stimulated-emission depletion microscopy

In STED microscopy [6], the sample is scanned by a subdiffraction excitation spot. This spot is realized by superimposing two lasers: an excitation laser with a focused beam waist limited by diffraction and a STED depletion laser in a donut-shaped mode (achieved by phase modulation) with a wavelength at the far end of the fluorescence spectrum of the fluorophore used (Fig. 2bi). As a consequence, all of the fluorophores in the focal spot of the excitation laser are excited, whereas those located within the area of the donut-shaped STED laser are again quickly depleted from the excited state and forced back to their ground state by stimulated emission, resulting in the release of a photon identical to the incident STED depletion photon. This process only leaves fluorophores at the subdiffraction-sized central spot in the excited state, and their spontaneous fluorescence emission is measured. By precisely scanning the entire sample and measuring the respective fluorescence intensity of each subdiffraction area (Fig. 2bi, bottom), then, without the need for any further post-processing steps (Fig. 2bii), an image is reconstructed (Fig. 2biii).

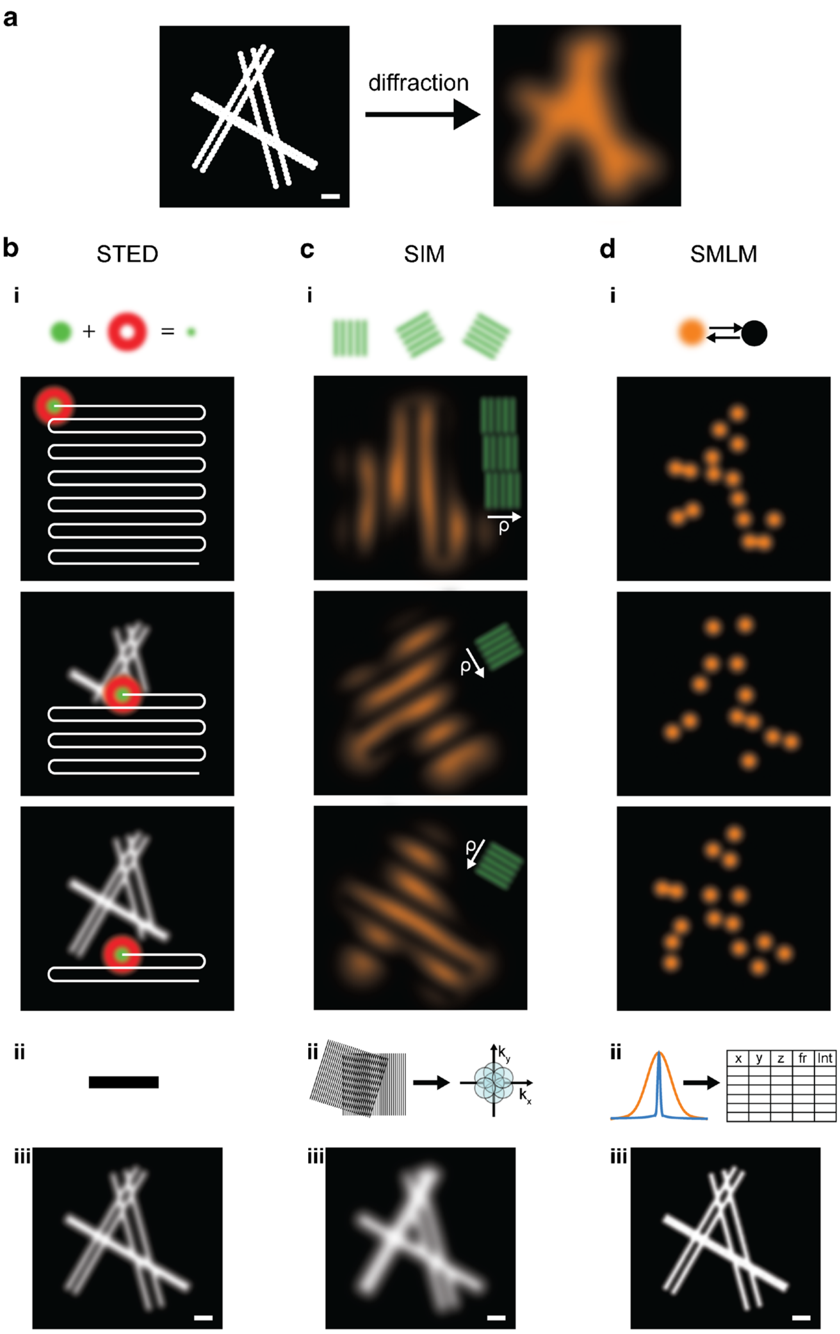

**Fig. 2a–d** Principles of super-resolution microscopy techniques. **a** *Left*: Scheme of six filaments decorated with fluorophores (represented by large icons for visibility) and grouped into three pairs at simulated distances of 50, 100, and 150 nm; *scale* 200 nm. *Right*: A typical image of this structure obtained by conventional fluorescence microscopy is limited by the diffraction of light. **b** *i*, *top*: For STED, the structure is scanned by a subdiffraction excitation spot obtained by combining an excitation laser (*green*) with a, by phase-modulation shaped, depletion laser (*red*). After scanning the entire structure (*i*, *bottom*), and without performing any further post-processing steps (*ii*), an image is reconstructed (*iii*). **c** In SIM, fluorophores are excited by a series of regularly spaced illumination patterns of known frequency, orientation, and phase which modulate the fluorophore emissions. This results in visible low-frequency Moiré patterns that are dependent on the structure imaged (*i*). By analyzing the images for their spatial frequencies, an enlarged frequency space is obtained (*ii*), and a subdiffraction image is reconstructed (*iii*). **d** In SMLM, the fluorescence is modulated by photoswitching between "off" and "on" states. Most of the fluorophores are forced to reside in a dark off state; only a small subset of spatially separated fluorophores in the on state is allowed to emit fluorescence at a given time. After sequentially imaging thousands of subsets of fluorophores (*i*), the nanometer-precise fluorophore positions can be extracted from the diffraction-limited individual emissions (*ii*), and an image is reconstructed (*iii*). The three super-resolved images labeled (*iii*) visualize typical resolutions obtained by the methods: on the order of 50 nm (STED), 100 nm (SIM), and 20 nm (SMLM); *scale* 200 nm

**Table 1** Overview of the characteristics of various super-resolution microscopy techniques

| | STED | Linear SIM | Nonlinear SIM | SMLM |
|---|---|---|---|---|
| Microscope type | Laser scanning | Widefield | Widefield | Widefield |
| xy resolution (nm) | 20–70 | 80–100 | ~45 | 10–40 |
| z resolution (nm) | 30–100 | ~300 | ~170 | 10–50 |
| Temporal resolution | ms to s | ms to s | ms to s | s to min |
| Laser intensities [W/cm$^2$] | ~$10^4$–$10^9$ | ~ 10–$10^2$ | ~ $10^2$–$10^6$ | ~ $10^3$–$10^4$ |
| Suitable fluorophores | Photostable fluorophores | All common fluorophores | Photostable or photoswitchable fluorophores | Photoswitchable fluorophores |
| Number of colors | 3 | 3 | 1 | 4 |
| Photobleaching | Moderate to high | Low to moderate | Moderate to high | Low to moderate (reversible switching)<br>High (irreversible switching) |

Values are taken from [10–15]

The size of this effective subdiffraction scanning beam can be varied depending on the intensity of the STED depletion beam. The resulting resolution of STED microscopy can be described by

$$d_{\mathrm{STED}} = \frac{d}{\sqrt{1 + I/I_{\mathrm{s}}}},$$

where $d$ is the conventional resolution limit as defined by the Rayleigh criterion, $I$ is the intensity of the STED depletion laser, and $I_{\mathrm{s}}$ is the effective saturation intensity, which can be defined as the intensity at which the probability of fluorescence emission is reduced by half [20].

By choosing the wavelength of the STED depletion laser to be at the far end of the fluorophore's spectrum, reabsorption from the ground state as well as further absorption processes from the excited state can be neglected. Further, the resulting stimulated photons identical to the STED depletion wavelength possess a longer wavelength than the majority of photons obtained by spontaneous fluorescence emission. They can therefore be easily spectrally filtered, and—as stimulated emission also occurs on faster timescales—filtered temporally too. As it is a confocal technique, STED microscopy naturally permits optical sectioning, but three-dimensional imaging schemes have been further improved by, for example, creating an isotropic focal scanning spot using two opposing objectives [21].

The sample is scanned in steps as small as the effective subdiffraction-sized excitation spot, but is irradiated by the much larger, diffraction-limited, foci of the excitation and STED depletion lasers. Thus, the fluorophores are subjected to multiple excitation and de-excitation steps under high STED laser intensities, which requires them to be extraordinarily photostable. STED microscopy was initially realized in a pulsed laser scheme [6]; continuous-wave illumination STED microscopy was implemented later [22]. However, rather high intensities are required in both imaging schemes, leading to increased photobleaching and phototoxicity in the sample. This negative effect can be reduced by employing sophisticated imaging modes which lower or shorten the applied laser intensities, e.g., by time gating [23], by selective, feedbacked use of the depletion beam to reduce the number of state transition cycles [24], or by replacing (a concept also termed RESOLFT: reversible saturable optical (fluorescence) transition) [25] or assisting [26] the stimulated depletion mechanism with an on–off photoswitch. STED utilizing moderate laser power schemes can be applied to the imaging of live cells as well as living tissue and living organisms (for a detailed review, see [27]).

For multicolor STED microscopy, either a pair of lasers is required for each fluorophore [28], or, for spectrally close fluorescence spectra, only one depletion laser is needed [29]. This further automatically coaligns the effective scanning spots of both colors. Very specific fluorophore pairs, chosen to be suitable for spectral demixing approaches or to demonstrate reverse photochromic behavior, can be operated by just one pair of lasers [30, 31].

## Structured illumination microscopy

SIM uses regularly spaced patterns of known spatial frequency, orientation, and phase to illuminate the sample by a structured excitation light series ([7]; detailed review [32]). This leads to modulated fluorescence emissions which form defined interference Moiré fringes of high and low frequencies, as the light emitted from a specific point in the sample is the product of the local structure of the sample (more precisely the spatial distribution of the fluorophores) and the local excitation intensity. As the corresponding fluorescence image seen through the microscope is diffraction limited and thus convolved with the PSF of the optical system, only the low-frequency Moiré patterns can be measured. These structure-specific patterns are registered for different sequential phases and orientations of the illumination pattern to sample the maximum isotropic frequency space (Fig. 2ci). By measuring the apparent Moiré fringes and knowing the properties of the chosen illumination patterns, it is possible to retrieve information at higher spatial frequencies than normally possible in a widefield microscope (Fig. 2cii): the diffraction limit can be described as a circular boundary in the transmitted frequency space with a maximal frequency of $k_{\max}$, equaling $1/d$. Thus, only the spatial frequencies with $k \ll k_{\max}$ pass through the optical system. Using structured illumination, which allows the detection of low-frequency Moiré interference patterns, spatial information about the sample from higher frequency bands is shifted into detectable lower frequency bands. All of the acquired images can be analyzed for their spatial frequencies and then be unmixed by their multiple overlapping components in frequency space. This allows the high frequencies obtained using the Moiré information to be shifted back to their original frequencies. The resulting enlarged frequency space encompasses about $2k_{\max}$, as the low-frequency Moiré patterns must remain visible above the diffraction limit. Using an inverse Fourier transform back into image space, a super-resolved SIM image showing a linear twofold increase in resolution can then be reconstructed (Fig. 2ciii).

Ignoring for a brief moment the rather complex post-processing of the raw data acquired by sophisticated SIM software (recently published open-source options are [33, 34]), SIM is the most straightforward approach in the field of super-resolution microscopy: the technique is based on standard widefield fluorescence microscopes, only requires (in the simplest version of SIM) a movable grating placed in a Fourier plane of the illumination path, and works for all common (albeit best for bright) fluorophores. SIM can be used to image live cells [11, 35] and has been extended to three-dimensional SIM [12], is capable of imaging live organisms [36], and allows for multicolor imaging [37]. Nevertheless, common artifacts (arising from imperfect imaging or algorithms) should be carefully considered, avoided, or corrected for: stripes in a reconstituted SIM image emerge from photobleaching, sample drift, or setup vibrations, a low fluorescence modulation contrast results in noise in the high-frequency range, and spherical aberration as well as refractive index mismatching creates halos or the doubling of features [38].

A higher resolution than that obtained by linear SIM is achieved by nonlinear SIM, which is realized by either saturating the fluorescence through the application of strong illumination intensities [39] or by using photoswitchable fluorophores [13, 40] (similar to RESOLFT [25]) to create illumination patterns that include higher harmonic frequencies. However, the increased resolution of this technique comes at the expense of a limited choice of fluorophores, which need to be either highly photostable (in order to withstand the strong illumination intensities) or photoswitchable. The resolution obtained using SIM approaches can be determined via

$$d_{SIM} \approx \frac{d}{2+h},$$

where $d$ is the conventional resolution limit and $h$ is the number of higher harmonics achieved when applying nonlinear SIM schemes [13, 39, 40]. For linear SIM, $h$ equals zero, so the resolution enhancement is about twofold.

## Single-molecule localization microscopy

Single-molecule localization-based techniques such as photoactivated localization microscopy (PALM) ([8], (*direct*) stochastic optical reconstruction microscopy ((*d*)STORM) [9, 10], ground-state depletion followed by individual molecule return (GSDIM) [41], and many other related techniques [42] are commonly grouped together under the term “single-molecule localization microscopy” (SMLM). They all require tight control over the photoswitching of individual fluorophores, as discussed in detail in this review, and they rely on the use of post-processing algorithms to generate the super-resolved data (see the review by Small and Stahlheber [43] and comparative studies of localization algorithms [44] and single-particle tracking algorithms [45]; most of the relevant algorithms are openly available).

In SMLM, the main principle is stochastic photoswitching and the detection of single spatially separated fluorophores. To achieve this, all fluorophores are modulated by photoswitching them between “off” and “on” states. Most of the fluorophores are forced to reside in a long-lasting dark off-state; only a small subset of fluorophores in the on state are allowed to emit fluorescence at a given time. By sequentially imaging typically several thousand subsets of spatially distinguishable fluorophores, all of the emitters are detected over time (Fig. 2di). The photons emitted from the fluorophores are distributed in diffraction-limited spots and registered in a stack of time-resolved images until all of the fluorophores have been read out. The spots can be identified by image-processing algorithms, allowing the positions of the fluorophores and other properties (fluorescence intensity, duration of fluorescence, precision of the positioning fit, etc.) to be precisely determined and then stored in a large table (Fig. 2dii). Using the fluorophore centroids, a super-resolved image is reconstructed (Fig. 2diii).

The resolution limit of SMLM is mainly determined by the precision with which individual fluorophores are localized, which can be simplified to

$$d_{\mathrm{SMLM}} \approx \frac{d}{\sqrt{\mathrm{N}}},$$

where $d$ is the conventional resolution limit and $N$ is the number of photons detected in a single fluorescence spot [46].

SMLM approaches are more sensitive to background signals than both of the previously described methods, as SMLM determines the positions of individual molecules to a high precision based on their individual fluorescence levels. To assign as many photons as possible to a single fluorophore, it is highly desirable to achieve the best possible signal-to-noise ratio. For thin (mainly two-dimensional) samples, effective background noise reduction can be achieved using total internal reflection fluorescence microscopy (TIRF), where the incident laser light is totally internally reflected at the glass–water boundary between the coverslip and sample [47]. In this illumination scheme, only the fluorophores in a very thin layer within the exponentially decaying evanescent field above the coverslip can fluoresce. Thus, a large fraction of the usual background signal caused by autofluorescence or by the scattering of the laser light and originating from the whole sample volume is suppressed. Another approach is to illuminate the sample in a highly inclined and laminated optical sheet (HILO) [48]. In this mode, the excitation laser light leaves the objective at a very narrow angle, which results in an inclined beam passing through the sample. This illumination in the form of an optical light sheet is then almost perpendicular to the detection path of the microscope.

To allow for three-dimensional SMLM imaging, several optical methods have been utilized to encode the third dimension: astigmatic PSF shaping by a cylindrical lens, biplane alignment, a dual-objective scheme allowing for the interference of the signal, and several further phase modulations have been developed that (for example) create a double-helically arranged PSF or a self-bending PSF which spans a large field of view at isotropic resolution [1]. These three-dimensional SMLM read-out schemes can be combined with spatially confined activation approaches based on temporal focusing [49], selective plane illumination microscopy [50], or lattice light sheet illumination [51].

SMLM allows for multicolor imaging if the photoswitching mechanisms of the fluorophores used fit together well; i.e., when they tolerate the same imaging environment such as the same specialized switching buffers [52–54] or a mounting medium combined with high laser intensities [55], by employing complementary photoactivation schemes [56, 57], or by using dye activator–reporter pairs [58]. Most multicolor approaches are assisted by sophisticated read-out schemes [59–63]. We discuss how to choose appropriate fluorophores to use in a particular study and the parameters that should be taken into account in the next section of this review, where we introduce the basic photophysics and explain how to switch or stabilize fluorophores.

Structural live-cell SMLM imaging of only slowly changing structures can be performed as the imaging speed is fast compared to the phenomenon being imaged. For these structures, it is possible to capture a sufficient number of subsets of fluorophores to fill a subdiffraction sampling space before the structure has changed significantly. Nevertheless, a gain in temporal resolution will always result in a loss of structural spatial resolution caused by lower sampling, and vice versa [55, 64–66]. Uniquely, SMLM can be combined with single-particle tracking (SPT); unlike diffraction-limited SPT methods, where only a strictly limited number of fluorophores can be followed per cell to keep them separable, sptPALM [67] is readily capable of measuring a large batch of statistics on single-molecule tracks for the same type of molecule inside a single cell by sequential photoactivation. It is thus possible to obtain spatially and temporally highly resolved diffusion maps that combine a multitude of tracks and accordingly unravel possible dynamic heterogeneities and subpopulations. sptPALM has been applied to a wide range of biological systems (some examples are given in [68–70]), and can be combined with structural SMLM imaging [71]. It is nevertheless important to note that the minimum time needed to precisely localize a single fluorophore is influenced by imaging parameters such as the camera sensitivity, the minimum applicable acquisition times (in the range of a few milliseconds), as well as the contrast of the fluorophore (determined by its quantum yield in the specific sample, the laser intensities, and the background noise). This means that sptPALM is only well suited to studying slow diffusion processes, where the fluorophores move slowly compared to the image acquisition time; it is not applicable to processes with faster dynamics such as that visualized in Fig. 1b.

## Designing the optimal experiment

### Choosing a suitable fluorophore

Normally, fluorophores reside in their most relaxed molecular state, the electronic ground state ($S_0$). When a fluorophore absorbs a photon, it is excited within femtoseconds to a higher energy state ($S_1$, $S_2$, …, $S_n$). Depending on the exact energy of the absorbed photon, the fluorophore can be excited to various energy levels that correspond to its electronic, vibrational, and rotational molecular configurations. As depicted in Fig. 3a (in which, for simplicity, only the $S_0$, $S_1$, and $T_1$ electronic states and the vibrational states for $S_1$ are shown), the fluorophore then relaxes within picoseconds to the lowest level of the excited electronic state $S_1$, transferring its vibrational energy to its surroundings.

The time a fluorophore spends in the lowest level of the excited state, often called the fluorescence lifetime, is normally in the nanosecond range, though it depends on the specific molecule and its environment. When returning to the electronic ground state, nonfluorescing molecules release their energy through nonradiative processes such as internal conversion. Fluorophores, on the other hand, exhibit a high probability of a radiative transition; they release energy through the emission of a single fluorescence photon. As a portion of the energy is also lost before this transition through vibrational state relaxation, the fluorescence photon actually has a longer wavelength than the wavelength of the photon originally absorbed. This phenomenon is known as the Stokes shift.

Besides relaxing directly to the ground state through either photon emission or nonradiative internal conversion, an excited fluorophore can release its excess energy by undergoing several other intramolecular and intermolecular processes. Such events decrease the photon yield and are collectively termed quenching. Through the intramolecular transition process known as intersystem crossing, fluorophores can reach an intermediate energy state called the triplet state ($T_1$). This process involves flipping the spin of the excited electron, and has a miniscule probability (i.e., it is quantum-mechanically forbidden) of occurring during each excitation–relaxation cycle. The triplet state has a much longer lifetime, typically several microseconds, during which the excited molecule remains prone to electron transfer reactions. The result of such a reaction can be a nonfluorescent radical state ($F^{\bullet -}$) in which the fluorophore can remain for several seconds or even minutes. Occasionally it can result in irreversible destruction of the fluorophore through photobleaching processes, leading to a permanent loss of fluorescence. Other dark, nonfluorescent states can be caused by conformational changes in the chromophore, the formation of complexes with other molecules, or a collision with a molecule that is capable of receiving the fluorophore's surplus energy (e.g., oxygen, halogens, and amines). Collisional quenching requires direct proximity of the quencher molecule to the chromophore, and its rate is drastically decreased in fluorescent proteins where the chromophore is protected by its beta-sheet barrel (Fig. 3bi). Finally, the energy of an excited fluorophore can also be transferred to another molecule by photoinduced electron transfer (PET) or Förster resonance energy transfer (FRET), both of which are often exploited in advanced imaging schemes that measure interaction dynamics within or between proteins of interest [82].

The most common types of fluorophores are fluorescent proteins such as GFP (Fig. 3bi) and organic dyes such as rhodamines, carbocyanines, and oxazines (Fig. 3bii). At the heart of every fluorophore is the chromophore, a conjugated π-electron system that gives a molecule its light-absorbing properties. A chromophore can consist of aromatic rings as well as C=C, C=O, or N=N bonds. Its spectral properties are determined by the length of the conjugated electronic system, the number of electrons, and different substituents [83]. Usually, elongation of the conjugated system will shift the absorption maximum and thus also the emission maximum to longer wavelengths. This can easily be seen in cyanines, a class of fluorescent dyes with different polymethine chain lengths. Stretching the chain from Cy3 to Cy7 shifts the emission spectrum from green to dark red (Fig. 3bii). Every fluorophore thus possesses a unique excitation and emission spectrum. These spectra need to be compatible with the available microscopic system (i.e., in terms of illumination wavelengths, spectral filter combinations, or the sensitivity of the given detector). The excitation and emission wavelengths should be separated by a sufficiently large Stokes shift, and, in multicolor experiments, the chosen set of fluorophores should exhibit sharp and defined spectra with ideally no overlap, thus minimizing crosstalk between the different colors. Alternatively, overlapping spectra can be separated by spectral demixing approaches, which also nicely avoid chromatic aberrations and can allow the use of a single excitation source [60–63]. Sample specifications must also be taken into account; live cells are usually more sensitive to irradiation with shorter-wavelength light; imaging for extended periods of time with light in the ultraviolet (UV) range can lead to a range of defects in cells, from DNA damage to death [84]. Certain biological samples exhibit pronounced autofluorescence in some spectral ranges, usually in shorter wavelengths. The majority of this background fluorescence is caused by aromatic amino acids (mainly tryptophan), the phosphate chain of DNA, intracellular nicotinamide adenine dinucleotide (NADH), and coenzymes [85]. Longer wavelengths of light can penetrate deeper into a tissue, making red and near-infrared fluorophores the most suitable for imaging thicker samples [18].

The chosen fluorophore should be as bright as possible to ensure that sufficient signal is detected to allow it to be distinguished from the background. This is especially crucial for single-molecule imaging when the fluorescence of individual fluorophores is captured. The fluorophore's brightness is determined by its dipole orientation in relation to the excitation light, its extinction coefficient (which quantifies how well a

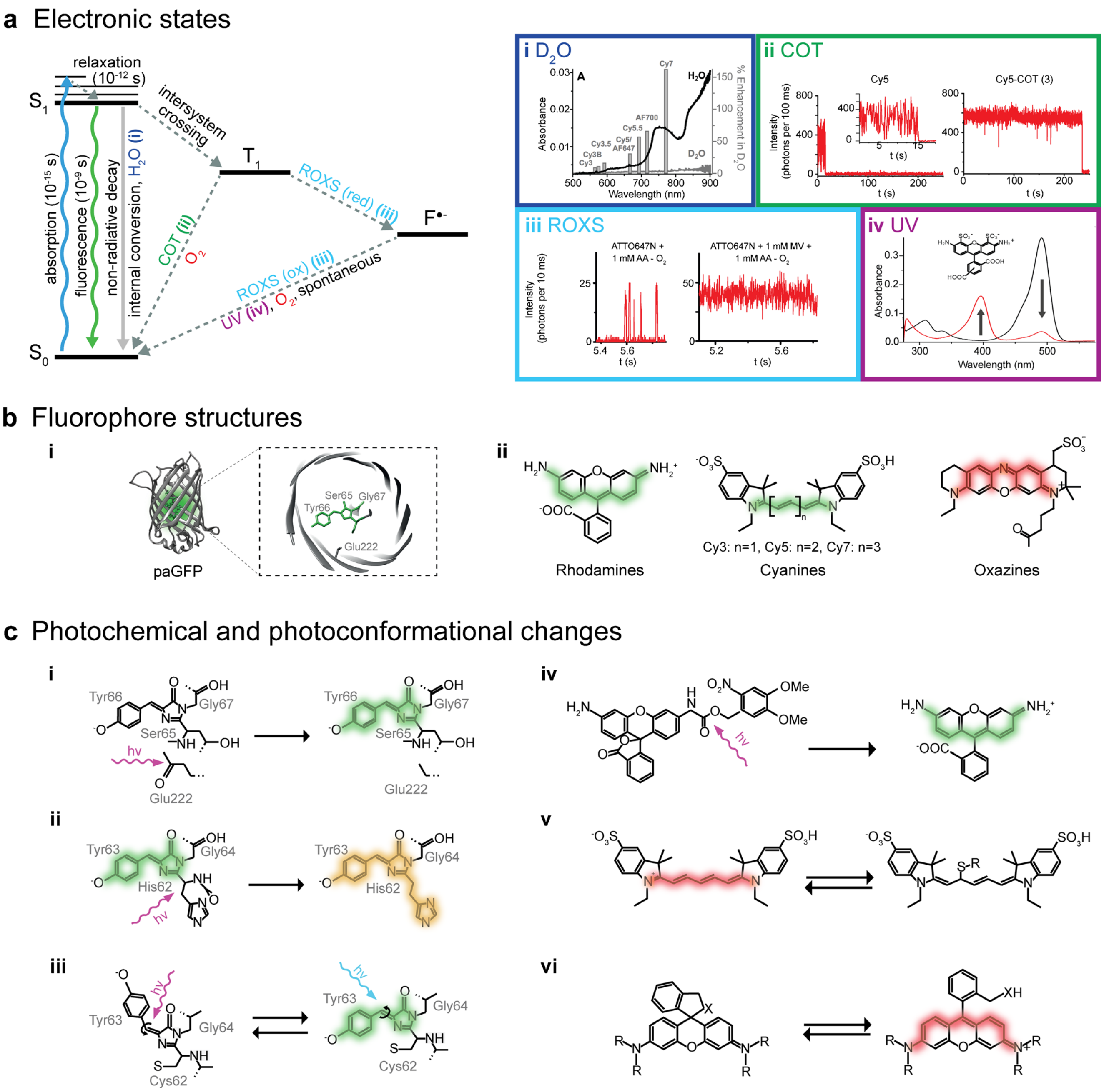

**Fig. 3a–b** Photophysics and photochemistry of fluorophores. **a** *Left*: Jabłoński energy diagram representing energy states and transitions of a fluorophore. *$S_0$* ground singlet state, *$S_1$* excited singlet state, *$T_1$* triplet state, *$F^{\bullet-}$* radical state. Different compounds can affect brightness and photostability or shift the fluorophore into a radical state. (*i*) absorption spectra of $H_2O$ and $D_2O$, and correlated enhancements of the fluorescence emissions of different fluorophores in $D_2O$ versus $H_2O$ for the visible range of light. Adapted from [72] with permission. (*ii*) Cyclooctatetraene (COT) quenches the triplet state by quickly transferring fluorophores back into the ground state and thus stabilizes the fluorescence. Adapted with permission from [73]. (*iii*) A reducing and oxidizing system (ROXS) accelerates the transition of a fluorophore from its triplet state back to the electronic ground state by performing fast sequential reducing and oxidizing steps. Adapted with permission from [74]. (*iv*) The radical states of some dyes (e.g., the Alexa Fluor 488 fluorophore, as shown in *black* here; *red* indicates the radical) possess an absorption peak in the UV range. By exciting the radicals with UV light to higher intermediate states, they can be quickly brought back down to their electronic ground state. Adapted with permission from [75]. **b** Different fluorophore structures: (*i*) Barrel structure of the photoactivatable green fluorescent protein (paGFP) and a close-up of its chromophore. (*ii*) Overview of organic dye classes. **c** Different photochemical and conformational changes that affect fluorescence: (*i*) photoactivation of paGFP [76], (*ii*) green-to-red photoconversion of mEos2 [77], (*iii*) reversible *cis*/*trans*-photoswitching of Dronpa [78], (*iv*) cleavage of a photocage from a rhodamine [79], (*v*) reversible fluorescence quenching of Cy5 by covalent binding of a thiol [80], and (*vi*) reversible cyclization of rhodamine HMSiR [81]

fluorophore absorbs a certain wavelength), and its quantum yield (the ratio of absorbed to emitted photons). Ideally, the excited fluorophore would emit a single photon in every excitation–emission cycle, thus exhibiting a quantum yield of 1. However, due to the alternative process of excited-state relaxation described earlier, this is not the case in practice. A fluorophore featuring a relatively low quantum yield can nevertheless produce a sufficient fluorescent signal, provided that its extinction coefficient is high enough and its rate of entry into the excited state is maximized by applying high excitation light intensities, leading to more rapid cycling through the excitation–emission cycle (Fig. 3a).

A constant flux of emitted photons (i.e., the fluorophore's photostability) is another important factor. Fluctuations in fluorescence can be attributed to reversible or irreversible losses of fluorescence, and depend on the chemical properties of the fluorophore, its environment, and the light intensities that it is exposed to. Oxygen and reactive oxygen species play a large role in irreversible bleaching, which is caused by a permanent change in the molecular structure of the fluorophore [86]. Absorption of a second photon while already in the excited state is believed to be another major cause of photobleaching. Low irreversible bleaching rates allow for longer measurements or at higher excitation light intensities. Reversible losses of fluorescence are caused by transitions to several intermediate nonfluorescent electronic or conformational states, as sketched in Fig. 3a. Minimizing the time a fluorophore spends in these states improves the fluorescence signal stability and increases the time that a fluorophore spends performing its excitation–emission cycle, yielding a more constant photon flux.

The solubility and cell permeability of fluorophores must also be considered. Relatively few fluorophores can be transported through a live cell membrane (these are highlighted in Table 2) due to either size or charge constraints. Fluorescent proteins are highly live-cell compatible but can be a steric hindrance in some cases, and can impact cell viability when fused to certain proteins. They have also been shown to form artificial aggregates, depending on the abundance and spatial organization of the target molecule [122].

Importantly, each super-resolution technique has special demands. The most common fluorophores employed, their properties, and (in the case of SMLM) the most popular multi-color combinations are given in Table 2. In STED, the molecules are constantly forced from the excited state into the electronic ground state via stimulated emission. Fluorophores with high extinction coefficients, high quantum yields, and high stimulated emission cross-sections are favorable, as they allow for the best possible contrast in the detection of the fluorescing fluorophores left in the center of the excitation pattern. The rate of stimulated depletion of the excited state scales with the depletion energy applied, so fluorophores chosen for STED have to be exceptionally photostable. Further, the depletion wavelength should be carefully chosen to ensure that it does not re-excite any of the fluorophores that are depleted to the ground state. For SIM, the most crucial parameters are the photostability and overall brightness of the fluorophore, as the technique works by measuring the fluorescence response of a defined patterned excitation. This modulation of fluorescence should be clearly detectable based on a strong and inherently stable fluorescence signal. Since illumination-independent fluctuations in fluorescence result in artifacts, the use of an effective antifading agent is common practice. Almost all modern fluorophores can be used for SIM (which is why we do not provide a selection of SIM fluorophores in Table 2). Finally, for SMLM techniques, rigid control of photoswitching is crucial. The nonfluorescing dark times of the fluorophores must be long enough to guarantee the separation of single-molecule signals in the sample at any time during the experiment. Even when applying algorithms that can handle high numbers of fluorescent molecules at a time, the techniques are easily impaired when the density of molecules is too high [123].

The dye Alexa Fluor 647 is the fluorophore of choice in a great majority of fixed cell SMLM studies, due to its robust photoswitching and good photon yields. Since it is not membrane permeable, ATTO 655, tetramethylrhodamine, SiR, and Oregon Green are utilized in most live cell studies. When multicolor imaging is desired, Alexa Fluor 568 and 532 are often used with Alexa Fluor 647. Fluorescent proteins are more suitable for quantitative approaches or noninvasive live cell studies. A collection of popular fluorophores as well as multicolor schemes is provided in Table 2. In this context, different photoswitching strategies (as evaluated in detail below) require individual optimizations such as customized specific photoactivation and photoconversion efficiencies for convertible fluorophores that allow for sequential activation [57] and tailored imaging buffers for selected organic dyes.

Even more complex imaging experiments involve additional considerations, such as the need to carefully choose the spectral overlap between donor emission and acceptor excitation for optimal FRET, the selection of appropriate strategies for optimal multiphoton absorbance or when utilizing fluorophores as biosensors [82].

## Labeling strategies

Choosing a strategy to label the biomolecule of interest is a crucial part of the experiment. Luckily, strategies suitable for many biological applications are commercially available and, for the best results, experiments should be planned with the labeling strategy in mind from the very beginning. It is important to emphasize that it is always the label attached to the molecule of interest that is visualized, not the molecule itself—the signal we see on the microscope is a label's length away. Using large labels in combination with high resolutions

**Table 2** List of recommended and promising new fluorophores for super-resolution microscopy

**STED**

| | Name | Appl. | Exc (nm) | Em (nm) | STED (nm) | Structure | ε ($M^{-1} * cm^{-1}$) | φ |
|---|---|---|---|---|---|---|---|---|
| Fluorescent proteins | **Citrine** | [23] | 516 | 529 | 595 | m | 77 000 | 0.76 |
| | **eYFP** | [30] | 514 | 527 | 598 | m | 84 000 | 0.61 |
| | **Dronpa** | [31] | 503 | 517 | 488 (405) | m | 95 000 | 0.85 |
| | **eGFP** | [30] | 488 | 510 | 575 | m | 55 000 | 0.6 |
| Organic dyes | **SiR (§)** | [87] | 652 | 674 | 775 | r | 100 000 | 0.32 |
| | **ATTO 647N** | [22] | 646 | 664 | 750 | r | 150 000 | 0.65 |
| | **AberriorStar635P** | [29] | 635 | 651 | 750-780 | | 125 000 | 0.92 |
| | **ATTO 594** | [29] | 603 | 626 | 775 | r | 120 000 | 0.85 |
| | **Alexa Fluor 594** | [88] | 590 | 617 | 690 | r | 92 000 | 0.66 |
| | **ATTO 565** | [22] | 564 | 590 | 640-660 | r | 120 000 | 0.9 |
| | **Aberrior Star 488** | [89] | 503 | 524 | 585-605 | | 64 500 | 0.89 |
| | **Alexa Fluor 488 (§)** | [23] | 495 | 519 | 592 | r | 83 000 | 0.92 |
| | **Aberrior Star 440SXP** | [89] | 432 | 511 | 590-620 | | 33 000 | 0.57 |

**SMLM**

| | Name | Appl. | Exc (nm) | Em (nm) | Act/con (nm) | UV abs radical state* | Structure | ε ($M^{-1} * cm^{-1}$) | φ | Dual color combinations | Triple color combinations |
|---|---|---|---|---|---|---|---|---|---|---|---|
| Fluorescent proteins | **mEos2 (G)** | [77] | 506 | 519 | | | m | 56 000 | 0.84 | AF 647 [90-92], ATTO 655 [53], Caged SiRhQ [57], Dronpa [56], psCFP2 [56] | |
| | **mEos2 (R)** | | 573 | 584 | 405 | | | 46 000 | 0.66 | | |
| | **PAmCherry1** | [59] | 564 | 595 | 405 | | m | 18 000 | 0.46 | paGFP [59] | eYFP + NileRed [93],<br>PAmKate + Dendra2 [60] |
| | **Dendra2 (G)** | [94] | 490 | 507 | | | m | 45 000 | 0.5 | | PAmKate + PAmCherry1 [60] |
| | **Dendra2 (R)** | | 553 | 573 | 405, 488 | | | 35 000 | 0.55 | | |
| | **paGFP** | [95] | 504 | 517 | 405 | | m | 17 400 | 0.79 | PAmCherry [59] | PAmKate + PAmCherry1 [60],<br>PAtagRFP + ATTO 655 [95] |
| Organic dyes | **Alexa Fluor 750** | [96] | 749 | 775 | | ++ | c | 290 000 | 0.12 | AF 647 [97] | |
| | **CF 680** | [63] | 681 | 698 | | - | c | 210 000 | | AF 647 (#) [62, 98, 99] | CF 660C + DyLight 650 + Dy 634 (#) [62], CF 647 + CF 568 (#) [63] |
| | **ATTO 655 (§)** | [100] | 663 | 680 | | + | o | 125 000 | 0.3 | ATTO 520 [52], mEos2 [53] | PAtagRFP + paGFP [95] |
| | **SiR (§)** | [101] | 652 | 674 | | - | r | 100 000 | 0.08 - 0.32 | mEos2 [57] | TMR + paGFP [102] |
| | **Alexa Fluor 647** | [10] | 650 | 665 | | ++ | c | 270 000 | 0.33 | ATTO 520 [103], AF 532 [104, 105], ATTO 532 [54], AF 546 [54], AF 568 [54], TMR [106], mEos2 [90-92], AF 488 [91], psCFP2 [56], mMaple [99], ATTO 488 [107], CF 680 (#) [62,98, 99], AF 700 (#) [61], AF 750 (#) [97], Dy678 (#) [108], Dronpa [109] | AF 568 + ATTO 488 [107] |
| | **CF 647** | [110] | 650 | 665 | | | c | 270 000 | | | CF 680 (#) + CF 568 [63] |
| | **Cy5** | [10] | 646 | 670 | | ++ | c | 250 000 | 0.28 | | |
| | **Alexa Fluor 568** | [75] | 578 | 603 | | + | r | 91 300 | 0.69 | AF 647 [54] | AF 647 + ATTO 488 [107] |
| | **CF 568** | [63] | 562 | 583 | | - | | 88 000 | | | CF 680 + CF 647 [63] |
| | **TMR (§)** | [106] | 557 | 576 | | - | r | | | AF 647 [106], Citrine [55] | SiR + paGFP [102] |
| | **Alexa Fluor 532** | [75] | 532 | 554 | | + | r | 81 000 | 0.61 | AF 647 [104, 105] | |
| | **ATTO 520** | [111] | 517 | 538 | | + | o | 110 000 | 0.9 | AF 647 [103], ATTO 655 [52] | |
| | **Alexa Fluor 488 (§)** | [111] | 490 | 519 | | + | r | 73 000 | 0.92 | AF 647 [91] | AF 647 + AF 568 [107],<br>Cy3 + ATTO 532 [55],<br>Rhodamine 3C + AF 514 [55] |
| | **Cy5/AF 647 readout dye pairs** | [9] | | 670 | | | | | | Reporter: AF 750 [112]<br>Activator: Cy3 + AF 405 [112] | Reporters: Cy7 + Cy5.5 [58]<br>Activators: Cy3 + Cy2 + AF 405 [58] |

**New promising fluorophores**

| Name | Ref. | Exc (nm) | Em (nm) | Act/con (nm) | Structure | ε ($M^{-1} * cm^{-1}$) | φ | Comments |
|---|---|---|---|---|---|---|---|---|
| **mEos3.1 (G)** | [113] | 505 | 513 | | m | 8 840 | 0.83 | Lower tendency for oligomerization than mEos2. |
| **mEos3.1 (R)** | | 570 | 580 | 405 | | 33 500 | 0.62 | |
| **mEos3.2 (G)** | [113] | 507 | 516 | | m | 63 400 | 0.84 | Lower tendency for oligomerization than mEos2. |
| **mEos3.2 (R)** | | 572 | 580 | 405 | | 32 200 | 0.55 | |
| **mEos4 (G)** | [114] | 505 | 516 | | m | ~ 80 000 | 0.85 | Fluorescence comparable to precursor, but lower tendency for oligomerization. |
| **mEos4 (R)** | | 570 | 580 | 405 | | ~ 58 000 | 0.71 | |
| **mMaple3 (G)** | [115] | 489 | 505 | | m | | | Improved version of mMaple. |
| **mMaple3 (R)** | | 566 | 583 | 405 | | | | |
| **NijiFP (G)** | [116] | 469 | 507 | | m | 41 100 | 0.64 | Reversibly photoswitchable in both colors. |
| **NijiFP (R)** | | 526 | 569 | 405 | | 42 000 | 0.65 | |
| **Skylan-S** | [117] | 499 | 513 | 405 | m | 152 400 | 0.64 | High brightness and photostability. |
| **HMSiR (§)** | [81] | 650 | 670 | | r | 100 000 | 0.39 | Cell-permeable, laser intensity-independent blinking. |

Numbers are taken from the manufacturers and from [59, 77, 81, 94, 101, 113–120]

*Appl* Example of the use of the fluorophore for super-resolution microscopy, *Exc* excitation peak, *Em* emission peak, *Act/con* activation or conversion wavelength, $\varepsilon$ molar extinction, $\varphi$ quantum yield, *m* monomeric, *c* cyanine, *o* oxazine, *r* rhodamine, (§) cell-permeable dyes

* [75, 121]; (#) spectral demixing

**Table 3** Summary of labeling strategies commonly used in super-resolution microscopy

| | Label | Appl. | Size | Description | Possible uses | Considerations |
|---|---|---|---|---|---|---|
| Affinity binding | **Antibody IgG or Fab fragment** | [125] | Up to 20 nm | IgG: antigen-specific immunoglobulin G antibodies consisting of two identical heavy chains and two identical light chains arranged in a Y-shape.<br>Fab: antigen-specific monovalent fragments from IgG and IgM, consisting of the variable regions of both heavy and light chains linked by a disulfide bond. | Classic immunofluorescence by primary and secondary antibody combination. | Requires no genetic modification of the target.<br>Modular, as secondary antibodies are available for a wide range of fluorophores.<br>Large tags which limit the image resolution.<br>Not cell-permeable, thus limiting live-cell staining as specialized delivery method is needed.<br>Prone to background from nonspecific labeling. |
| | **Nanobody** | [4, 126] | ~ 3 nm | Antigen-specific single variable domain (VHH) of single-chain antibody with nanomolar affinity. | Live-cell stain by recombinant expression of antigen-specific nanobody and fluorescent protein in living cells.<br>Classic immunofluorescence stain without the need for a secondary antibody. | Anti-GFP nanobody is a popular stain.<br>Live-cell stain results in nonspecific background due to lack of washing.<br>Prone to background in SMLM. |
| Click chemistry | **Unnatural amino acids** | [127] | < 1 nm | Not naturally occurring and chemically reactive cell component analogues, mostly with alkyne or azide groups for Huisgen cycloaddition. | Nonspecific labeling of newly synthesized proteins, membranes, nucleic acids.<br>Pulse labeling for a short time period.<br>Site-specific labeling of proteins by codon reassigment methods. | Require no genetic modification of the target for nonspecific incorporation.<br>Modular, as a large selection of fluorophores with reactive groups are available.<br>Incorporation of analogues may impact cell physiology.<br>Live-cell staining only possible for cell-permeable fluorophores or a specialized delivery method. |
| | **Unnatural lipids** | [128] | | | | |
| | **Unnatural nucleotides** | [129] | | | | |
| FISH | **Fluorescent oligonucleotides** | [130] | < 1 nm | Fluorescently labeled oligonucleotides | Sequence-specific 16S rRNA stain.<br>Specific gene/genetic region DNA stain.<br>RNA stain. | Highly modular: various oligonucleotides can be designed and coupled to a large selection of fluorophores.<br>Limited compatibility with live-cell studies due to harsh hybridization conditions. |
| Target specific drugs | **MitoTracker** | [35] | < 1 nm | Various small molecules that bind to specific targets. | Staining of fixed cells.<br>Live-cell staining for cell-permeable drugs. | Large selection of drugs coupled to various fluorophores.<br>Live-cell staining only possible for cell-permeable fluorophores or specialized delivery method. |
| | **LysoTracker** | [131] | | | | |
| | **Phalloidin** | [87] | | | | |
| | **SiR-Tubulin** | [132] | | | | |
| | **SiR-Actin** | [132] | | | | |
| | **SiR-DNA** | [133] | | | | |
| | **DAPI** | [37] | | | | |
| | **mCling** | [134] | | | | |
| | **LifeAct** | [13] | | | | |
| Genetic fusions | **SNAP** | [135] | ~ 3 nm | Genetic fusion of ligand binding enzyme to protein of interest. | Stable cell line under endogenous promoter.<br>Transient plasmid with known/inducible expression.<br>Staining with ligand coupled to fluorophore of choice. | Large selection of ligands coupled to various fluorophores.<br>Require an additional staining step which is highly specific and covalent.<br>Genetic fusion may interfere with protein localization and function.<br>Live-cell staining only possible for cell-permeable fluorophores or specialized delivery methods. |
| | **CLIP** | [136] | | | | |
| | **HALO** | [137] | | | | |
| | **eDHFR** | [138] | | | | |
| | **Fluorescent proteins** | [118] | ~ 3 nm | Genetic fusion of fluorophore to protein of interest. | Stable cell line under endogenous promoter.<br>Transient plasmid with known/inducible expression. | Live-cell imaging.<br>No need for staining step adding external fluorophores during the sample preparation.<br>Highly specific tag.<br>Genetic fusion may interfere with protein localization and function.<br>Factors like maturation time or misfolding must be taken into account.<br>Some fluorescent proteins tend to artificially aggregate for concentrations above a certain threshold. |

can thus lead to artificial inflation of the structure [4, 5]. The size and dipole orientation of the fluorophore and the achievable labeling density directly impact the resolution attained. High density—which requires at least an average nearest-neighbor label distance of less than twice the sampling rate according to the Shannon–Nyquist criterion—is necessary

[124], or important sample information can be missed. Here, we evaluate the common strategies used (see also Table 3).

Affinity-based labeling is probably the approach most widely used across all fluorescence microscopy applications [104, 105, 125, 139]. Antibodies can target virtually any cellular component as an antigen, making the technique extremely flexible. Using combinations of primary and secondary antibodies also makes the approach very modular. Nevertheless, the technique suffers from several drawbacks. First, background due to nonspecific staining is quite common [140], and antibodies may detach from their targets when irradiated with high laser intensities [141]. Second, a typical primary and secondary antibody combination is ~20 nm in size, which is sufficient to cause imaging artifacts at resolutions realized in super-resolution microscopy. Nanobodies [4], ~3 nm single-variable domains of single-chain antibodies isolated from cameloids, virtually eliminate this size problem. They can also be fused to fluorescent proteins and recombinantly expressed in live cells [126]. Aptamers—small RNA structures that function much like antibodies and are suitable for live-cell staining [142]—are worth mentioning, though their use is currently limited by poor availability. Much promise is shown by the GFP mimic family of aptamers, which form a GFP-like chromophore when bound to a nonfluorescent substrate [143].

Click chemistry is the term used to describe a set of reactions that occur at high yields in aqueous environments under mild conditions. It thus allows for effective labeling of biomolecules based on the incorporation of unnatural analogues of amino acids [127], nucleotides [129], or lipids [128] carrying a reactive chemical group such as an alkyne, azide, or cyclooctene into cellular structures. Fluorophores carrying the complementary group can then be covalently bound via (for example) cycloaddition [129]. Live-cell imaging is possible with some modifications [144]. This method is suitable for imaging DNA, RNA, proteins, and membranes, and produces very low background fluorescence but usually does not target specific biomolecules. Genetically programmable site-specific unnatural amino acid incorporation can be realized by codon reassignment [145, 146].

Fluorescence in situ hybridization (FISH) [130] allows nucleic acids to be labeled by complementary oligonucleotide probes coupled to fluorophores. The technique is often employed with 16S rRNA complementary probes to study microbe communities [147]. In super-resolution applications, it is a powerful tool for studying chromatin structure and organization, gene location [148, 149], RNA localization and quantification [148], telomere structure [150], etc. As the hybridization protocols involve harsh chemical and temperature treatments, this technique has limited live-cell compatibility.

Engineered ligand-binding enzymes which are genetically fused to the protein of interest are the basis of protein tags such as SNAP [135], CLIP [136], HALO [137], and eDHFR [138]. Such an enzyme label can then be stained by covalently binding its fluorophore-bound specific ligand (benzylguanine, benzylcytosine, chloroalkanes, and trimethoprim, respectively). Such ligands can be fused to virtually any fluorophore, which makes these tags very popular in multicolor applications [66, 95, 106].

Specific labeling options are available for several targets. Fluorescently labeled phalloidin is a toxin commonly used as a filamentous actin stain [87]. SiR-actin, SiR-tubulin [132], and LifeAct [13] are live-cell cytoskeleton stains. Some fluorescently labeled lipid analogues [151] and the recently developed mCling peptide [134] have been used as direct membrane stains. Other target-specific drugs include organelle specific probes such as the mitochondrion stain MitoTracker [35], the lysosome stain LysoTracker, or the ER stain ER-Tracker [131].

All these methods require the introduction of an extrinsic fluorophore into the cell. In fixed cells, this is usually not an issue, and this process can be greatly facilitated by introducing a permeabilization step in which the cell membrane or wall is perforated. Live-cell applications necessitate the use of membrane-permeable fluorophores such as the rhodamine dyes SiR [101], TMR-STAR [106], and Oregon Green [66] and, to a lesser degree, some oxazine dyes such as ATTO 655 [95]. Membrane permeability can be improved by performing certain modifications such as fusion to a permeable peptide [152]. Many alternative strategies for fluorophore delivery, such as electroporation, bead loading, membrane transfer, and micro- or nanoinjection techniques have been developed over the years [153–157].

The discovery and subsequent cloning of green fluorescent protein (GFP) [158] introduced the possibility of small, endogenous, and inherently fluorescent labels. Fluorescent protein fusions, which require no further staining, have become a widespread labeling strategy and are available in a variety of colors [118]. They are highly suited to live-cell studies as long as the cells are carefully checked for physiology after the genetic modification. Unfortunately, they exhibit relatively poor photostability and at best a fifth of the brightness of organic dyes [159]. Since the resolution achievable in SMLM increases with the square root of the amount of photons emitted by a single fluorophore, this can directly impact the resolution of SMLM [46]. Factors such as protein folding as well as the efficiency and velocity of chromophore maturation are important and can differ depending on the environment, e.g., the presence of molecular oxygen is usually needed for final chromophore maturation [160, 161]. Their properties can be readily modified by changing the amino acid sequence, and several versions have been designed to have improved brightness and photostability [162] and switching properties for SMLM imaging. These include photoactivatable proteins such as paGFP [119] and PAmCherry1 [59], reversibly switchable FPs such as Dronpa [120] and Dreiklang [163], and photoconvertible FPs such as Kaede [164], mEos2 [77], or Dendra2 [94]. An often overlooked factor is codon usage bias, and all endogenous tags, including self-labeling enzymes, should be codon-optimized for the organism used [165].

## Controlling the fluorescence of the sample

Robust control of the molecular states is crucial in most super-resolution microscopy applications. Certain steps can be taken to improve the stability, longevity, and intensity of fluorescence, as well as to achieve the on and off switching required for SMLM.

Considering that most microscope cameras record with millisecond-range exposure times, triplet-state transitions and collisional quenching events—which occur several orders of magnitude faster than these exposure times—are not registered as individual events but rather as a loss of signal intensity. Collisional quenching is mostly avoided by imaging in defined, impurity-free buffer solutions, though water shows absorbance in the visible range of light due to its molecular vibrations, as shown in Fig. 3ai. When these molecular vibrations are in resonance with the emission wavelength of a fluorophore, the fluorophore can transfer its excited-state energy to a water molecule during a collision. Heavy-water ($D_2O$) molecules vibrate at significantly lower frequencies due to the presence of deuterium. Substituting water in the imaging solution with $D_2O$ thus increases the overall photon yield. The magnitude of fluorescence enhancement in $D_2O$ versus $H_2O$ for a specific fluorophore thus correlates with the spectral overlap of the light absorption of $H_2O$ with the emission of the fluorophore, as seen for different fluorophores in Fig. 3ai [72].

Molecular oxygen plays an important role in many of the fluorophore's electronic state transitions. Since the ground state of molecular oxygen is also a triplet, it easily reacts with a triplet-state fluorophore in an electron transfer reaction. This can return the fluorophore to its ground state, but it also produces singlet oxygen and reactive oxygen species (ROS), which can then cause irreversible photobleaching [86]. To avoid the bleaching caused by a buildup of ROS, oxygen can be removed from the imaging solution by adding enzymatic systems such as a combination of glucose oxidase, glucose, and catalase (GLOX) [166], a mix of protocatechuate dioxygenase and protocatechuic acid (PCA/PCD) [167], or a system containing pyranose oxidase, glucose, and catalase [168], as summarized in Table 4. It is worth mentioning that it has recently been reported that most commercial glucose oxidase preparations used in the popular GLOX system suffer from nuclease contamination. Such contamination can cause fluorescent background and introduce artifacts into nucleic acid studies. Furthermore, the GLOX reaction lowers the pH of the solution over time, while other systems do not [177]. Fast, efficient chemical oxygen removal has also been reported to be achieved with methylene blue (MB) and mercaptoethylamine (MEA) [170].

However, since oxygen is such an efficient triplet-state quencher, its depletion can result in a high fraction of fluorophores populating the triplet state, significantly impairing the photon yield. There are several strategies that enable us to circumvent this problem while still removing the risk of bleaching by ROS. The first is to add the chemical cyclooctatetraene (COT), which, much like oxygen, directly returns triplet-state fluorophores to their ground states. As this process significantly shortens the residence time of the fluorophore in the triplet state, the overall fluorescence is stabilized and intensity fluctuations are reduced, as shown in Fig. 3aii [73, 176].

The second approach is to quench the triplet state by colliding the fluorophore with certain reducing agents, thus converting it into the dark, nonfluorescent, anionic radical form $F^{\bullet-}$, as shown in Fig. 3aiii. To do this, chemicals such as mercaptoethylamine (MEA) [176, 178], β-mercaptoethanol (BME) [166], dithiothreitol (DTT) [111], glutathione (GSH) [111], 6-hydroxy-2,5,7,8-tetramethylchroman-2-carboxylic acid (Trolox) [174, 179], ascorbic acid (AA) [74], and potassium iodide (KI) [180] can be added to the imaging buffer. However, to return to the ground state, the $F^{\bullet-}$ fluorophore must be oxidized, a task in which oxygen again plays a crucial role. Removing oxygen can thus lead to very long $F^{\bullet-}$ dark states, a property exploited in SMLM. Using high excitation light intensities ensures that the fluorophores are quickly cycled into the triplet state, from where they are promptly reduced to the dark radical state. Cyanine fluorophores such as Alexa Fluor 647 require a primary thiol (e.g., BME, MEA, GSH, or DTT) in the switching buffer, and undergo a thiol group addition reaction at one of the C atoms in the π-system (Fig. 3cv) [80]. A similar effect can be observed with a phosphine group upon the addition of tris(2-carboxyethyl)phosphine (TCEP) [172]. Since complete oxygen removal is impossible, the few residual oxygen molecules can stochastically oxidize individual fluorophores into the ground state, causing the on and off fluorescence "blinking" desired in SMLM. Many fluorophores develop a distinct absorption peak at shorter wavelengths in their radical state, likely due to disruption of the π-system. Indeed, in cyanine dyes, this system is thought to be practically split in two [80]. Irradiation by UV light thus expedites the return of $F^{\bullet-}$ fluorophores to the ground state [75], as depicted in Fig. 3aiv. Embedding samples in resin greatly suppresses collisional interactions, meaning that reactivation by UV is the only means of returning to the ground state [64], making the method viable for correlative light electron microscopy [181].

Oxygen in the solution can also be replaced with an alternative oxidizer such as methylviologen (MV) [74] or Trolox, which can be converted into an oxidizing quinone form upon UV irradiation [174]. The blinking rate can be adjusted by

**Table 4** Summary of labeling strategies commonly used in super-resolution microscopy

| | Buffer class | Buffer base | Compounds | Organic dyes used in switching buffer / description | Ref. |
|---|---|---|---|---|---|
| Switching buffers | **Reducer - $O_2$** | PBS/TRIS pH 7.4 - 9 - $O_2$ | 10 - 100 mM MEA | AF 750 [96], CF 680 [63], CF 647 [63], AF 647 and Cy5 [10], CF 568 [63], AF 532 [106], ATTO 520 [103] | [10] |
| | | | 0.5 - 1% BME | AF 750 [112], CF 680 [98], Cy5 readout pairs [9, 58], AF 647 [92] | [58] |
| | | | 10 - 100 mM GSH | AF 647 [106], TMR [106] | [106] |
| | **Reducer only** | PBS/TRIS pH 7.4 - 9 | 10 - 100 mM MEA | AF 647 [54], ATTO 655 [100], AF 568 [54], ATTO 520 [111], AF 532 [105], AF 488 [111] | [52, 111] |
| | | | 0.5 - 1% BME | ATTO 655 [100] | [100] |
| | | | 50 µM AA | ATTO 655 [169] | [169] |
| | | | 10 - 100 mM GSH | ATTO 655 [52], ATTO 520 [52] | [52, 111] |
| | | | 50 mM TCEP + 2 mM COT | AF 750 [97], AF 647 [97] | [97] |
| | **Oxygen removal (- $O_2$)** | PBS/TRIS pH 7.4 - 9 | GLOX* | AF 568 [121], ATTO 520 [121], AF 488 [121] | [121] |
| | | | PCD/PCA* | | [167] |
| | | | POC* | | [168] |
| | | | 100 mM MEA + 1 µM MB | Cy5 [170] | [170] |
| | **Switching ROXS** reducer and oxidizer - $O_2$ | PBS/TRIS pH 7.4 - 9 - $O_2$ | 500 µM AA + 25 µM MV | ATTO 655 [171] | [171] |
| | | | 1 mM AA + 1 mM MV + 25 mM TCEP, pH 9 | AF 750 [172], AF 647 [172], Cy5 [172] | [172] |
| | **Switching mount** | Vectashield | 20% Vectashield + 80% (95% glycerol 50 mM TRIS) | AF 647 [110], CF 647 [110] | [110] |
| | | Mowiol | 0.5% Mowiol + 50 mM DTT | SiR [101] | [101] |
| | | Resin | 100% dehydration + EM resin embedding | | [173] |
| | | PVA | 1% in PBS, spin coat | Oregon Green [41], AF 488 [41] | [41] |
| | **Live-cell media** | DMEM, modified to not contain phenol red | None | SiR [102], TMR [55, 102] | [55] |
| | | | 100 mM GSH + GLOX | AF 647 [106], TMR [106] | [106] |
| | | | 25 mM TCEP | AF 647 [172], Cy5 [172] | [172] |
| Stabilizing buffers | **Stabilizing ROXS** reducer and oxidizer - $O_2$ | PBS/TRIS pH 7.4 - 9 -$O_2$ | 1 mM AA + 1 mM MV | Triplet-state quenching and fluorescence stabilizer. | [74] |
| | | | 1 mM Trolox + Trolox-quinone | Triplet-state quenching and fluorescence stabilizer. | [174] |
| | **Mounting** | Vectashield | Sample mount | Sample mounting media that retard photobleaching, stabilize fluorescence, and can be used for longer-term sample preservation (Mowiol). | [175] |
| | | Mowiol | | | |
| | | SlowFade | | | |
| | | Fluor-Stop | | | |
| Additives | **TSQ** triplet-state quenchers | Cyclooctatetraene | 2 mM COT | Direct triplet-state quenching by energy transfer. | [73, 176] |
| | | Nitrobenzyl alcohol | 2 mM NBA | Fluorescence enhancer and stabilizer, redox triplet quencher. | [73] |
| | **Antifading agents** | n-Propyl gallate | 10 - 100 µM NPG | Antioxidant fluorescence protectant. | [176] |
| | | 1,4-Diazabicyclo [2.2.2]octane | 10 mM - 1 M | Antifading agent. | [167] |

The switching buffers section of the table includes a list of working dye/buffer combinations. Example buffer compilation: decide on buffer class (e.g., "Reducer with $-O_2$"), and then decide on the buffer base, the pH, oxygen removal ($-O_2$), and the final compounds based on the fluorophore used (e.g., CF 680 with 10–100 mM MEA [63])

AF Alexa Fluor, $-O_2$ oxygen removal, for the abbreviations of the chemicals, see the text or the corresponding references

* For the exact formulations of GLOX, PCD/PCA, and PCO, see the corresponding references

fine-tuning the ratios of these compounds while keeping the reducer at a high concentration and the oxidizer at a low concentration [171]. The exact concentrations heavily depend on the redox potentials of the fluorophore–reducer/oxidizer pairs. Since the reduction potential of the $F^{\bullet -}$ state varies with the fluorophore considered, different fluorophores can exhibit different blinking behaviors in the same buffer. The pH influences the redox potentials of the compounds in the solution, so changing the pH provides yet another way of adjusting blinking rates [111]. For some fluorophores, the reducing environment inside living cells is sufficient to induce long dark states [106]. In some cases, oxygen removal can be omitted and the addition of a reducer is sufficient [169].

In the cases of STED and SIM, the same strategy can be used to stabilize the fluorescence. Provided the concentrations of both the reducer and the oxidizer are high enough (usually in the millimolar range), the triplet state is efficiently reduced to a radical state that is rapidly oxidized back to the ground state upon formation. The rapidity of this process of reduction and oxidation significantly shortens the overall time the fluorophore spends in nonfluorescing states. The stabilizing effects of a reducing and oxidizing system (ROXS) such as that shown in Fig. 3aiii were reported before the development of SMLM [74].

Fluorophores can also be protected from bleaching by the addition of antioxidants such as *n*-propyl gallate (nPG) [176] or antifading reagents such as nitrobenzyl alcohol (NBA), paraphenylenediamine (PPD), 1,4-diazabicyclo[2.2.2]octane (DABCO), and commercial products such as Vectashield, Fluor-stop, Mowiol, or SlowFade [175, 182]. Vectashield has also been reported to be an effective and very simple SMLM switching medium for several dyes, acting through an unspecified mechanism [110]. COT, NBA, and Trolox have also been (covalently) linked to fluorophores, introducing the concept of "self-healing" dyes [183]. All of these components as well as some popular SMLM buffer formulations that facilitate photoswitching of common fluorophores are summarized in Table 4.

In addition to electronic state transitions, switching is also caused by conformational changes in the chromophore or its surrounding environment. Three main conformational blinking mechanisms exist in fluorescent proteins: photoactivation, photoconversion, and photoswitching [184]. In photoactivatable fluorescent proteins such as paGFP, interactions between the chromophore and a side chain in the beta-barrel stabilize the conjugated $\pi$-system in a neutral nonfluorescent state. Irradiation with UV decarboxylates the side chain, shifting the equilibrium of the chromophore towards its anionic state, thus making the protein fluorescent (Fig. 3ci) [76]. Similarly, photoconvertible fluorescent proteins such as mEos2 [77] undergo a fluorescence wavelength shift from green to orange when a peptide bond in the chromophore is cleaved by UV irradiation, causing an extension of the $\pi$-system, as seen in Fig. 3cii [185]. Finally, photoswitchable fluorescent proteins undergo reversible on and off switching as a result of UV-induced *cis*/*trans* isomerization like that shown for the fluorescent protein Dronpa in Fig. 3ciii. The isomerization causes protonation changes similar to those that occur in photoactivatable proteins, but which result in the reversible formation of a nonfluorescent form of the fluorophore [78]. Switching properties of fluorescent proteins can be adjusted by modifying the amino acid sequence. Two interesting examples of this are IrisFP and NijiFP [116], which can both be irreversibly photoconverted by UV light from their initial green fluorescing form into an orange fluorescing form, as well as reversibly photoswitched between their fluorescing and dark state (in both the green and the orange fluorescent forms).

Organic dyes can also be made nonfluorescent by inducing reversible changes to the molecule through either *cis*/*trans* isomerization [186] and the addition of certain chemical groups [187] or reduction by $NaBH_4$ [188] in a process called photocaging, as seen in Fig. 3civ for a rhodamine dye [189]. Irradiation with the correct wavelength returns the molecule to its fluorescent state [79, 189, 190]. Slow stochastic activation followed by prompt bleaching enables the use of such dyes in SMLM [79, 190].

The novel dye HMSiR represents a class all of its own. This silicon-rhodamine-derived dye naturally resides in a nonfluorescent cyclized form (Fig. 3cvi). It very rarely undergoes a spontaneous change in conformation and becomes fluorescent for a short time. Since this blinking does not require a specialized and probably live-cell-incompatible buffer and is independent of the excitation light intensity, it is very suitable for live-cell imaging [81].

The photochemical properties of individual fluorophores are especially important when designing multicolor experiments. Some fluorescent proteins need specific conditions for proper folding or switching. PAmCherry, for example, requires oxygen for activation, so it cannot be used in oxygen-free buffers [53, 161]. Further, the optimal imaging conditions of a fluorophore partially depend on its redox potential; a buffer that induces blinking in one fluorophore may stabilize another. Table 2 covers most of the working dual- and triple-fluorophore combinations used in SMLM to date.

## Super-resolved cell biology

Direct observations of the molecular processes that take place in cells can help to advance our understanding of life and how the complex interdependencies of single molecules enable it. Using super-resolution microscopy, we can follow these molecules, measure diffusion and progress in assembly processes, and quantify the molecules in subcellular structures at unrivaled spatiotemporal resolution. Over the past decade, rapid developments in these techniques have created a wide spectrum of advanced experimental settings that have already unraveled several mysteries associated with cells, some of which are depicted in Fig. 4 and are briefly summarized below.

### Molecular counting and spatial organization

SMLM data is built on individual single-molecule localizations, and thus allows the absolute stoichiometry of molecules in subcellular structures to be determined.

Here, several effects which compromise this straightforward strategy must be considered. First, undercounting of molecules occurs when some molecules are not counted during the experiment due to, for example, incomplete labeling by the fluorophore, immature or misfolded genetic fluorescent tags, limited photoactivation or switching efficiencies, or insufficient algorithmic registration. The latter problem can be resolved to some degree by using multiemitter fitting algorithms or fluorophore density estimators when there are high fluorescent spot densities,

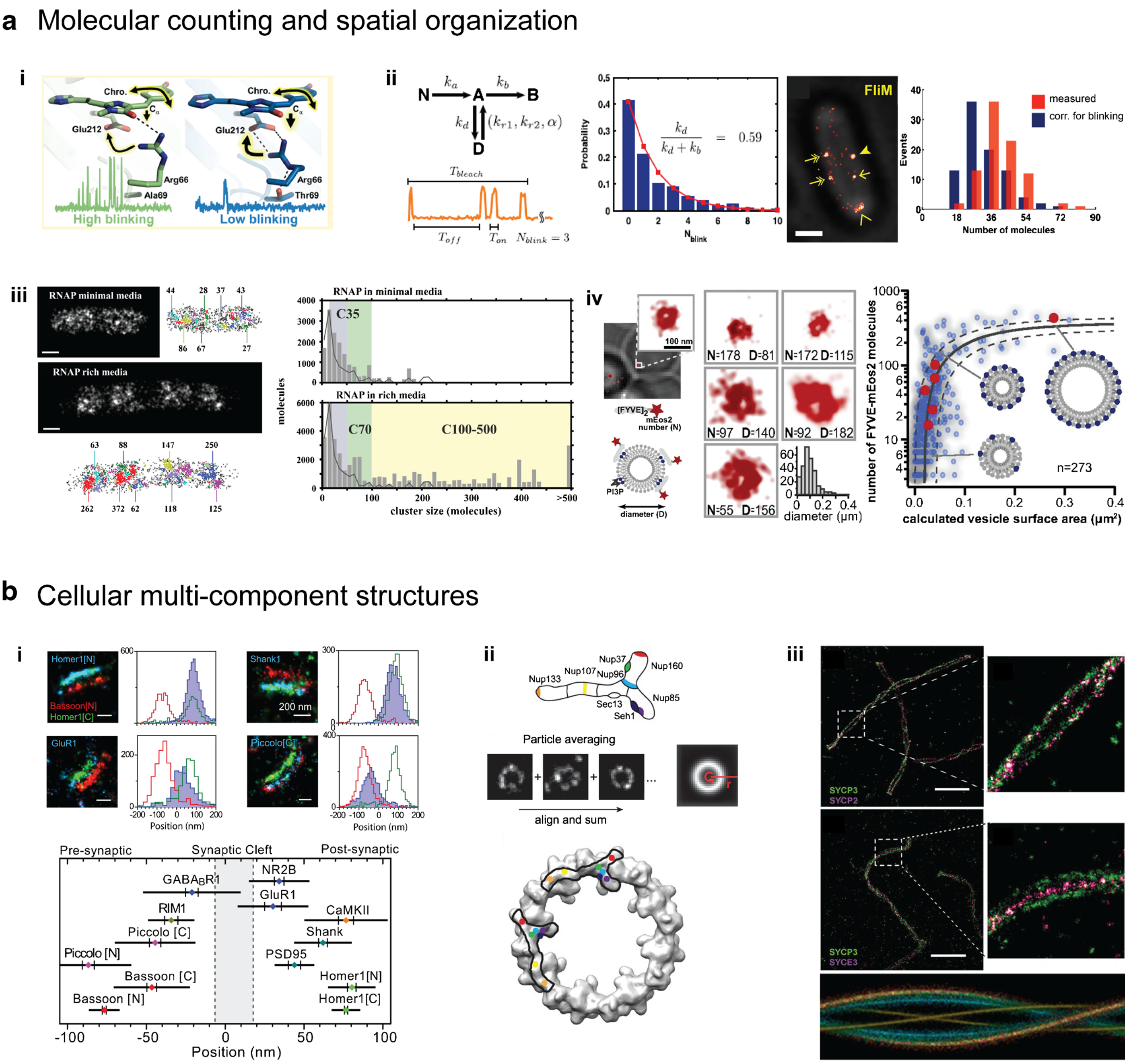

**Fig. 4a–b** Quantitative super-resolution microscopy. **a** SMLM allows the stoichiometry of a molecule to be determined, with several over- or undercounting effects taken into account. (*i*) The photochemical properties of fluorescent proteins lead to specific blinking and bleaching behaviors. The high-blinking and fast-bleaching behaviors shown by mEos2 (*left*) and Dendra2 (*right*), respectively, are largely determined by the orientation of the single residue arginine 66. Reprinted with permission from [191]. (*ii*) Fluorophore blinking behavior can be corrected for using kinetic fluorophore schemes. In this strategy, the number of FliM proteins per flagellar motor is counted in vivo. Reprinted from [192]. (*iii*) Spatial organization of *E. coli* RNA polymerases under minimal as well as rich growth conditions. Reprinted with permission from [193]. (*iv*) Maturation of endocytic vesicles into late endosomes. Reprinted from [194]. (*b*) Structural super-resolution microscopy reveals the molecular architecture of cellular multicomponent complexes. (*i*) Mutual organization of various pre- and postsynaptic proteins in relation to the proteins Bassoon and Homer1. Reprinted with permission from [139]. (*ii*) Combining data from identical particles yields a high-resolution average. Systematic SMLM imaging of the Y-shaped subunit of the nuclear pore complex allows it to be aligned onto the electron density of the nuclear pore (*bottom*). Reprinted with permission from [104]. (*iii*) Aligning different pairs of synaptonemal proteins onto a helical template yields the three-dimensional model of the synaptonemal complex with isotropic resolution. Reprinted from [105]. Scale bars: **a***ii* and **a***iii* 500 nm; **a***iv* 100 nm; **b***i* 200 nm; **b***iii* 2 µm

thus decreasing the number of missed localizations [43]. Second, overcounting effects can occur when localized local background fluctuations lead to falsely included positions, during multiple target counting by multiple antibodies or multiple fluorescent labels, or due to multiple localizations per fluorophore caused by blinking behavior. Uncorrected SMLM data can thus result in apparent self-clustering of localizations, which tends to be misinterpreted as clustered organization of the target molecule. These effects can be reduced by, for example, using a fast-maturing one-to-one endogenous fluorescent protein fusion with (engineered) low-blinking behavior. Recently, a mechanistic study revealed that the side-chain conformation of arginine 66 seen in Fig. 4ai is sufficient to cause the popular fluorophores mEos2 (left) and Dendra2 (right) to either blink or bleach, respectively. Consequently, the engineered single mutants mEos2-A69T and Dendra2-T69A show completely swapped behaviors [191].

To further account for miscounting effects, SMLM localizations can be tracked for fluorescent emissions spanning several imaging frames, weighted by known fluorophore detection efficiencies, and statistically corrected for fluorophore blinking [192, 194–196]. For example, as seen in Fig. 4aii, Lee et al. introduced kinetic fluorophore models and accessed the blinking probability of the fluorescent protein tag in order to then count 33 molecules of FliM protein per bacterial flagellar motor in vivo [192]. Further, the varying spatial organization of DNA transcribing *E. coli* RNA polymerase for different metabolic conditions (Fig. 4aiii) as well as the maturation pathway of small endocytic vesicles which form at the membrane and then develop into late endosomes in yeast (Fig. 4aiv) have been revealed.

## Cellular multicomponent structures

Using super-resolution methods, not only can individual molecules be precisely localized, but the large molecular architecture of multiprotein complexes and whole organelles as well as the organization of the genome or membrane can be targeted in the native cellular environment. This yields detailed quantitative molecular maps that capture these large assemblies and place hundreds of different molecules into assembled three-dimensional structures while maintaining the high spatiotemporal resolution of the method. These structures, such as the synapse depicted in Fig. 4bi, can allow us to advance our molecular understanding of their functions and reveal large-scale cellular organization. In the study shown in Fig. 4bi, various pre- and postsynaptic proteins were imaged in relation to the N-terminal localization of the protein Bassoon and the C-terminus of Homer1 by triple-color SMLM, which elucidated their mutual organization in proximity to the synaptic cleft. Indeed, the macromolecular assemblies studied so far using super-resolution techniques comprise an impressive list, including the nuclear pore complex, the ESCRT transport machinery, the neuronal architecture, focal adhesions, the centrosome and cellular division, the endocytosis pathway, as well as the organization of chromatin and membrane lipid domains (see the detailed review in [197]).

Averaging the data for super-resolved identical particles involves combining the individual copies of the same structure into a high-resolution average that complements the single images. This is useful because a single image may have some information missing due to absent affinity labels, imperfect photoswitching of the fluorophores, or nonisotropic resolution. Such a particle averaging strategy can help to elucidate the compositions and organization of macromolecular structures; for instance, the organization of the Y-shaped nuclear pore complex (NPC) subunit Nup107-160 was retrieved and matched with the electron density of the cytoplasmic ring of the nuclear pore via systematic two-dimensional SMLM imaging (Fig. 4bii) [104]. Aligning two-color and two-dimensional SMLM data from different pairs of synaptonemal proteins onto a helical template yielded a three-dimensional model of the synaptonemal complex with isotropic resolution (Fig. 4biii) [105]. The centrosomes of *Drosophila* [198], yeast [199], and humans [200] were studied by combining three-dimensional SIM images. Thus, super-resolution microscopy combined with particle averaging complements current structural biology studies, as it can target structures that are too large for cryoelectron microscopy or when preparation for X-ray crystallography fails. In this context, techniques like subtomogram averaging [201] adapted for three-dimensional super-resolution microscopy could allow us to resolve even more structures at higher in situ resolution, and correlative interaction networks combining super-resolved data with other (e.g., biochemical or genetic) analyzes could lead to large systems biology approaches, which could further refine current studies.

## Live-cell imaging

Fluorescence microscopy plays a key role in revealing the structures and functions of living cells in a minimally invasive manner through the use of genetic tags, and thus profits greatly from efficient genome engineering, such as the developing CRISPR-Cas technique [202]. For example, by applying STED microscopy to the visual cortex of YFP-transgenic and anesthetized (but live) mice, it has been possible to observe fine details and measure the dynamics of the tiny dendritic spines in vivo (Fig. 5ai) [203]. In order to improve live-cell super-resolution microscopy strategies, new designs are mainly focusing on three goals: accelerating the imaging speed, lowering the phototoxicity, and expanding the field of view in the lateral as well as vertical directions, all without compromising the resolution. The most critical issues to address are the laser intensities and imaging times used, which, depending on the wavelength of the laser and the irradiation dose, can compromise the health of the cells being studied [141, 207, 208]. Possible solutions involve developing new fast switching fluorophores that can be applied at lower laser

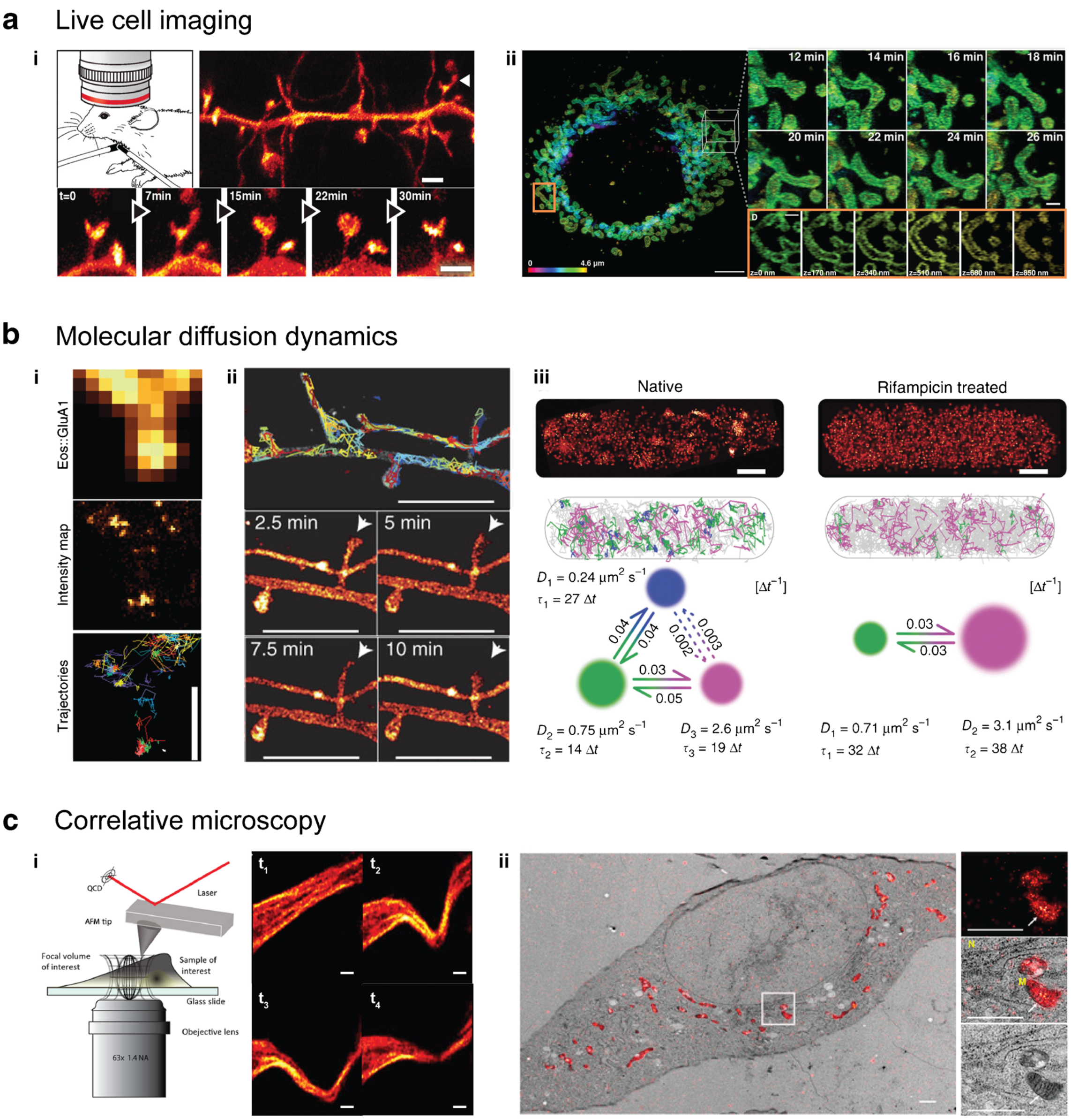

**Fig. 5a–c** Advanced dynamic and correlative super-resolution microscopy approaches. **a** Live imaging has been successfully performed on living cells and mammals. (*i*) STED microscopy of the dynamics of dendritic spines (*arrows*) in the visual cortex of living, YFP-transgenic, anesthetized mouse. Reprinted with permission from [203]. (*ii*) Mitochondrial fusion and fission dynamics imaged over a period of several tens of minutes by nonlinear SIM in lattice light sheet configuration. Reprinted with permission from [13]. **b** Single-particle tracking schemes elucidate molecular diffusional dynamics. (*i*) High-density tracking of AMPA receptors reveals confined nanodomains in the postsynaptic regions. Reprinted with permission from [204]. (*ii*) In contrast, membrane-bound GPI demonstrates a more homogeneous diffusion. Reprinted with permission from [4]. (*iii*) Bayesian hidden Markov model assessment of Hfq protein dynamics in *E. coli* cells. When mRNA synthesis is inhibited, the fraction of Hfq-binding mRNA (state of slowest diffusion) disappears. Reprinted with permission from [205]. **c** Correlative microscopy allows diverse features of a sample to be measured. (*i*) STED microscopy combined with atomic force microscopy (AFM) visualizes the response of the cytoskeleton upon nanomanipulation by the AFM tip. Reprinted with permission from [206]. (*ii*) Correlative PALM and electron microscopy of the mitochondrially targeted fluorescent protein mEos4 verifies its intact photoconversion and fluorescence under heavy osmium tetroxide fixation. Reprinted by permission from [114]. Scales: **a***i* 1 µm; **a***ii* 5 µm (*left*) and 1 µm (*right*); **b***i* 800 nm; **b***ii* 2 µm; **b***iii* 500 nm; **c***i* 2 µm, **c***ii* 1 µm

irradiations; fluorescent proteins that are usable in the longer (less toxic) near-infrared wavelength range, thus permitting deep-tissue imaging; as well as protected dyes that are shielded from the environment, similar to a fluorescent protein barrel. Such a protective structure could then also shield the cell from ROS and free radicals originating from photochemical reactions in the proximity of the chromophore during excitational or switching processes. New technical implementations which optimize the use of the limited photon budget per fluorophore as well as the imaging speed are favored, such as methods which confine but also parallelize the imaging by multifocal or lattice-like excitation or allow for multifocal detection [209–212]. New rapid and large sCMOS detectors increase the observation volume and allow for faster SMLM switching [3].

During the last few years it has therefore become possible to image whole living cells and organisms over longer timescales. One recent implementation of various types of SIM designs is a three-dimensional nonlinear SIM developed by Li et al. that uses photoswitchable fluorophores combined with lattice-lightsheet microscopy to show endocytic and cytoskeletal dynamics as well as the fission and fusion of mitochondria of whole live cells by labeling their membranes. They resolved the intracellular dynamics at individual mitochondrial constrictions over a period of several tens of minutes at a resolution of about 45 nm laterally and 170 nm vertically (Fig. 5aii) [13].

Another technical advance that is currently being explored is the implementation of adaptive optics to correct for aberrations in large sample volumes, e.g., multicellular organisms [213]. All three-dimensional localization microscopy algorithms have been challenged to participate in a large assessment, in order to evaluate their performance and identify common limitations on them. The results should ultimately guide development work aimed at optimizing three-dimensional SMLM resolution when studying protein ultrastructure in vivo [214].

## Following molecule diffusion dynamics

Single-particle tracking schemes directly monitor the kinetics of intracellular processes. In combination with photoactivatable fluorescent proteins in sptPALM, it is possible to follow the diffusion of individual proteins on cell membranes as well as in the cytoplasm of living cells, and to measure thousands of short single-molecule trajectories by sequential photoactivation. High-density tracking of the GluA1 subunits of AMPA receptors in the membranes of dendritic spines of live hippocampal neurons has revealed their discrete organization in 70–100 nm diameter nanodomains, and has shown that the receptors are mainly immobilized in the postsynapse (Fig. 5bi) [204], in contrast to the membrane-anchored glycosylphosphatidylinositol-GFP (Fig. 5bii). It is also possible to classify individual trajectories by their apparent diffusion constant into distinct states of diffusion, corresponding, for example, to different states of binding. This allows spatial and temporal heterogeneities in protein properties to be resolved. These are normally hidden in ensemble averages but are highly valuable when used in mathematical models for systems biology: by performing Bayesian assessments of hidden Markov models that combine the information from all short trajectories, it has recently been shown that the diffusion constants and state transition rates as well as the number of states in the model can be extracted [205]. This approach has been tested for the protein Hfq in *E. coli*, which mediates post-transcriptional gene regulation by facilitating interactions between mRNA and noncoding small RNA. The Hfq dynamics are highly altered when transcription is blocked using the drug rifampicin, as this decreases the mRNA level in the cell. The state with the slowest diffusion—most likely Hfq binding to the mRNA being transcribed—disappears, and the fraction occupying the intermediate state decreases substantially (Fig. 5biii).

## Correlative microscopy

Correlative microscopy combines the advantages of and opportunities provided by different methods, and thus allows different features of the exact same sample to be measured. For instance, a correlative approach can combine dynamic tracking studies with structural imaging when mapping intracellular vesicle transport on the cytoskeleton [71]. Also possible is the real-time visualization of the fast responses of the cytoskeleton of HeLa cells upon physical nanomanipulation by an atomic force microscopy tip in correlative STED microscopy (Fig. 5ci) [206]. Another direction in correlative imaging is to combine the high ultrastructural resolution and cellular context information of electron microscopy with the specific localization of molecules in super-resolution microscopy (Fig. 5cii) [215]. Unfortunately, most current correlative schemes still suffer from complex and tedious fixation protocols as well as limited labeling and imaging strategies, i.e., the cryo- or resin-covered environments used for electron microscopy impair the photophysics of most standard fluorophores. However, technical implementations develop rapidly; for instance, a correlative fluorescent protein tag, mEos4, which fluoresces and photoconverts normally under heavy osmium tetroxide fixation has recently been developed (Fig. 5c, ii) [114], and the dye TMR has been shown to not only preserve its fluorescence during high-pressure freezing and freeze substitution preparations, but to be able to photooxidize diaminobenzidine (DAB) too, which then yields high electron-microscopic contrast [173, 216].

In an optimistic but still realistic future, super-resolution microscopy will push beyond its current limits of routinely achieving experimental resolutions of tens of nanometers to approach the distances of typical single-molecule FRET measurements (2–10 nm) as well as the structural resolution of cryoelectron microscopy and X-ray crystallography (about 2–3 Å), which will allow us to more directly combine the heterogeneity and dynamics of protein complexes measured in vivo with the precise structural information available from purified protein complexes.

## Outlook

Over the last few decades, super-resolution microscopy has proven its value in the life sciences, and a myriad of biological applications of super-resolution microscopy have emerged. The super-resolution toolbox currently consists of many diverse methods and application strategies that complement traditional cell biology studies as well as techniques from molecular biology or biochemistry. Super-resolution microscopy is on its way to becoming a standard research tool, which is leading to a huge demand for computer-based data processing and openly available analysis software for (advanced) data evaluation, visualization, and comparison, as well as accessible, affordable, and simple-to-use hardware implementations. Also, super-resolution microscopy traditionally yields large volumes of microscopic data, which would ideally be stored and handled in open-access public platforms. Whether this vision comes to pass largely depends on the development of new algorithms as well as open-source software and strategies for efficient large-scale data handling.

**Acknowledgments** Open access funding provided by Max Planck Society.

### Compliance with ethical standards

**Conflicts of interest** The authors declare that they have no conflict of interest.

## References

1. Liu Z, Lavis LD, Betzig E. Imaging live-cell dynamics and structure at the single-molecule level. Mol Cell. 2015;58(4):644–59. doi:10.1016/j.molcel.2015.02.033.
2. Hell SW, Sahl SJ, Bates M, Zhuang XW, Heintzmann R, Booth MJ et al. The 2015 super-resolution microscopy roadmap. J Phys D Appl Phys. 2015;48(44). doi:10.1088/0022-3727/48/44/443001.
3. Winter PW, Shroff H. Faster fluorescence microscopy: advances in high speed biological imaging. Curr Opin Chem Biol. 2014;20:46–53. doi:10.1016/j.cbpa.2014.04.008.
4. Ries J, Kaplan C, Platonova E, Eghlidi H, Ewers H. A simple, versatile method for GFP-based super-resolution microscopy via nanobodies. Nat Methods. 2012;9(6):582–4. doi:10.1038/nmeth.1991.
5. Vreja IC, Nikic I, Gottfert F, Bates M, Krohnert K, Outeiro TF, et al. Super-resolution microscopy of clickable amino acids reveals the effects of fluorescent protein tagging on protein assemblies. ACS Nano. 2015;9(11):11034–41. doi:10.1021/acsnano.5b04434.
6. Klar TA, Hell SW. Subdiffraction resolution in far-field fluorescence microscopy. Opt Lett. 1999;24(14):954–6.
7. Gustafsson MG. Surpassing the lateral resolution limit by a factor of two using structured illumination microscopy. J Microsc. 2000;198(Pt 2):82–7.
8. Betzig E, Patterson GH, Sougrat R, Lindwasser OW, Olenych S, Bonifacino JS, et al. Imaging intracellular fluorescent proteins at nanometer resolution. Science. 2006;313(5793):1642–5. doi:10.1126/science.1127344.
9. Rust MJ, Bates M, Zhuang X. Sub-diffraction-limit imaging by stochastic optical reconstruction microscopy (STORM). Nat Methods. 2006;3(10):793–5. doi:10.1038/nmeth929.
10. Heilemann M, van de Linde S, Schuttpelz M, Kasper R, Seefeldt B, Mukherjee A, et al. Subdiffraction-resolution fluorescence imaging with conventional fluorescent probes. Angew Chem Int Ed. 2008;47(33):6172–6. doi:10.1002/anie.200802376.
11. Kner P, Chhun BB, Griffis ER, Winoto L, Gustafsson MGL. Super-resolution video microscopy of live cells by structured illumination. Nat Methods. 2009;6(5):339–42. doi:10.1038/nmeth.1324.
12. Gustafsson MG, Shao L, Carlton PM, Wang CJ, Golubovskaya IN, Cande WZ, et al. Three-dimensional resolution doubling in wide-field fluorescence microscopy by structured illumination. Biophys J. 2008;94(12):4957–70. doi:10.1529/biophysj.107.120345.
13. Li D, Shao L, Chen BC, Zhang X, Zhang M, Moses B, et al. Extended-resolution structured illumination imaging of endocytic and cytoskeletal dynamics. Science. 2015;349(6251), aab3500. doi:10.1126/science.aab3500.
14. Bückers J, Wildanger D, Vicidomini G, Kastrup L, Hell SW. Simultaneous multi-lifetime multi-color STED imaging for colocalization analyses. Opt Express. 2011;19(4):3130–43. doi:10.1364/OE.19.003130.
15. Xu K, Babcock HP, Zhuang X. Dual-objective STORM reveals three-dimensional filament organization in the actin cytoskeleton. Nat Methods. 2012;9(2):185–8.
16. Rayleigh XV. On the theory of optical images, with special reference to the microscope. Philos Mag. 1896;42(255):167–95. doi:10.1080/14786449608620902.
17. Siedentopf H, Zsigmondy R. Über Sichtbarmachung und Größenbestimmung ultramikoskopischer Teilchen, mit besonderer Anwendung auf Goldrubingläser. Ann Phys. 1902;315(1):1–39. doi:10.1002/andp.19023150102.
18. König K. Multiphoton microscopy in life sciences. J Microsc. 2000;200(2):83–104. doi:10.1046/j.1365-2818.2000.00738.x.
19. Betzig E, Lewis A, Harootunian A, Isaacson M, Kratschmer E. Near field scanning optical microscopy (NSOM): development and biophysical applications. Biophys J. 1986;49(1):269–79. doi:10.1016/S0006-3495(86)83640-2.
20. Harke B, Keller J, Ullal CK, Westphal V, Schonle A, Hell SW. Resolution scaling in STED microscopy. Opt Express. 2008;16(6):4154–62.
21. Schmidt R, Wurm CA, Jakobs S, Engelhardt J, Egner A, Hell SW. Spherical nanosized focal spot unravels the interior of cells. Nat Methods. 2008;5(6):539–44. doi:10.1038/nmeth.1214.
22. Willig KI, Harke B, Medda R, Hell SW. STED microscopy with continuous wave beams. Nat Methods. 2007;4(11):915–8. doi:10.1038/nmeth1108.
23. Vicidomini G, Moneron G, Han KY, Westphal V, Ta H, Reuss M, et al. Sharper low-power STED nanoscopy by time gating. Nat Methods. 2011;8(7):571–3. doi:10.1038/nmeth.1624.
24. Staudt T, Engler A, Rittweger E, Harke B, Engelhardt J, Hell SW. Far-field optical nanoscopy with reduced number of state transition cycles. Opt Express. 2011;19(6):5644–57. doi:10.1364/OE.19.005644.
25. Grotjohann T, Testa I, Leutenegger M, Bock H, Urban NT, Lavoie-Cardinal F, et al. Diffraction-unlimited all-optical imaging and writing with a photochromic GFP. Nature. 2011;478(7368):204–8. doi:10.1038/nature10497.
26. Danzl JG, Sidenstein SC, Gregor C, Urban NT, Ilgen P, Jakobs S, et al. Coordinate-targeted fluorescence nanoscopy

with multiple off states. Nat Photonics. 2016;10(2):122–8. doi:10.1038/nphoton.2015.266.

27. Eggeling C, Willig KI, Barrantes FJ. STED microscopy of living cells—new frontiers in membrane and neurobiology. J Neurochem. 2013;126(2):203–12. doi:10.1111/jnc.12243.
28. Donnert G, Keller J, Wurm CA, Rizzoli SO, Westphal V, Schönle A, et al. Two-color far-field fluorescence nanoscopy. Biophys J. 2007;92(8):L67–9. doi:10.1529/biophysj.107.104497.
29. Gottfert F, Wurm CA, Mueller V, Berning S, Cordes VC, Honigmann A, et al. Coaligned dual-channel STED nanoscopy and molecular diffusion analysis at 20 nm resolution. Biophys J. 2013;105(1):L01–3. doi:10.1016/j.bpj.2013.05.029.
30. Tonnesen J, Nadrigny F, Willig KI, Wedlich-Soldner R, Nagerl UV. Two-color STED microscopy of living synapses using a single laser-beam pair. Biophys J. 2011;101(10):2545–52. doi:10.1016/j.bpj.2011.10.011.
31. Willig KI, Stiel AC, Brakemann T, Jakobs S, Hell SW. Dual-label STED nanoscopy of living cells using photochromism. Nano Lett. 2011;11(9):3970–3. doi:10.1021/nl202290w.
32. Jost A, Heintzmann R. Superresolution multidimensional imaging with structured illumination microscopy. Annu Rev Mater Res. 2013;43(1):261–82. doi:10.1146/annurev-matsci-071312-121648.
33. Ball G, Demmerle J, Kaufmann R, Davis I, Dobbie IM, Schermelleh L. SIMcheck: a toolbox for successful super-resolution structured illumination microscopy. Sci Rep. 2015;5:15915. doi:10.1038/srep15915.
34. Muller M, Monkemoller V, Hennig S, Hubner W, Huser T. Open-source image reconstruction of super-resolution structured illumination microscopy data in ImageJ. Nat Commun. 2016;7:10980. doi:10.1038/ncomms10980.
35. Hirvonen LM, Wicker K, Mandula O, Heintzmann R. Structured illumination microscopy of a living cell. Eur Biophys J. 2009;38(6):807–12. doi:10.1007/s00249-009-0501-6.
36. York AG, Parekh SH, Dalle Nogare D, Fischer RS, Temprine K, Mione M, et al. Resolution doubling in live, multicellular organisms via multifocal structured illumination microscopy. Nat Methods. 2012;9(7):749–54. doi:10.1038/nmeth.2025.
37. Schermelleh L, Carlton PM, Haase S, Shao L, Winoto L, Kner P, et al. Subdiffraction multicolor imaging of the nuclear periphery with 3D structured illumination microscopy. Science. 2008;320(5881):1332–6. doi:10.1126/science.1156947.
38. Schaefer LH, Schuster D, Schaffer J. Structured illumination microscopy: artefact analysis and reduction utilizing a parameter optimization approach. J Microsc. 2004;216(2):165–74. doi:10.1111/j.0022-2720.2004.01411.x.
39. Gustafsson MG. Nonlinear structured-illumination microscopy: wide-field fluorescence imaging with theoretically unlimited resolution. Proc Natl Acad Sci USA. 2005;102(37):13081–6. doi:10.1073/pnas.0406877102.
40. Rego EH, Shao L, Macklin JJ, Winoto L, Johansson GA, Kamps-Hughes N, et al. Nonlinear structured-illumination microscopy with a photoswitchable protein reveals cellular structures at 50-nm resolution. Proc Natl Acad Sci USA. 2012;109(3):E135–43. doi:10.1073/pnas.1107547108.
41. Fölling J, Bossi M, Bock H, Medda R, Wurm CA, Hein B, et al. Fluorescence nanoscopy by ground-state depletion and single-molecule return. Nat Methods. 2008;5(11):943–5.
42. Moerner WE. Microscopy beyond the diffraction limit using actively controlled single molecules. J Microsc. 2012;246(3):213–20. doi:10.1111/j.1365-2818.2012.03600.x.
43. Small A, Stahlheber S. Fluorophore localization algorithms for super-resolution microscopy. Nat Methods. 2014;11(3):267–79. doi:10.1038/nmeth.2844.
44. Sage D, Kirshner H, Pengo T, Stuurman N, Min J, Manley S, et al. Quantitative evaluation of software packages for single-molecule localization microscopy. Nat Methods. 2015;12(8):717–24. doi:10.1038/nmeth.3442.
45. Chenouard N, Smal I, de Chaumont F, Maska M, Sbalzarini IF, Gong Y, et al. Objective comparison of particle tracking methods. Nat Methods. 2014;11(3):281–9. doi:10.1038/nmeth.2808.
46. Thompson RE, Larson DR, Webb WW. Precise nanometer localization analysis for individual fluorescent probes. Biophys J. 2002;82(5):2775–83.
47. Axelrod D. Total internal reflection fluorescence microscopy in cell biology. Methods Enzymol. 2003;361:1–33.
48. Tokunaga M, Imamoto N, Sakata-Sogawa K. Highly inclined thin illumination enables clear single-molecule imaging in cells. Nat Methods. 2008;5(2):159–61. doi:10.1038/nmeth1171.
49. York AG, Ghitani A, Vaziri A, Davidson MW, Shroff H. Confined activation and subdiffractive localization enables whole-cell PALM with genetically expressed probes. Nat Methods. 2011;8(4):327–33.
50. Cella Zanacchi F, Lavagnino Z, Perrone Donnorso M, Del Bue A, Furia L, Faretta M, et al. Live-cell 3D super-resolution imaging in thick biological samples. Nat Methods. 2011;8(12):1047–9.
51. Chen BC, Legant WR, Wang K, Shao L, Milkie DE, Davidson MW, et al. Lattice light-sheet microscopy: imaging molecules to embryos at high spatiotemporal resolution. Science. 2014;346(6208):1257998. doi:10.1126/science.1257998.
52. van de Linde S, Endesfelder U, Mukherjee A, Schuttpelz M, Wiebusch G, Wolter S, et al. Multicolor photoswitching microscopy for subdiffraction-resolution fluorescence imaging. Photochem Photobiol Sci. 2009;8(4):465–9. doi:10.1039/B822533H.
53. Endesfelder U, Malkusch S, Flottmann B, Mondry J, Liguzinski P, Verveer PJ, et al. Chemically induced photoswitching of fluorescent probes—a general concept for super-resolution microscopy. Molecules. 2011;16(4):3106.
54. Laine RF, Albecka A, van de Linde S, Rees EJ, Crump CM, Kaminski CF. Structural analysis of herpes simplex virus by optical super-resolution imaging. Nat Commun. 2015;6. doi:10.1038/ncomms6980.
55. Testa I, Wurm CA, Medda R, Rothermel E, von Middendorf C, Fölling J, et al. Multicolor fluorescence nanoscopy in fixed and living cells by exciting conventional fluorophores with a single wavelength. Biophys J. 2010;99(8):2686–94. doi:10.1016/j.bpj.2010.08.012.
56. Shroff H, Galbraith CG, Galbraith JA, White H, Gillette J, Olenych S, et al. Dual-color superresolution imaging of genetically expressed probes within individual adhesion complexes. Proc Natl Acad Sci USA. 2007;104(51):20308–13. doi:10.1073/pnas.0710517105.
57. Grimm JB, Klein T, Kopek BG, Shtengel G, Hess HF, Sauer M, et al. Synthesis of a far-red photoactivatable silicon-containing rhodamine for super-resolution microscopy. Angew Chem Int Ed. 2016;55(5):1723–7. doi:10.1002/anie.201509649.
58. Bates M, Huang B, Dempsey GT, Zhuang X. Multicolor super-resolution imaging with photo-switchable fluorescent probes. Science. 2007;317(5845):1749–53. doi:10.1126/science.1146598.
59. Subach FV, Patterson GH, Manley S, Gillette JM, Lippincott-Schwartz J, Verkhusha VV. Photoactivatable mCherry for high-resolution two-color fluorescence microscopy. Nat Methods. 2009;6(2):153–9.
60. Gunewardene Mudalige S, Subach Fedor V, Gould Travis J, Penoncello Gregory P, Gudheti Manasa V, Verkhusha Vladislav V, et al. Superresolution imaging of multiple fluorescent proteins with highly overlapping emission spectra in living cells. Biophys J. 2011;101(6):1522–8. doi:10.1016/j.bpj.2011.07.049.
61. Lampe A, Haucke V, Sigrist SJ, Heilemann M, Schmoranzer J. Multi-colour direct STORM with red emitting carbocyanines. Biol Cell. 2012;104(4):229–37. doi:10.1111/boc.201100011.
62. Zhang Z, Kenny SJ, Hauser M, Li W, Xu K. Ultrahigh-throughput single-molecule spectroscopy and spectrally resolved super-

resolution microscopy. Nat Methods. 2015;12(10):935–8. doi:10.1038/nmeth.3528.

63. Lehmann M, Lichtner G, Klenz H, Schmoranzer J. Novel organic dyes for multicolor localization-based super-resolution microscopy. J Biophotonics. 2016;9(1–2):161–70. doi:10.1002/jbio.201500119.
64. Biteen JS, Thompson MA, Tselentis NK, Bowman GR, Shapiro L, Moerner WE. Super-resolution imaging in live *Caulobacter crescentus* cells using photoswitchable EYFP. Nat Methods. 2008;5(11):947–9.
65. Wombacher R, Heidbreder M, van de Linde S, Sheetz MP, Heilemann M, Cornish VW, et al. Live-cell super-resolution imaging with trimethoprim conjugates. Nat Methods. 2010;7(9):717–9.
66. Jones SA, Shim S-H, He J, Zhuang X. Fast, three-dimensional super-resolution imaging of live cells. Nat Methods. 2011;8(6): 499–505.
67. Manley S, Gillette JM, Patterson GH, Shroff H, Hess HF, Betzig E, et al. High-density mapping of single-molecule trajectories with photoactivated localization microscopy. Nat Methods. 2008;5(2): 155–7.
68. Frost NA, Shroff H, Kong H, Betzig E, Blanpied TA. Single-molecule discrimination of discrete perisynaptic and distributed sites of actin filament assembly within dendritic spines. Neuron. 2010;67(1):86–99. doi:10.1016/j.neuron.2010.05.026.
69. Rossier O, Octeau V, Sibarita J-B, Leduc C, Tessier B, Nair D, et al. Integrins β1 and β3 exhibit distinct dynamic nanoscale organizations inside focal adhesions. Nat Cell Biol. 2012;14(10):1057–67.
70. Sanamrad A, Persson F, Lundius EG, Fange D, Gynnå AH, Elf J. Single-particle tracking reveals that free ribosomal subunits are not excluded from the *Escherichia coli* nucleoid. Proc Natl Acad Sci USA. 2014;111(31):11413–8. doi:10.1073/pnas.1411558111.
71. Bálint Š, Verdeny Vilanova I, Sandoval Álvarez Á, Lakadamyali M. Correlative live-cell and superresolution microscopy reveals cargo transport dynamics at microtubule intersections. Proc Natl Acad Sci USA. 2013;110(9):3375–80. doi:10.1073/pnas.1219206110.
72. Klehs K, Spahn C, Endesfelder U, Lee SF, Furstenberg A, Heilemann M. Increasing the brightness of cyanine fluorophores for single-molecule and superresolution imaging. ChemPhysChem. 2014;15(4):637–41. doi:10.1002/cphc.201300874.
73. Zheng Q, Jockusch S, Zhou Z, Altman RB, Warren JD, Turro NJ, et al. On the mechanisms of cyanine fluorophore photostabilization. J Phys Chem Lett. 2012;3(16):2200–3. doi:10.1021/jz300670p.
74. Vogelsang J, Kasper R, Steinhauer C, Person B, Heilemann M, Sauer M, et al. A reducing and oxidizing system minimizes photobleaching and blinking of fluorescent dyes. Angew Chem Int Ed. 2008;47(29):5465–9. doi:10.1002/anie.200801518.
75. van de Linde S, Krstic I, Prisner T, Doose S, Heilemann M, Sauer M. Photoinduced formation of reversible dye radicals and their impact on super-resolution imaging. Photochem Photobiol Sci. 2011;10(4):499–506. doi:10.1039/c0pp00317d.
76. Henderson JN, Gepshtein R, Heenan JR, Kallio K, Huppert D, Remington SJ. Structure and mechanism of the photoactivatable green fluorescent protein. J Am Chem Soc. 2009;131(12):4176–7.
77. McKinney SA, Murphy CS, Hazelwood KL, Davidson MW, Looger LL. A bright and photostable photoconvertible fluorescent protein. Nat Methods. 2009;6(2):131–3. doi:10.1038/nmeth.1296.
78. Habuchi S, Dedecker P, Hotta J-i, Flors C, Ando R, Mizuno H, et al. Photo-induced protonation/deprotonation in the GFP-like fluorescent protein Dronpa: mechanism responsible for the reversible photoswitching. Photochem Photobiol Sci. 2006;5(6):567–76.
79. Banala S, Maurel D, Manley S, Johnsson K. A caged, localizable rhodamine derivative for superresolution microscopy. ACS Chem Biol. 2011;7(2):289–93.
80. Dempsey GT, Bates M, Kowtoniuk WE, Liu DR, Tsien RY, Zhuang X. Photoswitching mechanism of cyanine dyes. J Am Chem Soc. 2009;131(51):18192–3. doi:10.1021/ja904588g.
81. Uno SN, Kamiya M, Yoshihara T, Sugawara K, Okabe K, Tarhan MC, et al. A spontaneously blinking fluorophore based on intramolecular spirocyclization for live-cell super-resolution imaging. Nat Chem. 2014;6(8):681–9. doi:10.1038/nchem.2002.
82. Lakowicz JR. Principles of fluorescence spectroscopy. New York: Springer; 2013.
83. Klessinger M. Konstitution und Lichtabsorption organischer Farbstoffe. Chem Unserer Zeit. 1978;12(1):1–11. doi:10.1002/ciuz.19780120102.
84. Sinha RP, Häder D-P. UV-induced DNA damage and repair: a review. Photochem Photobiol Sci. 2002;1(4):225–36.
85. Aubin JE. Autofluorescence of viable cultured mammalian cells. J Histochem Cytochem. 1979;27(1):36–43. doi:10.1177/27.1.220325.
86. DeRosa MC, Crutchley RJ. Photosensitized singlet oxygen and its applications. Coord Chem Rev. 2002;233:351–71.
87. D'Este E, Kamin D, Göttfert F, El-Hady A, Hell Stefan W. STED nanoscopy reveals the ubiquity of subcortical cytoskeleton periodicity in living neurons. Cell Rep. 2015;10(8):1246–51. doi:10.1016/j.celrep.2015.02.007.
88. Wildanger D, Medda R, Kastrup L, Hell SW. A compact STED microscope providing 3D nanoscale resolution. J Microsc. 2009;236(1):35–43. doi:10.1111/j.1365-2818.2009.03188.x.
89. Schachtrup C, Ryu JK, Mammadzada K, Khan AS, Carlton PM, Perez A, et al. Nuclear pore complex remodeling by p75(NTR) cleavage controls TGF-beta signaling and astrocyte functions. Nat Neurosci. 2015;18(8):1077–80. doi:10.1038/nn.4054.
90. Malkusch S, Endesfelder U, Mondry J, Gelleri M, Verveer PJ, Heilemann M. Coordinate-based colocalization analysis of single-molecule localization microscopy data. Histochem Cell Biol. 2012;137(1):1–10. doi:10.1007/s00418-011-0880-5.
91. Zessin PJ, Krüger CL, Malkusch S, Endesfelder U, Heilemann M. A hydrophilic gel matrix for single-molecule super-resolution microscopy. Opt Nanoscopy. 2013;2(1):1–8.
92. French JB, Jones SA, Deng H, Pedley AM, Kim D, Chan CY, et al. Spatial colocalization and functional link of purinosomes with mitochondria. Science. 2016;351(6274): 733–7. doi:10.1126/science.aac6054.
93. Gahlmann A, Ptacin JL, Grover G, Quirin S, von Diezmann AR, Lee MK, et al. Quantitative multicolor subdiffraction imaging of bacterial protein ultrastructures in three dimensions. Nano Lett. 2013;13(3):987–93. doi:10.1021/nl304071h.
94. Gurskaya NG, Verkhusha VV, Shcheglov AS, Staroverov DB, Chepurnykh TV, Fradkov AF, et al. Engineering of a monomeric green-to-red photoactivatable fluorescent protein induced by blue light. Nat Biotechnol. 2006;24(4):461–5. doi:10.1038/nbt1191.
95. Wilmes S, Staufenbiel M, Lisse D, Richter CP, Beutel O, Busch KB, et al. Triple-color super-resolution imaging of live cells: resolving submicroscopic receptor organization in the plasma membrane. Angew Chem Int Ed. 2012;51(20):4868–71. doi:10.1002/anie.201200853.
96. Baddeley D, Crossman D, Rossberger S, Cheyne JE, Montgomery JM, Jayasinghe ID, et al. 4D super-resolution microscopy with conventional fluorophores and single wavelength excitation in optically thick cells and tissues. PLoS One. 2011;6(5), e20645. doi:10.1371/journal.pone.0020645.
97. Zhao T, Wang Y, Zhai Y, Qu X, Cheng A, Du S, et al. A user-friendly two-color super-resolution localization microscope. Opt Express. 2015;23(2):1879–87. doi:10.1364/OE.23.001879.
98. Platonova E, Winterflood CM, Ewers H. A simple method for GFP- and RFP-based dual color single-molecule localization microscopy. ACS Chem Biol. 2015;10(6):1411–6. doi:10.1021/acschembio.5b00046.

99. Salvador-Gallego R, Mund M, Cosentino K, Schneider J, Unsay J, Schraermeyer U, et al. Bax assembly into rings and arcs in apoptotic mitochondria is linked to membrane pores. EMBO J. 2016;35(4):389–401. doi:10.15252/embj.201593384.
100. van de Linde S, Kasper R, Heilemann M, Sauer M. Photoswitching microscopy with standard fluorophores. Appl Phys B. 2008;93(4):725–31.
101. Lukinavicius G, Umezawa K, Olivier N, Honigmann A, Yang G, Plass T, et al. A near-infrared fluorophore for live-cell super-resolution microscopy of cellular proteins. Nat Chem. 2013;5(2):132–9. doi:10.1038/nchem.1546.
102. Beinlich FR, Drees C, Piehler J, Busch KB. Shuttling of PINK1 between mitochondrial microcompartments resolved by triple-color superresolution microscopy. ACS Chem Biol. 2015;10(9): 1970–6. doi:10.1021/acschembio.5b00295.
103. Loschberger A, van de Linde S, Dabauvalle MC, Rieger B, Heilemann M, Krohne G, et al. Super-resolution imaging visualizes the eightfold symmetry of gp210 proteins around the nuclear pore complex and resolves the central channel with nanometer resolution. J Cell Sci. 2012;125(Pt 3):570–5. doi:10.1242/jcs.098822.
104. Szymborska A, de Marco A, Daigle N, Cordes VC, Briggs JAG, Ellenberg J. Nuclear pore scaffold structure analyzed by super-resolution microscopy and particle averaging. Science. 2013;341(6146):655–8. doi:10.1126/science.1240672.
105. Schücker K, Holm T, Franke C, Sauer M, Benavente R. Elucidation of synaptonemal complex organization by super-resolution imaging with isotropic resolution. Proc Natl Acad Sci USA. 2015;112(7):2029–33. doi:10.1073/pnas.1414814112.
106. Klein T, van de Linde S, Sauer M. Live-cell super-resolution imaging goes multicolor. Chembiochem. 2012;13(13):1861–3. doi:10.1002/cbic.201200347.
107. Allen JR, Ross ST, Davidson MW. Sample preparation for single molecule localization microscopy. Phys Chem Chem Phys. 2013;15(43):18771–83. doi:10.1039/c3cp53719f.
108. Lampe A, Tadeus G, Schmoranzer J. Spectral demixing avoids registration errors and reduces noise in multicolor localization-based super-resolution microscopy. Methods Appl Fluoresc. 2015;3(3):034006.
109. Ribeiro SA, Vagnarelli P, Dong Y, Hori T, McEwen BF, Fukagawa T, et al. A super-resolution map of the vertebrate kinetochore. Proc Natl Acad Sci USA. 2010;107(23):10484–9. doi:10.1073/pnas.1002325107.
110. Olivier N, Keller D, Rajan VS, Gönczy P, Manley S. Simple buffers for 3D STORM microscopy. Biomedical optics express. 2013;4(6):885–99.
111. Heilemann M, van de Linde S, Mukherjee A, Sauer M. Super-resolution imaging with small organic fluorophores. Angew Chem Int Ed. 2009;48(37):6903–8. doi:10.1002/anie.200902073.
112. Bates M, Dempsey GT, Chen KH, Zhuang X. Multicolor super-resolution fluorescence imaging via multi-parameter fluorophore detection. ChemPhysChem. 2012;13(1):99–107. doi:10.1002/cphc.201100735.
113. Zhang M, Chang H, Zhang Y, Yu J, Wu L, Ji W, et al. Rational design of true monomeric and bright photoactivatable fluorescent proteins. Nat Methods. 2012;9(7):727–9.
114. Paez-Segala MG, Sun MG, Shtengel G, Viswanathan S, Baird MA, Macklin JJ, et al. Fixation-resistant photoactivatable fluorescent proteins for CLEM. Nat Methods. 2015;12(3):215–8.
115. Wang S, Moffitt JR, Dempsey GT, Xie XS, Zhuang X. Characterization and development of photoactivatable fluorescent proteins for single-molecule-based superresolution imaging. Proc Natl Acad Sci USA. 2014;111(23):8452–7.
116. Adam V, Moeyaert B, David CC, Mizuno H, Lelimousin M, Dedecker P, et al. Rational design of photoconvertible and biphotochromic fluorescent proteins for advanced microscopy applications. Chem Biol. 2011;18(10):1241–51. doi:10.1016/j.chembiol.2011.08.007.
117. Zhang X, Chen X, Zeng Z, Zhang M, Sun Y, Xi P, et al. Development of a reversibly switchable fluorescent protein for super-resolution optical fluctuation imaging (SOFI). ACS Nano. 2015;9(3):2659–67.
118. Chudakov DM, Matz MV, Lukyanov S, Lukyanov KA. Fluorescent proteins and their applications in imaging living cells and tissues. Physiol Rev. 2010;90(3):1103–63. doi:10.1152/physrev.00038.2009.
119. Patterson GH, Lippincott-Schwartz J. A photoactivatable GFP for selective photolabeling of proteins and cells. Science. 2002;297(5588):1873–7. doi:10.1126/science.1074952.
120. Andresen M, Stiel AC, Trowitzsch S, Weber G, Eggeling C, Wahl MC, et al. Structural basis for reversible photoswitching in Dronpa. Proc Natl Acad Sci USA. 2007;104(32):13005–9. doi:10.1073/pnas.0700629104.
121. Dempsey GT, Vaughan JC, Chen KH, Bates M, Zhuang X. Evaluation of fluorophores for optimal performance in localization-based super-resolution imaging. Nat Methods. 2011;8(12):1027–36. doi:10.1038/nmeth.1768.
122. Landgraf D, Okumus B, Chien P, Baker TA, Paulsson J. Segregation of molecules at cell division reveals native protein localization. Nat Methods. 2012;9(5):480–2.
123. Wolter S, Endesfelder U, van de Linde S, Heilemann M, Sauer M. Measuring localization performance of super-resolution algorithms on very active samples. Opt Express. 2011;19(8):7020–33.
124. Shannon CE. Communication in the presence of noise. P IEEE. 1949;37(1):10–21.
125. Coons AH, Creech HJ, Jones RN. Immunological properties of an antibody containing a fluorescent group. Exp Biol Med. 1941;47(2):200–2. doi:10.3181/00379727-47-13084p.
126. Rothbauer U, Zolghadr K, Tillib S, Nowak D, Schermelleh L, Gahl A, et al. Targeting and tracing antigens in live cells with fluorescent nanobodies. Nat Methods. 2006;3(11):887–9.
127. Beatty KE, Liu JC, Xie F, Dieterich DC, Schuman EM, Wang Q, et al. Fluorescence visualization of newly synthesized proteins in mammalian cells. Angew Chem Int Ed. 2006;45(44):7364–7. doi:10.1002/anie.200602114.
128. Neef AB, Schultz C. Selective fluorescence labeling of lipids in living cells. Angew Chem Int Ed. 2009;48(8):1498–500. doi:10.1002/anie.200805507.
129. Salic A, Mitchison TJ. A chemical method for fast and sensitive detection of DNA synthesis in vivo. Proc Natl Acad Sci USA. 2008;105(7):2415–20. doi:10.1073/pnas.0712168105.
130. Rudkin GT, Stollar BD. High resolution detection of DNA-RNA hybrids in situ by indirect immunofluorescence. Nature. 1977;265(5593):472–3.
131. Shim SH, Xia C, Zhong G, Babcock HP, Vaughan JC, Huang B, et al. Super-resolution fluorescence imaging of organelles in live cells with photoswitchable membrane probes. Proc Natl Acad Sci USA. 2012;109(35):13978–83. doi:10.1073/pnas.1201882109.
132. Lukinavicius G, Reymond L, D'Este E, Masharina A, Gottfert F, Ta H, et al. Fluorogenic probes for live-cell imaging of the cytoskeleton. Nat Methods. 2014;11(7):731–3. doi:10.1038/nmeth.2972.
133. Lukinavicius G, Blaukopf C, Pershagen E, Schena A, Reymond L, Derivery E, et al. SiR-Hoechst is a far-red DNA stain for live-cell nanoscopy. Nat Commun. 2015;6: 8497. doi:10.1038/ncomms9497.
134. Revelo NH, Kamin D, Truckenbrodt S, Wong AB, Reuter-Jessen K, Reisinger E, et al. A new probe for super-resolution imaging of membranes elucidates trafficking pathways. J Cell Biol. 2014;205(4):591–606. doi:10.1083/jcb.201402066.

135. Sun X, Zhang A, Baker B, Sun L, Howard A, Buswell J, et al. Development of SNAP-tag fluorogenic probes for wash-free fluorescence imaging. ChemBioChem. 2011;12(14):2217–26. doi:10.1002/cbic.201100173.
136. Gautier A, Juillerat A, Heinis C, Corrêa Jr IR, Kindermann M, Beaufils F, et al. An engineered protein tag for multiprotein labeling in living cells. Chem Biol. 2008;15(2):128–36. doi:10.1016/j.chembiol.2008.01.007.
137. Los GV, Encell LP, McDougall MG, Hartzell DD, Karassina N, Zimprich C, et al. HaloTag: a novel protein labeling technology for cell imaging and protein analysis. ACS Chem Biol. 2008;3(6):373–82. doi:10.1021/cb800025k.
138. Chen Z, Jing C, Gallagher SS, Sheetz MP, Cornish VW. Second-generation covalent TMP-tag for live cell imaging. J Am Chem Soc. 2012;134(33):13692–9. doi:10.1021/ja303374p.
139. Dani A, Huang B, Bergan J, Dulac C, Zhuang X. Superresolution imaging of chemical synapses in the brain. Neuron. 2010;68(5):843–56.
140. Fritschy J-M. Is my antibody-staining specific? How to deal with pitfalls of immunohistochemistry. Eur J Neurosci. 2008;28(12):2365–70. doi:10.1111/j.1460-9568.2008.06552.x.
141. Hinterdorfer P, Van Oijen A. Handbook of single-molecule biophysics. New York: Springer; 2009.
142. Opazo F, Levy M, Byrom M, Schafer C, Geisler C, Groemer TW, et al. Aptamers as potential tools for super-resolution microscopy. Nat Methods. 2012;9(10):938–9.
143. Paige JS, Wu KY, Jaffrey SR. RNA mimics of green fluorescent protein. Science. 2011;333(6042):642–6. doi:10.1126/science.1207339.
144. Nikić I, Kang JH, Girona GE, Aramburu IV, Lemke EA. Labeling proteins on live mammalian cells using click chemistry. Nat Protoc. 2015;10(5):780–91. doi:10.1038/nprot.2015.045.
145. Lajoie MJ, Rovner AJ, Goodman DB, Aerni H-R, Haimovich AD, Kuznetsov G, et al. Genomically recoded organisms expand biological functions. Science. 2013;342(6156):357–60. doi:10.1126/science.1241459.
146. Uttamapinant C, Howe JD, Lang K, Beránek V, Davis L, Mahesh M, et al. Genetic code expansion enables live-cell and super-resolution imaging of site-specifically labeled cellular proteins. J Am Chem Soc. 2015;137(14):4602–5. doi:10.1021/ja512838z.
147. Amann R, Fuchs BM. Single-cell identification in microbial communities by improved fluorescence in situ hybridization techniques. Nat Rev Microbiol. 2008;6(5):339–48.
148. Patel NS, Rhinn M, Semprich CI, Halley PA, Dollé P, Bickmore WA, et al. FGF signalling regulates chromatin organisation during neural differentiation via mechanisms that can be uncoupled from transcription. PLoS Genet. 2013;9(7), e1003614. doi:10.1371/journal.pgen.1003614.
149. Nora EP, Lajoie BR, Schulz EG, Giorgetti L, Okamoto I, Servant N, et al. Spatial partitioning of the regulatory landscape of the X-inactivation center. Nature. 2012;485(7398):381–5. doi:10.1038/nature11049.
150. Doksani Y, Wu JY, de Lange T, Zhuang X. Super-resolution fluorescence imaging of telomeres reveals TRF2-dependent T-loop formation. Cell. 2013;155(2):345–56. doi:10.1016/j.cell.2013.09.048.
151. Vicidomini G, Ta H, Honigmann A, Mueller V, Clausen MP, Waithe D, et al. STED-FLCS: an advanced tool to reveal spatiotemporal heterogeneity of molecular membrane dynamics. Nano Lett. 2015;15(9):5912–8. doi:10.1021/acs.nanolett.5b02001.
152. Pan D, Hu Z, Qiu F, Huang ZL, Ma Y, Wang Y, et al. A general strategy for developing cell-permeable photo-modulatable organic fluorescent probes for live-cell super-resolution imaging. Nat Commun. 2014;5:5573. doi:10.1038/ncomms6573.
153. Taylor DL, Wang Y-L. Molecular cytochemistry: incorporation of fluorescently labeled actin into living cells. Proc Natl Acad Sci USA. 1978;75(2):857–61.
154. Neumann E, Schaefer-Ridder M, Wang Y, Hofschneider P. Gene transfer into mouse lyoma cells by electroporation in high electric fields. EMBO J. 1982;1(7):841.
155. McNeil PL, Warder E. Glass beads load macromolecules into living cells. J Cell Sci. 1987;88(5):669–78.
156. Barber K, Mala RR, Lambert MP, Qiu R, MacDonald RC, Klein WL. Delivery of membrane-impermeant fluorescent probes into living neural cell populations by lipotransfer. Neurosci Lett. 1996;207(1):17–20.
157. Bruckbauer A, James P, Zhou D, Yoon JW, Excell D, Korchev Y, et al. Nanopipette delivery of individual molecules to cellular compartments for single-molecule fluorescence tracking. Biophys J. 2007;93(9):3120–31.
158. Prasher DC, Eckenrode VK, Ward WW, Prendergast FG, Cormier MJ. Primary structure of the *Aequorea victoria* green-fluorescent protein. Gene. 1992;111(2):229–33.
159. Xu K, Shim S-H, Zhuang X. Super-resolution imaging through stochastic switching and localization of single molecules: an overview. In: Tinnefeld P, Eggeling C, Hell SW, editors. Far-field optical nanoscopy. Berlin: Springer; 2013. p. 27–64.
160. Heim R, Prasher DC, Tsien RY. Wavelength mutations and post-translational autoxidation of green fluorescent protein. Proc Natl Acad Sci USA. 1994;91(26):12501–4.
161. Subach FV, Malashkevich VN, Zencheck WD, Xiao H, Filonov GS, Almo SC, et al. Photoactivation mechanism of PAmCherry based on crystal structures of the protein in the dark and fluorescent states. Proc Natl Acad Sci USA. 2009;106(50):21097–102.
162. Cormack BP, Valdivia RH, Falkow S. FACS-optimized mutants of the green fluorescent protein (GFP). Gene. 1996;173(1 Spec No):33–8.
163. Brakemann T, Stiel AC, Weber G, Andresen M, Testa I, Grotjohann T, et al. A reversibly photoswitchable GFP-like protein with fluorescence excitation decoupled from switching. Nat Biotechnol. 2011;29(10):942–7. doi:10.1038/nbt.1952.
164. Schafer SP, Dittrich PS, Petrov EP, Schwille P. Single molecule fluorescence imaging of the photoinduced conversion and bleaching behavior of the fluorescent protein Kaede. Microsc Res Tech. 2006;69(3):210–9. doi:10.1002/jemt.20283.
165. Shin YC, Bischof GF, Lauer WA, Desrosiers RC. Importance of codon usage for the temporal regulation of viral gene expression. Proc Natl Acad Sci USA. 2015;112(45):14030–5. doi:10.1073/pnas.1515387112.
166. Kishino A, Yanagida T. Force measurements by micromanipulation of a single actin filament by glass needles. Nature. 1988;334(6177):74–6.
167. Aitken CE, Marshall RA, Puglisi JD. An oxygen scavenging system for improvement of dye stability in single-molecule fluorescence experiments. Biophys J. 2008;94(5):1826–35. doi:10.1529/biophysj.107.117689.
168. Swoboda M, Henig J, Cheng HM, Brugger D, Haltrich D, Plumere N, et al. Enzymatic oxygen scavenging for photostability without pH drop in single-molecule experiments. ACS Nano. 2012;6(7):6364–9. doi:10.1021/nn301895c.
169. Cordes T, Strackharn M, Stahl SW, Summerer W, Steinhauer C, Forthmann C, et al. Resolving single-molecule assembled patterns with superresolution blink-microscopy. Nano Lett. 2010;10(2):645–51. doi:10.1021/nl903730r.
170. Schäfer P, van de Linde S, Lehmann J, Sauer M, Doose S. Methylene blue- and thiol-based oxygen depletion for super-resolution imaging. Anal Chem. 2013;85(6):3393–400. doi:10.1021/ac400035k.
171. Vogelsang J, Cordes T, Forthmann C, Steinhauer C, Tinnefeld P. Controlling the fluorescence of ordinary oxazine dyes for single-molecule switching and superresolution microscopy. Proc Natl Acad Sci USA. 2009;106(20):8107–12. doi:10.1073/pnas.0811875106.

172. Vaughan JC, Dempsey GT, Sun E, Zhuang X. Phosphine quenching of cyanine dyes as a versatile tool for fluorescence microscopy. J Am Chem Soc. 2013;135(4):1197–200. doi:10.1021/ja3105279.
173. Perkovic M, Kunz M, Endesfelder U, Bunse S, Wigge C, Yu Z, et al. Correlative light-and electron microscopy with chemical tags. J Struct Biol. 2014;186(2):205–13.
174. Cordes T, Vogelsang J, Tinnefeld P. On the mechanism of Trolox as antiblinking and antibleaching reagent. J Am Chem Soc. 2009;131(14):5018–9. doi:10.1021/ja809117z.
175. Longin A, Souchier C, Ffrench M, Bryon P. Comparison of anti-fading agents used in fluorescence microscopy: image analysis and laser confocal microscopy study. J Histochem Cytochem. 1993;41(12):1833–40.
176. Widengren J, Chmyrov A, Eggeling C, Lofdahl PA, Seidel CA. Strategies to improve photostabilities in ultrasensitive fluorescence spectroscopy. J Phys Chem A. 2007;111(3):429–40. doi:10.1021/jp0646325.
177. Senavirathne G, Liu J, Lopez Jr MA, Hanne J, Martin-Lopez J, Lee JB, et al. Widespread nuclease contamination in commonly used oxygen-scavenging systems. Nat Methods. 2015;12(10):901–2. doi:10.1038/nmeth.3588.
178. Song L, Varma CA, Verhoeven JW, Tanke HJ. Influence of the triplet excited state on the photobleaching kinetics of fluorescein in microscopy. Biophys J. 1996;70(6):2959–68. doi:10.1016/S0006-3495(96)79866-1.
179. Rasnik I, McKinney SA, Ha T. Nonblinking and long-lasting single-molecule fluorescence imaging. Nat Methods. 2006;3(11):891–3. doi:10.1038/nmeth934.
180. Chmyrov A, Sanden T, Widengren J. Iodide as a fluorescence quencher and promoter—mechanisms and possible implications. J Phys Chem B. 2010;114(34):11282–91. doi:10.1021/jp103837f.
181. Johnson E, Seiradake E, Jones EY, Davis I, Grunewald K, Kaufmann R. Correlative in-resin super-resolution and electron microscopy using standard fluorescent proteins. Sci Rep. 2016;6:22681. doi:10.1038/srep22681.
182. Valnes KR, Brandtzaeg P. Retardation of immunofluorescence fading during microscopy. J Histochem Cytochem. 1985;33(8):755–61.
183. Tinnefeld P, Cordes T. 'Self-healing' dyes: intramolecular stabilization of organic fluorophores. Nat Methods. 2012;9(5):426–7. doi:10.1038/nmeth.1977.
184. Lukyanov KA, Chudakov DM, Lukyanov S, Verkhusha VV. Innovation: photoactivatable fluorescent proteins. Nat Rev Mol Cell Biol. 2005;6(11):885–91. doi:10.1038/nrm1741.
185. Wiedenmann J, Ivanchenko S, Oswald F, Schmitt F, Rocker C, Salih A, et al. EosFP, a fluorescent marker protein with UV-inducible green-to-red fluorescence conversion. Proc Natl Acad Sci USA. 2004;101(45):15905–10. doi:10.1073/pnas.0403668101.
186. Levitus M, Ranjit S. Cyanine dyes in biophysical research: the photophysics of polymethine fluorescent dyes in biomolecular environments. Q Rev Biophys. 2011;44(1):123–51. doi:10.1017/S0033583510000247.
187. Marriott G, Ottl J. Synthesis and applications of heterobifunctional photocleavable cross-linking reagents. Methods Enzymol. 1998;291:155–75.
188. Vaughan JC, Jia S, Zhuang X. Ultrabright photoactivatable fluorophores created by reductive caging. Nat Methods. 2012;9(12):1181–4. doi:10.1038/nmeth.2214.
189. Mitchison TJ, Sawin KE, Theriot JA, Gee K, Mallavarapu A. Caged fluorescent probes. Methods Enzymol. 1998;291:63–78.
190. Wysocki LM, Grimm JB, Tkachuk AN, Brown TA, Betzig E, Lavis LD. Facile and general synthesis of photoactivatable xanthene dyes. Angew Chem Int Ed. 2011;50(47):11206–9. doi:10.1002/anie.201104571.
191. Berardozzi R, Adam V, Martins A, Bourgeois D. Arginine 66 controls dark-state formation in green-to-red photoconvertible fluorescent proteins. J Am Chem Soc. 2016;138(2):558–565.
192. Lee S-H, Shin JY, Lee A, Bustamante C. Counting single photoactivatable fluorescent molecules by photoactivated localization microscopy (PALM). Proc Natl Acad Sci USA. 2012;109(43):17436–41.
193. Endesfelder U, Finan K, Holden SJ, Cook PR, Kapanidis AN, Heilemann M. Multiscale spatial organization of RNA polymerase in *Escherichia coli*. Biophys J. 2013;105(1):172–81. doi:10.1016/j.bpj.2013.05.048.
194. Puchner EM, Walter JM, Kasper R, Huang B, Lim WA. Counting molecules in single organelles with superresolution microscopy allows tracking of the endosome maturation trajectory. Proc Natl Acad Sci USA. 2013;110(40):16015–20.
195. Lando D, Endesfelder U, Berger H, Subramanian L, Dunne PD, McColl J, et al. Quantitative single-molecule microscopy reveals that CENP-A(Cnp1) deposition occurs during G2 in fission yeast. Open Biol. 2012;2(7):120078. doi:10.1098/rsob.120078.
196. Durisic N, Laparra-Cuervo L, Sandoval-Álvarez Á, Borbely JS, Lakadamyali M. Single-molecule evaluation of fluorescent protein photoactivation efficiency using an in vivo nanotemplate. Nat Methods. 2014;11(2):156–62.
197. Sydor AM, Czymmek KJ, Puchner EM, Mennella V. Super-resolution microscopy: from single molecules to supramolecular assemblies. Trends Cell Biol. 2015;25(12):730–48.
198. Mennella V, Keszthelyi B, McDonald KL, Chhun B, Kan F, Rogers GC, et al. Subdiffraction-resolution fluorescence microscopy reveals a domain of the centrosome critical for pericentriolar material organization. Nat Cell Biol. 2012;14(11):1159–68. doi:10.1038/ncb2597.
199. Burns S, Avena JS, Unruh JR, Yu Z, Smith SE, Slaughter BD, et al. Structured illumination with particle averaging reveals novel roles for yeast centrosome components during duplication. Elife. 2015;4, e08586.
200. Sonnen KF, Schermelleh L, Leonhardt H, Nigg EA. 3D-structured illumination microscopy provides novel insight into architecture of human centrosomes. Biol Open. 2012;1(10):965–76. doi:10.1242/bio.20122337.
201. Briggs JA. Structural biology in situ—the potential of subtomogram averaging. Curr Opin Struct Biol. 2013;23(2):261–7. doi:10.1016/j.sbi.2013.02.003.
202. Ran FA, Hsu PD, Wright J, Agarwala V, Scott DA, Zhang F. Genome engineering using the CRISPR-Cas9 system. Nat Protoc. 2013;8(11):2281–308.
203. Berning S, Willig KI, Steffens H, Dibaj P, Hell SW. Nanoscopy in a living mouse brain. Science. 2012;335(6068):551. doi:10.1126/science.1215369.
204. Maglione M, Sigrist SJ. Seeing the forest tree by tree: super-resolution light microscopy meets the neurosciences. Nat Neurosci. 2013;16(7):790–7.
205. Persson F, Lindén M, Unoson C, Elf J. Extracting intracellular diffusive states and transition rates from single-molecule tracking data. Nat Methods. 2013;10(3):265–9.
206. Chacko JV, Harke B, Canale C, Diaspro A. Cellular level nanomanipulation using atomic force microscope aided with superresolution imaging. J Biomed Opt. 2014;19(10):105003. doi:10.1117/1.JBO.19.10.105003.
207. Wagner M, Weber P, Bruns T, Strauss WS, Wittig R, Schneckenburger H. Light dose is a limiting factor to maintain cell viability in fluorescence microscopy and single molecule detection. Int J Mol Sci. 2010;11(3):956–66.
208. Wäldchen S, Lehmann J, Klein T, van de Linde S, Sauer M. Light-induced cell damage in live-cell super-resolution microscopy. Sci Rep. 2015;5:15348.

209. Keller PJ, Schmidt AD, Santella A, Khairy K, Bao Z, Wittbrodt J, et al. Fast, high-contrast imaging of animal development with scanned light sheet-based structured-illumination microscopy. Nat Methods. 2010;7(8):637–42.

210. Gao L, Shao L, Higgins CD, Poulton JS, Peifer M, Davidson MW, et al. Noninvasive imaging beyond the diffraction limit of 3D dynamics in thickly fluorescent specimens. Cell. 2012;151(6):1370–85.

211. Ingaramo M, York AG, Wawrzusin P, Milberg O, Hong A, Weigert R, et al. Two-photon excitation improves multifocal structured illumination microscopy in thick scattering tissue. Proc Natl Acad Sci USA. 2014;111(14):5254–9.

212. Hajj B, Wisniewski J, El Beheiry M, Chen J, Revyakin A, Wu C, et al. Whole-cell, multicolor superresolution imaging using volumetric multifocus microscopy. Proc Natl Acad Sci USA. 2014;111(49):17480–5.

213. Ji N, Milkie DE, Betzig E. Adaptive optics via pupil segmentation for high-resolution imaging in biological tissues. Nat Methods. 2010;7(2):141–7.

214. Holden S, Sage D. Imaging: super-resolution fight club. Nat Photonics. 2016;10(3):152–3.

215. Endesfelder U. Advances in correlative single-molecule localization microscopy and electron microscopy. NanoBioImaging. 2014;1(1).

216. Liss V, Barlag B, Nietschke M, Hensel M. Self-labelling enzymes as universal tags for fluorescence microscopy, super-resolution microscopy and electron microscopy. Sci Rep. 2015;5:17740.

# 5 | Novel Tool for High Resolution STORM Imaging

## 5.1 A peptide tag-specific nanobody enables high-quality labeling for dSTORM imaging

# A peptide tag-specific nanobody enables high-quality labeling for dSTORM imaging

David Virant, Bjoern Traenkle,Julia Maier, Philipp D. Kaiser, Mona Bodenhöfer, Christian Schmees, Ilijana Vojnovic, Borbála Pisak-Lukáts, Ulrike Endesfelder and Ulrich Rothbauer

This part of the thesis is written in the style of a manuscript and was published in Nature Communications. I contributed to this work by designing and executing experiments, analyzing data and writing part of the text. It presents a novel nanobody-based fluorescent labelling system and is the first SRM tool I helped to develop. The system was effective for structural imaging of large multi-protein assemblies such as the cytoskeleton, tracking of mobile membrane proteins, and even quantitative measurements of bacterial ferritin complexes. It proved to be transferable to all chosen targets. [2]

nature
COMMUNICATIONS

ARTICLE

DOI: 10.1038/s41467-018-03191-2 OPEN

# A peptide tag-specific nanobody enables high-quality labeling for dSTORM imaging

David Virant[1], Bjoern Traenkle[2], Julia Maier[2], Philipp D. Kaiser[3], Mona Bodenhöfer[3], Christian Schmees[3], Ilijana Vojnovic[1], Borbála Pisak-Lukáts[1], Ulrike Endesfelder[1] & Ulrich Rothbauer[2,3]

Dense fluorophore labeling without compromising the biological target is crucial for genuine super-resolution microscopy. Here we introduce a broadly applicable labeling strategy for fixed and living cells utilizing a short peptide tag-specific nanobody (BC2-tag/bivBC2-Nb). BC2-tagging of ectopically introduced or endogenous proteins does not interfere with the examined structures and bivBC2-Nb staining results in a close-grained fluorophore labeling with minimal linkage errors. This allowed us to perform high-quality dSTORM imaging of various targets in mammalian and yeast cells. We expect that this versatile strategy will render many more demanding cellular targets amenable to dSTORM imaging.

---

[1] Department of Systems and Synthetic Microbiology, Max Planck Institute for Terrestrial Microbiology and LOEWE Center for Synthetic Microbiology (SYNMIKRO), Karl-von-Frisch Strasse 16, Marburg 35043, Germany. [2] Pharmaceutical Biotechnology, Eberhard Karls University Tuebingen, Markwiesenstrasse 55, Reutlingen 72770, Germany. [3] Natural and Medical Sciences Institute at the University of Tuebingen, Markwiesenstrasse 55, Reutlingen 72770, Germany. These authors contributed equally: David Virant, Bjoern Traenkle, Ulrike Endesfelder and Ulrich Rothbauer. Correspondence and requests for materials should be addressed to U.E. (email: ulrike.endesfelder@synmikro.mpi-marburg.mpg.de) or to U.R. (email: ulrich.rothbauer@uni-tuebingen.de)

Fluorescence-based super-resolution microscopy (SRM) is becoming increasingly applied in cell biology. Single-molecule localization microscopy (SMLM) techniques, such as (direct) stochastic optical reconstruction microscopy ((d)STORM) provide outstanding spatial resolutions and have enabled unprecedented insights into the organization of subcellular components[1–3]. However, the quality and value of SMLM imaging can be limited due to poor photon emission or detection efficiency, low fluorophore labeling densities, linkage errors or steric hindrances[4–6]. Most current SMLM labeling approaches employ antibodies or recombinant proteins either fused to photoactivatable fluorescent proteins (FPs) or fluorogen-labeling enzymes, such as the Halo-, CLIP-, or SNAP-tag[7–10]. While conventional antibodies introduce significant linkage errors by displacing the fluorophore from the target, large protein/enzyme tags can affect expression, cellular localization, folding and/or function of the respective fusion protein[11–13]. Although small peptide tags, such as FLAG-, HA-, or Myc-tag[14–16] are available, those epitopes often have to be arranged in multiple arrays to recruit medium-affine binding antibodies[17] and thus do not provide dense labeling sufficient for high-quality SRM.

Instead of using antibodies, a 15-amino-acid peptide-tag can be visualized by high-affinity fluorescently labeled monomeric streptavidin[18], which, however, can be affected by the binding of endogenously biotinylated proteins. Alternatively, reversibly on- and off-binding labels in point accumulation for imaging of nanoscale topography (PAINT) microscopy allow for a continuous and therefore ultra-high density readout as they are not limited by a predefined fluorophore tagging pattern[19]. Yet, this approach can only be used for distinguishable structures like membranes or DNA combined with illumination-confined arrangements, such as in surface-near or lightsheet illuminations[20]. The visualization of other structures by PAINT approaches relies on a specific labeling commonly achieved by DNA-PAINT[21, 22].

As a promising substitute for conventional antibodies, small-sized nanobodies (antibody fragments derived from heavy-chain-only camelid antibodies) coupled to organic dyes were recently introduced for SRM. Nanobodies targeting native proteins, such as components of the nuclear pore complex, tubulin, or vimentin were described for dSTORM imaging[23–25]. Despite their capability to directly probe endogenous antigens, the de novo generation of gene-specific nanobodies and their validation for SRM imaging purposes is cumbersome and time-consuming[26, 27], which is reflected by the fact that only a very limited number of SRM-compatible nanobodies are available by now[25]. Due to their applicability for nanoscopy of widely used FP-fusions, GFP-, and RFP-nanobodies became very popular tools for SMLM[28, 29]. However, this strategy relies on the correct expression of FP-fusions and does not cope with problems arising from mislocalization or dysfunction[12, 13, 30]. Thus, nanobodies directed against short and inert tags might prove advantageous for SRM.

Here we introduce a versatile labeling and detection strategy comprised the short and inert BC2 peptide-tag (PDRKAAVSHWQQ) and a corresponding high-affinity bivalent nanobody (bivBC2-Nb) for high-quality dSTORM imaging. We demonstrate the benefits of our approach for close-grained fluorophore labeling with minimal linkage error of various ectopically introduced and endogenous targets in fixed and living cells.

## Results

**Development of a dSTORM suitable BC2-tag/bivBC2-Nb system**. As originally described, we first labeled the BC2-Nb at accessible lysine residues by N-hydroxysuccinimide (NHS) ester fluorophores, such as Alexa Fluor 647 (AF647)[31]. While BC2-Nb$_{\mathrm{AF647\ (NHS)}}$ is sufficient for wide-field microscopy (Fig. 1a, left panel, Supplementary Fig. 1a, b), dSTORM imaging of BC2-tagged proteins revealed a rather low-staining efficiency resulting in inferior structural labeling coverage (Fig. 1b, left panel). Thus, we analyzed the binding properties of a bivalent format of the BC2-Nb (bivBC2-Nb) (Fig. 1a, right panel). We assessed its binding kinetics by biolayer interferometry (BLI) and observed a considerably reduced dissociation rate compared to monovalent BC2-Nb (Supplementary Fig. 1c). Notably, this decrease in dissociation rate is not caused by simultaneous binding of the bivBC2-Nb to two BC2 epitopes as confirmed by a BLI assay using a tandem-BC2-tag of two consecutively linked BC2 epitopes (BC2-BC2-tag) (Supplementary Fig. 1d).

Nevertheless, antigen labeling using the bivBC2-Nb conjugated to NHS-ester fluorophores (bivBC2-Nb$_{\mathrm{AF647\ (NHS)}}$) did not yield the expected visual improvement of staining specificity (Fig. 1a, right panel). Considering the crystal structure[31], we designed a site-directed, enzymatic coupling strategy, which should not affect the paratope and binding properties of bivBC2-Nb. Using the Sortase A system, we linked peptides conjugated to a single-AF647 fluorophore in a defined 1:1 ratio to the C-terminus of bivBC2-Nb (bivBC2-Nb$_{\mathrm{AF647\ (sort)}}$)[32, 33]. This approach significantly improved the staining specificity by a factor of two compared to bivBC2-Nb$_{\mathrm{AF647\ (NHS)}}$ (Fig. 1a, right panel, Fig. 1c and Supplementary Fig. 1a, b, e). An exemplary dSTORM image of a HeLa cell transiently expressing vimentin$_{\mathrm{BC2T}}$ and stained with the bivBC2-Nb$_{\mathrm{AF647\ (sort)}}$ illustrates the remarkable quality of the BC2-tag/bivBC2-Nb labeling strategy (Fig. 1b, right panel). For a better understanding bivBC2-Nb$_{\mathrm{AF647\ (sort)}}$ is referred to bivBC2-Nb$_{\mathrm{AF647}}$ in the following.

Since the BC2-Nb was originally developed against β-catenin[34], we assessed the influence of the background staining of endogenous β-catenin on the labeling quality. To distinguish background due to general unspecific staining from additional β-catenin staining, we compared HeLa cells (not expressing any GFP epitope) stained with a GFP-targeting nanobody (GFP-Nb$_{\mathrm{AF647}}$) to HeLa cells stained with bivBC2-Nb$_{\mathrm{AF647}}$. Further, we performed bivBC2-Nb$_{\mathrm{AF647}}$ staining in HeLa cells transiently expressing the non-structural, autophagosomal marker protein LC3B fused to the BC2-tag ($_{\mathrm{BC2T}}$LC3B), which is - in the absence of autophagy- homogeneously distributed throughout the cytoplasm. By analyzing the dSTORM data using DBSCAN clustering[35], we measured a slightly increased level of 1.7 (±0.3 S.D.) nanobodies per square micrometer for bivBC2-Nb$_{\mathrm{AF647}}$ compared to the unspecific background staining of 0.61 (±0.03 S.D.) GFP-Nb$_{\mathrm{AF647}}$ per μm$^2$. However, this level is considerably lower compared to 7.2 (±1.3 S.D.) bivBC2-Nb$_{\mathrm{AF647}}$ per μm$^2$ which we obtained for the staining of $_{\mathrm{BC2T}}$LC3B expressing cells (Fig. 1d, Supplementary Fig. 2a). We then compared signal intensities derived from bivBC2-Nb$_{\mathrm{AF647}}$-stained HeLa cells, which were either left untreated or incubated with CHIR99021 (CHIR) to accumulate endogenous β-catenin[34]. While immunolabeling with a β-catenin-specific antibody showed a strong enrichment in CHIR-treated cells (Supplementary Fig. 2b), dSTORM imaging revealed only a minor increase of bivBC2-Nb$_{\mathrm{AF647}}$ localizations (Supplementary Fig. 2c, left panel). Moreover, in CHIR-treated HeLa cells transiently expressing vimentin$_{\mathrm{BC2T}}$, the nanobody signal was almost exclusively detectable at vimentin fibers (Supplementary Fig. 2c, right panel). Overall, bivBC2-Nb$_{\mathrm{AF647}}$ staining resulted in 36 (±2 S.D.) localizations per μm$^2$ for untreated HeLa cells, 133 (±5 S.D.) localizations per μm$^2$ for CHIR-treated HeLa cells, 2493 (±285 S.D.) localizations per μm$^2$ for HeLa-vimentin$_{\mathrm{BC2T}}$ cells and 2490 (±456 S.D.) localizations per μm$^2$ for CHIR-treated HeLa-vimentin$_{\mathrm{BC2T}}$ cells (Supplementary Fig. 2d). From this we conclude that even if present at high levels, the BC2-epitope of β-catenin has a negligible impact on staining of ectopically introduced antigens.

For a stoichiometric quantification of the labeling quality of the BC2-tag/bivBC2-Nb detection system, we utilized the *Escherichia coli* protein ferritin (FtnA) recently described as a homo-oligomeric protein standard of 24 subunits[36]. We expressed BC2-tagged, as well as SNAP-tagged FtnA-24mers in U2OS cells and performed dSTORM imaging on cell lysates immobilized on coverslips[36]. By measuring single-AF647 blinking events, we obtained the parameters of the corresponding log-normal distribution ($\mu = 5.68$, $\sigma = 0.4$), which describes the probability distribution of single-molecule fluorescence intensities (Supplementary Fig. 3a). We then measured the fluorescence intensities of immobilized FtnA oligomers labeled with the BC2-tag/bivBC2-Nb or SNAP-tag system. We compared these distributions to the expected fluorescence intensity distributions of fully labeled FtnA-24mers, calculated from the single-molecule fluorescence intensity distribution and the degree of labeling of each component (Methods section). As a result, the BC2-tag/bivBC2-Nb FtnA-oligomer staining revealed a completeness of labeling of

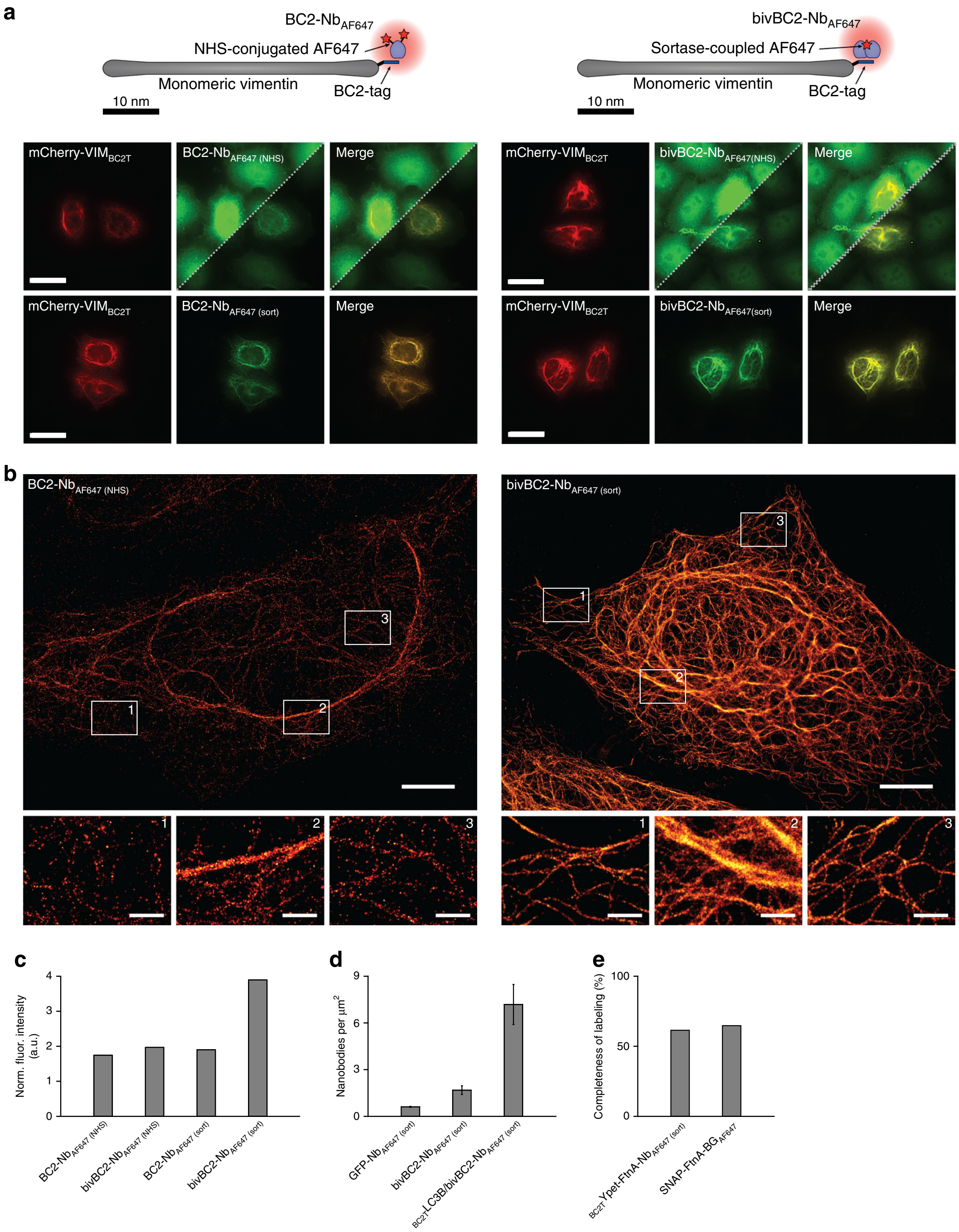

61.4% which competes with the covalent SNAP-tag FtnA-staining efficiency of 64.7% (Fig. 1e, Supplementary Fig. 3b) and outcompetes photoactivation/photoconversion efficiencies of fluorescent proteins[37]. Notably, our observation of a rather low efficiency of about 65% for the SNAP-tag labeling is in agreement with reported assessments[36, 38], and conference presentations by K. Yserentant (2017).

**Comparison of different labeling strategies for SMLM**. As genetic tagging of structural proteins like vimentin often impairs their structure and function[39, 40], we evaluated the influence of the short BC2-tag on vimentin structure formation and compared the BC2-tag/bivBC2-Nb detection system with established strategies focusing on image quality and apparent organization of the vimentin network. We performed SMLM on native vimentin in comparison to vimentin fused to photoactivatable mCherry (PAmCherry-vimentin), eGFP (GFP-vimentin), or the BC2-tag (Fig. 2a, b). For our studies, we transiently expressed the corresponding proteins for 24 h in HeLa cells followed by chemical fixation of the cells. Native vimentin was visualized with the recently described vimentin-specific nanobody bivVB6-$Nb_{AF647}$[25, 41], while PAmCherry-vimentin was mapped directly. The other constructs were labeled with the nanobodies GFP-$Nb_{AF647}$ or bivBC2-$Nb_{AF647}$, respectively. Image analysis of the vimentin network visualized by the different labeling strategies revealed considerable phenotypic differences (Fig. 2b, c; images of all cells quantitatively analyzed Supplementary Fig. 4a–d; analysis routine Supplementary Fig. 4e and Methods section). 94% of native vimentin fibers labeled with the bivVB6-$Nb_{AF647}$ showed widths lower than 150 nm. In contrast, cells with incorporated PAmCherry-vimentin were smaller and showed a high percentage (20%) of thick vimentin bundles above 150 nm width, while in GFP-vimentin expressing cells more than 96% of all detectable vimentin fibers had widths below 75 nm (Fig. 2c). Compared to the N-terminally labeled counterparts, cells expressing vimentin-PAmCherry displayed a highly similar phenotype whereas cells expressing vimentin C-terminally fused to GFP (vimentin-GFP) showed an even more severely fragmented vimentin network (Supplementary Fig. 5). Obviously, both type and position of the FP affects the formation of the vimentin network and induce altered cellular phenotypes. The various observed morphological alterations are likely caused by several mislocalization and self-oligomerization artifacts induced by the different FP moieties derived either from jelly fish (GFP) or red corals (DsRed)[40, 42]. Notably, no phenotypic changes or significant differences in the abundance of fiber widths were detected between native and BC2-tagged vimentin (96% of all fibers below 150 nm, 4% above 150 nm; Fig. 2b, c and Methods section).

We then assessed the SMLM image quality achievable by the different labeling approaches. The quality is dependent on two main factors; (i) the optical resolution dictated by the precision with which fluorescent spots can be localized, and (ii) the structural resolution determined by the labeling density (coverage) and the physical distance between fluorophore and target (linkage error). We assessed these parameters for each analyzed fiber individually. The localization precision was calculated by a Nearest Neighbor based Analysis (NeNA)[43], the labeling density was determined by the lengthwise fluorescent signal coverage along each fiber, and the linkage error by quantifying the apparent width of fibers of the smallest fiber category. For further comparison, we calculated the Fourier Image REsolution (FIRE) values[44] (see Supplementary Note 1). Since the readout of all three nanobody labeling strategies relies on the same bright fluorophore (AF647), NeNA yielded the same optical resolution statistics with a mean NeNA localization precision of about 9–12 nm. The fluorescent-protein PAmCherry has a lower photon yield and achieves an average NeNA value of 17 nm (Supplementary Fig. 6). The structural resolution as assessed by the different labeling coverage statistics revealed significant differences (Fig. 2c, Supplementary Fig. 6 and Methods section). For PAmCherry-vimentin, we observed the lowest coverage among all labeling strategies for thin fibers, and a maximum coverage of ~75% for thick fibers, which is likely due to inefficient chromophore formation and photoactivation. The low coverage of ~50% for the GFP-Nb is more likely explained by a steric hindrance in incorporating GFP-tagged molecules into the native vimentin network, which is in line with our observation of only thin fibers. The highest labeling coverage was observed for bivBC2-Nb with a coverage of ~80% for fibers below 75 nm width, and nearly full coverage of fibers exceeding a width of 150 nm. For thin fibers it exceeds the coverage obtained with the bivVB6-Nb for native vimentin, which might be due to a reduced accessibility of the native epitope within assembled vimentin filaments. To assess the impact of the size of the labeling probe on the structural resolution, we compared our bivBC2-Nb-based approach with conventional, monoclonal antibody staining (Supplementary Fig. 7a). Antibody labeling resulted in nearly complete coverage of thin vimentin fibers (>75 nm) (Supplementary Fig. 7b), and the AF647-based readout resulted in the same localization precision and optical

**Fig. 1** Comparison and characterization of BC2-nanobody (BC2-Nb) formats for wide-field and dSTORM imaging. **a** Schematic illustration of the BC2-Nb dye-conjugation strategies. Monovalent and bivalent BC2-Nbs were either conjugated with Alexa Fluor 647 (AF647) via N-hydroxysuccinimide (NHS) ester (left panel) or linked to AF647 by enzymatic sortase coupling (right panel). Wide-field imaging of chemically fixed HeLa cells expressing mCherry-$vimentin_{BC2T}$ (mCherry-$VIM_{BC2T}$) stained with modified BC2-Nbs. Monovalent versions of the BC2-Nbs (NHS- and sortase-coupled) are depicted on the left panel, corresponding bivBC2-Nbs are displayed on the right side. Stainings with NHS-conjugated nanobodies are shown in two different image contrasts, the upper half in the same brightness and contrast as the sortase-coupled nanobodies; in the lower half with an adjusted contrast. Scale bars, 25 µm. **b** Representative dSTORM images of chemically fixed HeLa cells expressing $vimentin_{BC2T}$, stained with the monomeric NHS-conjugated BC2-$Nb_{AF647\ (NHS)}$ (left) and the sortase-coupled bivBC2-$Nb_{AF647\ (sort)}$ (right). Scale bars, images 5 µm, insets 1 µm. Image reconstruction details are given in Methods section. **c** Assessment of staining quality in wide-field fluorescence imaging. Labeling of the different nanobody formats was quantified by calculating the ratio of the signal intensity of mCherry-$VIM_{BC2T}$ expressing cells to non-transfected cells (background), (BC2-$Nb_{AF647\ (NHS)}$: $n = 115$; bivBC2-$Nb_{AF647\ (NHS)}$: $n = 134$; BC2-$Nb_{AF647\ (sort)}$: $n = 150$; bivBC2-$Nb_{AF647\ (sort)}$: $n = 195$) (Methods section, Supplementary Fig. 1). **d** Assessment of bivBC2-$Nb_{AF647}$ staining of endogenous β-catenin. Bar chart summarizes measured nanobody per µm$^2$ values for untransfected chemically fixed HeLa cells stained with GFP-$Nb_{AF647}$ or bivBC2-$Nb_{AF647}$ in comparison to chemically fixed HeLa cells transiently expressing $_{BC2T}$LC3B stained with bivBC2-$Nb_{AF647}$, errors given as standard deviation (S.D.), $N = 3$ cells for each condition (Methods section, Supplementary Fig. 2). **e** Quantification of completeness of labeling for the bivBC2-Nb and SNAP-tag labeling systems using FtnA-oligomers of 24 subunits. Bar chart summarizes median values of FtnA-24mer fluorescence intensities as percentage of theoretical maxima (Methods section, Supplementary Fig. 3)

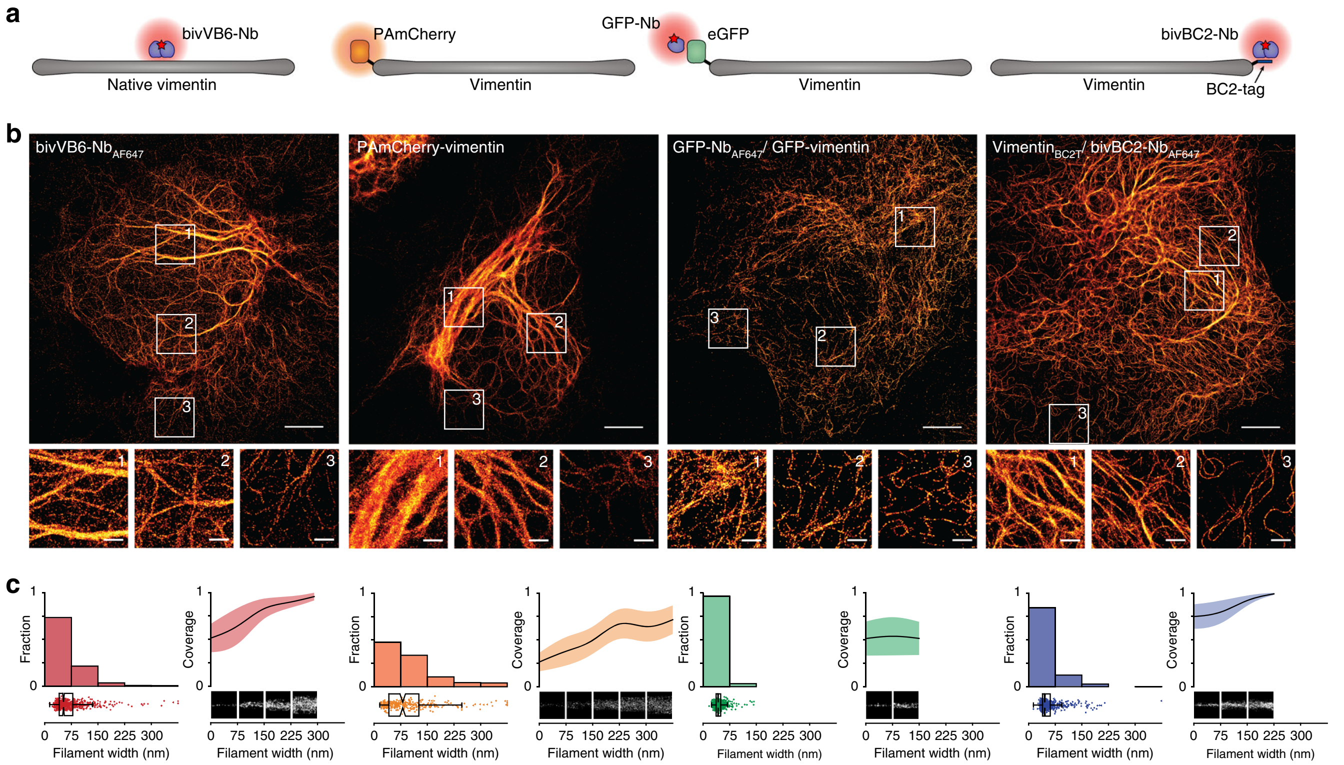

**Fig. 2** Super-resolution imaging and analysis of differently labeled vimentin constructs. **a** Schematic illustration of labeling strategies used for comparative SRM imaging of native or ectopically expressed vimentin. **b** Representative PALM/dSTORM images of chemically fixed Hela cells expressing the corresponding constructs outlined in **a** or native vimentin (left panel). Insets show magnifications of representative vimentin filaments of varying thickness (1—thick, 2—medium, 3—thin, peripheral). Scale bars, 5 µm in main images, 1 µm in insets. **c** Filament widths as histograms (left) with a bin size of 75 nm (*x*-axis) plotted against relative fraction (*y*-axis). Full data are represented underneath the histograms as box + scatter plots with the same *x*-axis. The box marks the three quartiles and the whiskers mark 95% of all the data. The average lengthwise fluorophore coverage was calculated for each bin and plotted (right) as mean filament width (black line) and standard deviation (colored area) against relative fraction covered by fluorophores (*y*-axis). Width and lengthwise fluorophore coverage were analyzed for a total of 676 (bivVB6-Nb$_{\text{AF647}}$), 295 (PAmCherry), 724 (GFP-Nb$_{\text{AF647}}$), and 620 (bivBC2-Nb$_{\text{AF647}}$) filaments, $N = 5$ cells for each condition, cells, and selected filaments are shown in Supplementary Fig. 4. Image reconstruction details are given in Methods section

resolution statistics (Supplementary Fig. 7c). Despite the high-labeling coverage, the antibody-mediated displacement of the fluorophore led to an increased linkage error. Accordingly, we measured an average width of ~55 nm for thin vimentin fibers probed with the antibody, whereas a smaller apparent width of ~40 nm was observed with bivBC2-Nb (Supplementary Fig. 7c).

**Detection of various cellular targets with the bivBC2-Nb**. Next we analyzed whether the BC2-tag/bivBC2-Nb detection system is transferable to other structural proteins. To test whether orientation of the BC2-tag affects the incorporation of the recombinant protein into endogenous structures, we transiently expressed cDNAs of mouse *TUBA1B*, human *LMNB1*, or *ACTB* either comprising the BC2-tag on the N- or the C-terminus in different cell lines followed by detection with bivBC2-Nb$_{\text{AF647}}$. As exemplarily shown for tubulin alpha-1B, C-terminal addition of the BC2-tag yielded more distinct microtubule structures compared to the N-terminally tagged version (Supplementary Fig. 8). For lamin B1, we observed no differences regarding the tag position whereas ectopically expressed β-actin is only incorporated into the actin cytoskeleton when the BC2-tag is located at the N-terminus, which is in accordance to previously tested tagging approaches[45]. dSTORM imaging of HeLa cells expressing either lamin$_{\text{BC2T}}$ or $_{\text{BC2T}}$actin, as well as U2OS cells transiently expressing tubulin$_{\text{BC2T}}$ revealed that BC2-tagged proteins are efficiently incorporated in the corresponding structures and could be imaged at high-resolution reaching localization precisions of 9–12 nm as previously shown for vimentin$_{\text{BC2T}}$ (Fig. 3a–c, Supplementary Fig. 9). As individual microtubules have a defined diameter of 25 nm these structures serve as an experimental benchmark for SRM[24, 28, 46]. Simulations on nanobody labeling of microtubules using a maximal probe displacement of 5 nm and a localization precision cutoff of 10 nm have yielded an apparent fiber width of about 40 nm[24], which is in perfect agreement to our measured fiber width of 38.2 ± 9.2 nm (Supplementary Fig. 9a). Moreover, a detailed analysis of individual actin fibers comprising transiently expressed $_{\text{BC2T}}$actin showed comparable labeling densities as previously obtained for vimentin$_{\text{BC2T}}$ (Supplementary Fig. 9b-d).

Additionally, we used our approach to visualize non-structural proteins, namely the autophagosomal marker protein LC3B and the extracellular membrane marker GFP-GPI[47, 48]. To monitor induction of autophagy, we co-expressed $_{\text{BC2T}}$LC3B and GFP-LC3B in HeLa or A549 cells followed by incubation with DMSO or rapamycin to induce autophagosome formation. Wide-field imaging of chemically fixed cells, stained with bivBC2-Nb$_{\text{AF647}}$, showed a clear co-localization of GFP and nanobody signals at defined spots in rapamycin-treated cells, indicating correct localization of BC2-tagged LC3B at autophagosomes[47, 49]

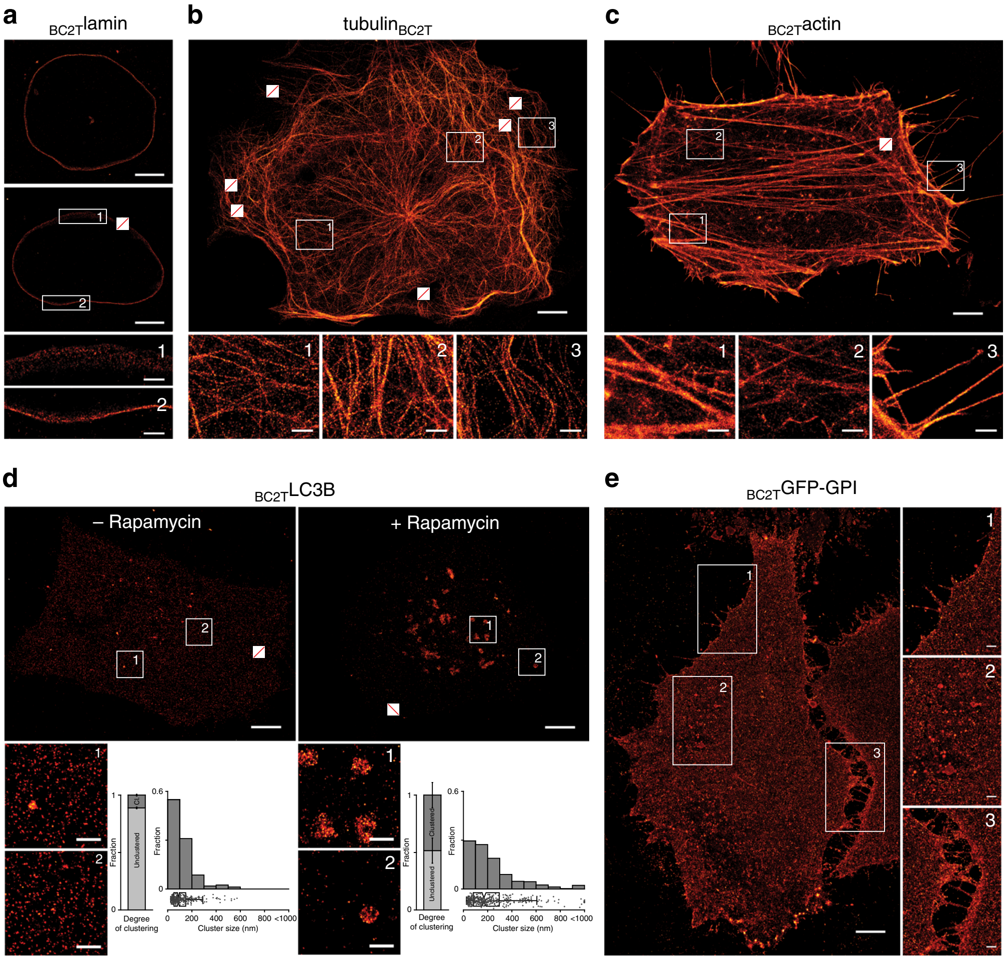

**Fig. 3** Super-resolution imaging of transiently expressed BC2-tagged proteins in chemically fixed cells. Representative dSTORM images of a **a** HeLa cell expressing $_{\text{BC2T}}$lamin, **b** U2OS cell expressing tubulin$_{\text{BC2T}}$ (filament width statistics in Supplementary Fig. 9a), **c** HeLa cell expressing $_{\text{BC2T}}$actin (coverage statistics in Supplementary Fig. 9b), **d** HeLa cells expressing $_{\text{BC2T}}$LC3B either left untreated or treated with rapamycin. Bar charts represent the degree of clustering, given as a relative fraction of cluster points versus noise points, errors given as standard deviation (S.D.). Histograms represent cluster diameters as determined by DBSCAN analysis with a bin size of 100 nm ($x$-axis) plotted against relative fraction ($y$-axis). Full data are represented underneath the histograms as box + scatter plots with the same $x$-axis. The box marks the three quartiles and the whiskers mark 95% of all the data. Total number of clusters $n = 342$ in non-treated cells, $n = 405$ in treated cells, $N = 3$ cells for untreated cells and $N = 4$ cells for rapamycin-treated cells (Supplementary Fig. 11), and **e** HeLa cells expressing $_{\text{BC2T}}$GFP-GPI. All cells were stained with bivBC2-Nb$_{\text{AF647}}$ (Methods section). Scale bars, images 5 µm, insets 1 µm. Crossed out rectangles mark the position of fiducial markers used for drift correction. Image reconstruction details are given in Methods section

(Supplementary Fig. 10a). Further, dSTORM imaging and subsequent DBSCAN cluster analysis of newly formed autophagosomes in $_{\text{BC2T}}$LC3B expressing cells after incubation with rapamycin revealed diameters of ~0.3–1.0 µm for these foci (Fig. 3d, Supplementary Fig. 11, Methods section), which is in accordance to previous findings[50, 51]. For BC2-tagged GFP-GPI ($_{\text{BC2T}}$GFP-GPI), we observed a clear co-localization of the nanobody and the GFP signal at the plasma membrane in chemically fixed HeLa cells (Supplementary Fig. 10b). Notably, with dSTORM, we detected a defined spatial organization of $_{\text{BC2T}}$GFP-GPI, e.g., the formation of small clusters and enrichment of $_{\text{BC2T}}$GFP-GPI molecules at cell–cell contacts, compared to a diffraction-limited, homogenous distribution observable by wide-field microscopy (Fig. 3e, Supplementary Fig. 10b).

**Visualization of endogenous proteins with the bivBC2-Nb.** To utilize the BC2-tag as an endogenous marker under native promotor expression, we first replaced the gene coding for the nuclear DNA-binding protein cbp1 at its endogenous loci in the fission yeast *Schizosaccharomyces pombe* (*S. pombe)* by a C-terminally BC2-tagged version (cbp1$_{\text{BC2T}}$). Cells expressing cbp1$_{\text{BC2T}}$ show growth rates comparable to wild type (wt) and exhibit no morphological changes (Supplementary Fig. 12a, b). As *S. pombe* possesses a thick cell wall and a highly packed cellular environment, any immunofluorescence-based SRM approach suffers from high-unspecific background and low-staining quality. Notably, by staining endogenously expressed cbp1$_{\text{BC2T}}$ utilizing the bivBC2-Nb$_{\text{AF647}}$ we were now able to visualize an endogenous nuclear protein in *S. pombe* by dSTORM imaging (Supplementary Fig. 12a). Second, we stably introduced the coding sequence of the BC2-tag under the native β-actin promotor at the 5′-end of the first exon of endogenous β-actin in HeLa and A549 cells using the CRISPR/Cas9 technology. After monoclonal selection of cells exhibiting a heterozygous integration of $_{\text{BC2T}}$actin (HeLa-$_{\text{BC2T}}$ACTB; A549-$_{\text{BC2T}}$ACTB, Methods section) we treated both cell lines with transforming growth

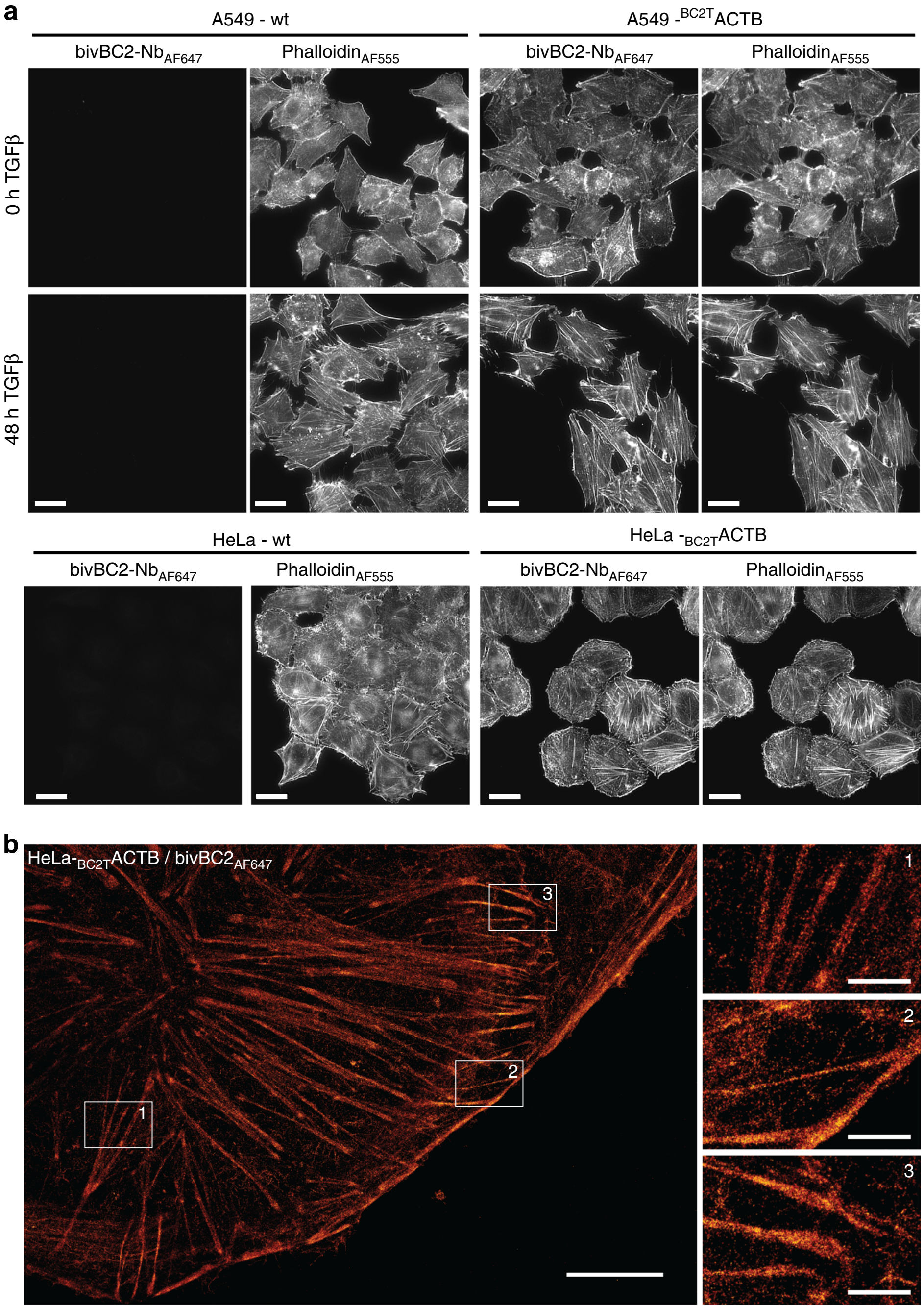

**Fig. 4** Visualization of endogenously expressed BC2-tagged actin labeled with bivBC2-Nb$_{AF647}$. **a** Wide-field images of chemically fixed wild-type A549 and HeLa (-wt; left panel), as well as chemically fixed A549-$_{BC2T}$ACTB and HeLa-$_{BC2T}$ACTB cells (right panel). Cells were either left untreated (0 h) or stimulated for 48 h with TGFβ (5 ng ml$^{-1}$) followed by staining with phalloidin$_{AF555}$ and bivBC2-Nb$_{AF647}$. Scale bars, 25 µm. **b** dSTORM image of a representative HeLa-$_{BC2T}$ACTB cell. Scale bars, image 5 µm, insets 1 µm. Image reconstruction details are given in Methods section. Imaging sequence taken from raw data acquisition can be found in Supplementary Movie 5, assessment of AF647 photophysics under dSTORM imaging conditions can be found in Supplementary Fig. 15

factor β (TGFβ) and monitored the induction of actin stress fibers by co-staining with bivBC2-Nb$_{AF647}$ and phalloidin$_{AF555}$. As expected, we detected the formation of stress fibers only in A549 wt and A549-$_{BC2T}$ACTB cells, which are described to respond to TGFβ[52] (Fig. 4a). dSTORM imaging further allowed a detailed insight into the non-disturbed actin network (Fig. 4b). These findings indicate that BC2-tagging of endogenous proteins is a viable approach for SRM studies to visualize cellular targets at endogenous levels and with minimal functional interference.

**bivBC2-Nb visualizes its target proteins in living cells.** To realize the advantages of the BC2-tag/bivBC2-Nb system also for live-cell applications, we first performed time-lapse imaging of HeLa cells transiently expressing $_{BC2T}$GFP-GPI. After addition of bivBC2-Nb$_{AF647}$ to the imaging medium, we observed a fast recruitment of the nanobody to its membrane-located antigen (Supplementary Fig. 13a), with a saturation of the nanobody signal within 20–30 min (Supplementary Fig. 13b). Single-particle tracking dSTORM imaging further allowed us to trace the highly

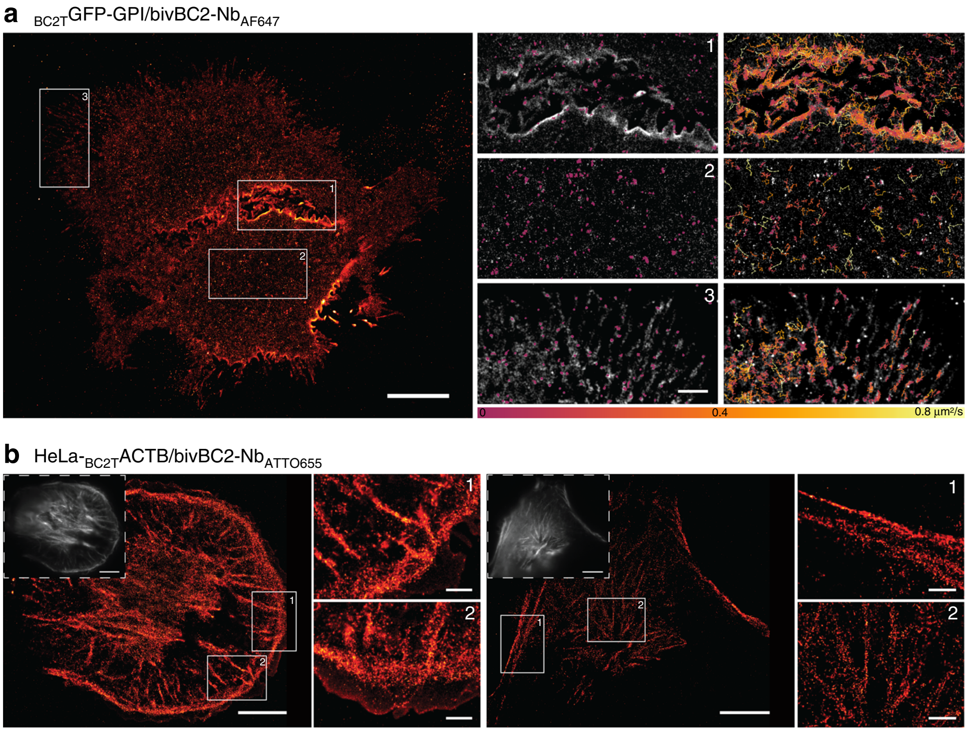

**Fig. 5** Super-resolution imaging and single-particle tracking in live HeLa cells. **a** dSTORM image of live $_{BC2T}$GFP-GPI expressing HeLa cells stained with bivBC2-Nb$_{AF647}$ and insets in gray scale overlaid with single-particle trajectories of immobile (diffusion coefficient below 0.02 µm$^2$ s$^{-1}$, left) and mobile (diffusion coefficient above 0.02 µm$^2$ s$^{-1}$, right). Color scale of diffusion coefficients is given under insets. Scale bars 10 µm in images, 2 µm in insets. Supplementary Movies 1-4 show the recorded live $_{BC2T}$GFP-GPI dynamics of the whole cell and the corresponding insets. **b** Live-cell dSTORM images of two HeLa-$_{BC2T}$ACTB cells stained with bivBC2-Nb$_{ATTO655}$. Wide-field fluorescence images in upper left corners. Scale bars in 10 µm, 2 µm in insets. Image reconstruction details are given in Methods section. Imaging sequence taken from raw data acquisition can be found in Supplementary Movie 6, assessment of ATTO655 photophysics under live cell dSTORM imaging conditions can be found in Supplementary Fig. 15

dynamic movements of thousands of $_{BC2T}$GFP-GPI molecules along the plasma membrane in high spatial and temporal resolution, e.g., the increased dynamics at cell-to-cell contact areas (Fig. 5a, Supplementary Movies 1–4). Second, for bivBC2-Nb staining of intracellular targets in living cells, we adapted a lipid-based protein transfection protocol[53, 54] and introduced bivBC2-Nb conjugated to different dyes into our cell lines HeLa-$_{BC2T}$ACTB and A549-$_{BC2T}$ACTB. Within 2 h, we observed cellular uptake of nanobody and its accumulation at the actin cytoskeleton irrespective of the attached fluorophore (Supplementary Fig. 14a). Prolonged time-lapse imaging of live HeLa-$_{BC2T}$ACTB cells for 5 h revealed a stable staining of the cytoskeleton (Supplementary Fig. 14b). Finally, we performed live-cell dSTORM imaging replacing AF647 with the fluorophore ATTO655 which is currently one of the few organic dyes exhibiting sufficient photoswitching under physiological intracellular conditions[8]. Two hours after nanobody transduction, dSTORM imaging of the bivBC2-Nb$_{ATTO655}$ staining revealed the intracellular actin network of HeLa-$_{BC2T}$ACTB cells (Fig. 5b) with sub-diffraction details as previously seen for chemically fixed HeLa-$_{BC2T}$ACTB cells (Fig. 4b). We further documented the photophysical differences in performance of the ATTO655 fluorophore, which is outcompeted by AF647 both in blinking statistics and brightness (Supplementary Fig. 15, Supplementary Movies 5 and 6). In summary, these data demonstrate that the bivBC2-Nb is functional within living cells where it retains its outstanding binding capacities allowing for live-cell dSTORM imaging. Other recently reported protein transduction approaches offer numerous alternatives to introduce the bivBC2-Nb in various cell types for live-cell imaging of BC2-tagged proteins[41, 55–61].

## Discussion

In this study, we developed and extensively characterized a broadly applicable and transferable labeling strategy based on a structurally minimal tag in combination with the first peptide-specific nanobody suitable for SRM. In contrast to the widely established GFP/GFP-Nb system[28, 62] for dSTORM imaging of fusion proteins comprising a large fluorescent moiety, the short and inert BC2-tag allows an efficient and dense incorporation of ectopically and endogenously expressed proteins into higher-ordered cellular structures in mammalian and yeast cells. In particular, it does not interfere with the native organization of structural proteins, such as vimentin, lamin, actin, and tubulin known to be easily compromised by large protein tags. We demonstrated that all tested BC2-tagged proteins are efficiently detected with a high affinity, bivalent nanobody format, robustly labeled in a one-to-one nanobody to fluorophore ratio exhibiting a high-labeling efficiency competing with covalent detection systems. Together, this enables high-labeling coverage with minimal linkage error and thus allows for genuine SRM studies of physiologically undisturbed cellular structures. Moreover, the bivBC2-Nb is functional in living cells where it retains its binding capacity and labels its target structures over extended time periods, which renders the BC2-tag/bivBC2-Nb labeling system into a versatile tool for SRM imaging of fixed and living cells.

## Methods

**Expression constructs**. All primer sequences used for cloning are listed in a Supplementary Table 1. The expression construct coding for vimentin N-terminally fused to eGFP (GFP-vimentin) was previously described[41]. For generation of a photoactivatable (PA) mCherry (PAmCherry) fusion construct of vimentin (PAmCherry-vimentin) the coding sequence of PAmCherry was PCR-amplified from the pBAD/HisB-PAmCherry1 vector using the following primer set: PAmCherry-F and PAmCherry-R. The PCR product was purified, digested with the restriction enzymes AgeI and BglII and ligated in the AgeI/BglII sites of a vector coding for mCherry-vimentin thereby replacing mCherry with PAmCherry. An expression construct coding for vimentin with a C-terminal BC2-tag (vimentin$_{BC2T}$) was generated by the replacement of the mCherry sequence from a mCherry-Vimentin-BC2T (mCherry-vimentin$_{BC2T}$) fusion construct previously described[31]. Thus, vimentin$_{BC2T}$ cDNA was PCR-amplified using the primer VIM-BC2T-for and ligated into NheI and BamHI restriction sites of the template construct. Constructs coding for vimentin C-terminally fused to PAmCherry (vimentin-PAmCherry) and vimentin C-terminally fused to eGFP (vimentin-GFP) were generated by Gibson assembly of the three following fragments: fragment 1- pEGFP-N1 vector backbone digested with NheI and BsrGI, fragment 2- vimentin amplified from vimentin$_{BC2T}$ with the primer set VIM-for and VIM-rev, fragment 3- PAmCherry amplified from PAmCherry-vimentin or eGFP amplified from GFP-vimentin using the primer set PAmCherry/eGFP-for and PAmCherry/eGFP-rev. Fragments were assembled using the Gibson-Assembly Master Mix (New England Biolabs, cat. #E2611) according to the manufacturer's protocol. An expression construct coding for BC2-tagged β-actin ($_{BC2T}$actin) was generated by the combination of two PCR fragments derived from an eGFP-actin construct previously described in ref. [62]. The first PCR fragment was generated using primer BC2TActb(1)-for and BC2TActb(1)-rev. The second PCR fragment was generated using primer BC2TActb(2)-for and BC2TActb(2)-rev. Both DNA fragments were purified and ligated by compatible sticky ends generated by BssHII and SexAI restriction enzymes. To generate a BC2-tagged laminB1 ($_{BC2T}$lamin) expression construct the lamin B1 cDNA was PCR-amplified from a GFP-Lamin B1 DNA template[62] by PCR using primer BC2TLamin-for and BC2TLamin-rev and cloned into XhoI and NheI restriction sites of pEGFP-N1 vector thus introducing the BC2-tag sequence. The expression construct coding for C-terminally BC2-tagged lamin (lamin$_{BC2T}$) was generated by the replacement of the vimentin cDNA of the above described vimentin$_{BC2T}$ by lamin cDNA PCR-amplified from GFP-Lamin B1 using the primer laminBC2T-for and laminBC2T-rev. DNA fragments were purified and ligated by compatible sticky ends generated by NheI and BssHII restriction enzymes. The expression construct coding for C-terminally BC2-tagged tubulin (tubulin$_{BC2T}$) was generated by substituting vimentin cDNA of the above described vimentin$_{BC2T}$ with the tubulin cDNA PCR-amplified from pPAmCherry-tubulin (addgene 31930) with primers tubulinBC2T-for and tubulinBC2T-rev using restriction enzymes NheI and BssHII.

The expression construct coding for N-terminally BC2-tagged tubulin ($_{BC2T}$tubulin) was generated by substituting actin cDNA of the above described $_{BC2T}$actin with the tubulin cDNA PCR-amplified from pPAmCherry-tubulin (addgene 31930) with primers BC2Ttubulin-for and BC2Ttubulin-rev using restriction enzymes BssHII and BamHI. Mammalian expression construct coding for GFP-LC3B fusion protein, was generated by insertion of LC3B cDNA into BglII and EcoRI restriction sites of pEGFP-C1 expression vector. The expression construct coding for N-terminally BC2-tagged LC3B ($_{BC2T}$LC3B) was generated by substituting actin cDNA of the above described $_{BC2T}$actin with the LC3B cDNA PCR-amplified from GFP-LC3B using primers BC2TLC3B-for and BC2TLC3B-rev using restriction enzymes BssHII and BamHI. BC2T-tagged GFP-GPI construct for mammalian expression was generated by insertion of synthetic DNA fragment with an ORF coding for signal peptide of human CD59 (aa 1–25), BC2-Tag, eGFP and amino acids 92–128 of huCD59, which contains the GPI attachment site at aa 102 into BglII and NotI restriction sites of pEGFP-N2 vector DNA. Plasmids coding for Ypet-FtnA and SNAP-FtnA were purchased from addgene (cat. #98280 and 98282). To generate the expression construct coding for $_{BC2T}$Ypet-FtnA, BC2T was inserted to the N-terminus of Ypet-FtnA by PCR amplification of the complete Ypet-FtnA plasmid using BC2TYpet-for and BC2TYpet-rev. Subsequent recircularization of the amplified plasmid was performed using BssHII restriction sites.

All generated expression constructs were confirmed by sequencing and SDS-PAGE followed by western blot analysis using antibodies directed against eGFP (ChromoTek, cat. #3H9, dilution 1:1000), mCherry (ChromoTek, cat. #6G6, dilution 1:4000) or a BC2-Nb coupled to Alexa Fluor 647 (Thermo Fisher Scientific, cat. #A20006) (BC2-Nb$_{AF647}$, dilution 1:200) as previously described[31].

Bacterial expression vectors coding for the GFP-nanobody (GFP-Nb), the BC2-nanobody (BC2-Nb), and the bivalent BC2 nanobody (bivBC2-Nb) were provided by ChromoTek with a corresponding material transfer agreement. The bacterial expression construct of the bivalent VB6 nanobody (bivVB6-Nb) was previously described[41]. For all three constructs the original tag was replaced by a Sortase-tag (GSLPETG) upon PCR amplification of the full plasmid using the forward primer SorTag-Ins_for and SorTag-Ins_rev and subsequent recircularization using terminal AgeI restriction sites. The resulting expression constructs were confirmed by sequencing and bacterial expression followed by SDS-PAGE and immunoblot analysis using a C-terminal anti-His antibody (ThermoFisher Scientific, cat. #R930-25, dilution 1:1000). An expression vector coding for SortaseΔ59 (pET28a-SrtAdelta59) was a gift from Hidde Ploegh (Addgene plasmid #51138)[63].

**Recombinant protein production and nanobody labeling**. GFP-Nb, bivVB6-Nb, BC2-Nb, and bivBC2-Nb all comprising a C-terminal Sortase-tag were expressed and purified as previously described[41, 64] and stored at −80 °C or immediately used for labeling. SortaseΔ59 was expressed and purified as described[63]. Alexa Fluor 647 (AF647)-coupled peptide H-Gly-Gly-Gly-Doa-Lys-$NH_2$ (sortase substrate) was purchased from Intavis AG. Chemical dye conjugation of BC2-Nb or bivBC2-Nb was carried out as described previously[31]. Briefly, purified nanobody was labeled with the N-hydroxysuccinimide (NHS) ester activated AF647 (ThermoFisher Scientific, cat. #A20006) according to manufacturer's guidelines. After coupling, unbound dye was removed by separation on Zeba Spin Desalting Columns (ThermoFisher Scientific, cat. #89890). For analysis, 0.1 µg of nanobodies were subjected to SDS-PAGE and analyzed on a Typhoon Trio (GE-Healthcare, excitation 633 nm, emission filter settings 670 nm BP 30) and subsequent Coomassie staining.

Degree of labeling (DOL, dye-to-protein ratio) was determined by absorption spectroscopy according to the instructions provided by ThermoFisher Scientific (stated for cat. #A20173). For BC2-Nb and bivBC2-Nb NHS-conjugated nanobodies DOLs of 1.8 ± 0.5 and 2.1 ± 0.7 were determined.

Sortase coupling of nanobodies was performed as previously described[33]. Briefly, 25 µM nanobody, 75 µM dye-labeled peptide dissolved in sortase buffer (50 mM Tris, pH 7.5, and 150 mM NaCl) and 100 µM sortase were mixed in coupling buffer (50 mM Tris, pH 7.5, 150 mM NaCl, and 10 mM $CaCl_2$) and incubated for 5 h at 25 °C. Uncoupled nanobody and sortase were depleted using Ni-NTA resin (Biorad, cat. #1560131). Unbound dye was removed using Zeba Spin Desalting Columns (ThermoFisher Scientific, cat. #89890). The dye-labeled protein fraction was analyzed by SDS-PAGE followed by fluorescent scanning on a Typhoon Trio (GE-Healthcare, excitation 633 nm, emission filter settings 670 nm BP 30) and subsequent Coomassie staining. For all sortase-coupled nanobodies DOLs of 0.7 ± 0.15 were determined.

**Bio-layer interferometry (BLI)**. The dissociation constants of BC2-Nb and bivBC2-Nb were determined on BLItz system (Pall ForteBio). Synthetic BC2 and BC2-BC2 (with $(GGGGS)_2$ linker) peptides with an N-terminal biotin-DoA-DoA-linker (Intavis AG) were immobilized on Streptavidin (SA) dip and read biosensors (Pall ForteBio, cat. #18-5020) using a concentration of 50 µM. For kinetic measurements of BC2- or bivBC2-Nbs three concentrations (120 nM, 240 nM, and 480 nM) of the Nbs in diluent buffer (1× PBS, 0.1% (w/V) BSA (Carl Roth, cat. #8076), 0.1 % (w/V) Triton X-100 (Sigma-Aldrich, cat. #T8787)) were used. Each measurement was done in duplicates with an association time of 180 s followed by 240 s dissociation in diluent buffer. Kinetic constants were determined using BLItz software (BLItz Pro 1.2, Pall ForteBio) according to global fitting of data sets.

**Cell culture and transfection**. The HeLa Kyoto cell line (Cellosaurus no. CVCL_1922) was obtained from S. Narumiya (Kyoto University, Japan), and the A549, U2OS and COS-7 cell lines were obtained from ATCC (CCL-185, HTB-96, CRL-1651). All cell lines were tested negative for mycoplasma using the PCR mycoplasma kit Venor GeM Classic (Minerva Biolabs, cat. #11-1025) and the Taq DNA Polymerase (Minerva Biolabs, cat. #53-0100). Since this study does not include cell line specific analysis, all cell lines were used without additional authentication. HeLa Kyoto, U2OS and COS-7 cells were cultured in DMEM +GlutaMAX (Life Technologies, cat. #31966-021) supplemented with 10% FCS (Life Technologies, cat. #10270-106) and 1 unit ml$^{-1}$ pen/strep (Life Technologies, cat. #15140-122). A549 cells were cultured in DMEM/F-12 (1:1) (Life Technologies, cat. #21331-020) supplemented with 10% FCS (Life Technologies, cat. 10270-106), 1 unit ml$^{-1}$ pen/strep (Life Technologies, cat. #15140-122) and 2 mM L-glutamine (Life Technologies, cat. #25030-024). Cells were trypsinized for passaging and cultivated at 37 °C in a humidified chamber with a 5% $CO_2$ atmosphere. Transient transfection of HeLa Kyoto, U2OS, and COS-7 cells with Lipofectamine 2000 (ThermoFisher Scientific, cat. #11668019) and transfection of A549 cells with Lipofectamine LTX (ThermoFisher Scientific, cat. #15338100) was carried out according to manufactures instruction.

***S. pombe* strain construction**. The cloning strategy for BC2-tagging of the *CBP1* gene at the C-terminus was adapted from[65]. The *Saccharomyces cerevisiae* ADH1 terminator and kanamycin resistance gene were amplified from the PAW8 plasmid[66] using the following primer pair F_KanR_BC2 and R_KanR. ~250 bp sequences up- and down-stream of the *cbp1* gene were amplified from purified *S. pombe* DNA, with the primer pairs F1_cbp1, cbp1_BC2_R1, and F2_cbp1, R2_cbp1. Primers were designed to generate PCR products with overlapping regions of at least 20 bp. DNA fragments were assembled with overlap-extension PCR[67], using melting temperatures of the overlapping regions as the annealing temperature. All PCRs were performed with Q5 High-Fidelity DNA polymerase (New England Biolabs, cat. #M0491L). Volume of 10 µl of the PCR product was transformed into wild-type *S.pombe* using the Frozen-EZ Yeast Transformation II Kit (Zymo Research, cat. #T2001), plated onto YES agar plates and incubated overnight at 30 °C, then replica plated onto 200 µg ml$^{-1}$ G418 (Thermo Fisher

Scientific,) YES agar plates and incubated at 30 °C until single colonies were visible. Genomic integration was confirmed by colony PCR and DNA sequencing (Eurofins).

***S. pombe* cell culture**. *S.pombe* was grown in YES medium (5 g yeast extract, 30 g glucose, 225 mg of each l-adenine, histidine, leucine, uracil, lysine hydrochloride in 1 l of Milli-Q water) at 30 °C overnight, then inoculated into fresh YES to a starting $OD_{600}$ of 0.1, grown to an OD600 of 0.4 and collected by centrifugation. Pellets were washed once with PEM buffer (100 mM Pipes, 1 mM EGTA, 1 mM $MgSO_4$, pH 6.9), then fixed for 15 min in 3.7% paraformaldehyde (PFA, Sigma-Aldrich, cat. #F8775) in PEM, washed 3 × 10 min with PEM containing 100 mM $NH_4Cl$ to quench the fixation, then permeabilized with a 1:1 mixture of methanol and acetone at −20 °C for 10 min. Fixed and permeabilized cells were then washed 3 × with PEMBAL buffer (PEM + 1% BSA, 0.1% $NaN_3$, 100 mM lysine hydrochloride) and incubated in PEMBAL overnight. Before staining, cells were blocked with Image-iT FX signal enhancer (ThermoFisher Scientific, cat. #I36933) for 1 h, then stained for 48 h at 4 °C in PEMBAL containing ~0.5 μg $ml^{-1}$ of bivBC2–$Nb_{AF647}$ and 0.1% Triton X-100 (Sigma-Aldrich, cat. #T8787). Finally, cells were washed 2× with PEM containing 0.1% Tween-20 (Sigma-Aldrich, cat. #P7949), post-fixed with 4% PFA (Sigma-Aldrich, F8775) and 0.25% (w/V) glutaraldehyde (Sigma-Aldrich, cat. #G5882) in PEM for 10 min, then washed 2× with PEM and immobilized on poly-L-lysine coated Ibidi 8-well glass bottom slides (Ibidi GmbH, cat. #80826), previously cleaned with a 2% solution of Hellmanex III (Helma Analytics).

**CRISPR/Cas9D10A expression vector construct and HDR template**. Paired sgRNAs were designed for the *ACTB* (actin beta, *Homo sapiens*; PubMed Gene ID: 60) target gene locus using an online CRISPR gRNA design tool[68, 69] and synthesized as Ultramer DNA Oligonucleotides (Integrated DNA Technologies), *ACTB*_sgRNA and *ACTB*_HDR (Supplementary Table 1).

Next, paired sgRNAs were cloned according to a previously described procedure into a plasmid harboring Cas9D10A and a puromycin resistance cassette[70]. Briefly, the sgRNA fragment were PCR amplified using sgRNA_fw and sgRNA_rev primer thereby adding 3′ and 5′ domains homologous to plasmid encoded hU6 promotor and gRNA scaffold sequences, respectively. The 148 bp PCR amplicon was gel-purified and ligated at a 3:1 ratio to the 415 bp fragment generated by BbsI digest of the pDonor_U6 plasmid (a gift from Andrea Ventura, Addgene plasmid #69312)[70] using the NEBuilder Cloning Kit (New England Biolabs, cat. #E5520S). After treatment with Exonuclease RecBCD (New England Biolabs, cat. # M0345L) the column purified DNA plasmid was digested over night at 37 °C with BbsI. The linearized plasmid was then ligated into the BbsI-digested and dephosphorylated pSpCas9n(BB)-2A-Puro plasmid (a gift from Feng Zhang, Addgene plasmid #62987)[71] using T4 DNA ligase (NEB). Single-clone derived DNA plasmids were purified using QIAGEN Plasmid Midi Kit (Qiagen, cat. #12145) and verified by sequencing. The homology directed repair (HDR) template ACTB_HDR was synthesized as Ultramer DNA Oligonucleotides (IDT). HDR templates encoded for the HDR insert carrying the intended BC2-tag knock-in mutation flanked by left and right homology arms (each 50 bp) homologous to the *ACTB* target gene locus.

**Generation of BC2-tag knock-in cell lines**. $1 \times 10^6$ Hela Kyoto and A549 cells, respectively, were co-transfected at 50% confluency with 6.5 μg *ACTB*_HDR template oligonucleotide and 5.5 μg cloned Cas9N_Puro_*ACTB*_sgRNA expression vector construct or pEGFP plasmid (to control for transfection efficiency), respectively. For transfection of Hela cells Lipofectamine 2000 (ThermoFisher Scientific, cat. #11668019) and for A549 cells Lipofectamine LTX reagent (Thermo Fisher Scientific, cat. #15338100) was used. After 24 h, cells were trypsinized and re-plated in culture medium containing 1 μg $ml^{-1}$ puromycin dihydrochloride (Sigma-Aldrich, cat. #P8833). Forty-eight hours later mock-transfected control cells were completely killed by the antibiotic. Puromycin-resistant cell pools were expanded for 1 week and subsequently used for detection of CRISPR/Cas9D10A-induced BC2-tag knock-in by immunofluorescence staining using the bivBC2-$Nb_{AF647}$ and genomic PCR. Monoclonal knock-in cell lines were derived from cell pools showing successful BC2-tag knock-in by limiting dilution.

**Genomic PCR of BC2-tag knock-in cells**. Genomic DNA was isolated from puromycin-resistant cells using the QIAamp DNA Mini Kit (Qiagen, cat. #12125) according to manufacturer's instructions. Quantity 500 ng of purified genomic DNA was used for PCR amplification of the integrated BC2-tag sequence from the *ACTB* target gene locus using the primer ACTB_fw and BC2_rev. PCR products were separated on 1.5% agarose gels and visualized using ethidium bromide staining.

**Immunofluorescence staining for wide-field microscopy**. For immunofluorescence staining ~$1.5 \times 10^4$ HeLa Kyoto, U2OS cells, COS-7, or A549 cells per well of an 8-well μ-slide (Ibidi GmbH, cat. #80826) were plated. Next day, cells were transfected with plasmids coding for GFP-vimentin, mCherry-vimentin$_{\mathrm{BC2T}}$, PAmCherry-vimentin, vimentin-GFP, vimentin-PAmCherry, vimentin$_{\mathrm{BC2T}}$, $_{\mathrm{BC2T}}$actin, $_{\mathrm{BC2T}}$lamin, lamin$_{\mathrm{BC2T}}$, $_{\mathrm{BC2T}}$tubulin, tubulin$_{\mathrm{BC2T}}$, GFP-LC3B, $_{\mathrm{BC2T}}$LC3B, $_{\mathrm{BC2T}}$GFP-GPI, and Ypet-FtnA or $_{\mathrm{BC2T}}$Ypet-FtnA.

Twenty-four hours after transfection or in case of U2OS cells expressing $_{\mathrm{BC2T}}$tubulin, tubulin$_{\mathrm{BC2T}}$, Ypet-FtnA, or $_{\mathrm{BC2T}}$Ypet-FtnA cells 72 h after transfection, cells were washed twice with PBS and fixed with 3.7% w/V paraformaldehyde (PFA) in PBS for 10 min at RT. Fixed cells were washed three times with PBS and permeabilized with a 1:1 mixture of methanol/acetone for 5 min at −20 °C. After three washing steps with PBS, cells were blocked with Image-iT FX signal enhancer (Thermo Fisher Scientific, cat. #I36933) for 30 min. Subsequently cells were washed with and stored in PBS until staining. For nanobody staining, GFP-$Nb_{AF647}$, BC2-$Nb_{AF647\ (NHS)}$, BC2-$Nb_{AF647\ (sort)}$, bivBC2-$Nb_{AF647\ (NHS)}$, bivBC2-$Nb_{AF647\ (sort)}$, or bivVB6-$Nb_{AF647}$ was added with a final concentration of ~50 ng $ml^{-1}$ in 5% BSA in TBS-T (0.05% (w/V) Tween) and incubated overnight at 4 °C. Unbound nanobodies were removed by three additional washing steps with TBS-T. Images were acquired with a MetaXpress Micro XL system (Molecular Devices) and ×40 magnification.

For staining of endogenous β-catenin, ~5000 HeLa Kyoto cells per well were seeded in a μclear 96-well plate (Greiner Bio One, cat. #655090). Cells were either transfected with an expression plasmid coding for vimentin$_{\mathrm{BC2T}}$ or left untransfected. Twenty-four hours after transfection cells were further left untreated or continuously cultured in the presence of 10 μM CHIR99021 for 16 h. Subsequently, cells were washed twice with PBS and fixed with 3.7% w/V paraformaldehyde (PFA) in PBS for 10 min at RT. After three washing steps with PBS, cells were permeabilized and blocked with 0.1% Triton X-100 in 5% BSA in TBS-T for 30 min. For detection of endogenous β-catenin, cells were incubated with an anti-β-catenin antibody (BD Biosciences, cat. #610154, dilution 1:200) followed by detection with an Alexa Fluor 488 labeled anti-mouse-antibody (Invitrogen, cat. #A10680, dilution 1:1000).

**Generation of $_{\mathrm{BC2T}}$Ypet-FtnA and SNAP-FtnA lysates**. Cell lysates comprising BC2-tagged FtnA oligomers were generated from transiently $_{\mathrm{BC2T}}$Ypet-FtnA transfected U2OS cells and immobilized on Poly-L-lysine-coated 8-well μ-slides (Sigma-Aldrich cat. # P4707; Ibidi, cat. # 80826)[36].

**Staining of $_{\mathrm{BC2T}}$Ypet-FtnA and SNAP-FtnA lysates**. Wells of an 8-well μ-slide (Ibidi, cat. #80826) containing lysates of $_{\mathrm{BC2T}}$Ypet-FtnA and SNAP-FtnA expressing U2OS cells were blocked with 10% BSA in PBS for 30 min, then with Image-iT FX signal enhancer (ThermoFisher Scientific, cat. #I36933) for an additional 60 min. Nanobodies were diluted to ~0.5 μg $ml^{-1}$ in staining (PBS, 10% BSA, 0.1% (V/V) Triton X-100 (Sigma-Aldrich, cat. #T8787)). SNAP-Surface Alexa Fluor 647 (New England Biolabs, cat. #S9136S) was diluted to 0.1 μM in the same solution. Volume of 200 μl of the staining solution was added to each well and stained for 6 h at room temperature. After staining, wells were washed three times for 15 min with PBS containing 0.1% Tween-20. The nanobody staining was post-fixed with 4% PFA and 0.25% glutaraldehyde in PBS for 5 min to make the binding permanent. In the case of SNAP, the binding is already covalent. Wells were then washed an additional three times for 15 min with PBS and imaged overlaid with 300 μl of PBS.

**Protein transduction**. HeLa_$_{\mathrm{BC2T}}$ACTB, or A549_$_{\mathrm{BC2T}}$ACTB were plated at ~5000 cells per well of a μclear 96-well plates (Greiner Bio One, cat. #655090) and cultivated at standard conditions. Next day, Nbs were transduced using Pro-DeliverIN (OZ Biosciences, cat. #PI10250) according to manufacturer's protocol. Per well of a 96-well plate 0.25 μl of Pro-DeliverIN was mixed with 0.75 μg Nb and incubated for 15 min at RT. Volume of 20 μl Opti-MEM (ThermoFisher Scientific, cat. #31985062) was added to the mixture and immediately transferred to the cell culture medium in the well. After 2 h, medium was replaced by imaging medium $DMEM^{gfp}$-2 (Evrogen, cat. #MC102) supplemented with 10% FCS, 2 mM L-glutamine and cells were imaged.

**Live-cell staining and imaging**. HeLa Kyoto transiently expressing $_{\mathrm{BC2T}}$GFP-GPI, HeLa-$_{\mathrm{BC2T}}$ACTB, or A549-$_{\mathrm{BC2T}}$ACTB cells were plated at ~5000 cells per well of a μclear 96-well plate (Greiner Bio One, cat. #655090) and cultivated at standard conditions. Next day, time-lapse imaging was performed in a humidified chamber (37 °C, 5% $CO_2$) of a MetaXpress Micro XL system (Molecular Devices) at ×40 magnification. For live-cell staining of $_{\mathrm{BC2T}}$GFP-GPI, culture medium was replaced without washing by live-cell visualization medium $DMEM^{gfp}$-2 (Evrogen, cat. #MC102) supplemented with 10% FCS, 2 mM L-glutamine and 1 μg $ml^{-1}$ bivBC2-$Nb_{AF647}$. Time-lapse imaging with 4–5 min intervals was started immediately upon medium replacement. For live-cell staining of HeLa-$_{\mathrm{BC2T}}$ACTB and A549-$_{\mathrm{BC2T}}$ACTB upon protein transduction of nanobodies, cells were washed once with and placed in $DMEM^{gfp}$-2 medium 2 h after addition of transduction mix (see "protein transduction" section above) and imaged in hourly intervals.

**Quantification of staining intensities**. HeLa Kyoto cells were plated at ~5000 cells per well of a μclear 96-well plates (Greiner Bio One, cat. #655090) and transfected with expression plasmid for mCherry-VIM$_{\mathrm{BC2T}}$. Next day, cells were fixed and stained with the same concentration (1 μg $ml^{-1}$) of monovalent or bivalent BC2-Nbs conjugated to AF647 either by NHS conjugation or via sortase coupling. To assess staining q uality of the different nanobody formats we calculated the ratio of the staining intensity in mCherry-VIM$_{\mathrm{BC2T}}$ expressing cells and in non-transfected cells (background). Staining intensities were determined using a custom-written cell identification algorithm (MetaXpress, Custom module editor). In brief, transfected cells were identified based on cell size parameters and a threshold setting for mCherry fluorescence intensity above local background. Background fluorescence was defined as the average fluorescence of the remaining image area precluding mCherry-VIM$_{\mathrm{BC2T}}$ expressing cells. For statistical significance the average fluorescence intensity of a large number of transfected cells was determined (BC2-Nb$_{\mathrm{AF647\ (NHS)}}$: $n = 115$; bivBC2-Nb$_{\mathrm{AF647\ (NHS)}}$: $n = 134$; BC2-Nb$_{\mathrm{AF647\ (sort)}}$: $n = 150$; bivBC2-Nb$_{\mathrm{AF647\ (sort)}}$: $n = 195$).

**Immunofluorescence staining for dSTORM imaging**. To achieve the higher labeling density required for dSTORM imaging the staining protocol was slightly modified. Cells were prepared the same way as described up to the storage step in PBS. After storage, cells were blocked with 10% (w/V) BSA (Carl Roth, cat. #8076) in PBS for 30 min, then additionally with Image-iT FX signal enhancer (ThermoFisher Scientific, cat. #I36933) for 60 min. Antibodies and nanobodies were diluted to ~0.5 µg ml$^{-1}$ in staining/permeabilization solution (PBS, 10% BSA, 0.1% (V/V) Triton X-100 (Sigma-Aldrich, cat. #T8787)). Conventional immunostaining was done at 4 °C for 24 h with the primary antibody (V9, mouse monoclonal, Sigma-Aldrich, cat. #347M-1)[72] followed by two washes with PBS, and then stained at 4 °C for 24 h with the secondary antibody (donkey-anti-mouse AF647, ThermoFisher Scientific, cat. #A-31571). For staining with nanobodies, cells were incubated at 4 °C for 48 h. Unbound Nbs were removed by two washes with PBS-T (0.1% w/V Tween-20 (Sigma-Aldrich, cat. #P7949)) and samples were post-fixed with 4% PFA (Sigma-Aldrich, cat. #F8775) and 0.25% (w/V) glutaraldehyde (Sigma-Aldrich, cat. #G5882) in PBS for 5 min to make the binding permanent. Finally, cells were washed twice with PBS to remove fixation solution and stored in PBS with 0.1% (w/V) sodium azide (Carl Roth, cat. #4221) until imaging.

**dSTORM imaging and post-processing**. A 1:5000 dilution of fluorescent beads (FluoSpheres 715/755, ThermoFisher Scientific, cat. #F8799) was sonicated to break up clumps of beads. Volume of ~5 µl of the beads were added to the sample and allowed to settle and adhere for 15 min, to serve as fiducial markers for drift correction. Images were recorded on a customized Nikon Ti-Eclipse inverted microscope, equipped with a CFI Apochromat TIRF ×100 objective with a numerical aperture of 1.49 (Nikon) and an iXON ULTRA 888 EMCCD camera (Andor). AF647 was imaged in 100 mM MEA (Sigma-Aldrich, cat. #M6500-25G) with a glucose oxidase (Sigma-Aldrich, cat. #G2133, C100) oxygen scavenger system[73]. The sample was illuminated with an OBIS LX 637 nm laser (Coherent) which was filtered through a ZET 640/10 bandpass, modulated by an Acousto-Optic Tunable Filter (Gooch & Housego, TF525-250-6-3-GH18) and focused by a ZET405/488/561/640 m dichroic mirror (Chroma) onto the back focal plane of the objective resulting in a final intensity of 2–4 kW cm$^{-2}$ in the sample. The readout was collected by blocking the laser light by the bandpass ZET405/488/561/640 and passing through a 689/23 nm single-band bandpass filter (All filters AHF Analysentechnik AG). For each dSTORM image reconstruction, 10,000–20,000 imaging frames with an exposure time of 70 ms were recorded at a pixel size of 129 nm. The camera, microscope and AOTF were controlled by µManager software[74] on a PC workstation. Single-molecule localizations were extracted from the movies with the open-source software Rapidstorm 3.2.[75] Drift correction was performed by custom written Python 2.7 algorithms that extract and correct for fluorescent bead tracks. NeNA as described in ref. [43] was done with the open-source software Lama[76] on a section of the image that contained no fiducial markers. Localizations appearing within the radius of the NeNA value on several frames were grouped into one localization using the Kalman tracking filter in Rapidstorm 3.2. Final images were reconstructed at a pixel size of 10 nm. For visualization, a Gaussian blur filter was applied in the ImageJ software using NeNA as the sigma value. dSTORM imaging in yeast cells was performed in PEM buffer containing 10 mM MEA (Sigma-Aldrich, M6500) and 1 mM methyl viologen dichloride hydrate (MV) (Sigma-Aldrich, cat. #856177).

**PALM imaging and post-processing**. For imaging of PAmCherry-vimentin, the sample was illuminated with an OBIS LX 561 laser (Coherent), filtered through a ZET 561/10 clean-up filter (AHD Analysentechnik, Germany) at an intensity of 800 W cm$^{-2}$ and an OBIS LX 405 laser (Coherent) at intensites of ~25–5000 mW cm$^{-2}$. The readout was collected through a 610/75 bandpass filter (AHF Analysentechnik, Germany). Twenty thousand imaging frames were recorded at an exposure time of 70 ms. The number of PAmCherry molecules activated each frame was kept at a steady rate by increasing 405 laser intensity until all of the PAmCherry was readout. All other microscope parameters and image post-processing remained the same as for dSTORM imaging.

**Super-resolution analysis of endogenous β-catenin staining**. To evaluate the effect of endogenous β-catenin staining on dSTORM imaging of low-abundance non-structural proteins, non-transfected HeLa and $_{\mathrm{BC2T}}$LC3B expressing HeLa cells were fixed and stained with bivBC2-Nb$_{\mathrm{AF647}}$ or GFP-Nb$_{\mathrm{AF647}}$ for 48 h, imaged and post-processed as described in the "Immunofluorescence staining for dSTORM imaging" and "dSTORM imaging and post-processing" sections".

Analysis was performed on non-transfected HeLa cells stained with bivBC2-Nb$_{\mathrm{AF647}}$ or GFP-Nb$_{\mathrm{AF647}}$, in comparison to $_{\mathrm{BC2T}}$LC3B-expressing cells stained with bivBC2-Nb$_{\mathrm{AF647}}$. The GFP-Nb$_{\mathrm{AF647}}$ staining served as a baseline of non-specific nanobody binding. Three 15 × 15 µm ROIs for each condition were analyzed with DBSCAN (DBSCAN parameters: $\varepsilon = 40$ nm; MinPts = 6)[35] to identify single nanobodies. The density of nanobodies per µm$^2$ was calculated for each ROI and the means of each condition plotted as bar charts with S.D. as the error.

To evaluate the effect of endogenous β–catenin staining when imaging abundant structural proteins, non-treated and CHIR99021-treated non-transfected and vimentin$_{\mathrm{BC2T}}$ expressing HeLa cells were stained with bivBC2-Nb$_{\mathrm{AF647}}$ and imaged as described in the "Immunofluorescence staining for dSTORM imaging" and "dSTORM imaging and post-processing" sections. Localization counts for three cells per condition were obtained with the RapidSTORM software[75] and cell areas were measured in Fiji[77]. Localizations per µm$^2$ were calculated and the means of each condition plotted as bar charts with S.D. as the error.

**Imaging of $_{\mathrm{BC2T}}$Ypet-FtnA and SNAP-FtnA lysates**. A 488 nm Sapphire laser (Coherent Inc., Santa Clara, California USA) was used to excite the Ypet and the readout was collected through a 525/50 single bandpass filter (AHF Analysentechnik AG). Otherwise, the microscope setup was the same as described in the dSTORM paragraph above. The red laser intensity was reduced to ~0.4 kW cm$^{-2}$, to avoid pixel saturation when imaging stained FtnA oligomers while still allowing for the detection of single-AF647 molecule blinking events. In the case of $_{\mathrm{BC2T}}$Ypet-FtnA, fluorescent spots were identified by their Ypet signal. Since the SNAP-tagged FtnA oligomers lacked the Ypet signal, they were excited with very low 640 nm laser (>0.01 W cm$^{-2}$) and chosen within 2 s to avoid photobleaching. Both were then imaged for 200 frames with an exposure time of 50 ms.

**$_{\mathrm{BC2T}}$Ypet-FtnA and SNAP-FtnA analysis**. The fluorescence microscopy movies were analyzed with a custom ImageJ script in the open access software Fiji[77]. AF647 single-molecule blinking events were identified in the last 100 frames of the movies. Molecules that blinked at least twice in the last 100 frames were selected in different quadrants of the imaged area. A round ROI with a diameter of 10 pixels was drawn around each molecule and the intensity trace of the ROI for all 200 frames was extracted. The integrated intensity value was plotted over time using the software OriginPro (Origin Lab Corp.). Only blinking events with a clear jump in the integrated intensity values co-inciding with a visual blink in the movie were measured. Intensity of blinking events was measured by calculating the difference between baseline and peak intensity of the event (Supplementary Fig. 3a). A total of $N = 157$ blinking events were measured. The single-molecule integrated intensity values were binned with a bin size of 100 AD counts, plotted as a relative frequency histogram and fitted with the log-normal distribution function in OriginPro (Origin Lab Corp.):

$$f(x) = \frac{1}{x\sigma\sqrt{2\pi}}\,\mathrm{e}^{-\frac{(\ln-\mu)^2}{2\sigma^2}}$$

as described in ref. [78] yielding $\mu = 5.68$ and $\sigma = 0.4$ (Supplementary Fig. 3a). FtnA-oligomer spots were analyzed in a similar manner, with the integrated intensity value of the diameter of 10 pixels ROI of the second frame used for further analysis. A total of 130 $_{\mathrm{BC2T}}$Ypet-FtnA spots and 89 SNAP-FtnA spots were analyzed. The integrated intensity data was binned with a bin size of 1000 AD counts and plotted as relative frequency histograms (Supplementary Fig. 3b). Approximating the labeling of FtnA oligomers with AF647 molecules with a binomial distribution, with the degree of labeling (0.7 ± 0.15 in case of the bivBC2-Nb$_{\mathrm{AF647}}$ nanobody and 0.95 ± 0.05 in case of the AF647-BG) representing the p and the number of FtnA molecules in an oligomer representing the n parameter, we could calculate the probability for the occurrence of each labeling state (e.g., 24, 23, 22… AF647 per oligomer). Data sets assuming full labeling were simulated by calculating the linear combination of calibration distributions following the binomial mixture of visual oligomeric states due to the degree of labeling by recursively convolving the single-fluorophore log-normal distribution ($\mu = 5.68$, $\sigma = 0.4$) using a MatLab (MathWorks, Natick, MA-US)-based tool, as published and described in ref. [78]. To evaluate the completeness of labeling with the bivBC2-Nb$_{\mathrm{AF647}}$ nanobody and the SNAP-tag, we then compared the medians of the simulated fully labeled scenario data sets with our measured distributions.

**Image analysis of dSTORM images**. A custom ImageJ script was used to measure the widths and coverages of vimentin, actin, and tubulin fibers on reconstructed non-blurred images. The segmented line tool in ImageJ was used to manually draw lines along vimentin filaments and line thickness was adjusted to fit the filament. Each image was divided into 10 × 10 µm sections and 15 random filaments were measured in each section. Line selections were straightened using the straighten tool and an intensity profile was plotted for each filament. To determine filament width, the intensity profile was fitted with a Gaussian curve and the resulting sigma value was multiplied with 2.35 to obtain the full width at half maximum (FWHM). To determine lengthwise coverage the image was converted into a binary image and the fraction of covered area of the middle 3 pixels was calculated. To reduce measurement error, line selections were wobbled by 0.5 pixels in four directions and values from all 5 measurements were averaged. To estimate image resolution, custom written Python 2.7 (Python Software Foundation) and Fiji[77] algorithms utilizing code from the Lama software[76] and GDSC SMLM ImageJ plugin (http://

www.sussex.ac.uk/gdsc/intranet/microscopy/imagej/gdsc_plugins) were used. NeNA localization precision[43] and Fourier Image Resolution (FIRE)[44] were calculated for all analyzed regions. To calculate FIRE, localization files were split into two by alternating frames ("random split" option unchecked). The threshold was set to Fixed 1/7 and the Fourier image scale was set to a constant 16 for all analyzed regions. Other parameters were left as default (auto image scale = 2048, sampling factor = 1). The results were plotted using the software OriginPro (Origin Lab Corp.).

**LC3B clustering analysis**. Imaging and post-processing of $_{\mathrm{BC2T}}$LC3B cells was done as described in the "dSTORM imaging and post-processing" section. The obtained localization files were loaded into the MatLab-based software PALMsiever[79]. Density-based clustering analysis was performed with the density-based spatial clustering of applications with noise (DBSCAN) algorithm (DBSCAN parameters: $\varepsilon = 50$ nm; MinPts = 40)[35]. Three cells were analyzed for the untreated conditions and four cells for the rapamycin-treated conditions. To compare the degree of clustering, the ratio of non-clustered to clustered localizations was calculated for each cell. Points assigned as core and border points by DBSCAN were considered as clustered, while noise points were considered as non-clustered. Cluster size was calculated with a custom-written Python 2.7 script, measuring the average distance of cluster points from the cluster center of mass. Degree of clustering results were plotted as stacked bar charts, using S.D. as the error and the cluster sizes were plotted as histograms with a bin size of 100 nm, as well as individual data points and box + whisker plots, the ends of the box marking the 1st and 3rd quartiles, notch marking the median and whiskers encompassing 95% of the data in OriginPro (Origin Lab Corp.).

**Live cell dSTORM imaging**. HeLa Kyoto transiently expressing $_{\mathrm{BC2T}}$GFP-GPI and HeLa-$_{\mathrm{BC2T}}$ACTB were seeded in 8-well Ibidi µ-slides to an approximate density of 7500–15,000 cells per well, cultivated for 24 h at standard conditions then sealed in falcon tubes containing equilibrated culture medium. Upon arrival, cells were placed in an incubator for 3 h to recover and re-equilibrate. Meanwhile, 3 µl of Pro-DeliverIN was mixed with 9 µg of nanobody and incubated at RT for 15 min. After incubation, 60 µl of Opti-MEM were added to the mix and transferred into culture wells containing 300 µl of culturing medium. Cells were incubated for 2 h in the incubator, then washed two times with pre-equilibrated imaging medium DMEMgfp-2 without FCS. Volume of 300 µl of pre-equilibrated imaging medium without FCS, supplemented with the appropriate STORM buffer components were added to the wells. Well slide lids were sealed with parafilm and imaged on a custom built piezo-electric heating stage at 37 °C.

For imaging of $_{\mathrm{BC2T}}$GFP-GPI, cells were stained with the bivBC2-Nb$_{\mathrm{AF647}}$ and the imaging medium without FCS was supplemented with filter sterilized Tris-Hydrochloride to a final concentration of 100 mM and 10 mM MEA. The microscope setup remained as before. To record single-molecule tracks, 640 nm laser intensity was reduced to 1–2 W cm$^{-2}$ and 20,000 imaging frames were recorded with an exposure time of 40 ms. For imaging of $_{\mathrm{BC2T}}$ACTB, cells were stained with the bivBC2-Nb$_{\mathrm{ATTO655}}$ and the imaging medium without FCS was supplemented with 50 µM ascorbic acid. ATTO655 was excited with 2-4 W cm$^{-2}$ of 640 nm laser and 20,000 imaging frames were recorded with an exposure time of 50 ms. $_{\mathrm{BC2T}}$ACTB images were processed as described in the "dSTORM imaging and post-processing" section.

**Live cell image processing and analysis**. Single-$_{\mathrm{BC2T}}$GFP-GPI particles were tracked with the help of customized tracking software written in C++ and visualized by customized software written in C++, to filter for trajectories of at least 5 steps and group single-molecule localizations or trajectories by their apparent diffusion coefficient (as calculated by MSD analysis). Only trajectories with 5 or more steps were used for analysis and visualization. Single-particle trajectories were grouped into immobile (diffusion coefficient <0.02 µm$^2$ s$^{-1}$) and mobile particles (diffusion coefficient >0.02 µm$^2$ s$^{-1}$) and overlaid on top of a super resolution image reconstructed in Rapidstorm 3.2[75].

**General statistical analysis of vimentin, actin, and tubulin**. All labeling methods were repeated at least twice and imaged on at least two different days using the same setup and imaging parameters. Five cells from each labeling method were chosen based on the quality of drift correction. Cells were divided into 10 × 10 µm quadrants and 15 filaments in each quadrant were randomly chosen for analysis by at least two different people. All measured values were plotted as individual data points and box + whisker plots, the ends of the box indicating the first and third quartiles and the notch indicating the median. The whiskers encompass 95% of all the data. To confirm that the results of the different labeling methods differ significantly, vimentin filament widths were divided into a thin (0–75 nm), medium (75–150 nm), and thick (150 nm and above) category on which we performed a $\chi^2$-test of homogeneity. The total number of measured filaments was high enough to ensure adequate test power ($n$-values for all conditions given in Supplementary Fig. 4). $\chi^2$-values confirmed that the filament phenotypes for the labeling methods do differ at a 0.001 level of significance. To confirm that the ratio of fiber thicknesses does not significantly differ between bivVB6-Nb$_{\mathrm{AF647}}$ and bivBC2-Nb$_{\mathrm{AF647}}$, a $\chi^2$ homogeneity test was performed on the categories 0–150 nm width and 150 nm and above, yielding a 0.001 level of significance. To test for correlation between FIRE, NeNA and coverage values, linear regression was performed pairwise on FIRE/NeNA, FIRE/coverage, and NeNA/coverage for all labeling methods. For FIRE/NeNA pairs, the slope of the linear correlation fits for bivVB6-Nb$_{\mathrm{AF647}}$, GFP-Nb$_{\mathrm{AF647}}$, and bivBC2-Nb$_{\mathrm{AF647}}$ was significantly different from 0 at a 0.05 level of significance, while in the case of PAmCherry it was not. Correlating FIRE and NeNA to coverage, the slope of the linear fit was never significantly different from 0 at a 0.05 level of significance.

**Data availability**. The data that support the findings of this study are available from the corresponding authors upon reasonable request.

Received: 29 June 2017 Accepted: 26 January 2018

## References

1. Betzig, E. et al. Imaging intracellular fluorescent proteins at nanometer resolution. *Science* **313**, 1642–1645 (2006).
2. Hess, S. T., Girirajan, T. P. & Mason, M. D. Ultra-high resolution imaging by fluorescence photoactivation localization microscopy. *Biophys. J.* **91**, 4258–4272 (2006).
3. Rust, M. J., Bates, M. & Zhuang, X. Sub-diffraction-limit imaging by stochastic optical reconstruction microscopy (STORM). *Nat. Methods* **3**, 793–796 (2006).
4. Thompson, R. E., Larson, D. R. & Webb, W. W. Precise nanometer localization analysis for individual fluorescent probes. *Biophys. J.* **82**, 2775–2783 (2002).
5. Fernández-Suárez, M. & Ting, A. Y. Fluorescent probes for super-resolution imaging in living cells. *Nat. Rev. Mol. Cell Biol.* **9**, 929–943 (2008).
6. Deschout, H. et al. Precisely and accurately localizing single emitters in fluorescence microscopy. *Nat. Methods* **11**, 253–266 (2014).
7. Fornasiero, E. F. & Opazo, F. Super-resolution imaging for cell biologists: concepts, applications, current challenges and developments. *Bioessay.: News Rev. Mol., Cell. Dev. Biol.* **37**, 436–451 (2015).
8. Turkowyd, B., Virant, D. & Endesfelder, U. From single molecules to life: microscopy at the nanoscale. *Anal. Bioanal. Chem.* **408**, 6885–6911 (2016).
9. Grimm, J. B. et al. A general method to fine-tune fluorophores for live-cell and in vivo imaging. *Nat. Methods* **14**, 987–994 (2017).
10. Li, C., Tebo, A. G. & Gautier, A. Fluorogenic labeling strategies for biological imaging. *Int. J. Mol. Sci.* **18**, 1473 (2017).
11. Hosein, R. E., Williams, S. A., Haye, K. & Gavin, R. H. Expression of GFP-actin leads to failure of nuclear elongation and cytokinesis in *Tetrahymena thermophila*. *J. Eukaryot. Microbiol.* **50**, 403–408 (2003).
12. Snapp, E. L. Fluorescent proteins: a cell biologist's user guide. *Trends Cell Biol.* **19**, 649–655 (2009).
13. Stadler, C. et al. Immunofluorescence and fluorescent-protein tagging show high correlation for protein localization in mammalian cells. *Nat. Methods* **10**, 315–323 (2013).
14. Hopp, T. P. et al. A short polypeptide marker sequence useful for recombinant protein identification and purification. *Nat. Biotechnol.* **6**, 1204–1210 (1988).
15. Wilson, I. A. et al. The structure of an antigenic determinant in a protein. *Cell* **37**, 767–778 (1984).
16. Evan, G. I., Lewis, G. K., Ramsay, G. & Bishop, J. M. Isolation of monoclonal antibodies specific for human c-myc proto-oncogene product. *Mol. Cell Biol.* **5**, 3610–3616 (1985).
17. Viswanathan, S. et al. High-performance probes for light and electron microscopy. *Nat. Methods* **12**, 568–576 (2015).
18. Chamma, I. et al. Mapping the dynamics and nanoscale organization of synaptic adhesion proteins using monomeric streptavidin. *Nat. Commun.* **7**, 10773 (2016).
19. Sharonov, A. & Hochstrasser, R. M. Wide-field subdiffraction imaging by accumulated binding of diffusing probes. *Proc. Natl Acad. Sci. USA* **103**, 18911–18916 (2006).
20. Legant, W. R. et al. High-density three-dimensional localization microscopy across large volumes. *Nat. Methods* **13**, 359–365 (2016).
21. Agasti, S. S. et al. DNA-barcoded labeling probes for highly multiplexed Exchange-PAINT imaging. *Chem. Sci.* **8**, 3080–3091 (2017).
22. Schnitzbauer, J., Strauss, M. T., Schlichthaerle, T., Schueder, F. & Jungmann, R. Super-resolution microscopy with DNA-PAINT. *Nat. Protoc.* **12**, 1198 (2017).
23. Pleiner, T. et al. Nanobodies: site-specific labeling for super-resolution imaging, rapid epitope-mapping and native protein complex isolation. *Elife* **4**, e11349 (2015).
24. Mikhaylova, M. et al. Resolving bundled microtubules using anti-tubulin nanobodies. *Nat. Commun.* **6**, 7933 (2015).

25. Traenkle, B. & Rothbauer, U. Under the microscope: single-domain antibodies for live-cell imaging and super-resolution microscopy. *Front. Immunol.* **8**, 1030 (2017).
26. Fridy, P. C. et al. A robust pipeline for rapid production of versatile nanobody repertoires. *Nat. Methods* **11**, 1253–1260 (2014).
27. Moutel, S. et al. NaLi-H1: a universal synthetic library of humanized nanobodies providing highly functional antibodies and intrabodies. *Elife* **5**, e16228 (2016).
28. Ries, J., Kaplan, C., Platonova, E., Eghlidi, H. & Ewers, H. A simple, versatile method for GFP-based super-resolution microscopy via nanobodies. *Nat. Methods* **9**, 582–584 (2012).
29. Tang, A.-H. et al. A trans-synaptic nanocolumn aligns neurotransmitter release to receptors. *Nature* **536**, 210–214 (2016).
30. Margolin, W. The price of tags in protein localization studies. *J. Bacteriol.* **194**, 6369–6371 (2012).
31. Braun, M. B. et al. Peptides in headlock–a novel high-affinity and versatile peptide-binding nanobody for proteomics and microscopy. *Sci. Rep.* **6**, 19211 (2016).
32. Popp, M. W. L. & Ploegh, H. L. Making and breaking peptide bonds: protein engineering using sortase. *Angew. Chem. Int. Ed.* **50**, 5024–5032 (2011).
33. Massa, S. et al. Sortase A-mediated site-specific labeling of camelid single-domain antibody-fragments: a versatile strategy for multiple molecular imaging modalities. *Contrast Media Mol. Imaging* **11**, 328–339 (2016).
34. Traenkle, B. et al. Monitoring interactions and dynamics of endogenous beta-catenin with intracellular nanobodies in living cells. *Mol. Cell Proteom.* **14**, 707–723 (2015).
35. Endesfelder, U. et al. Multiscale spatial organization of RNA polymerase in *Escherichia coli*. *Biophys. J.* **105**, 172–181 (2013).
36. Finan, K., Raulf, A. & Heilemann, M. A set of homo-oligomeric standards allows accurate protein counting. *Angew. Chem. Int. Ed.* **54**, 12049–12052 (2015).
37. Durisic, N., Laparra-Cuervo, L., Sandoval-Alvarez, A., Borbely, J. S. & Lakadamyali, M. Single-molecule evaluation of fluorescent protein photoactivation efficiency using an in vivo nanotemplate. *Nat. Methods* **11**, 156–162 (2014).
38. Szymborska, A. et al. Nuclear pore scaffold structure analyzed by super-resolution microscopy and particle averaging. *Science* **341**, 655–658 (2013).
39. Mendez, M. G., Kojima, S. & Goldman, R. D. Vimentin induces changes in cell shape, motility, and adhesion during the epithelial to mesenchymal transition. *FASEB J.* **24**, 1838–1851 (2010).
40. Wang, S., Moffitt, J. R., Dempsey, G. T., Xie, X. S. & Zhuang, X. Characterization and development of photoactivatable fluorescent proteins for single-molecule–based superresolution imaging. *Proc. Natl. Acad. Sci. USA* **111**, 8452–8457 (2014).
41. Maier, J., Traenkle, B. & Rothbauer, U. Real-time analysis of epithelial-mesenchymal transition using fluorescent single-domain antibodies. *Sci. Rep.* **5**, 13402 (2015).
42. Cranfill, P. J. et al. Quantitative assessment of fluorescent proteins. *Nat. Methods* **13**, 557 (2016).
43. Endesfelder, U., Malkusch, S., Fricke, F. & Heilemann, M. A simple method to estimate the average localization precision of a single-molecule localization microscopy experiment. *Histochem. Cell Biol.* **141**, 629–638 (2014).
44. Nieuwenhuizen, R. P. et al. Measuring image resolution in optical nanoscopy. *Nat. Methods* **10**, 557–562 (2013).
45. Brault, V., Sauder, U., Reedy, M. C., Aebi, U. & Schoenenberger, C.-A. Differential epitope tagging of actin in transformed *Drosophila* produces distinct effects on myofibril assembly and function of the indirect flight muscle. *Mol. Biol. Cell* **10**, 135–149 (1999).
46. Vale, R. D. The molecular motor toolbox for intracellular transport. *Cell* **112**, 467–480 (2003).
47. Hansen, T. E. & Johansen, T. Following autophagy step by step. *BMC.Biol.* **9**, 39 (2011).
48. Legler, D. F. et al. Differential insertion of GPI-anchored GFPs into lipid rafts of live cells. *FASEB J.* **19**, 73–75 (2005).
49. Yang, Z. & Klionsky, D. J. Mammalian autophagy: core molecular machinery and signaling regulation. *Curr. Opin. Cell Biol.* **22**, 124–131 (2010).
50. Mizushima, N., Ohsumi, Y. & Yoshimori, T. Autophagosome formation in mammalian cells. *Cell Struct. Funct.* **27**, 421–429 (2002).
51. Jin, M. & Klionsky, D. J. Regulation of autophagy: modulation of the size and number of autophagosomes. *FEBS Lett.* **588**, 2457–2463 (2014).
52. Tirino, V. et al. TGF-β1 exposure induces epithelial to mesenchymal transition both in CSCs and non-CSCs of the A549 cell line, leading to an increase of migration ability in the CD133+A549 cell fraction. *Cell Death Dis.* **4**, e620 (2013).
53. Róna, G. et al. Dynamics of re-constitution of the human nuclear proteome after cell division is regulated by NLS-adjacent phosphorylation. *Cell Cycle* **13**, 3551–3564 (2014).
54. Oba, M. & Tanaka, M. Intracellular internalization mechanism of protein transfection reagents. *Biol. Pharm. Bull.* **35**, 1064–1068 (2012).
55. Avignolo, C. et al. Internalization via Antennapedia protein transduction domain of an scFv antibody toward c-Myc protein. *FASEB J.* **22**, 1237–1245 (2008).
56. Marschall, A. L., Frenzel, A., Schirrmann, T., Schungel, M. & Dubel, S. Targeting antibodies to the cytoplasm. *MAbs* **3**, 3–16 (2011).
57. Sharei, A. et al. A vector-free microfluidic platform for intracellular delivery. *Proc. Natl. Acad. Sci. USA* **110**, 2082–2087 (2013).
58. Aigrain, L., Sustarsic, M., Crawford, R., Plochowietz, A. & Kapanidis, A. N. Internalization and observation of fluorescent biomolecules in living microorganisms via electroporation. *J. Vis. Exp.* **96**, 52208 (2015).
59. Hennig, S. et al. Instant live-cell super-resolution imaging of cellular structures by nanoinjection of fluorescent probes. *Nano Lett.* **15**, 1374–1381 (2015).
60. Teng, K. W. et al. Labeling proteins inside living cells using external fluorophores for microscopy. *Elife* **5**, e20378 (2016).
61. Roder, R. et al. Intracellular delivery of nanobodies for imaging of target proteins in live cells. *Pharm. Res.* **34**, 161–174 (2017).
62. Rothbauer, U. et al. Targeting and tracing antigens in live cells with fluorescent nanobodies. *Nat. Methods* **3**, 887–889 (2006).
63. Guimaraes, C. P. et al. Site-specific C-terminal and internal loop labeling of proteins using sortase-mediated reactions. *Nat. Protoc.* **8**, 1787–1799 (2013).
64. Rothbauer, U. et al. A versatile nanotrap for biochemical and functional studies with fluorescent fusion proteins. *Mol. Cell Proteom.* **7**, 282–289 (2008).
65. Hayashi, A. et al. Localization of gene products using a chromosomally tagged GFP-fusion library in the fission yeast *Schizosaccharomyces pombe*. *Genes Cells* **14**, 217–225 (2009).
66. Watson, A. T., Garcia, V., Bone, N., Carr, A. M. & Armstrong, J. Gene tagging and gene replacement using recombinase-mediated cassette exchange in *Schizosaccharomyces pombe*. *Gene* **407**, 63–74 (2008).
67. Bryksin, A. V. & Matsumura, I. Overlap extension PCR cloning: a simple and reliable way to create recombinant plasmids. *Biotechniques* **48**, 463–465 (2010).
68. Labun, K., Montague, T. G., Gagnon, J. A., Thyme, S. B. & Valen, E. CHOPCHOPv2: a web tool for the next generation of CRISPR genome engineering. *Nucleic Acids Res.* **44**, W272–W276 (2016).
69. Montague, T. G., Cruz, J. M., Gagnon, J. A., Church, G. M. & Valen, E. CHOPCHOP: a CRISPR/Cas9 and TALEN web tool for genome editing. *Nucleic Acids Res.* **42**, W401–W407 (2014).
70. Vidigal, J. A. & Ventura, A. Rapid and efficient one-step generation of paired gRNA CRISPR-Cas9 libraries. *Nat. Commun.* **6**, 8083 (2015).
71. Ran, F. A. et al. Genome engineering using the CRISPR-Cas9 system. *Nat. Protoc.* **8**, 2281–2308 (2013).
72. Nahidiazar, L., Agronskaia, A. V., Broertjes, J., van den Broek, B. & Jalink, K. Optimizing imaging conditions for demanding multi-color super resolution localization microscopy. *PLoS ONE* **11**, e0158884 (2016).
73. Van De Linde, S. et al. Direct stochastic optical reconstruction microscopy with standard fluorescent probes. *Nat. Protoc.* **6**, 991–1009 (2011).
74. Edelstein, A. D. et al. Advanced methods of microscope control using μManager software. *J. Biol. Methods* **1**, e10 (2014).
75. Carlini, L., Holden, S. J., Douglass, K. M. & Manley, S. Correction of a depth-dependent lateral distortion in 3D super-resolution imaging. *PLoS ONE* **10**, e0142949 (2015).
76. Malkusch, S. & Heilemann, M. Extracting quantitative information from single-molecule super-resolution imaging data with LAMA–LocAlization MicroscopyAnalyzer. *Sci. Rep.* **6**, 34486 (2016).
77. Schindelin, J. et al. Fiji: an open-source platform for biological-image analysis. *Nat. Methods* **9**, 676–682 (2012).
78. Zanacchi, F. C. et al. A DNA origami platform for quantifying protein copy number in super-resolution. *Nat. Methods* **14**, 789–792 (2017).
79. Pengo, T., Holden, S. J. & Manley, S. PALMsiever: a tool to turn raw data into results for single-molecule localization microscopy. *Bioinformatics* **31**, 797–798 (2014).

## Acknowledgements

The authors thank Christian Linke-Winnebeck and Benjamin Ruf (both ChromoTek GmbH) for technical support in nanobody production and labeling, Yana Parfyonova for cloning of the $_{\mathrm{BC2T}}$GFP-GPI construct and performing corresponding live cell studies, Maruša Kustec for help with general statistical tests, Urban Završnik for help with Python programming language scripting, Alex Herbert for help with his GDSC SMLM FIRE ImageJ Plugin and Knut Drescher for kindly providing his mammalian cell culture equipment. D.V., I.V., B.P.-L., and U.E. acknowledge funding by the Max Planck Society, SYNMIKRO and the Fonds der Chemischen Industrie. U.R., B.T., and J.M. gratefully acknowledge the Ministry of Science, Research and Arts of Baden-Württemberg (V.1.4.-H3-1403-74) for financial support.

## Author contributions

U.E. and U.R. conceived the study. D.V., B.T., J.M., P.D.K., M.B., C.S., I.V., B.P.-L., U.E., and U.R. performed all experiments, U.E. and U.R. wrote the manuscript with the input from all authors.

## Additional information

**Supplementary Information** accompanies this paper at https://doi.org/10.1038/s41467-018-03191-2.

**Competing interests:** U.R. is shareholder of the company ChromoTek GmbH. All other authors declare no competing financial interests.

# 6 | A New Photo-Conversion Mechanism for Quantitative, Multi-Color PALM Imaging

## 6.1 A General Mechanism of Photoconversion of Green-to-Red Fluorescent Proteins Based on Blue and Infrared Light Reduces Phototoxicity in Live-Cell Single-Molecule Imaging

# A General Mechanism of Photoconversion of Green-to-Red Fluorescent Proteins Based on Blue and Infrared Light Reduces Phototoxicity in Live-Cell Single-Molecule Imaging

Bartosz Turkowyd, Alexander Balinovic, David Virant, Haruko G. Gölz Carnero, Fabienne Caldana, Marc Endesfelder, Dominique Bourgeois, and Ulrike Endesfelder

This part of the thesis is written in the style of a manuscript and was published in Angewandte Chemie. I contributed to this work by desiging and executing the cloning and mutagenesis experiments, doing literature research and analysing and discussing the acquired data. [3]

Single-Molecule Microscopy

International Edition: DOI: 10.1002/anie.201702870
German Edition: DOI: 10.1002/ange.201702870

# A General Mechanism of Photoconversion of Green-to-Red Fluorescent Proteins Based on Blue and Infrared Light Reduces Phototoxicity in Live-Cell Single-Molecule Imaging

*Bartosz Turkowyd⁺, Alexander Balinovic⁺, David Virant, Haruko G. Gölz Carnero, Fabienne Caldana, Marc Endesfelder, Dominique Bourgeois, and Ulrike Endesfelder**

**Abstract:** *Photoconversion of fluorescent proteins by blue and complementary near-infrared light, termed primed conversion (PC), is a mechanism recently discovered for Dendra2. We demonstrate that controlling the conformation of arginine at residue 66 by threonine at residue 69 of fluorescent proteins from Anthozoan families (Dendra2, mMaple, Eos, mKikGR, pcDronpa protein families) represents a general route to facilitate PC. Mutations of alanine 159 or serine 173, which are known to influence chromophore flexibility and allow for reversible photoswitching, prevent PC. In addition, we report enhanced photoconversion for pcDronpa variants with asparagine 116. We demonstrate live-cell single-molecule imaging with reduced phototoxicity using PC and record trajectories of RNA polymerase in Escherichia coli cells.*

Photoconvertible fluorescent proteins (pcFPs) irreversibly change their optical properties when illuminated by specific wavelengths. They are key for single-molecule super-resolution imaging,[1] single-molecule tracking[2] and dynamic imaging.[3] Fast maturing and monomeric variants are a common choice in quantitative fluorescence microscopy applications.[4] Among the various fluorescent proteins available, green-to-red pcFPs, that change their fluorescence spectra from GFP- to RFP-type fluorescence upon near-UV illumination, have been particularly popular, owing to their high brightness, photostability, photoconversion contrast and the option for imaging the initial green as well as the converted red form.[1a,b]

Green-to-red pcFPs primarily originate from stony corals of suborder Faviina and in a few cases from closely related soft corals and one corallimorph coral.[5] Improved versions were derived from either naturally green-to-red converting, non-monomeric proteins like Kaede,[6] the Eos family[7] and Dendra2,[8] or from only green fluorescing but monomeric proteins, which were modified into pcFPs like mKikGR[9] and the mMaple[10] and Dronpa families.[11] All green-to-red pcFPs are monophyletically related and exhibit a very similar chromophore structure and neighboring amino acid residues.

Green-to-red pcFPs initially fold into their green form. The chromophores settle in a pH-dependent equilibrium between their neutral (N) and anionic (A) state. Only the anionic chromophore fluoresces upon 488 nm illumination and exhibits a fluorescence maximum in the 500–520 nm range (Figure 1 a, left). 405 nm irradiation mediated photoconversion into the red form occurs from the neutral (non-fluorescent) chromophore state (Figure 1 a, left). While the exact mechanism is still under debate, it was shown to involve the cleavage of the histidine 62 $N^{\alpha}$–$C^{\alpha}$ bond (numbering according to *Aequorea victoria* GFP) and the formation of a $C^{\alpha}$–$C^{\beta}$ double bond in the histidine 62 side chain, which extends the delocalized π-electron system of the His-Tyr-Gly tripeptide chromophore (Figure 1 a (ii)).[12] The anionic state of the red form fluoresces with a maximum in the 570–590 nm range upon 561 nm illumination (Figure 1 a, right). Dendra2 has shown to also photoconvert from its anionic green chromophore when irradiated by 488 nm light, but at a reduced efficiency.[8]

However, a novel switching mechanism, termed primed conversion (PC), using combined illumination at 488 nm and near-infrared light at 700–800 nm has recently shown to be very efficient for Dendra2 although it was poor for mEos2.[13] This mechanism is of particularly high interest for live-cell microscopy, as it avoids phototoxic illumination by 405 nm light.[13–14] The exact mechanism is not yet understood, but pH dependence and 488 nm irradiation hint at an excitation of the anionic green chromophore from which it is "primed" into a millisecond long intermediate state, followed by a conversion into the red chromophore induced by irradiation with near-infrared light[13–14] (Figure 1 a (i)).

As the Anthozoan pcFPs only differ slightly among each other, we were able to identify several amino acid residues which we expected to be critical for PC by systematically comparing their structural characteristics and photophysical behavior as reported in the literature (see Figure S1 a in the Supporting Information).

Of particular interest was residue 69, as it was shown that Dendra2 and mEos2 interchange their photophysical proper-

---

[*] B. Turkowyd,[+] A. Balinovic,[+] D. Virant, H. G. G. Carnero, F. Caldana, Dr. U. Endesfelder
Department of Systems and Synthetic Microbiology, Max Planck Institute for Terrestrial Microbiology &
LOEWE Center for Synthetic Microbiology (SYNMIKRO)
Karl-von-Frisch-Str. 16, 35043 Marburg (Germany)
E-mail: ulrike.endesfelder@synmikro.mpi-marburg.mpg.de

M. Endesfelder
Institut für Assyriologie und
Ludwig-Maximilians-Universität München
Geschwister-Scholl-Platz 1, 80539 München (Germany)

Dr. D. Bourgeois
Institut de Biologie Structurale, CNRS
Université Grenoble Alpes, CEA, IBS, 38044 Grenoble (France)

[+] These authors contributed equally to this work.

Supporting information and the ORCID identification number(s) for the author(s) of this article can be found under: https://doi.org/10.1002/anie.201702870.

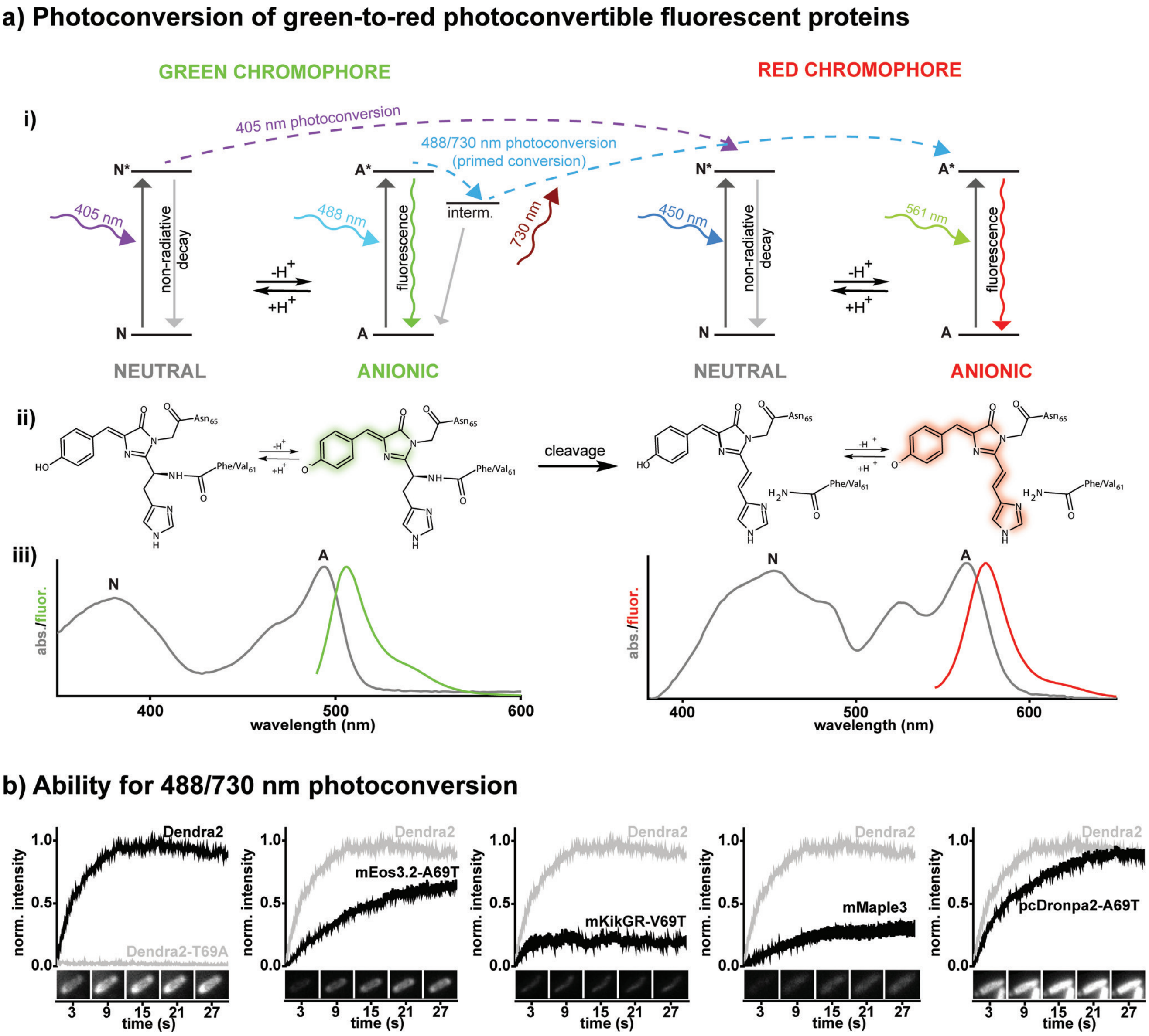

*Figure 1.* a) Photoconversion of green-to-red pcFPs. The green chromophore of pcFPs absorbs in the near-UV range in its neutral (N) and in the blue range in its anionic (A) form (left, i–iii)). Fluorescence occurs from the excited anionic state (A*) with a maximum at about 500–520 nm (left, colored in green). A light-induced cleavage of the fluorophore backbone extends the chromophore which then absorbs in the blue range in its neutral and in the green/orange range in its anionic form. The latter emits orange/red fluorescence in the range of 570–590 nm (right, colored in red). UV-light mediated photoconversion (violet dashed arrow) starts from the neutral state, whereas PC (blue dashed arrows) originates from the anionic form which can be "primed" into a millisecond long intermediate state. By additional irradiation with near-infrared 730 nm light, the chromophore is converted into its red form. b) 488/730 nm photoconversion ability of pcFPs from different protein families. Protein variants of different families were irradiated by 488/730 nm to characterize their ability to undergo PC by measuring the increase in red fluorescence. Insets show the fluorescence increase of transiently overexpressed free pcFPs upon 488/730 illumination in single *Escherichia coli* cells.

ties (i.e. their brightness, photoblinking and -bleaching behavior) when transposing residue 69 in the variants mEos2-A69T and Dendra2-T69A.[15] Crystal structures reveal that this can be explained by the altered conformation of arginine 66 which interacts with the chromophore and glutamate 212.[15] The latter is responsible for redox-induced photobleaching by decarboxylation.[15] We thus tested mEos2-A69T for PC which indeed efficiently photoconverts under 488/730 nm light, while Dendra2-T69A does not (Figure S1 b (i)).

We then generated threonine 69 variants for several pcFPs (Table S1) and found them capable of PC while their originals (with alanine or valine 69) were not (Figure 1 b, Figure S1 b). The mMaple family, which already contains threonine 69, naturally shows PC (Figure 1 b).

When investigating the properties of the threonine 69 pcFPs variants, we found them to exhibit a lower extinction coefficient and a hypsochromic shift of absorption and emission maxima of about 10 nm, compared to the alanine or valine 69 variants (Table 1, Table S2). Their p$K_a$ values are

***Table 1:*** Properties of green-to-red pcFPs capable of PC.[a]

| Name | Genetic background | $\lambda_{exc}$ [nm] | $\lambda_{em}$ [nm] | oligomeric state | $\varepsilon$ [$M^{-1}cm^{-1}$] | $\Phi$ | p$K_a$ | $k_{488/730\,nm}$ [$10^{-2}\,s^{-1}$] | rel. photon counts | $t_{0.5*int}$ [s] | opt. $pH_{405}$ | opt. $pH_{488/730}$ | Ref. |
|---|---|---|---|---|---|---|---|---|---|---|---|---|---|
| Dendra2 | Dendra A224V | 490[a]/ 553[a] | 507[a]/ 573[a] | m | 33 300[a]/ 17 300[a] | 0.53[a]/ 0.74[a] | 7.5[a]/ 7.9[a] | 21.3 | 1 | 1/1 | 8 | 8.5–10 | [a],[15] this work |
| mMaple | mClavGR2 220-224 HSGLP to RNSTD and A145V G171S G225S | 489[b]/ 566[b] | 505[b]/ 583[b] | m | 15 000[b]/ 30 000[b] | 0.74[b]/ 0.56[b] | 8.2[b]/ 7.3[b] | 11.6 | ND | 4.0/ 1.2 | 7–8 | 8.5–9 | [b],[10a] this work |
| mMaple3 | mMaple I111N Y198A E82R D83K D197K | 489[b]/ 566[b] | 505[b]/ 583[b] | m | 74 000/ ND | ND | 7.9/ 7.2 | 5.5 | 1.5 | 3.3/ 1.4 | 7–8 | 8–10 | [b],[10b] this work |
| mMaple3-V157I | mMaple3 V157I | 490/ 570 | 505/ 582 | m | 28 000/ ND | ND | 8.2/ 7.8 | 3.3 | ND | 2.4/ 2.0 | 6–8 | 8.5–10 | this work |
| mEos2-A69T | EosFP N11K E70K A69T H74N H121Y | 495[a]/ 565[a] | 509[a]/ 580[a] | m | 24 300[a]/ 11 500[a] | 0.87[a]/ 0.66[a] | 8.2[a]/ 7.4[a] | 9.4 | ND | 3.4/ 1.1 | 6–8 | 8.5–10 | [a],[15] this work |
| mEos3.2-A69T | mEos2 A69T I102N H158E Y189A | 494/ 562 | 507/ 573 | m | 44 000/ ND | ND | 6.7/ 6.7 | 7.7 | 1.2 | 3.8/ 1.5 | 6–8 | 7.5–10 | this work |
| mEos4b-V69T | mEos4b V69T | 494/ 562 | 505/ 581 | m | 50 000/ ND | ND | 7.7/ 7.1 | 6.2 | 1.1 | 3.0/ 0.5 | 6–8 | 8–10 | this work |
| pcDronpa-A69T | Dronpa V60A C62H A69T N94S N102I E218G | 494[c] | 507[c] | t | 34 000[c] | 0.82[c] | 8.0[c] | 7.9 | ND | 1.0/ 3.1 | 6–7 | 8–10 | [c],[11b] this work |
| pcDronpa2-A69T | pcDronpa Y116N A69T | 494/ 564 | 506/ 575 | t | 51 000/ ND | ND | 8.6/ 7.9 | 16.2 | 1.2 | 1.9/ 0.9 | 6–8 | 8–10 | this work |
| mKikGR-V69T | mKikGR V69T | 492/ 570 | 506/ 580 | m | ND | ND | 8.2/ 7.2 | 19.5 | ND | 4.8/ 0.3 | 7–7.5 | 8.5–10 | this work |

[a] Table summarizing the properties of green-to-red pcFPs which can by photoconverted by 488/730 nm illumination. Listed are their key photophysical properties with $\lambda_{exc}$—excitation wavelength; $\lambda_{em}$—emission wavelength; $\varepsilon$—molar extinction coefficient at pH 7.5; $\Phi$—fluorescence quantum yield; $k_{488/730\,nm}$—photoconversion rate for ensemble measurements at pH 8 (Figure S3); relative photon counts of fluorescence spots in single molecule experiments in relation to Dendra2 (Figure S8) and $t_{0.5*int}$—time of 50% intensity loss when irradiated by 488 nm or 561 nm light, respectively at pH 7.5 in relation to Dendra2 (Figure S3e). Furthermore, their genetic background, oligomeric state (m—monomeric; t—tetrameric), the pKa values of the chromophores (Figure S2) as well as the optimal pH for 405 nm and 488/730 nm light-mediated photoconversion are given (Figure S3). Values are either from the literature as labeled or were measured in this study. ND—not determined.

higher as the imidazolinone moiety of the chromophore is no longer stabilized by the repositioned arginine 66 residue (Figure S1c(i), Figure S2). These findings are consistent with reported data.[11b,15]

The PC rate, as measured for Dendra2, increases with the applied laser intensities, but the PC efficiency drops at higher 488 nm intensities, probably due to photobleaching (Figure S3a,b). 405 nm-mediated photoconversion generally dominates the lower and PC the higher pH range (Figure S3c). This can be related to the ratio of near-UV light absorbing neutral chromophores and blue light absorbing anionic ones dependent on the p$K_a$ value of the hydroxyphenyl group of the chromophore. We do not, however, find a one-to-one correlation. In agreement with previous studies, the rate of conversion instead seems to be determined by the local p$K_a$ values of several residues close to the chromophore which form an internal charge network and are directly involved in the photoconversion mechanism.[11b,16]

To investigate the intermediate state possibly induced by 488 nm irradiation and suspected to be the entry point for 730 nm mediated photoconversion in Dendra2,[13] we probed its expected half-life in threonine 69 pcFPs by delaying the conversion laser by 0–30 ms in relation to the 488 nm laser pulse. In all FPs, the attained fluorescence intensity of the converted fluorophores decreased exponentially when prolonging the delay and was consistent with a 4–5 ms half-life of the intermediate state (Figure S4).

An advantage of all threonine 69 variants is an increased photostability, as we found their loss of fluorescence to be significantly slower for both their green and red form, enabling longer imaging times (Table 1 and Figure S3d). Furthermore, they also convert to some extent when using 640 nm instead of 730 nm light and under 488 nm light only (Figure S3e). For 640 nm illumination, this reduces efficiency by 55–75% but it makes them, like Dendra2,[17] accessible to fluorescence microscopes equipped with a red laser source.

We then investigated whether mutations that introduce chromophore flexibility and allow for *cis–trans* isomerization may interfere with the PC mechanism, as reversible off-switching from the fluorescent *cis*- to the non-planar, dark *trans*-isoform is facilitated by 488 nm illumination.[16a,18] For reversible photoswitching NijiFP (= Dendra2-F173S) and Dendra2-M159A we did not observe any 488/730 nm mediated photoconversion (Figure S1b(ii), c(ii)).

We hypothesized that the inability of mKikGR-V69T, mMaple and mMaple3 to undergo efficient PC (Figure 1b, Figure S3c(iii,iv)) is related to valine 157 and a possibly twisted or *trans*-chromophore dark state.[19] As mMaple3 is a monomeric, bright fluorophore and thus a good choice for super-resolution studies (Figure S8), we constructed mMaple3-V157I. Unfortunately, mMaple3-V157I lost fluorescence brightness. However, the comparatively high ratio between the maximal red fluorescence intensities attained by 488/730 nm and 405 nm conversion, respectively suggests a higher PC efficiency for the mutant (Figure S3 c (iii)).

As all photoswitching GFP-type FPs[11b, 19a,c, 20] and also the green forms of mEos2 and Dendra2[15–16] are reported to enter temporary, UV-reversible dark states upon 488 nm illumination, we measured the liability of all pcFPs to do so and compared the results to their ability to undergo PC. We found the green fluorescence of all pcFPs to decrease significantly under extended moderate 488 nm illumination (Figure S5). Subsequent UV illumination restored 60–100 % of the lost intensity, demonstrating that a large fraction of pcFPs had entered reversible dark states (Figure S5 b). Remarkably, the fluorescence of all pcFPs not capable of PC rapidly dropped to the background level, whereas all FP variants that can undergo PC decayed more slowly and retained significant fluorescence after 60 s of 488 nm illumination (Figure S5). As the recovery was equal or larger for non-PC-converting pcFPs, this difference cannot be explained by increased photobleaching or -conversion of the latter (Figure S5). Instead, the experiment suggests an increased tendency for non-PC-converting pcFPs to enter seconds to minutes long, by 405 nm-light reversible dark states which also relates to the observed difference in photostability (Figure S3 d).

We then focused on the residues close to the chromophore which are described to be involved in UV-light mediated photoconversion.[12] pcDronpa-A69T possesses tyrosine 116, a position identified as critical for enhanced photoconversion,[11b, 12d, 21] and has been reported as non-converting under 405 nm illumination.[11b] We wondered whether pcDronpa-A69T may photoconvert under 488/730 nm light and indeed found moderately effective PC (Figure S1 b (iii), c (iii), Figure S3 c (v)). We then mutated tyrosine 116 to asparagine, a common amino acid for efficiently converting pcFPs, which significantly improved PC and restored 405 nm photoconversion (Figure 1 b).

For Dendra2, the only pcFP exhibiting PC with glutamine 116 (Figure S1 a,c (iii)), we generated Q116N and Q116Y mutants. We hypothesized that changes to the charge network surrounding the Dendra2 chromophore (S105/Q116), which differs from all other pcFPs (N105/N116), would affect the photoconversion capability. Indeed, the mutants neither showed UV- nor PC photoconversion but displayed photoswitching dynamics comparable to only UV-converting pcFPs (Figure S5). A further mutation to Dendra2-S105N-Q116N mimics the N105/N116 network and restored photoconversion, but at a significantly lower level than for Dendra2 (Figure S1 b (iii)). This might hint at a reduced chromophore stability of the mutant.

In conclusion, the ability of pcFPs to undergo PC critically depends on threonine 69 which controls the conformation of arginine 66. A short, milliseconds long intermediate state appears to be the entry point into the PC mechanism. PC appears to be in direct competition with the FP′s tendency to photoswitch into a long-lasting dark state reversible by 405 nm light (Figure S6). This explains the immediate dependency of PC on the conformation of arginine 66[15] as well as the (partial) suppression of PC in NijiFP, Dendra2-M159A or the Eos proteins with alanine 69 as well as mKikGR-V69T and the mMaple family. Changes to the amino acid network known to be involved in the UV-light mediated photoconversion process seem to affect PC and UV conversion efficiency equally, suggesting similar charge transfer processes inducing the backbone cleavage. However, as in the case of pcDronpa-A69T, (moderately efficient) PC might be possible when UV conversion is not.

Finally, we tested whether the new pcFPs can be applied advantageously in single-particle tracking photoactivated localization microscopy (sptPALM).[22] sptPALM imaging typically involves irradiation of the probe by 405 nm light for FP photoconversion and 561 nm light for fluorescence read-out. We investigated whether PC, involving 488/730 nm instead of 405 nm irradiation, might reduce photoinduced damages to the probe which primarily depend on the applied laser intensity and wavelength.[23] We recorded single-molecule trajectories (i.e. individual molecules traced through several images) of RNA polymerases tagged with Dendra2 in living *Escherichia coli* cells under common sptPALM conditions and monitored their growth before and after sptPALM imaging by recording brightlight movies for several hours (Figure 2 a and Videos S1–6). Cells, for which the single-molecule dynamics were recorded over 6 minutes using PC-photoconversion, resembled control cells which were only irradiated by the 561 nm read-out laser for the same period. Both exhibited a high percentage of cells which continue to grow normally. Cells whose single-molecule dynamics were imaged by 405 nm photoconversion showed an already significantly reduced cell survival after only 4 minutes of sptPALM imaging and a significant fraction of cells which paused their growth for 2–3 hours (Figure 2 b and Videos S1–6). For PC experiments, the continuous 561 nm read-out turned out to be the most limiting factor for cell viability. The impact of its accumulating illumination dose becomes severe after 8 minutes of sptPALM imaging at critical doses similar to doses observed before.[23]

We then assessed the quality of the sptPALM data. PC yielded more trajectories at slightly lower conversion intensity whereas the obtained trajectory lengths and spot intensities for both modes were comparable (Figure S7). Even though 405 nm irradiation caused growth delay and death in many cells, the observed RNA polymerase dynamics did not deviate from cells measured using PC and were similar to previously reported statistics:[24] on average, 70 % of RNA polymerases appeared to be actively transcribing, 27 % to be mostly DNA-bound and about 3 % diffused freely (Figure S7).

We then measured the apparent single-molecule brightness for all PC-converting FPs by preparing single-molecule surfaces (Figure S8). The threonine 69 variants showed slightly decreased photon counts, for example, Dendra2-T69A was about 20 % brighter than Dendra2. mMaple3 displayed the highest photon count being 30 % brighter than Dendra2 but its PC efficiency on the single-molecule level was, like in ensemble measurements, low (data not shown) which largely disqualifies it from quantitative imaging purposes using PC.

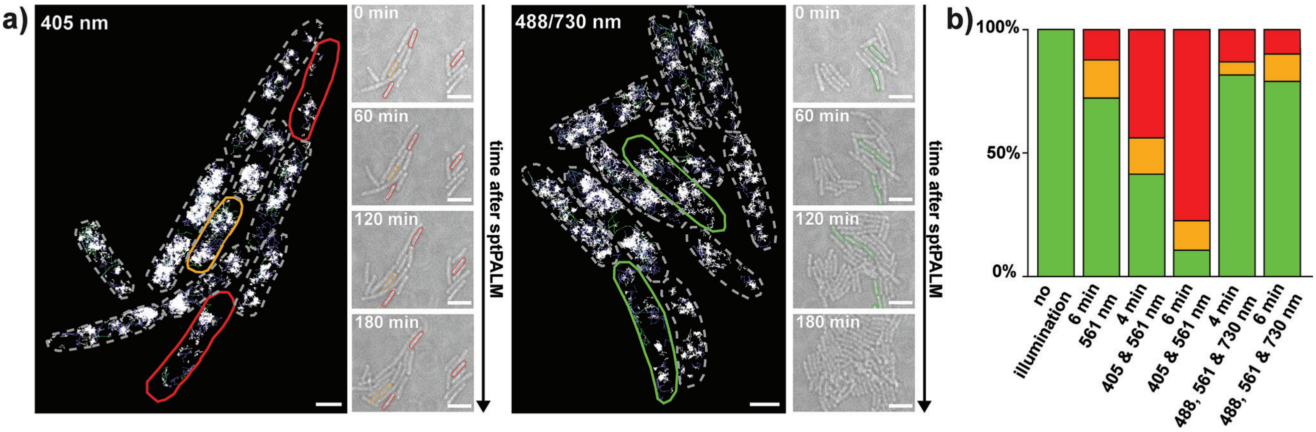

***Figure 2.*** Phototoxicity of 488/730 and 405 nm photoconversion in sptPALM experiments in living *Escherichia coli* cells when imaging Dendra2-tagged RNA polymerase dynamics. a) Trajectories of single RNA polymerase molecules obtained over 6 minutes of sptPALM imaging. Trajectories are color coded by their apparent diffusion coefficient D: 0.0–0.15 $\mu m^2 s^{-1}$ (white), 0.15–0.8 $\mu m^2 s^{-1}$ (blue), larger than 0.8 $\mu m^2 s^{-1}$ (green). Cell shapes are marked by dashed outlines, solid outlines (red dead, orange paused, green undisturbed) highlight exemplary cells which are also marked in the brightlight images depicting cell growth after sptPALM over several hours (right, and Videos S1–6). Scale bars 1 µm (sptPALM), 5 µm (brightlight). b) Cell viability after sptPALM experiments. Controls were not illuminated by any laser or for 6 minutes by 561 nm laser light only. sptPALM experiments of 4 and 6 minutes were conducted using either 405 nm or 488/730 nm irradiation (Materials and Methods). Cellular growth of the imaged areas was monitored by brightlight imaging and evaluated for cell viability. Green bars mark the fraction of cells growing without any visible effects, orange bars represent cells which paused their growth for 2–3 hours and red bars mark cells with no detectable growth until the end of the experiment after 8 hours. $n=368$ cells.

In summary, PC can be enabled for all green-to-red pcFP families by generating threonine 69 variants. Dendra2, pcDronpa2-A69T and the Eos family exhibit efficient PC, whereas mKikGR and mMaple variants only show reduced efficiency. As pcDronpa2-A69T is efficiently photoconverted by both modes and offers the highest quantum yield of all considered pcFPs, it is an interesting FP for future studies. However, its tetrameric behavior considerably limits its usefulness in practice.[10b] We therefore recommend the use of mEos3.2-A69T or Dendra2, which also show good performance. We predict that threonine 69 variants of other pcFPs like Kaede or calcium sensors based on Eos (CamPARI[25]) and mMaple (GR-GECOs[26]) will also exhibit PC. Even though our efforts to improve PC efficiencies and fluorescence brightness by modifying residues 105/116 of Dendra2 and 157 of mMaple3 proved unsuccessful, we believe that different strategies, for example, suppressing the transition into the dark states, might yield more favorable results. For example, a promising route could be to systematically modify other important amino acids like serine 142 or histidine 194. Furthermore, to advance live-cell compatibility, proteins converting and emitting at longer wavelengths would be especially desirable, which immediately raises the question if PC-like mechanisms can be transferred to FPs absorbing these wavelengths, for example, psmOrange[27] or new pcFPs found/designed in future studies.

## Acknowledgements

We thank V. Adam, IBS Grenoble, France, S. Wang and X. Zhuang, Harvard University, US and P. Dedecker, Leuven University, Belgium for kindly sharing their fluorescent protein plasmids. This work was funded by the Max Planck Society, SYNMIKRO and the Fonds der Chemischen Industrie.

## Conflict of interest

The authors declare no conflict of interest.

**Keywords:** fluorescent proteins · live-cell microscopy · phototoxicity · primed conversion · single-molecule microscopy

**How to cite:** *Angew. Chem. Int. Ed.* **2017**, *56*, 11634–11639
*Angew. Chem.* **2017**, *129*, 11792–11798

---

[1] a) K. Nienhaus, G. U. Nienhaus, *Chem. Soc. Rev.* **2014**, *43*, 1088–1106; b) E. A. Rodriguez, R. E. Campbell, J. Y. Lin, M. Z. Lin, A. Miyawaki, A. E. Palmer, X. Shu, J. Zhang, R. Y. Tsien, *Trends Biochem. Sci.* **2017**, *42*, 111–129; c) B. Turkowyd, D. Virant, U. Endesfelder, *Anal. Bioanal. Chem.* **2016**, *408*, 6885–6911.

[2] a) L. Cognet, C. Leduc, B. Lounis, *Curr. Opin. Chem. Biol.* **2014**, *20*, 78–85; b) A. Gahlmann, W. E. Moerner, *Nat. Rev. Microbiol.* **2014**, *12*, 9–22.

[3] I. Nemet, P. Ropelewski, Y. Imanishi, *Photochem. Photobiol. Sci.* **2015**, *14*, 1787–1806.

[4] a) S. H. Lee, J. Y. Shin, A. Lee, C. Bustamante, *Proc. Natl. Acad. Sci. USA* **2012**, *109*, 17436–17441; b) D. Lando, U. Endesfelder, H. Berger, L. Subramanian, P. D. Dunne, J. McColl, D. Klenerman, A. M. Carr, M. Sauer, R. C. Allshire, M. Heilemann, E. D. Laue, *Open Biol.* **2012**, *2*, 120078; c) E. M. Puchner, J. M. Walter, R. Kasper, B. Huang, W. A. Lim, *Proc. Natl. Acad. Sci. USA* **2013**, *110*, 16015–16020.

[5] N. O. Alieva, K. A. Konzen, S. F. Field, E. A. Meleshkevitch, M. E. Hunt, V. Beltran-Ramirez, D. J. Miller, J. Wiedenmann, A. Salih, M. V. Matz, *PLoS One* **2008**, *3*, e2680.

[6] R. Ando, H. Hama, M. Yamamoto-Hino, H. Mizuno, A. Miyawaki, *Proc. Natl. Acad. Sci. USA* **2002**, *99*, 12651 – 12656.

[7] a) S. A. McKinney, C. S. Murphy, K. L. Hazelwood, M. W. Davidson, L. L. Looger, *Nat. Methods* **2009**, *6*, 131 – 133; b) M. Zhang, H. Chang, Y. Zhang, J. Yu, L. Wu, W. Ji, J. Chen, B. Liu, J. Lu, Y. Liu, J. Zhang, P. Xu, T. Xu, *Nat. Methods* **2012**, *9*, 727 – 729; c) M. G. Paez-Segala, M. G. Sun, G. Shtengel, S. Viswanathan, M. A. Baird, J. J. Macklin, R. Patel, J. R. Allen, E. S. Howe, G. Piszczek, H. F. Hess, M. W. Davidson, Y. Wang, L. L. Looger, *Nat. Methods* **2015**, *12*, 215 – 218.

[8] D. M. Chudakov, S. Lukyanov, K. A. Lukyanov, *Biotechniques* **2007**, *42*, 553.

[9] S. Habuchi, H. Tsutsui, A. B. Kochaniak, A. Miyawaki, A. M. van Oijen, *Plos One* **2008**, *3*, e3944.

[10] a) A. L. McEvoy, H. Hoi, M. Bates, E. Platonova, P. J. Cranfill, M. A. Baird, M. W. Davidson, H. Ewers, J. Liphardt, R. E. Campbell, *PLoS One* **2012**, *7*, e51314; b) S. Wang, J. R. Moffitt, G. T. Dempsey, X. S. Xie, X. Zhuang, *Proc. Natl. Acad. Sci. USA* **2014**, *111*, 8452 – 8457.

[11] a) R. Ando, H. Mizuno, A. Miyawaki, *Science* **2004**, *306*, 1370 – 1373; b) B. Moeyaert, N. Nguyen Bich, E. De Zitter, S. Rocha, K. Clays, H. Mizuno, L. van Meervelt, J. Hofkens, P. Dedecker, *ACS Nano* **2014**, *8*, 1664 – 1673.

[12] a) K. Nienhaus, G. U. Nienhaus, J. Wiedenmann, H. Nar, *Proc. Natl. Acad. Sci. USA* **2005**, *102*, 9156 – 9159; b) I. Hayashi, H. Mizuno, K. I. Tong, T. Furuta, F. Tanaka, M. Yoshimura, A. Miyawaki, M. Ikura, *J. Mol. Biol.* **2007**, *372*, 918 – 926; c) H. Tsutsui, H. Shimizu, H. Mizuno, N. Nukina, T. Furuta, A. Miyawaki, *Chem. Biol.* **2009**, *16*, 1140 – 1147; d) H. Kim, T. Zou, C. Modi, K. Dorner, T. J. Grunkemeyer, L. Chen, R. Fromme, M. V. Matz, S. B. Ozkan, R. M. Wachter, *Structure* **2015**, *23*, 34 – 43.

[13] W. P. Dempsey, L. Georgieva, P. M. Helbling, A. Y. Sonay, T. V. Truong, M. Haffner, P. Pantazis, *Nat. Methods* **2015**, *12*, 645 – 648.

[14] M. A. Mohr, P. Argast, P. Pantazis, *Nat. Protoc.* **2016**, *11*, 2419 – 2431.

[15] R. Berardozzi, V. Adam, A. Martins, D. Bourgeois, *J. Am. Chem. Soc.* **2016**, *138*, 558 – 565.

[16] a) V. Adam, B. Moeyaert, C. C. David, H. Mizuno, M. Lelimousin, P. Dedecker, R. Ando, A. Miyawaki, J. Michiels, Y. Engelborghs, J. Hofkens, *Chem. Biol.* **2011**, *18*, 1241 – 1251; b) H. Kim, T. J. Grunkemeyer, C. Modi, L. Chen, R. Fromme, M. V. Matz, R. M. Wachter, *Biochemistry* **2013**, *52*, 8048 – 8059.

[17] N. V. Klementieva, K. A. Lukyanov, N. M. Markina, S. A. Lukyanov, E. V. Zagaynova, A. S. Mishin, *Chem. Commun.* **2016**, *52*, 13144 – 13146.

[18] V. Adam, M. Lelimousin, S. Boehme, G. Desfonds, K. Nienhaus, M. J. Field, J. Wiedenmann, S. McSweeney, G. U. Nienhaus, D. Bourgeois, *Proc. Natl. Acad. Sci. USA* **2008**, *105*, 18343 – 18348.

[19] a) A. C. Stiel, S. Trowitzsch, G. Weber, M. Andresen, C. Eggeling, S. W. Hell, S. Jakobs, M. C. Wahl, *Biochem. J.* **2007**, *402*, 35 – 42; b) M. Andresen, A. C. Stiel, J. Folling, D. Wenzel, A. Schonle, A. Egner, C. Eggeling, S. W. Hell, S. Jakobs, *Nat. Biotechnol.* **2008**, *26*, 1035 – 1040; c) R. Ando, C. Flors, H. Mizuno, J. Hofkens, A. Miyawaki, *Biophys. J.* **2007**, *92*, L97 – L99.

[20] H. Chang, M. Zhang, W. Ji, J. Chen, Y. Zhang, B. Liu, J. Lu, J. Zhang, P. Xu, T. Xu, *Proc. Natl. Acad. Sci. USA* **2012**, *109*, 4455 – 4460.

[21] S. F. Field, M. V. Matz, *Mol. Biol. Evol.* **2010**, *27*, 225 – 233.

[22] S. Manley, J. M. Gillette, J. Lippincott-Schwartz, *Methods Enzymol.* **2010**, *475*, 109 – 120.

[23] S. Wäldchen, J. Lehmann, T. Klein, S. van de Linde, M. Sauer, *Sci. Rep.* **2015**, *5*, 15348.

[24] a) U. Endesfelder, K. Finan, S. J. Holden, P. R. Cook, A. N. Kapanidis, M. Heilemann, *Biophys. J.* **2013**, *105*, 172 – 181; b) M. Stracy, C. Lesterlin, F. Garza de Leon, S. Uphoff, P. Zawadzki, A. N. Kapanidis, *Proc. Natl. Acad. Sci. USA* **2015**, *112*, E4390 – E4399.

[25] B. F. Fosque, Y. Sun, H. Dana, C. T. Yang, T. Ohyama, M. R. Tadross, R. Patel, M. Zlatic, D. S. Kim, M. B. Ahrens, V. Jayaraman, L. L. Looger, E. R. Schreiter, *Science* **2015**, *347*, 755 – 760.

[26] H. Hoi, T. Matsuda, T. Nagai, R. E. Campbell, *J. Am. Chem. Soc.* **2013**, *135*, 46 – 49.

[27] O. M. Subach, G. H. Patterson, L. M. Ting, Y. Wang, J. S. Condeelis, V. V. Verkhusha, *Nat. Methods* **2011**, *8*, 771 – 777.

Manuscript received: March 20, 2017
Revised manuscript received: April 27, 2017
Accepted manuscript online: June 2, 2017
Version of record online: July 17, 2017

## 6.2 Aberration-Free, Live-Cell Compliant Multi-Color Single-Molecule Localization Microscopy Imaging

# Combining Primed Photoconversion and UV-Photoactivation for Aberration-Free, Live-Cell Compliant Multi-Color Single-Molecule Localization Microscopy Imaging

David Virant, Bartosz Turkowyd, Alexander Balinovic,
Ulrike Endesfelder

This part of the thesis is written in the style of a manuscript and was published in the International Journal of Molecular Sciences. It covers the development process of an Fluorescent Protein (FP) based dual-color SMLM imaging technique. In this manuscript we demonstrate that this imaging scheme can be used universally in mammalian, yeast and bacterial cells and allows for a quantitative readout of the chosen Protein Of Interest (POI). It is now an established dual-color imaging technique in the Endesfelder lab and is used for several studies, including the structural and stoichiometric characterization of the fission yeast kinetochore (see **section 7.2**). I contributed to this work by conceiving the idea, designing and performing experiments, analyzing data and writing most of the text. [4]

International Journal of
*Molecular Sciences*

*Article*

# Combining Primed Photoconversion and UV-Photoactivation for Aberration-Free, Live-Cell Compliant Multi-Color Single-Molecule Localization Microscopy Imaging

**David Virant, Bartosz Turkowyd, Alexander Balinovic and Ulrike Endesfelder ***

Department of Systems and Synthetic Microbiology, Max Planck Institute for Terrestrial Microbiology & LOEWE Center for Synthetic Microbiology (SYNMIKRO), Karl-von-Frisch-Str. 16, 35043 Marburg, Germany; david.virant@synmikro.mpi-marburg.mpg.de (D.V.); bartosz.turkowyd@synmikro.mpi-marburg.mpg.de (B.T.); alexander.balinovic@synmikro.mpi-marburg.mpg.de (A.B.)

* Correspondence: ulrike.endesfelder@synmikro.mpi-marburg.mpg.de; Tel.: +49-6421-28-21619

Received: 11 June 2017; Accepted: 5 July 2017; Published: 14 July 2017

**Abstract:** Super-resolution fluorescence microscopy plays a major role in revealing the organization and dynamics of living cells. Nevertheless, single-molecule localization microscopy imaging of multiple targets is still limited by the availability of suitable fluorophore combinations. Here, we introduce a novel imaging strategy which combines primed photoconversion (PC) and UV-photoactivation for imaging different molecular species tagged by suitable fluorescent protein combinations. In this approach, the fluorescent proteins can be specifically photoactivated/-converted by different light wavelengths using PC and UV-activation modes but emit fluorescence in the same spectral emission channel. We demonstrate that this aberration-free, live-cell compatible imaging method can be applied to various targets in bacteria, yeast and mammalian cells and can be advantageously combined with correlative imaging schemes.

**Keywords:** multi-color imaging; primed conversion; live cell imaging; single-molecule localization microscopy

---

## 1. Introduction

Over the past decade, rapid advances in single-molecule localization microscopy (SMLM) techniques have created a large, quantitative imaging toolbox which allows for the direct observations of molecular processes of life at the nanometer scale [1–3]. Part of its tremendous impact is owed to the fact that, just like in conventional fluorescence microscopy, individual species of molecules can be visualized and placed into context to each other by specific fluorescence tags in situ as well as in vivo.

Nowadays, multi-color SMLM imaging is frequently performed. However, while several approaches for multi-color SMLM imaging in fixed cells have been optimized for ideal combinations of bright fluorophores with complementary staining (e.g., antibody, nanobody or protein-tag stainings), similar photoswitching requirements and distinct read-out, the choice of fluorophore combinations for multi-color imaging of difficult-to-access or densely packed samples or under physiological conditions and in living cells remains challenging [3–5]. Especially in live-cell applications the choice of suitable fluorophore pairs is limited: apart from a small number of membrane-permeable, fluorescent dyes, which photoswitch in cellular environments without the need of further imaging buffers (e.g., tetramethylrhodamine (TMR) or Atto655 [3] or the recently developed paJF549 [6]), the most popular fluorophores are genetically encoded, photoactivatable or photoconvertible fluorescent proteins (pa- and pcFPs) like the widespread Anthozoan green-to-red pcFPs (e.g., the Eos, Dendra, Maple and Dronpa families) and DsRed derived dark-to-red paFPs (e.g., PAmCherry, PAmKate and

PAtagRFPs) [1,4,5,7]. Despite being popular in quantitative imaging and single-particle tracking approaches [2,5,8], the simultaneous use of multiple pcFPs and paFPs is largely precluded by their overlapping absorption and emission spectra: they are photoactivated/-converted by illumination in the near UV light range and a vast majority of common FPs with desirable properties (being bright and monomeric, exhibiting robust photophysics in varying redox-environment and a quantitative read-out [1,4,5]) emit fluorescence in a narrow, orange-red emission channel with only a few alternative FPs in other color channels, e.g., the green fluorescing paGFP [9], psCFP2 and Dronpa [10], or the red fluorescing psmOrange [11], which have been used for dual-color SMLM.

By utilizing the recently developed photoconversion technique of primed conversion (PC) for green-to-red pcFPs, we here introduce a new dual-color strategy. PC, which was first identified and characterized for Dendra2 [12,13] and has recently been shown to be very efficient for green-to-red pcFPs with threonine at residue 69, makes use of a combined illumination of 488 nm and near-infrared light in the range 700–800 nm instead of the common UV-photoconversion to convert common pcFPs from their green to their red form [12,14]. paFPs, on the other hand, only absorb light in the ultraviolet range prior to activation. As such, the 488 nm light used for PC should have no effect on the paFP. We propose that this fact could be advantageously exploited in a dual-phase, dual-color imaging scheme with a single fluorescence read-out channel. First, a PC-suitable pcFP, e.g., Dendra2 [12–15] or mEos3.2-A69T [14], is imaged using a combination of 488 and 730 nm light for photoconversion. After all pcFPs have been read out, the still-intact paFP, e.g., the commonly used PAmCherry [16], can be imaged in the second phase by UV-light mediated photoactivation. The benefits of such an approach are substantial. Since both targets are imaged in the same channel, chromatic aberration is eliminated. Both FP-tags can be endogenous, requiring no additional staining, and the above chosen FPs are bright and show no oligomerization tendencies [17]. In addition, as they fluoresce with a maximum in the 570–590 nm range upon 561 nm illumination, possible auto-fluorescence of biological samples and phototoxicity are reduced when compared to techniques using shorter wavelength channels [14,18]. This makes this labeling choice favorable compared to other, e.g., non-red, less bright and photostable or potentially self-oligomerizing pcFPs and paFPs such as paGFP [9,19], psCFP2 and Dronpa [10] or PAtagRFP [20] and PAmKate [7]. Finally, our strategy works hand in hand with existing, multi-channel approaches and can be easily used to expand them.

## 2. Results and Discussion

To evaluate the viability of the proposed imaging scheme, two main concerns had to be addressed. First, does PC illumination have any effect on the paFP? Second, is it possible to sufficiently eliminate the pcFP imaged by PC to not cause any cross-talk during the second imaging phase as any residual, non-converted pcFP molecule would also be read-out by UV light. To test this, we performed experiments on fixed *Escherichia coli* cells, where the native RNA polymerase (RNAP) protein was endogenously tagged with either Dendra2 or PAmCherry (Supplementary Material and Methods). RNAP molecules appear in large nucleoid-like patterns as they decorate the bacterial chromosome. Their numbers per unit of cell size are relatively stable when expressed under the native promoter, making RNAP a satisfactory target for quantitative controls [21].

First, we determined the minimum dose of 488 nm light required to permanently bleach all Dendra2-RNAP molecules in the *E. coli* cells (Figure S1a). A bleaching approach like this would be necessary in a worst-case scenario, where full readout of the PC-suitable pcFP is not feasible, e.g., in cases where the POI is highly abundant. We then evaluated the effect of this high 488 nm dose on the PAmCherry molecules (Figure S1a). While the vast majority of the Dendra2-RNAP read-out in the red channel was gone after 30 s of illumination with 1 kW/cm$^2$ of 488 nm light, we used 120 s for subsequent imaging since that is where the bleaching curve stabilized. Using the same settings, we found that 488 nm illumination slightly increased the fluorescence intensity in cells with PAmCherry-tagged RNAP, suggesting some minor activation (Figure S1a). With this information we were able to design a worst-case scenario control imaging scheme (Figure S1b, left). To quantify the loss of PAmCherry during the first, PC-photoconversion stage of imaging and potential bleed-through of Dendra2 into the second UV-photoactivation phase, we performed localization counting on *E. coli* cells expressing RNAP-Dendra2 and RNAP-PAmCherry under several different illumination schemes (Figure S1b, right). RNAP-Dendra2 produced a mean of 1092 ± 175 (standard deviation) localization counts/$\mu m^2$ converted by primed conversion (I) and a mean of 999 ± 131 localization counts/$\mu m^2$ (II) by UV photoconversion which is in agreement with previous results on RNAP numbers [21,22] and reconfirms data of a recent study which did not show any differences in quality and quantitative numbers obtained in sptPALM tracking studies comparing UV and PC photoconversion of Dendra2 [14]. After 120 s of bleaching with 1 kW/$cm^2$ 488 nm light, Dendra2 was activated by UV conversion and produced 54 ± 18 localization counts/$\mu m^2$ (III), which is at the level of false positive localization counts in wild type *E. coli* (data not shown), confirming that little to no Dendra2 survives the bleaching step. Next, we evaluated the UV readout of RNAP-PAmCherry, resulting in 1054 ± 217 counts/$\mu m^2$ (IV), which is comparable to the Dendra2 PC readout. To test the effects of high intensity 488 nm light on PAmCherry, RNAP-PAmCherry expressing cells were illuminated with the same high intensity of 1 kW/$cm^2$ 488 nm light for 120 s, and then read out with UV activation, producing 916 ± 182 counts/$\mu m^2$ (V), further suggesting that 488 nm light activates PAmCherry with low efficiency. This, however, proved not to be an issue during the conversion imaging phase, where the overall dosage of 488 nm light is much lower (less than 0.1% of the bleaching dose of 1 kW/$cm^2$ used in this experiment). PAmCherry read out by PC activation, produced 45 ± 19 counts/$\mu m^2$ (VI), again at the level of background in wild type *E. coli*. To eliminate cross-talk, we thus implemented a brief, ~10 s pre-bleaching step with the 561 nm light readout laser before reading out the PAmCherry, bleaching away any pre-activated FP. These findings suggest that if the FP in the first phase of imaging is read out in full and a high intensity 488 nm post-bleaching step is not required, loss of PAmCherry is completely negligible. In such a case, both phases allow for a full quantitative SMLM readout.

Encouraged by the promising results of the controls, we decided to evaluate how well our approach performs in dual-color imaging of different biomolecules in *E. coli* and in a second step, how well it integrates with additional correlative imaging schemes such as membrane point accumulation for imaging of nanoscale topography (PAINT) and DNA stains [23]. To test this, we utilized the imaging scheme on an *E. coli* strain where RNAP was endogenously tagged with the PC-suitable mEos3.2-A69T mutant and transformed with the pJB063 plasmid bearing the sequence for FtsZ-PAmCherry. The green-to-red pcFP mEos3.2-A69T mutant has proven, like Dendra2, to be an excellent candidate for tagging native proteins in our previous work but with a 15–20% higher photoncount for single-molecule-spots than Dendra2—thus allowing for more precise sptPALM data [14]. RNAP-mEos3.2-A69T was imaged first and read out in full (Figure 1a), followed by a full readout of FtsZ-PAmCherry (Figure 1b). Nile-red was then added to the imaging solution to image the membrane by PAINT [24] (Figure 1c) and was finally replaced with a Sytox orange containing solution, to stain the DNA (Figure 1d), for a total of four effective colors all in the orange-red channel (Figure 1e).

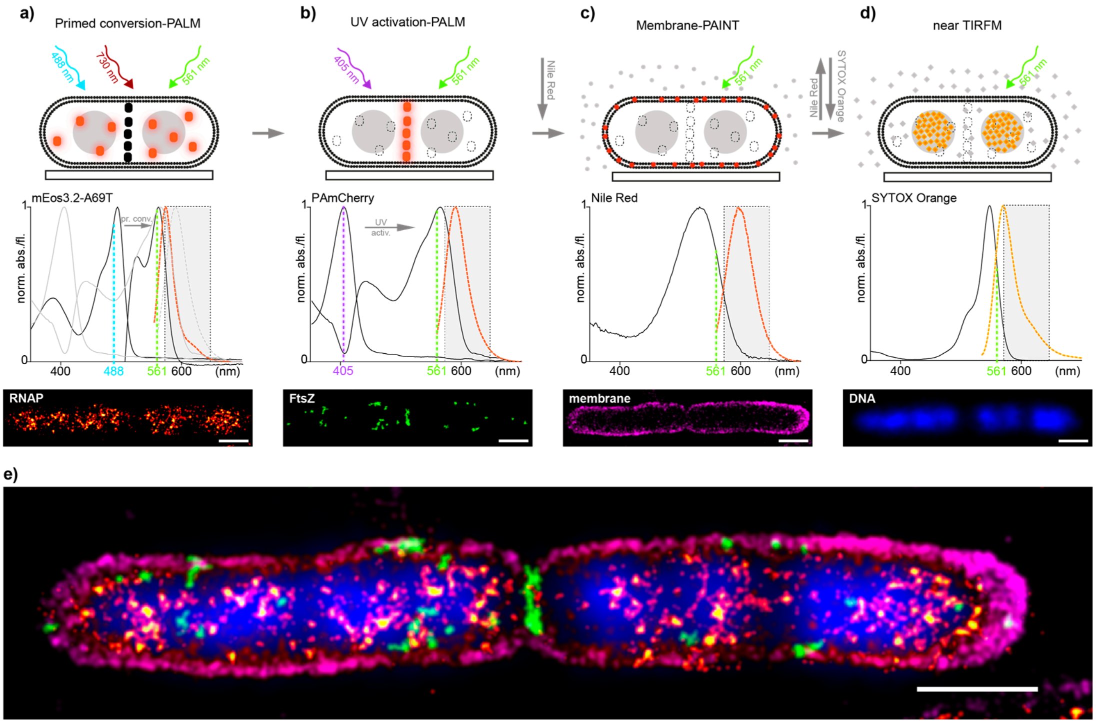

**Figure 1.** (**a**–**d**) Multi-color imaging workflow in *E. coli* cells. Top: scheme representing the acquisition sequence by first imaging RNAP-mEos3.2-A69T (orange dots) by primed conversion-PALM, not activated FtsZ-PAmCherry molecules are depicted as black dots (**a**); FtsZ-PAmCherry (orange dots) by UV activation-PALM, permanently bleached RNAP-mEos3.2-A69T are presented as dashed-lined white dots (**b**); The outer membrane by PAINT using NileRed- red dots depict fluorescent fraction of NileRed molecules in the membrane, whereas gray dots represent non-fluorescent NileRed in buffer/medium (**c**) and last the DNA stained by SYTOX Orange (orange diamonds) and read-out by near TIRF microscopy (**d**). Middle: Measured absorption and emission spectra of all four fluorophores used (Supplementary Material and Methods). Dashed line rectangle represents the optical bandpass-filter used to visualize the fluorescence channel of all four acquisitions. Bottom: SMLM image reconstructions (**a**–**c**) and nearTIRF-snapshot (**d**) recorded; (**e**) Overlay of all individual images to show the mutual organization of imaged compounds, aligned by fiducial markers (Supplementary Material and Methods). Localization precision of the channels after drift correction (whole ROI, NeNA values): mEos3.2-A69T (RNAP) 12.1 nm, PamCherry (FtsZ) 12.3 nm, NileRed (membrane) 11.8 nm, scale bars: 1 µm.

Next, we assessed how well the technique performs on larger samples in other organisms by imaging HeLa cells transiently transfected with a combination of an actin-PAmCherry plasmid together with either a keratin-Dendra2 plasmid (Figure 2a) or an H2B-Dendra2 plasmid (Figure 2b), details can be found in Supplementary Material and Methods. As before, the pcFP, Dendra2, was read out first. Due to the large size of the cell and large number of (overexpressed) molecules a full read-out was rather time consuming, thus we decided to bleach the residual Dendra2 molecules after obtaining a sufficient number of localizations for image reconstruction. The intensity of 488 nm bleaching step had to be increased to 4 kW/cm$^2$ in order to fully bleach the residual Dendra2 molecules above and below the imaging plane. No visible cross talk was present on any of the images, as showcased by the dark background around the H2B (Figure 2b(v)).

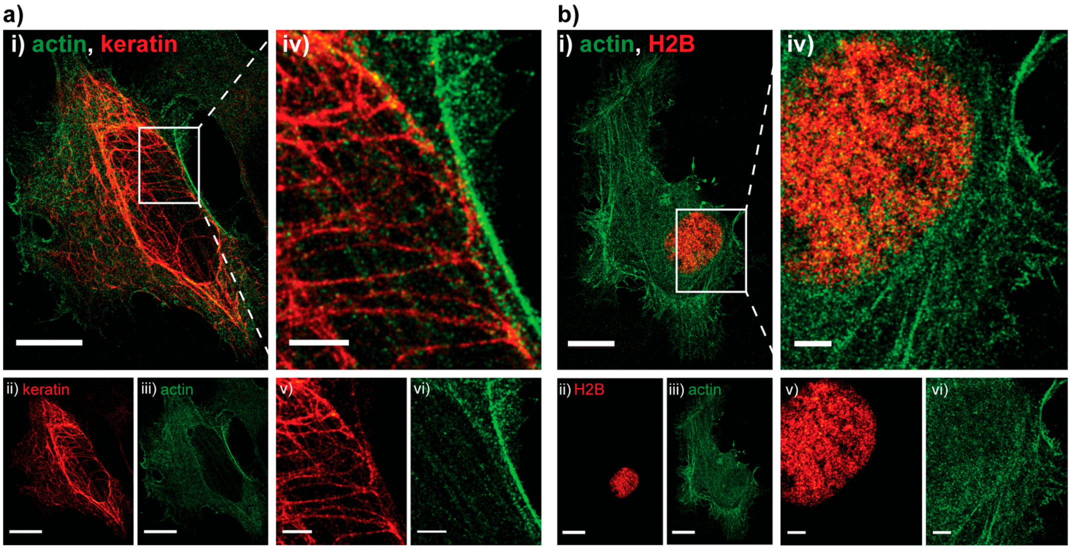

**Figure 2.** Two examples of Hela cells imaged with sequential PC activation. (**a**): (**i**) Dual-color PALM image of actin tagged with PamCherry (green) and keratin tagged with Dendra2 (red); (**ii**,**iii**) split channel PALM images of the same cell. Localization precision of the channels after drift correction (whole ROI, NeNA values): Dendra2 (red, keratin) 17.2 nm, PamCherry (green, actin) 17.4 nm, scale bars 5 µm; (**iv**–**vi**) zoom in on an area with details only visible in the super resolved image, scale bars 2 µm; (**b**): (**i**) Dual-color PALM image of actin tagged with PAmCherry (green) and H2B tagged with Dendra2 (red) and split channel images of the same cell (**ii**,**iii**). Localization precision of the channels after drift correction (whole ROI, NeNA values): Dendra2 (red, H2B) 16.1 nm, PamCherry (green, actin) 18.9 nm, scale bars 5 µm; (**iv**–**vi**) zoom in on the nucleus, showcasing the absence of bleed through (dark background on (**vi**)), scale bars 2 µm.

A major advantage of the approach is its potential for use in living cells, especially for targets which are difficult-to-reach by extrinsic fluorescent markers or have precluded SMLM read-out channels due to low signal-to-noise/high background, e.g., arising from intracellular autofluorescence. Like all (sequential) SMLM techniques, our approach is limited by the temporal resolution needed for structural studies of abundant proteins but offers the read-out of two different proteins by intrinsic FP labels with excellent SMLM properties to measure their molecule dynamics within the same compartment or cell [25].

We thus first tested our *E. coli* strain under live conditions (Figure S2a), measuring diffusion dynamics for RNAP and FtsZ (Figure S2b,c) as reported before [14,26] and could confirm the cell survival after sptPALM imaging [14] (Figure S2d).

We then challenged our approach by creating a strain of the fission yeast *Schizosaccharomyces pombe*, where the DNA binding protein cbp1 and the centromeric histone variant protein cnp1 were endogenously tagged with Dendra2 and PAmCherry, respectively (Supplementary Material and Methods). Introducing fluorophores for live cell SMLM imaging into *S. pombe* is difficult. In our hands, only few extrinsic labels can be delivered to protein-tag-fusions but are prone to unspecific background staining due to the cell wall and dense intracellular environment and do not blink in the intracellular living yeast environment (unpublished data). Additionally, dual-color SMLM imaging including a green FP does not provide satisfactory single molecule signal above the intracellular background (unpublished data). Thus, even most recent SMLM studies of living *S. pombe* have remained exclusively single-color using mEos2/mEos3 [27,28] which is in contrast to mammalian cell studies, where multi-color SMLM introducing dye molecules that blink in the intracellular environment has been applied in various studies [1,3].

As in *E. coli*, control measurements characterizing the viability of our living cells revealed no negative effect of our imaging approach on the cellular growth (Figure S3a–d). As before, Dendra2 was read out first, with lower 561 nm readout laser intensities and shorter exposure times, to capture the movement of single molecules (Figure 3a,b(i)). PAmCherry-cnp1 was successfully read out in the second phase, with no apparent crosstalk (Figure 3a,b(ii)). The cells were then fixed and stained with DAPI (Figure 3a,b(iii)), since Sytox Orange penetrated the thick yeast cell wall poorly in our hands (data not shown). As expected, reconstructed PALM images showed cbp1 is present throughout the nucleus and co-localizes with DNA, while cnp1 appears as a single centromeric spot at the edge of the DNA (Figure 3a,b(iv)). We then applied a custom single particle tracking algorithm on the same data and visualized the results (details in materials and methods), which showed that the cbp1 diffuses around the nucleus, while the cnp1 is largely immobile (Figure 3a(v)). Finally, we calculated diffusion coefficients for tracks longer than four consecutive frames, revealing a mobile (fast) and an immobile (slow) fraction of cbp1 (Figure 3b(iv)) and exemplary mean squared displacement (MSD)-curves in Figure S4a). Imaging fixed cbp1 molecules as a control under otherwise same conditions reveals that the slow fraction is indeed not moving within the precision of the sptPALM measurements and represents immobile, DNA-bound cbp1 molecules whereas the fraction of mobile cbp1 with a more heterogeneous distribution of diffusion coefficients represents DNA-associated, but mobile cbp1 molecules (Figure S4b(i,ii)) [29,30].

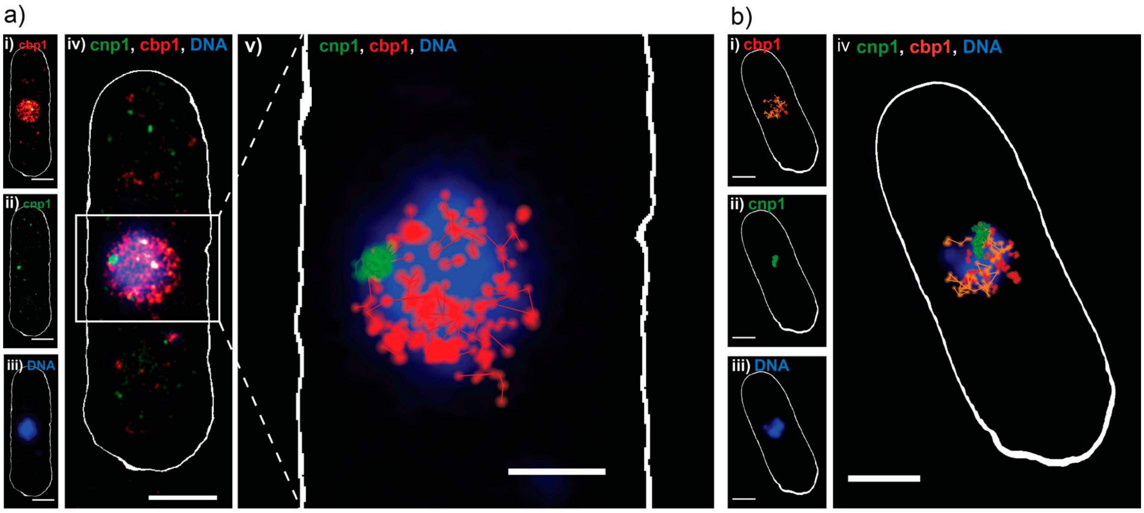

**Figure 3.** Sequential dual-color PALM on *S. pombe*. (**a**) Dual-color PALM image of a representative *S. pombe* cell, expressing the DNA binding protein cbp1 tagged with Dendra2 (red) and the centromeric protein cnp1 tagged with PAmCherry (green) and a widefield fluorescence image of DAPI stained DNA (blue): (**i**–**iii**) Split channels of the same cell and (**iv**) combined; (**v**) single particle track analysis performed on the same data, with tracks $\geq$3 consecutive frames represented in red (cbp1) and green (cnp1), on top of DNA (blue). Scale bars 2 μm; (**b**) single particle tracking analysis done on a different *S. pombe* cell: (**i**) single particle tracks of cbp1 $\geq$4 consecutive frames, color coded for their apparent diffusion coefficient D as calculated from a MSD analysis of the individual tracks, orange for fast moving particles ($D > 0.26\ \mu m^2/s$) and red for slow or immobile ($D < 0.26\ \mu m^2/s$); (**ii**) single particle tracks of cnp1 $\geq$ 4 consecutive frames; (**iii**) widefield fluorescence image of DNA in the same cell, after fixation; (**iv**) overlay of all three channels. Scale bars 2 μm.

## 3. Materials and Methods

Strain constructions for *E. coli* and *S. pombe* cell lines, transient transformations for mammalian samples, protein purification, live and fixed cell sample preparations for *E. coli*, *S. pombe* and mammalian cells as well as the microscopic and spectroscopic equipment are described in detail in the Supplementary Information (Supplementary Material and Methods).

### *3.1. Imaging Procedures*

#### 3.1.1. Influence of High Intensity of 488 nm Light on PAmCherry and Dendra2

To determine, whether high intensity of 488 nm light leads to irreversible bleaching of Dendra2 molecules while leaving PAmCherry intact, we imaged fixed MG1655 rpoC_Dendra2 and MG1655 rpoC_PAmCherry cells. First, cells were illuminated with 1 kW/cm$^2$ of 488 nm for 0 to 180 s (Figure S1a) and then illuminated for 15 s with 2.5 W/cm$^2$ of 405 nm light to perform photoactivation or photoconversion of non-bleached fluorescent proteins. In last step, three 60 ms frame snapshots with 800 W/cm$^2$ of the 561 nm laser were taken.

#### 3.1.2. Quantitative Controls-RNAP Molecule Counting

To evaluate possible false positives of residual Dendra2 and the amount of pre-activated PAmCherry of the second phase of imaging (Dendra2 converted via UV light or PAmCherry preactivated via 488 nm light), a set of control experiments was performed (Figure S1b). In experiment (I) fixed MG1655 RNAP-Dendra2 cells were illuminated with three lasers: 488 nm pulsed every 20th frame and continuous 561 and 730 nm. Laser intensities were: 100–2500 mW/cm$^2$ of 488 nm (intensity was gradually increased during movie acquisition to keep the number of detected spots roughly on the same level), 800 W/cm$^2$ of 561 nm and 450 W/cm$^2$ of 730 nm. Movies were recorded at 16.67 Hz image acquisition (60 ms per frame) until no new fluorescent spots appeared to ensure for a full read-out of the FP. In experiment (II), MG1655 RNAP-Dendra2 was illuminated by conventional UV-conversion PALM: The 405 nm laser was pulsed every 20th frame, gradually increasing the intensity from 250–6500 mW/cm$^2$ and continuous 561 nm laser at a constant intensity of 800 W/cm$^2$. The field of view (FOV) was imaged until no new fluorescent spots appeared anymore. As a negative control (III), MG1655 RNAP-Dendra2 was first illuminated for two minutes with 1 kW/cm$^2$ of 488 nm laser to irreversibly bleach the Dendra2 molecules. Next, the same FOV was imaged with standard UV-conversion PALM. Laser intensities were the same as for (II). The FOV was imaged for 5 min with 60 ms exposure time per frame. Experiments (IV)–(VI) were performed on the MG1655 RNAP-PAmCherry strain. Experiment (IV) was a positive control where cells were imaged with UV-conversion PALM: 405 and 561 nm laser settings were the same as for experiment (II) and the FOV was imaged until no new spots appeared. In experiment (V) MG1655 RNAP-PAmCherry cells were imaged in a similar way as cells in experiment (III) with an extended imaging time until no new spots appeared, achieving full read-out. In experiment (VI) which serves as negative control, cells were imaged as the MG1655 RNAP-Dendra2 cells in experiment (I), to evaluate the activation of PAmCherry via primed conversion. FOV was imaged for 5 min. For each control experiment two FOVs were imaged.

#### 3.1.3. *E. coli* Multi-Color Imaging

Detection of RNA polymerase (RNAP) fused with mEos3.2-A69T, FtsZ fused with PAmCherry, bacterial membrane and chromosomal DNA in fixed MG1655 rpoC_mEos3.2-A69T+pJB063 cells was performed sequentially (Figure 1). First, RNAP-mEos3.2-A69T molecules were imaged by primed conversion [14] (Figure 1a). Briefly, the sample was illuminated with three lasers: 488 nm pulsed every 20th frame and continuous 561 and 730 nm light. Laser intensities were: 100–2500 mW/cm$^2$ of 488 nm (intensity was gradually increased during movie acquisition), 800 W/cm$^2$ of 561 nm and 450 W/cm$^2$ of 730 nm. Movies were recorded at 16.67 Hz image acquisition (60 ms per frame) until no new spots appeared. After primed conversion PALM, the sample was illuminated for one minute with 1 kW/cm$^2$ of 488 nm laser to irreversibly bleach residual green form mEos3.2-A69T. In the second phase (Figure 1b) FtsZ-PAmCherry molecules were detected with UV-activation PALM: 405 nm laser pulsed every 20th frame (intensity gradually increasing from 250–6500 mW/cm$^2$) and continuous 800 W/cm$^2$ 561 nm laser at 60 ms until all PAmCherry was read out. After finishing imaging both, RNAP-mEos3.2-A69T and FtsZ-PAmCherry, Nile Red (Sigma-Aldrich, Darmstadt, Germany) was added (final concentration in imaging buffer: 7 nM) to visualize the bacterial membrane in the same cells by PAINT microscopy [24] (Figure 1c). Movies were recorded for 7 min with 60 ms exposure time per frame and the sample was illuminated with constant 1.2 kW/cm$^2$ of 561 nm laser. In the last, fourth step (Figure 1d), chromosomal DNA was visualized by addition of SYTOX Orange (Thermo Fischer, Darmstadt, Germany) to a final concentration 20 nM. One-frame 60 ms snapshots were taken with low intensity 561 nm laser (10 W/cm$^2$). For all fixed bacteria images, the Nearest Neighbor Analysis (NeNA) values [31] were in the range of 10–15 nm, exact values of the exemplary images are given in the respective captions.

Single-particle tracking PALM (sptPALM) imaging (Figure S2) of rpoC_mEos3.2-A69T+pJB063 cells was performed on a heating stage and heated objective at 32 °C. As for the fixed samples, RNAP-mEos3.2-A69T was imaged first and FtsZ-PAmCherry was imaged afterwards. Applied laser intensities were: 2 W/cm$^2$ of 405 nm, 600 mW/cm$^2$ of 488 nm, 450 W/cm$^2$ of 730 nm and 800 W/cm$^2$ of 561 nm laser light. 405 and 488 nm lasers were pulsed every 20th frame. Movies were recorded at 77 Hz image acquisition rate for two minutes to follow the diffusing RNA polymerase and at 33 Hz image acquisition rate for five minutes to follow the FtsZ protein. For the FtsZ imaging we used slower acquisition mode to exclude cytosolic FtsZ molecules—as they diffuse much faster than FtsZ built into the ring structures, their point-spread functions are blurred, thus most of the cytosolic FtsZ molecules are not included in further analysis steps. This approach was first used by Etheridge et al. in their work [32]. mEos3.2-A69T molecules were converted by primed conversion, while PAmCherry was photoactivated using UV. Right after recording the RNAP-mEos3.2-A69T molecules, a two minute bleaching step to bleach the remaining unconverted mEos3.2-A69T molecules was performed using 1 kW/cm$^2$ 488 nm laser light illumination to avoid false positives during the FtsZ-PAmCherry readout. After sptPALM imaging, the cells of the imaged FOVs were tested for their cell viability. For this, all FOVs were imaged under bright light for three hours with two minutes interval to quantify their cellular growth after the sptPALM experiment.

### 3.1.4. HeLa Dual-Color Imaging

Keratin-Dendra2 or H2B-Dendra2 were imaged first, activated with 450 W/cm$^2$ of the 730 nm laser and 100–2500 mW/cm$^2$ of the 488 nm laser (pulsed every 20th frame) with the intensity gradually increased to keep the number of localizations per frame constant and read out with the 561 (800 W/cm$^2$) laser for 20 thousand frames at an exposure of 60 ms per frame. The sample was then illuminated with 4 kW/cm$^2$ of the 488 nm laser for 2 min, to bleach any residual Dendra2. Actin-PAmCherry was imaged second, activated with the 405 nm laser, pulsed on every 12th frame, with the intensity gradually adjusted from 250–6500 mW/cm$^2$ and read out with constant 561 illumination at 800 W/cm$^2$ for 10 to 20 thousand frames at an exposure time of 60 ms per frame. Lasers were angled to achieve near-TIRF illumination. For all mammalian images, the NeNA values were in the range of 15–20 nm, exact values of the exemplary images are given in the respective captions.

### 3.1.5. *S. pombe* Multi-Color Imaging

Cbp1-Dendra2 was imaged first, activated with 450 W/cm$^2$ of the 730 nm laser and 100–2500 mW/cm$^2$ of the 488 nm laser (pulsed every 20th frame) with the intensity gradually increased to keep the number of localizations per frame constant and read out with the 561 (500 W/cm$^2$) laser for 20 thousand frames at an exposure of 20 ms per frame. The sample was then illuminated with 2 kW/cm$^2$ of the 488 nm laser for 1 min, to bleach any residual Dendra2. Cnp1-PAmCherry was imaged second, activated with the 405 laser, pulsed on every 12th frame, with the intensity gradually adjusted from 250–6500 mW/cm$^2$ and read out with constant 561 illumination at 500 W/cm$^2$ for 10 thousand frames at an exposure time of 20 ms per frame. Finally, cells were fixed with 1% paraformaldehyde (Sigma-Aldrich, F8775) without moving the sample and stained for DNA with 1 µg/mL DAPI, read out by the 405 nm laser (10 W/cm$^2$).

### 3.1.6. Viability Controls

*S. pombe* cbp1-Dendra2 cnp1-PAmCherry cells were grown in YES medium at 25 °C overnight, then inoculated into fresh YES to a starting $OD_{600}$ of 0.1 and grown for ~6 h before imaging. 1 mL of culture was spun down at 500× *g* for 5 min and resuspended in 10 µL fresh YES medium. Cells were immobilized on a 1% low-gelling temperature agarose pad (Sigma-Aldrich, A9414) in YES medium and covered with a coverslip previously cleaned with Hellmanex. Cells were imaged on a custom-built heating stage at 30 °C. To compare growth, 8 FOVs at least 1000 µm apart were chosen and bright field images were taken at time $t_0$. The first two FOVs were imaged with PC activation 450 W/cm$^2$ of the 730 nm laser and 100–2500 mW/cm$^2$ of the 488 nm laser (pulsed every 20th frame) with the intensity gradually increased to keep the number of localizations per frame constant and read out with the 561 (500 W/cm$^2$) laser for 20 thousand frames at an exposure of 15 ms per frame. The next two FOVs were imaged with the same conditions but also post-bleached with 2 kW/cm$^2$ of the 488 nm laser for 2 min. Two further FOVs were then imaged and post-bleached as described above, then also imaged with UV activation, 405 laser pulsed on every 12th frame, with the intensity gradually adjusted from 250–6500 mW/cm$^2$ and read out with constant 561 illumination at 500 W/cm$^2$ for 5 thousand frames at an exposure time of 30 ms per frame. A bright field of each position was taken every 10 min for 12 h after imaging with an automated µManager script, though FOVs were lost after ~4 h due to drift. Exemplary cells are depicted in Figure S3.

## 3.2. Data Analysis

### 3.2.1. Analysis of the Influence of High Intensity 488 nm Images

Acquired three-frame snapshots were analyzed with a custom written script in *Fiji software (ImageJ 1.51f)* [33]. Cell FOVs were extracted by identifying individual bacterial shapes from fluorescence averages excluding overlapping or out-of-focus cells. Averaged fluorescence intensity for each cell was used as a parameter of bleaching degree (Figure S1b).

### 3.2.2. Super-Resolution Image Reconstruction of Bacterial and Mammalian Multi-Color Images

Localizations of the fitted single fluorescent spots were obtained by the open source software *rapidSTORM* (version 3.3) [34]. Fitting parameters were determined individually for each kind of fluorophore (Dendra2, mEos3.2-A69T, PAmCherry and Nile Red). In the next step, localization precision for all FOVs was estimated using NeNA [31] as implemented in the open-source software *LAMA* (version 16.10) [35] on a section of the image that contained no fiducial markers. For all FOVs localization precision was determined between 10 and 15 nm for bacteria and 15 and 20 nm for mammalian cells. Localization data were filtered to connect neighboring localizations in adjacent frames, to avoid several-fold counting of molecules with fluorescence lifetimes exceeding the framerate of the movie. In the last post-processing step, all localization files were drift corrected with custom written *Python* algorithms that extract and correct for fluorescent bead trajectories. Additionally, for FtsZ-PAmCherry localizations, density based clustering analysis was performed with the density-based spatial clustering of applications with noise (DBSCAN) algorithm [36], as single cytosolic FtsZ-PAmCherry proteins were abundantly present in cell. Only clustered molecules (DBSCAN parameters: $\varepsilon$ = 35 nm; MinPts = 10) were used for image reconstruction of FtsZ-PAmCherry. Super-resolution image reconstructions and DNA-Sytox Orange image were stacked and superimposed in *Fiji* software. For HeLa cells, images were reconstructed with a pixel size of 20 nm.

### 3.2.3. Single Particle Tracking in *E. coli* and *S. pombe*

Single molecule localizations were extracted from the movies with the open-source software *rapidSTORM*. Final images were reconstructed with a pixel size of 10 nm. Single particles were tracked with the help of customized tracking software written in C++ and visualized by customized software written in C++, to filter and group single molecule localizations or trajectories by their apparent diffusion coefficient (as calculated by MSD analysis). For MSD analysis, only trajectories with 4 and more steps were used for calculating the MSD values. Independent of the total length of each trajectory, only the first steps of each trajectory were used for the MSD calculation (for the first 3 $\Delta t$ values) to account for heterogeneous diffusion behavior over time as well as the confinement of the yeast nucleus/*E. coli* cell. To account for the localization precision $\sigma$ of the data, the constant offset of $4{*}\sigma^2$ was included into the fit-function. For diffusion coefficient statistics, only MSD fits with an $R^2$ value of 0.85 or higher were used.

## 4. Summary and Conclusions

In summary, our new technique produced high quality PALM images on all tested samples. The controls showed there is little to no crosstalk between the two proteins and loss of PAmCherry is minimal. This can be further reduced by avoiding the post-bleaching step with high intensity of 488 nm light, by reading out the entire signal in the first phase of imaging and, for fixed cells, by increasing the pH to 8–8.5 where PC is most efficient [14]—making both phases of imaging fully quantitative. We have also shown that the approach is easily combined with other sequential imaging techniques, such as membrane PAINT. This correlative approach could be extended further, by e.g., substituting the Sytox Orange DNA stain for the transiently binding Hoechst-JF646 probe for DNA-PAINT [37].

Perhaps most importantly, the combination of a PC-suitable pcFP and an only UV-activatable paFP allows for dual-color SMLM imaging in living specimens, without the need for any additional staining steps, as shown in *E. coli* and *S. pombe*. Previously, this could only be done through the use of proteins with different emission spectra, such as paGFP or psCFP2. This requires imaging in different readout channels, introducing chromatic aberration, which makes overlaying the channels more difficult. Additionally, many biological samples, e.g., including *S. pombe*, can exhibit high degrees of autofluorescence in the GFP channel. Combined with the lower brightness of paGFP and psCFP2 compared to red paFPs, this results in a limited achievable resolution. Also, the superior brightness of FPs such as Dendra2, mEos3.2-A69T and PAmCherry allows for single particle tracking experiments, where brightness is essential due to shorter exposure times and lower excitation light intensities. That being said, our approach could potentially be combined with other FPs that emit in different channels, further expanding the palette of available colors for live-cell imaging or be used in tandem with enzyme tags such as Halo-tag [38] and SNAP-tag [39] together with membrane-permeable dyes (and e.g., as well using sequential orange stainings like TMR and paJF549).

In conclusion, our measurements demonstrate that this new method can be applied to various targets in different organisms and can be advantageously combined with existing imaging schemes. As it is an aberration-free, live-cell compatible method, which is simple to implement on conventional SMLM systems (even when using a red instead of an infrared laser source, PC can be efficient enough for SMLM imaging [13,14]), we believe it is a valuable addition to the current SMLM toolbox.

**Supplementary Materials:** Supplementary materials can be found at www.mdpi.com/1422-0067/18/7/1524/s1.

**Acknowledgments:** We thank Matthias Plessner, Institute of Pharmacology, Marburg, for the transient transfections of the Hela cells and Ilijana Vojnovic, MPI Marburg for her help with the cell culture during the revision of the manuscript. We further thank Jie Xiao, John Hopkins, Baltimore, USA, for kindly sharing their FtsZ-PAmCherry-plasmid pJB063. This work was funded by the Max Planck Society, SYNMIKRO and the Fonds der Chemischen Industrie.

**Author Contributions:** Ulrike Endesfelder and David Virant conceived the idea; Ulrike Endesfelder, David Virant, Alexander Balinovic and Bartosz Turkowyd designed the experiments; David Virant, Alexander Balinovic and Bartosz Turkowyd performed the experiments and analyzed the data; Ulrike Endesfelder and David Virant wrote the paper with the help of all authors.

**Conflicts of Interest:** The authors declare no conflict of interest.

## Abbreviations

| | |
|---|---|
| FP | Fluorescent protein |
| paFP | Photoactivatable fluorescent protein |
| PAINT | Points accumulation for imaging in nanoscale topography |
| PALM | Photoactivated localization microscopy |
| PC | Primed conversion |
| pcFP | Photoconvertible fluorescent protein |
| SMLM | Single molecule localization microscopy |

## References

1. Turkowyd, B.; Virant, D.; Endesfelder, U. From single molecules to life: Microscopy at the nanoscale. *Anal. Bioanal. Chem.* **2016**, *408*, 6885–6911. [CrossRef] [PubMed]
2. Nicovich, P.R.; Owen, D.M.; Gaus, K. Turning single-molecule localization microscopy into a quantitative bioanalytical tool. *Nat. Protoc.* **2017**, *12*, 453–460. [CrossRef] [PubMed]
3. Sauer, M.; Heilemann, M. Single-molecule localization microscopy in eukaryotes. *Chem. Rev.* **2017**, *117*, 7478–7509. [CrossRef] [PubMed]
4. Nienhaus, K.; Nienhaus, G.U. Fluorescent proteins for live-cell imaging with super-resolution. *Chem. Soc. Rev.* **2014**, *43*, 1088–1106. [CrossRef] [PubMed]
5. Shcherbakova, D.M.; Sengupta, P.; Lippincott-Schwartz, J.; Verkhusha, V.V. Photocontrollable fluorescent proteins for superresolution imaging. *Annu. Rev. Biophys.* **2014**, *43*, 303–329. [CrossRef] [PubMed]
6. Grimm, J.B.; English, B.P.; Choi, H.; Muthusamy, A.K.; Mehl, B.P.; Dong, P.; Brown, T.A.; Lippincott-Schwartz, J.; Liu, Z.; Lionnet, T.; et al. Bright photoactivatable fluorophores for single-molecule imaging. *Nat. Methods* **2016**, *13*, 985–988. [CrossRef] [PubMed]
7. Gunewardene, M.S.; Subach, F.V.; Gould, T.J.; Penoncello, G.P.; Gudheti, M.V.; Verkhusha, V.V.; Hess, S.T. Superresolution imaging of multiple fluorescent proteins with highly overlapping emission spectra in living cells. *Biophys. J.* **2011**, *101*, 1522–1528. [CrossRef] [PubMed]
8. Gahlmann, A.; Moerner, W.E. Exploring bacterial cell biology with single-molecule tracking and super-resolution imaging. *Nat. Rev. Microbiol.* **2014**, *12*, 9–22. [CrossRef] [PubMed]
9. Wilmes, S.; Staufenbiel, M.; Lisse, D.; Richter, C.P.; Beutel, O.; Busch, K.B.; Hess, S.T.; Piehler, J. Triple-color super-resolution imaging of live cells: Resolving submicroscopic receptor organization in the plasma membrane. *Angew. Chem.* **2012**, *51*, 4868–4871. [CrossRef] [PubMed]
10. Shroff, H.; Galbraith, C.G.; Galbraith, J.A.; White, H.; Gillette, J.; Olenych, S.; Davidson, M.W.; Betzig, E. Dual-color superresolution imaging of genetically expressed probes within individual adhesion complexes. *Proc. Natl. Acad. Sci. USA* **2007**, *104*, 20308–20313. [CrossRef] [PubMed]
11. Nahmani, M.; Lanahan, C.; DeRosier, D.; Turrigiano, G.G. High-numerical-aperture cryogenic light microscopy for increased precision of superresolution reconstructions. *Proc. Natl. Acad. Sci. USA.* **2017**, *114*, 3832–3836. [CrossRef] [PubMed]
12. Dempsey, W.P.; Georgieva, L.; Helbling, P.M.; Sonay, A.Y.; Truong, T.V.; Haffner, M.; Pantazis, P. In vivo single-cell labeling by confined primed conversion. *Nat. Methods* **2015**, *12*, 645–648. [CrossRef] [PubMed]
13. Klementieva, N.V.; Lukyanov, K.A.; Markina, N.M.; Lukyanov, S.A.; Zagaynova, E.V.; Mishin, A.S. Green-to-red primed conversion of dendra2 using blue and red lasers. *Chem. Commun.* **2016**, *52*, 13144–13146. [CrossRef] [PubMed]
14. Turkowyd, B.; Balinovic, A.; Virant, D.; Golz Carnero, H.G.; Caldana, F.; Endesfelder, M.; Bourgeois, D.; Endesfelder, U. A general mechanism of photoconversion of green-to-red fluorescent proteins based on blue and infrared light reduces phototoxicity in live-cell single-molecule imaging. *Angew. Chem.* **2017**. [CrossRef]
15. Mohr, M.A.; Argast, P.; Pantazis, P. Labeling cellular structures in vivo using confined primed conversion of photoconvertible fluorescent proteins. *Nat. Protoc.* **2016**, *11*, 2419–2431. [CrossRef] [PubMed]
16. Subach, F.V.; Patterson, G.H.; Manley, S.; Gillette, J.M.; Lippincott-Schwartz, J.; Verkhusha, V.V. Photoactivatable mcherry for high-resolution two-color fluorescence microscopy. *Nat. Methods* **2009**, *6*, 153–159. [CrossRef] [PubMed]

17. Wang, S.; Moffitt, J.R.; Dempsey, G.T.; Xie, X.S.; Zhuang, X. Characterization and development of photoactivatable fluorescent proteins for single-molecule–based superresolution imaging. *Proc. Natl. Acad. Sci. USA* **2014**, *111*, 8452–8457. [CrossRef] [PubMed]
18. Wäldchen, S.; Lehmann, J.; Klein, T.; van de Linde, S.; Sauer, M. Light-induced cell damage in live-cell super-resolution microscopy. *Sci. Rep.* **2015**, *5*, 15348. [CrossRef] [PubMed]
19. Patterson, G.H.; Lippincott-Schwartz, J. A photoactivatable gfp for selective photolabeling of proteins and cells. *Science* **2002**, *297*, 1873–1877. [CrossRef] [PubMed]
20. Subach, F.V.; Patterson, G.H.; Renz, M.; Lippincott-Schwartz, J.; Verkhusha, V.V. Bright monomeric photoactivatable red fluorescent protein for two-color super-resolution sptpalm of live cells. *J. Am. Chem. Soc.* **2010**, *132*, 6481–6491. [CrossRef] [PubMed]
21. Endesfelder, U.; Finan, K.; Holden, S.J.; Cook, P.R.; Kapanidis, A.N.; Heilemann, M. Multiscale spatial organization of rna polymerase in escherichia coli. *Biophys. J.* **2013**, *105*, 172–181. [CrossRef] [PubMed]
22. Stracy, M.; Lesterlin, C.; Garza de Leon, F.; Uphoff, S.; Zawadzki, P.; Kapanidis, A.N. Live-cell superresolution microscopy reveals the organization of rna polymerase in the bacterial nucleoid. *Proc. Natl. Acad. Sci. USA* **2015**, *112*, E4390–E4399. [CrossRef] [PubMed]
23. Spahn, C.; Cella-Zannacchi, F.; Endesfelder, U.; Heilemann, M. Correlative super-resolution imaging of rna polymerase distribution and dynamics, bacterial membrane and chromosomal structure inescherichia coli. *Methods Appl. Fluoresc.* **2015**, *3*, 014005. [CrossRef]
24. Sharonov, A.; Hochstrasser, R.M. Wide-field subdiffraction imaging by accumulated binding of diffusing probes. *Proc. Natl. Acad. Sci. USA* **2006**, *103*, 18911–18916. [CrossRef] [PubMed]
25. Jung, S.R.; Fujimoto, B.S.; Chiu, D.T. Quantitative microscopy based on single-molecule fluorescence. *Curr. Opin. Chem. Biol.* **2017**, *39*, 64–73. [CrossRef] [PubMed]
26. Niu, L.; Yu, J. Investigating intracellular dynamics of ftsz cytoskeleton with photoactivation single-molecule tracking. *Biophys. J.* **2008**, *95*, 2009–2016. [CrossRef] [PubMed]
27. Laplante, C.; Huang, F.; Tebbs, I.R.; Bewersdorf, J.; Pollard, T.D. Molecular organization of cytokinesis nodes and contractile rings by super-resolution fluorescence microscopy of live fission yeast. *Proc. Natl. Acad. Sci. USA* **2016**, *113*, E5876–E5885. [CrossRef] [PubMed]
28. Daigaku, Y.; Etheridge, T.J.; Nakazawa, Y.; Nakayama, M.; Watson, A.T.; Miyabe, I.; Ogi, T.; Osborne, M.A.; Carr, A.M. Pcna ubiquitylation ensures timely completion of unperturbed DNA replication in fission yeast. *PLoS Genet.* **2017**, *13*, e1006789. [CrossRef] [PubMed]
29. Zaratiegui, M.; Vaughn, M.W.; Irvine, D.V.; Goto, D.; Watt, S.; Bahler, J.; Arcangioli, B.; Martienssen, R.A. Cenp-b preserves genome integrity at replication forks paused by retrotransposon ltr. *Nature* **2011**, *469*, 112–115. [CrossRef] [PubMed]
30. Mizuguchi, T.; Barrowman, J.; Grewal, S.I. Chromosome domain architecture and dynamic organization of the fission yeast genome. *FEBS Lett.* **2015**, *589*, 2975–2986. [CrossRef] [PubMed]
31. Endesfelder, U.; Malkusch, S.; Fricke, F.; Heilemann, M. A simple method to estimate the average localization precision of a single-molecule localization microscopy experiment. *Histochem. Cell Biol.* **2014**, *141*, 629–638. [CrossRef] [PubMed]
32. Etheridge, T.J.; Boulineau, R.L.; Herbert, A.; Watson, A.T.; Daigaku, Y.; Tucker, J.; George, S.; Jonsson, P.; Palayret, M.; Lando, D.; et al. Quantification of DNA-associated proteins inside eukaryotic cells using single-molecule localization microscopy. *Nucleic Acids Res.* **2014**, *42*, e146. [CrossRef] [PubMed]
33. Schindelin, J.; Arganda-Carreras, I.; Frise, E.; Kaynig, V.; Longair, M.; Pietzsch, T.; Preibisch, S.; Rueden, C.; Saalfeld, S.; Schmid, B.; et al. Fiji: An open-source platform for biological-image analysis. *Nat. Methods* **2012**, *9*, 676–682. [CrossRef] [PubMed]
34. Wolter, S.; Loschberger, A.; Holm, T.; Aufmkolk, S.; Dabauvalle, M.C.; van de Linde, S.; Sauer, M. Rapidstorm: Accurate, fast open-source software for localization microscopy. *Nat. Methods* **2012**, *9*, 1040–1041. [CrossRef] [PubMed]
35. Malkusch, S.; Heilemann, M. Extracting quantitative information from single-molecule super-resolution imaging data with lama—Localization microscopy analyzer. *Sci. Rep.* **2016**, *6*, 34486. [CrossRef] [PubMed]
36. Ester, M.; Kriegel, H.P.; Sander, J.; Xu, X. *A Density-Based Algorithm for Discovering Clusters in Large Spatial Databases with Noise*; Kdd: Portland, OH, USA, 1996; pp. 226–231.

37. Legant, W.R.; Shao, L.; Grimm, J.B.; Brown, T.A.; Milkie, D.E.; Avants, B.B.; Lavis, L.D.; Betzig, E. High-density three-dimensional localization microscopy across large volumes. *Nat. Methods* **2016**, *13*, 359–365. [CrossRef] [PubMed]
38. Los, G.V.; Encell, L.P.; McDougall, M.G.; Hartzell, D.D.; Karassina, N.; Zimprich, C.; Wood, M.G.; Learish, R.; Ohana, R.F.; Urh, M.; et al. Halotag: A novel protein labeling technology for cell imaging and protein analysis. *ACS Chem. Biol.* **2008**, *3*, 373–382. [CrossRef] [PubMed]
39. Sun, X.; Zhang, A.; Baker, B.; Sun, L.; Howard, A.; Buswell, J.; Maurel, D.; Masharina, A.; Johnsson, K.; Noren, C.J.; et al. Development of snap-tag fluorogenic probes for wash-free fluorescence imaging. *Chembiochem* **2011**, *12*, 2217–2226. [CrossRef] [PubMed]

# 7 | Discussion and Outlook

## 7.1 Newly Developed Tools: Overview and Implications

### 7.1.1 Study of Multi-Protein Complexes with SMLM

Proteins are the main workforce of every living cell. In the past decades, scientists have become quite proficient at studying single proteins, from determining their crystal structure to measuring different parameters that describe all aspects of their activity. While many proteins, e. g. nucleic acid polymerases can carry out their tasks independently in-vitro, there is no such thing as a one-protein-army in a living organism. The function of virtually every protein inside a living cell relies on the successful actions of other cellular components. Looking at the example of a DNA polymerase; the enzyme is perfectly capable of synthesizing DNA on its own, given a template, sufficient building blocks in the form of nucleotides and the isolated space of a PCR tube. This becomes immensely more complicated inside of a living cell. The relatively simple task of adding complementary nucleotides to a stretch of single stranded DNA expands to a whole multitude of tasks. To name a few, the DNA must be uncoiled, split into strands, stabilized, ligated after synthesis - all while other cellular processes such as transcription must remain undisturbed. A DNA polymerase cannot do all of this on its own. Instead, it cooperates with several other proteins in a complex called the replisome, where each protein carries out its own designated function [5]. In fact, nearly every crucial process inside a cell is carried out by such a multi-protein complex. Studying single proteins in a vacuum is undoubtedly useful, but to truly understand the mechanisms of life, we must expand our knowledge to how proteins function as parts of a whole. Unfortunately, this is easier said than done. Intact large multi-protein complexes are notoriously difficult to crystallize, making high-resolution structural data on them rather scarce. Electron microscopy of structures captured in vitreous ice or Cryogenic Electron Microscopy (Cryo-EM) [6] and Nuclear Magnetic Resonance (NMR) spectroscopy [7] have been instrumental in bridging the knowledge gap between single protein and multi-protein complex structures. As important as these tools are, they can offer only limited information on protein complexes in the context of a whole cell. While these approaches yield high-resolution structures of the entire complex, they do not enable direct identification of its subunits and are not inherently quantitative.

While methods such as X-ray crystallography, NMR spectroscopy and Cryo-EM span the angstrom spatial domain and conventional light microscopy covers the micrometer domain, SRM links the two spatial domains together. Combining resolutions superior to conventional light microscopy (down to a few nanometers) with the specificity of versatile fluorescent tags that Cryo-EM and NMR lack, SRM has been successfully used to study multi-protein assemblies in the recent years. As its name suggests, SMLM is especially suitable for this for this. Several landmark scientific works clearly demonstrate the potential of the technique.

Many of these landmark studies have already been touched upon in the introduction chapter of this thesis [1]. To recap, one of the first truly remarkable works was done on the human nuclear pore complex [8]. The nuclear pore complex is a large, 110 mega-Dalton structure, consisting of several hundred nucleoporin proteins. It was known before from X-ray crystallographic studies that these proteins form Y-shaped complexes which further assemble into the even larger nuclear pore scaffold. The arrangement of the specific proteins was not known. To solve this issue, the authors of the paper imaged the individual nucleoporins with direct Stochastic Optical Reconstruction Microscopy (dSTORM) (the technique is described in detail in the introduction section [1]). Under ideal experimental conditions, dSTORM and Stochastic Optical Reconstruction Microscopy (STORM) can reach resolutions of 10-15 nanometers. While high, this was not enough to solve the spatial arrangement of the individual nucleoporins. To bypass this issue, the authors imaged several thousands of these circular structures for each tagged protein, aligned them using computer algorithms and combined them in a process called particle averaging. This allowed them to calculate the diameters of the rings formed by each nucleoporin with extremely high precision. Overlaying these diameters with known crystallographic and Cryo-EM data then allowed them to work out the location of each of the nucleoporin proteins in the context of the entire nuclear pore (see Figure 4b ii of the introduction section [1]). This work was not only revolutionary because of its complex biological target but also because it was the first time the particle averaging approach was used in SMLM to improve resolution enough to elucidate the molecular organization of a large multi-subunit complex. In the following years, several other studies followed suit; from a 3-dimensional reconstruction of the synaptonemal complex [9], a temporal and spatial model of endocytic vesicle formation in yeast [10] to the medically relevant images of human cilia, revealing potential causes of certain diseases [11]. A recent publication even describes the development of a general computational and analytical framework for the reconstruction of 3-dimensional molecular complexes by particle averaging [12].

However, reviewing the existing literature on the subject leaves one fact quite clear. Despite the obvious power of the approach, the number of publications using SMLM to study multi-protein complexes remains firmly in the low double digits. Contrasting this with the tens of thousands of available protein crystal structures, it is obvious that this is an emerging field where much work remains to be done. Reading them in more detail also reveals some key similarities that allude to the current limitations of the approach. First, all of the studies rely on pre-existing knowledge of the studied complex obtained through different methods, e. g. crystallography, Cryo-EM or conventional fluorescence microscopy in the case of larger structures. In most cases, the complexes exhibit some form of symmetry, which makes alignment of multiple structures much easier. The SMLM approach has never solved a structure *de-novo*. In the absence of pre-existing knowledge or structure symmetry, there simply is no reference point for structure orientation and alignment, which brings up the second similarity; all of the studies rely heavily on a single fluorophore - the well established work horse of SMLM, Alexa Fluor 647 (AF647). While some add a second color, it is more common to image the different components of a complex separately, rather than in parallel. Tools for tagging target proteins as well as novel fluorophores for multi-color imaging are currently in high demand in the field of SRM. In this thesis, I present several novel tools that contribute to the overall arsenal of the super-resolution microscopist, hopefully enabling studies on multi-protein complexes that were not possible before.

### 7.1.2 The BC2 Tag

In theory, the pool of fluorophores and tags available for fluorescent microscopy is nearly inexhaustible. In practice, the list is reduced to a number that may not suffice for a single ambitious experiment. To study biology, the first and foremost consideration a scientist should take is whether or not the tagging system used preserves the biological process being studied. Protein function can easily be perturbed by the attachment of a cumbersome FP, especially if the FP is prone to homooligomerization [13]. Even if the FP is completely monomeric, it is still a relatively large structure that can physically interfere with the protein it is attached to, as well as its surroundings. Unfortunately, this factor has often been neglected in the past, leading to some wrong conclusions that were widely accepted by the scientific community for a long time. For example, the belief that the *Escherichia coli* actin homolog MreB forms helical structures inside the bacterial cell was entirely the result of an artifact caused by FP tagging [14]. Taking precautions while designing an experiment by taking note of protein active sites and potential functions of the C- and N- terminal regions can alleviate these issues. In the case of MreB, a more unorthodox measure had to be taken; for the protein to function properly, it was tagged inside of an internal loop instead of one of the two termini [15]. These effects can of course be avoided completely by using antibody-based staining approaches, which do not require any sort of genetic modifications of the investigated target. However, in the world of ever increasing resolutions of SMLM, these pose a different problem: when the imaging resolution is in the 15-20 nanometer range, the roughly 15 nanometer long primary and secondary antibodies can significantly inflate the observed structure. This effect, also referred to as linkage error (the error introduced by the linker between the target and the fluorophore), leads to the second most important consideration in SRM imaging: is the recorded data representative of the actual structure?

The BC2 Nanobody, a small single-chain antibody fragment consisting of one variable domain with a diameter of roughly 3nm (Nb) presented in **Section 5** [2] of this thesis aims to address both of these considerations. To summarize, it is a tag that consists of 12 amino acids that must be attached to the target protein at the desired location. The peptide is then targeted by a bivalent Nb which binds to it with high affinity and specificity, even changing its molecular conformation to "lock" the peptide in [16]. Being a small Nb, it is also much easier to get into a cell than conventional antibodies, without the need for harsh permeabilization steps [17]. While the system does entail a genetic fusion, the introduced peptide is much smaller than the average FP and hence much less intrusive. In the published work, we demonstrated that the tag does not interfere with the function of any of the investigated proteins. This is especially notable in the cases of vimentin, actin and tubulin, all of which are well known to be impacted by FP fusions [18, 19, 20]. Such effects are shown in our own work in the case of Green Fluorescent Protein (GFP) and Photo-Activatable Monomeric Cherry Fluorescent Protein (PAmCherry)-tagged vimentin as well. A stable genomic integration of the BC2 tag into the actin locus under the native promoter by CRISPR/Cas9 and subsequent observations of stress fiber formation also showed no signs of disturbance. Furthermore, the tagging system proved to be suitable for the observation of non-structural proteins such as the autophagosome marker protein LC3B and the GFP-GPI extracellular membrane marker. Cells expressing LC3B tagged with the BC2 tag successfully formed autophagosomes upon treatment with autophagy inducing chemicals. Finally, the system even functioned in living cells, allowing for single-particle tracking of the GFP-GPI diffusing through the membrane and revealing some interesting dynamics - though the purpose of this particular experiment was a technical demonstration of the capabilities of the system, not investigating a specific biological process.

In addition to evaluating the impact of the tag on cell physiology and protein function, we performed rigorous technical characterizations. One worry was that since the Nb was originally developed to target $\beta$-catenin (the 12 amino acid BC2 tag is actually a fragment of the $\beta$-catenin protein), the system might produce significant background staining in cells expressing higher amounts of $\beta$-catenin. To evaluate this, cells treated with a chemical that induces endogenous $\beta$-catenin accumulation were imaged with the BC2 system and while they did show a slightly increased background compared to non-treated cells, it was not high enough to interfere with imaging of the relatively low-copy number, non-structural LC3B. When the same was repeated with a specific anti-$\beta$-catenin antibody, the staining was dramatically higher, leading to the safe conclusion that even though endogenous $\beta$-catenin may be present, only a minute fraction will be stained by the BC2 Nb. As mentioned earlier, the BC2 system aimed to address the issue of linkage error introduced by large tagging molecules. When measuring the thickness of imaged vimentin filaments stained either with the BC2 system or a conventional primary/secondary antibody system, the BC2 tagged filaments were significantly thinner and in perfect agreement with the literature [21]. As an added benefit, the defined 1:1 labeling ratio of fluorophore to nanobody offers a semi-quantitative readout. This fact was used in the publication to determine the degree of labeling the system can produce. Using a BC2-tagged bacterial ferritin, a known homooligomer with 24 subunits, the degree of labeling was shown to be comparable with the covalent SNAP tag at around 60% [22]. This experiment also points to the fact that with the appropriate standards and control experiments, the system may prove suitable for single molecule counting. Finally, the sytem was also successfully tested on a DNA binding protein in the fission yeast *Schizosaccharomyces pombe*.

In summary, the BC2 tag proved to be a non-interfering tag in every cell process we observed. It allowed for dense integration into the targeted structures, producing the dense labeling desirable in SMLM. As a small tag, the BC2 system competes with enzyme tags such as SNAP, CLIP, DHFR and HALO [1]. These consist of a genetically encoded non-fluorescent enzyme that covalently binds a fluorescent ligand when stained. Such tags exhibit superior brightness and image quality over FPs due to the organic dyes they use and higher specificity and ease of labeling over conventional antibodies. The BC2 system improves upon that concept by inversing it; taking the larger, more cumbersome and potentially damaging tag off the POI and replacing it with something much less invasive (see Figure 7.1). That being said, there are thousands of proteins and processes that have not been evaluated in this work, as well as many different organisms that were not used. We know through personal communication with two other research groups that the BC2 system proved to be advantageous in their as-of-yet unpublished studies (Cecile Leduc, Institut Pasteur, Paris and Irina Gutsche, IBS, Grenoble). As it stands now, the BC2 system looks to be a promising new

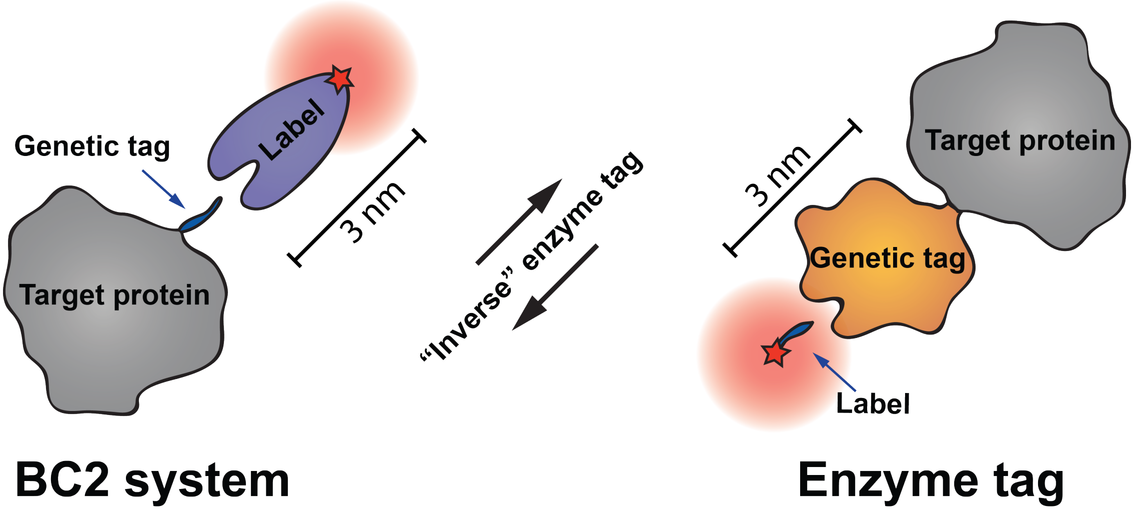

**Figure 7.1:** A schematic representation of the BC2 system (left) compared to an enzyme tag such as SNAP, CLIP, HALO or DHFR [1] (right). The genetic tag introduced by the BC2 system is much smaller than the POI, eliminating more potential issues with protein function. The Nb with its 3nm diameter is still small enough to into most cell interiors, enabling dense labeling.

tool in SMLM. While no multi-protein complex was studied in the scope of this work, conclusions obtained from the study of multi-protein assemblies such as vimentin, actin and tubulin can be expanded to the former as well. The low physiological impact of the system may prove especially valuable in the tightly packed confines of a large protein complex. Combined with the high labeling density, low linkage error and potentially quantitative readout, the BC2 system seems to be ideal tag for this purpose. As more scientists adopt the system and report their findings, it remains to be seen just how big of an impact this tag will have on the field.

### 7.1.3 Primed-Conversion for Quantitiative Multi-Color Imaging

While FP fusions may cause artefacts in cell physiology as discussed earlier, they are one of the most popular fluorescent tags for good reason. Many of the issues one has to deal with when using exogenous staining methods — methods where the fluorescent tag is introduced to the sample from the outside — are simply not a factor when using FPs. For one, they are completely specific, completely eliminating the worry over background staining. Since they are expressed by the organism itself, FPs require no sample processing prior to imaging, making them the simplest option for live-cell observations. This can also prove advantageous in fixed cells, when the examined structures are easily perturbed by the often-harsh staining protocols used by other methods. Finally, since FP fusions are part of the same peptide chain as the target protein, they offer the most reliable 1:1 labeling ratio and are inherently quantitative. If an FP fusion is proven to not impact the studied cell process, it is arguably the most elegant solution for fluorescent tagging.

FPs are widely utilized by all forms of fluorescence microscopy and there are hundreds to choose from [13]. FPs are also the basis of the SMLM technique called Photoactivated Localization Microscopy (PALM) [23], discussed in detail in the introduction chapter of this thesis [1]. PALM, however, requires a specific subset of FPs called Photo-Switchable Fluorescent Protein (psFP)s. More specifically, Photo-Activatable Fluorescent Protein (paFP)s such as PAmCherry [24], reversibly switchable FPs such as Dronpa [25] or Photo-Convertible Fluorescent Protein (pcFP)s such as Dendra2 [26]. This important criterion drastically reduces the number of usable proteins. When factors such as brightness, stability, speed of maturation and background fluorescence of the sample are taken into account, only a handful of proteins remain. These are primarily the green-to-red family of pcFPs derived from Anthozoa, and the photoactivatable PAmCherry and Photo-Activatable Monomeric Kate Fluorescent Protein (PAmKate) [4]. These proteins all share a common characteristic — they fluoresce in the red part of the light spectrum, differing by only a few nanometers in their emission peaks. This of course makes them less-than-ideal for multi-color imaging schemes. Scientists have been quite resourceful though, and managed to expand PALM imaging with dSTORM dyes or spectral demixing approaches to expand the color palette of SMLM imaging. However, the requirement of exogenous staining diminishes one of the greatest advantages of FPs, while spectral demixing approaches are technically challenging and not accessible for many microscopists.

pcFPs and paFPs are usually converted into their red-fluorescent state by absorbing light in the ultraviolet range of the light spectrum. While paFPs start off completely non-fluorescent and incapable of absorbing (or emitting) any other wavelength, pcFPs start in their green forms, absorbing blue to emit green light (similar to GFP). This process does not end up converting them into their red form, eventually leading to permanent bleaching of the FP. The Ultra-Violet light (UV) paradigm was accepted as the only photo-conversion mechanism for a long time, until the discovery of a novel mechanism called primed conversion [27]. The discovery showed that Dendra2, a protein from the green-to-red anthozoan FP family, can be "primed" by illumination with blue light. When illuminated with Infrared light (IR) primed state, the protein is converted into its red form. In addition to breaking a long-standing paradigm, this new mechanism carried a range of implications. Is the mechanism specific for this particular protein or can it be replicated in others? Since UV light is a known mutagen, could this mechanism potentially be used for less damaging live-cell SMLM imaging? And finally, could this different mechanism be utilized in a multi-color imaging scheme, in a manner similar to the different activator dyes used in the original STORM technique [28]?

In the work presented in **section 1** of **chapter 6** in this thesis [3], it is demonstrated that the mechanism can be generalized for any protein in the green-red anthozoan FP family, as long as its amino acid at the highly conserved position 69 is a threonine. The mechanism of this effect has been described in detail in the past [29]. This knowledge led to the design of several FPs where the residue at this position was replaced with a threonine, resulting in a collection of pcFPs capable of undergoing primed conversion. The conversion was shown to be efficient and while the modifications did reduce the brightness of the FPs slightly, they were still perfectly suitable for PALM imaging. Furthermore, we showed that primed conversion was indeed less phototoxic than the standard UV conversion imaging scheme, leading to reduced cell death in *E. coli*. While this was an important finding in the field of live-cell super-resolution microscopy, the benefit for SMLM of multi-protein complexes came a bit later. As mentioned earlier, paFPs start off completely dark and unable to absorb any other wavelength save for UV. As such, it should theoretically be possible to have a paFP and a Primed Convertible Photo-Convertible Fluorescent Protein (pc-pcFP) in the same sample and image them separately in a two-stage imaging scheme. In such a scheme, the pc-pcFP would be imaged first, with a combination of blue and IR, neither of which should have any effect on the paFP, followed by UV conversion of the paFP. Both proteins would therefore be imaged sequentially in the same color channel. In a follow-up to the first primed-conversion publication, we demonstrated that such an imaging approach can in fact be used to great advantage on a multitude of targets. The results of this are described in detail in **Section 2** of **Chapter 6**.

While sound in theory, there were a few concerns regarding this method. Most importantly, the paFP must remain entirely dormant throughout the entire process of imaging the pc-pcFP. Any activation of the paFP by primer conversion illumination would compromise the specificity of the first imaging stage. Conversely, any residual pc-pcFP would have the same effect on the second stage. Last, any loss of the paFP during the first stage would compromise the image quality and quantitative readout of the second. Fortunately, neither of these were the case as the paFP of choice, PAmCherry, did not absorb any blue light and remained intact during the first stage of imaging, even under very intense illumination. Furthermore, the pc-pcFP could be read out completely if a sufficiently long imaging time was used. If complete readout was not necessary, it was also possible to permanently bleach any residual pc-pcFP with intense blue light, with no apparent effect on the second stage. Since the method essentially expands one color channel into two possible targets, it is also compatible with other sequential or parallel multi-color techniques, as demonstrated by a proof of concept 4-target single-channel image of *E. coli* cell membrane, DNA and the FtsZ and RNAP proteins [4]. As light of different wavelengths travels through the optical path of microscopes slightly differently, an artefact called chromatic aberration must be accounted for in image analysis. Imaging two targets with the same wavelength completely avoids this effect. Finally, the system was also shown to function nicely for imaging structural proteins in mammalian cells, as well as proteins belonging to the large, multi-protein kinetochore complex in the fission yeast *S. pombe*. Due to its thick cell wall and dense cytosol, fluorescent staining of cellular structures is quite difficult. Furthermore, multiple experiments revealed that even when specific staining is achieved, something inside the *S. pombe* cell interferes with the photophysics of the exposed fluorophore of fluorescent dyes. While STORM in fission yeast is possible [2], it proved to be highly variable from experiment to experiment, leaving FPs as the only reliable SMLM imaging tool. This left the described two-stage imaging scheme as the sole multi-color approach in our toolkit at the time and it allowed us to produce SMLM data on the *S. pombe* kinetochore complex for the first time.

Perhaps the main limitation of the approach is that it requires illumination with infrared light. Since this particular wavelength was not very popular outside of two-photon microscopy prior to the discovery of primed-conversion, not many microscopists have access to an IR light source for their microscopes. This is changing as primed-conversion is becoming more and more popular in the field. In time, our two-stage system may become more accessible to other research groups.

## 7.2 Application of the Developed Tools

### 7.2.1 The Kinetochore

Following DNA replication in eukaryotic cells, each chromosome in the cell consists of two sister chromatids, both of which contain identical genetic information. In order for cell division to result in two new fully functional cells, these chromatids must be divided and pulled apart with great precision, so that both cells end up with identical genomes. The force required to move DNA to the opposite poles of the mother cell is exerted by microtubules organized into a structure called the mitotic spindle, through a combination of polymerization, depolymerization and motor protein activity [30]. However, microtubules cannot attach directly to DNA, they require a specialized linker. The role of this linker is carried out by a large multi-protein complex called the kinetochore. However, the tasks of this complex extend beyond that of a simple mechanical linker. Each kinetochore can be thought of as having three functional modules - one that ensures cohesion to the chromatid, one that ensures cohesion to microtubules, and one that acts as a sensor (the Spindle Assembly Checkpoint (SAC)) of chromosome bi-orientation [31]. Once this sensor is satisfied that all kinetochores are bi-oriented (attached to two microtubules from opposite poles), it allows for the separation of the sister chromatids. If the sensor of a single kinetochore is not satisfied, it triggers a signaling cascade that prevents all the others from going forward with segregation. Since incorrect distribution of genetic material during division usually results in non-viable or heavily deficient cells, the importance of the kinetochore complex in virtually any eukaryotic organism cannot be understated. The roughly fifty structural and kinetochore-associated proteins are highly conserved among all eukaryotes. While kinetochore proteins in different organisms often go by different names (many were named before it was known they were kinetochore proteins), most of them have clear homologs throughout eukaryota. This can lead to some confusion, since names of human kinetochore proteins are often used to describe their homologs in other organisms e. g. CENP-A in humans, cnp1 in fission yeast, cse4 in budding yeast, Cenpa in mice etc. Much of the research on kinetochores is spread through different model organisms and often has to be pieced together to get a complete picture. In this thesis, conserved mechanisms will be referred to by the names of their counterparts in humans, as per community agreement. Organism-specific terminology will be used when appropriate, and explicitly specified.

Though the kinetochore component proteins of different eukaryotes are very similar, the overall assembly of kinetochores can vary quite drastically. The region of the chromosome upon which kinetochores assemble is called the centromere. These regions, normally defined by the presence of a special H3 histone variant called Centromeric H3 (CenH3) in the nucleosomes, can cover anything between 125 base pairs and a single nucleosome as in budding yeast, to several hundred kilobases in humans [32]. In this thesis, the focus was on the fission yeast *Schizosaccharomyces pombe* kinetochore, which falls somewhere between these two extremes. Its 30-110 kb long centromeres that span about 20 nucleosomes [33] are much more similar to the human ones [34] in terms of kinetochore construction than those of budding yeast, making possible discoveries more transferable to a human model. Furthermore, *S. pombe* cells are much simpler to culture and genetically modify than human cells, which facilitates fluorescent tagging and sample preparation. In addition, they divide symmetrically just like human cells and possess only three chromosomes, simplifying image acquisition and analysis.

The kinetochore is a challenging target to study, highly relevant in terms of biological and medical impact and relatively little is known about its structure and stoichiometry. Therefore, it is an excellent albeit difficult candidate for the application of the methodologies described in this work.

### 7.2.2 Structure of the kinetochore complex

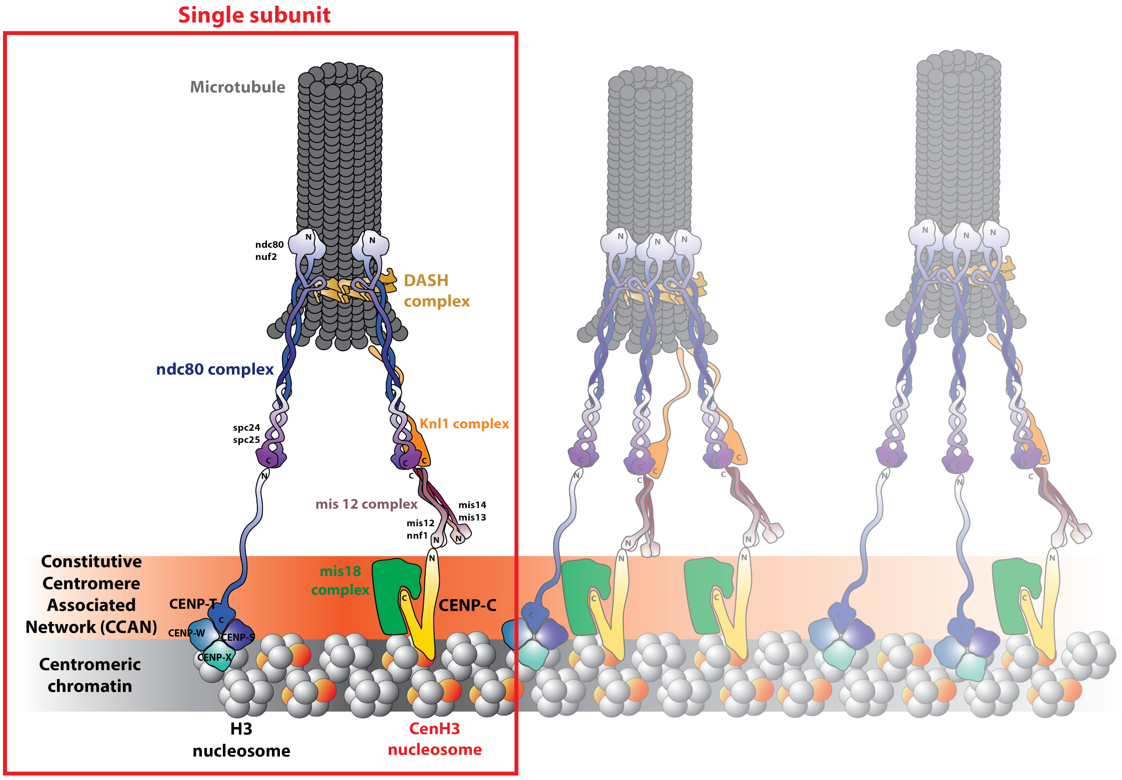

**Figure 7.2:** A schematic representation of the kinetochore complex. The schematic was constructed by combining knowledge from protein interaction and fluorescence microscopy studies, backed with crystal structure data where available. A single subunit of the proposed repeat-subunit model [35, 36] is marked by a red rectangle. CenH3 molecules in nucleosomes (grey) are marked as red and the region of centromeric chromatin is shaded grey. Due to the lack of knowledge on several members of the Constititive Centromere Associated Network (CCAN) complex [37], it is represented as a diffuse orange bar. All proteins with known crystal structures in at least one organism are drawn roughly in scale with each other. The N-terminal regions of proteins where data on orientation and protein-protein interaction is available are represented with darker colors (and marked with the letter N) while C-terminal regions are colored with lighter colors.

Structurally, the kinetochore can be divided into two main parts: the inner kinetochore, which provides attachment to the centromere, and the outer kinetochore, which provides attachment to the microtubule. Each of these consists of several multi-protein complexes. Complexes of the inner kinetochore assemble upon scaffolds called centromeres. These are epigenetically defined regions of DNA that are marked by the presence of a variant of the H3 histone termed CenH3 (CENP-A in humans, Cse4 in *S. cerevisiae*, cnp1 in *S. pombe*). This protein replaces the H3 histone in nucleosomes of the centromeric region and triggers kinetochore assembly through mechanisms of post-translational modification, deposition timing and chromatin organization [38]. Interestingly, there is currently only one known exception where centromeres are not defined by this CenH3, which is *Trypanosoma* [39]. The mechanisms of centromere definition are complex and not entirely understood to this day [32]. Though the epigenetic definition of centromeres is conserved in most eukaryota, centromeres of different organisms vary significantly in both length and nucleotide sequence. We can roughly distinguish three types of centromeres: point, regional and holocentromeres. In *S. cerevisiae* and some other budding yeasts, the centromere is defined by a specific sequence of 125 base pairs and contains a single CenH3 (cse4) nucleosome [40, 41]. Such a centromere is called a point centromere and the kinetochores that assemble on it bind to a single microtubule [42]. In higher eukaryotes with regional centromeres, the situation is quite different. Regional centromeres cover multiple thousand base pairs, depending on the organism. Holocentromeres are found in certain nematodes, insects and plants. In this relatively uncommon type, microtubules attach along the entire length of the chromosomes [43]. While point and regional centromeres are very different, many of the molecular mechanisms are conserved [44]. In fact, the copy number of kinetochore proteins is proportional to the number of microtubule binding sites at the kinetochore, rather than the length of the centromeric region. It is therefore likely that kinetochores of organisms with regional centromeres are simply repeats of the basic, point centromere kinetochores. Such a model has been termed the "Repeat subunit model" and is backed by significant amounts of evidence [35, 36] (see Figure 7.2).

The centromere serves as a scaffold for the assembly of a network of roughly 16 proteins called CCAN (**C**onstitutive **C**entromere **A**ssociated **N**etwork). In human cells, CCAN proteins are called CENP-B, C, H, I, K, L, M, N, O, P, Q, R, S, T, U, W and X [45, 46, 47, 48]) and these names are often used when referring to conserved homologues in other organisms. While small amounts of CenH3 can be found in different parts of the chromosome, CCAN proteins are only present on active centromeres. Most CCAN proteins remain at the centromere throughout the cell cycle, though they undergo varied turnover patterns [49, 50]. Relatively little is known about most members of the CCAN. CENP-O/P/Q/R/U are known to associate into a complex [51] and require the presence of the remaining proteins (CENP-C/H/I/K/L/M/N) to localize at the centromere [47]. Loss of the entire OPQRU complex has no effect on the recruitment of other kinetochore proteins and its importance seems to depend highly on the specific organism in question and even different cell types within the same organism [52, 53]. Some of these proteins were shown to play a role in chromosome congression to the metaphase plate [54] and in kinetochore-microtubule attachment [55].

A few CCAN proteins have been extensively studied. Two important representatives, CENP-C (cnp3 in *S. pombe*) and CENP-N (mis15 in *S. pombe*) stand out. These two proteins ensure the assembly of the two main pathways of inner-to-outer kinetochore attachment. CENP-C and CENP-N can both identify specific structural properties of CenH3. CENP-C interacts with the C-terminus of CenH3 [56, 57], as well as a region of CenH3 called the CATD [58]. CENP-N also interacts with the CATD and both proteins preferably interact with nucleosomal instead of free CENP-A (CenH3) [59, 60].

CENP-C binds to CenH3 with its central region while its long C- and N-terminal tails extend away from the DNA. While the C-terminus plays an important role in the epigenetic mechanisms of centromere specification, the N-terminus of CENP-C interacts with the N-terminal regions of the outer kinetochore mis12 complex (mis12, nnf1, dsn1, nsl1 in *S. pombe*) [61]. The mis12 complex C-terminal region then binds to the C-terminal domains of the spc24/25 part of the highly conserved ndc80 complex [62]. The large ndc80 complex consists of four subunits; **ndc80, nuf2, spc24 and spc25**. Each of the four component proteins has a globular domain and a long, coiled-coil domain. Proteins of the two heterodimers assemble in a parallel fashion – the globular domains at the N-terminal ends of ndc80 and nuf2 and the coiled-coil regions at their C-terminal ends bind together in a pseudo-2-fold symmetry. The inverse is true for the spc24/spc25 heterodimer, with globular domains at their C-terminal ends and coiled-coil rods at their N-terminal ends [63, 64, 65, 66]. The dimers bind to each other via their coiled-coil termini (C-terminus of ndc80/nuf2 to N-terminus of spc24/spc25), forming a tetrameric junction through conserved amino-acid interactions [67]. The globular domain of ndc80 directly interacts with microtubules and has been shown to be responsible for high-affinity microtubule binding and proposed to act as a sensor that recognizes straight microtubule filaments [68, 69]. Through these other complexes, CENP-C provides the first major pathway of centromere-microtubule tethering [62, 70] (see Figure 7.2).

CENP-N binding to CenH3 triggers the recruitment of several kinetochore components, but most importantly the CENP-T/W/S/X (cnp20, wip1, mhf1, mhf2 in *S. pombe*) complex [32]. The CENP-T/W/S/X proteins all contain histone fold domains and form heterotetramers. It is not clear if these proteins form nucleosome-like structures, with DNA wrapping around them, or simply bind to DNA from the outside, but they are vital for kinetochore assembly [71, 72]. The CENP-T (cnp20 in *S. pombe*) component has a long, conserved N-terminus that extends away from the DNA and binds to the C-terminal globular domains of the spc24/25 end of the ndc80 complex, which then binds to microtubules via the N-terminal domains of ndc80. This interaction provides the second major centromere-microtubule connecting pathway [73, 74]. It is known from pulldown assays that the T/W/S/X complex interacts with regular H3 histones, not CenH3 [75]. A third pathway exists via the Knl1 (spc7 in *S. pombe*) complex. The Knl1 protein is a large protein with a long, disordered tail at the N-terminal end and a globular head at the C- terminal end. Similar to the ndc80 complex, the globular head binds directly to the C-terminal regions of the mis12 while the tail interacts directly with the microtubule [37] (see Figure 7.2).

Interestingly, experiments in *S. cerevisiae* showed that artificially tethering just the N-terminus of CENP-T to a different part of the chromosome led to chromatid segregation, even in the complete absence of CenH3 [76, 77]. Alternatively, tethering the N-terminus of CENP-C to DNA also allows for chromatid segregation, by linking DNA to kinetochore via the CENP-C/mis12 complex/ndc80 pathway [76]. These findings suggest that these mechanisms might be mutually redundant and act as backups for each other, which is corroborated by the fact that some organisms like *Drosophila* and *C. elegans* lack a CENP-T homologue and rely entirely on the mis12 linkage [78]. However, as mentioned earlier, centromeres have stretches of H3 and CenH3 nucleosomes. Since each of these mechanisms connects to the DNA via different nucleosomes, it is likely that they are simply a way of utilizing the entire available length of the centromere for microtubule attachment. The Knl1 tethering pathway seems to be largely redundant, though it has been shown to have a role in mis12 complex localization and spindle assembly checkpoint signaling [79, 80].

Finally, at the outermost part of the outer kinetochore, the dam1/DASH (dam1 in *S. pombe*) complex assists in transferring forces exerted by microtubules to the rest of the kinetochore. It does so by associating with a characteristic loop region the ndc80 protein [81]. It has been shown that dam1 cannot be the only coupling between kinetochore and microtubules, since it is not essential in fission yeast [82] and only present in fungi, though Ska1 may replace it in human cells [83].

### 7.2.3 Multi-Color, Quantitative Imaging of the Fission Yeast Kinetochore

The *S. pombe* kinetochore is undoubtedly a challenging target for SMLM imaging. It contains over 50 different proteins, making it completely impossible to crystallize as a whole complex with

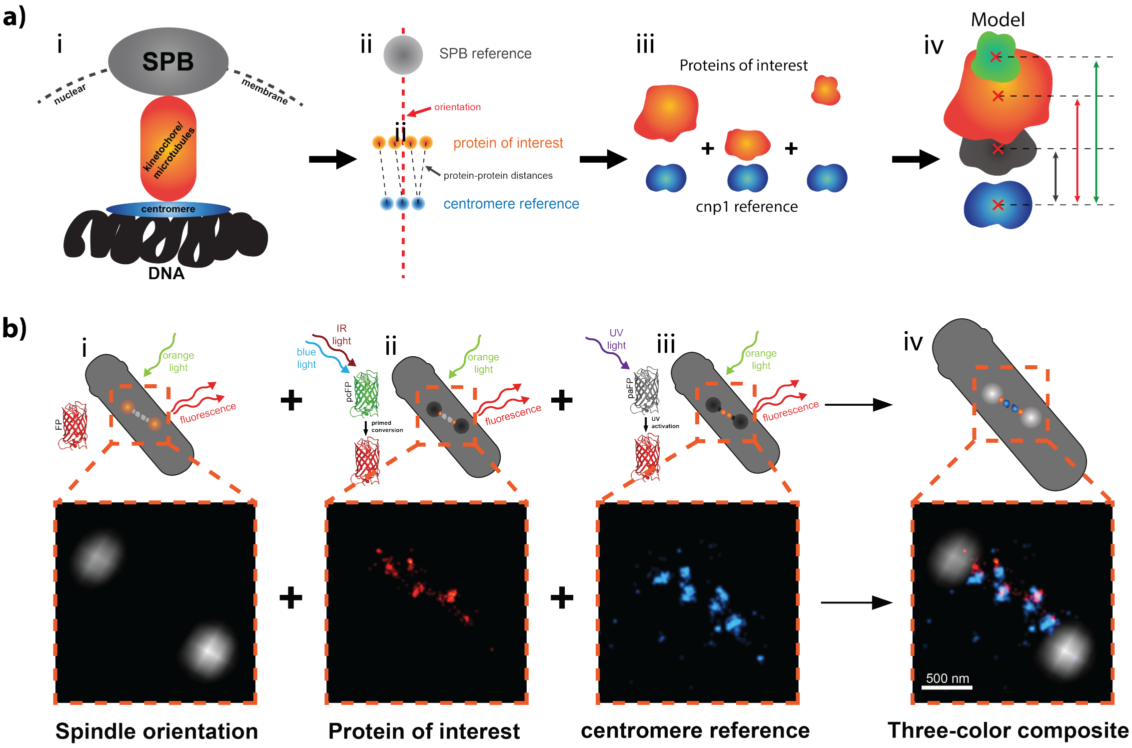

**Figure 7.3:** **a)** Representation of the procedure used to image the *S. pombe* kinetochore. **i** simplified representation of the imaged components. **ii** Using the fluorescently tagged Spindle Pole Body - yeast microtubule organizing element (SPB)s to determine the orientation and focal plane of the structure and the fluorescently tagged cnp1 as a reference point for each POI. **iii** Measuring the protein-protein distances between cnp1 and the POI for each kinetochore protein sequentially to build a 2-D model **iv** of the kinetochore architecture. **b)** Actual imaging procedure with real data. **i** Imaging the sad1-bound mScarlet-I with conventional fluorescence microscopy to find the focal plane of the kinetochores. **ii** Imaging the Monomeric Photoconvertible Eos Fluorescent Protein Version with a threonine substitition at position 69 (mEos3.2-A69T) attached to the POI with primed-conversion. **iii** Imaging the cnp1 via PAmCherry whith UV activation. **iv** Three-color composite, with the 6 kinetochores clearly visible.

current technology. Attempts to isolate the intact complex and image it with Cryo-EM have been wholly unsuccessful and conventional transmission-EM images reveal only hints of an overall shape [84]. Since SMLM can be used while the kinetochore is in its natural environment inside of a cell, it seemed the ideal technique to try instead. However, unlike the nuclear pore complex or endocytic vesicle, it exhibits no known radial symmetries and it is far too small to be visible as anything more than a fluorescent spot when imaged by conventional fluorescent microscopy. To put it short, besides crystal structures of individual complexes and some known interactions, the architecture of the kinetochore complex is an open book. As mentioned earlier, most SMLM studies on multi-protein complexes in the past built upon some form of existing shape or structure. In the case of the kinetochore, this was obviously not possible. While a difficult challenge, solving the architecture of the kinetochore with SMLM is by no means impossible. To tackle this issue, two starting points could be considered. First, the kinetochore is always built upon the scaffold of the centromere, which means that the cnp1 protein will always mark the innermost region of the kinetochore. Second, during cell division, kinetochores are being pulled apart by microtubules originating from SPBs, providing a second reference point. In *S. pombe*, the SPBs remain associated with the nuclear membrane throughout the division process [85]. Assuming that the forces exerted on the kinetochore by microtubules on one side and DNA on the other will stretch each kinetochore along the axis formed by the two spindle pole bodies, it should be possible to determine the orientation of each kinetochore. Knowing this, we envisioned a 3-target imaging strategy in which fluorescently tagged SPBs serve as reference points for finding the orientation of the mitotic spindle and consequentially the focal plane containing the kinetochores. A tagged cnp1 would serve as a common reference point for each kinetochore POI, all of which would be imaged in a third color, sequentially. The cnp1 anchor point would then allow us to measure the distance of each POI population from the centromere, building up a 2-dimensional model.

The first obvious challenge to overcome in such a strategy was imaging the three targets at once. Two-color SMLM can be difficult on its own, as discussed in the first three chapters of this thesis. While adding a third color is possible in some samples, it proved to be an enormous technical challenge in *S. pombe*. Fission yeast cells proved to be extremely difficult to stain with any known system, from nanobodies to enzyme tags and even when specific staining was achieved, the amount of background staining was too high for the single-molecule precision of SMLM. Furthermore, for reasons we cannot explain, even when staining was achieved, fluorescent dyes exhibited unpredictable photophysical behavior, often refusing to blink. The fortunate solution came in the form of the sequential multi-target imaging scheme described in **Section 6.2** of this thesis. Without the use of exogenous tags, this scheme would only enable SMLM imaging of two targets. However, since the SPB references were only there to provide orientation, they did not need to be imaged in super-resolution. *S. pombe* is simple to genetically modify, readily recombining transformed DNA into its genome given the appropriate flanking homologies. Hence, constructing a template strain with the SPB sad1 protein tagged with the bright, conventional FP monomeric Scarlet Fluorescent Protein with a a threonine to isoleucine mutation at position 74 (mScarlet-I) [86] and the cnp1 protein tagged with the photo-activatable PAmCherry was quite simple. The strain was then used as a parent for a library of strains with different kinetochore proteins tagged with the primed-photoconvertible variant of the mEos3.2-A69T. As mentioned, fluorescent protein fusions come with a range of worries, especially in the context of a tightly packed multi-protein complex as essential as the kinetochore. Each strain carrying the FP fusions was evaluated by cell morphology shape assessment through microscopy and flow-cytometry analysis, as well as microtubule destabilizing drugs. In fact, several strains did not pass the evaluation. For example, cells of the strain in which cnp3 (the very important CENP-C) was tagged with mEos3.2-A69T exhibited an extremely elongated phenotype, as well as slower growth. Such defects will be thoroughly examined in the future and alternative tagging strategies for the defect strains will be considered. This is, however, outside of the scope of this thesis, which stands primarily as a proof-of-principle work.

After some protocol optimization (**Appendix B, section 9.3**), the imaging scheme was finalized as described in Figure 7.3. The mScarlet-I bearing SPBs were imaged first, to determine the focal plane of the mitotic spindle Fig 7.3 b) i. This had no effect on the other FPs, since they did not absorb orange light at this point. The mScarlet-I was then bleached completely with intense orange illumination. The POI was imaged next by converting the mEos3.2-A69T to orange with a combination of blue and infrared light Fig 7.3 b) ii. The acquisition was stopped only when no more mEos3.2-A69T was detectable, to ensure a quantitative readout. Finally, the cnp1-attached PAmCherry was activated with UV and imaged in full Fig 7.3 b) iii. After post processing, the three images were aligned with the help of fluorescent fiducial markers in the sample Fig 7.3 b) iv, producing a three-color composite.

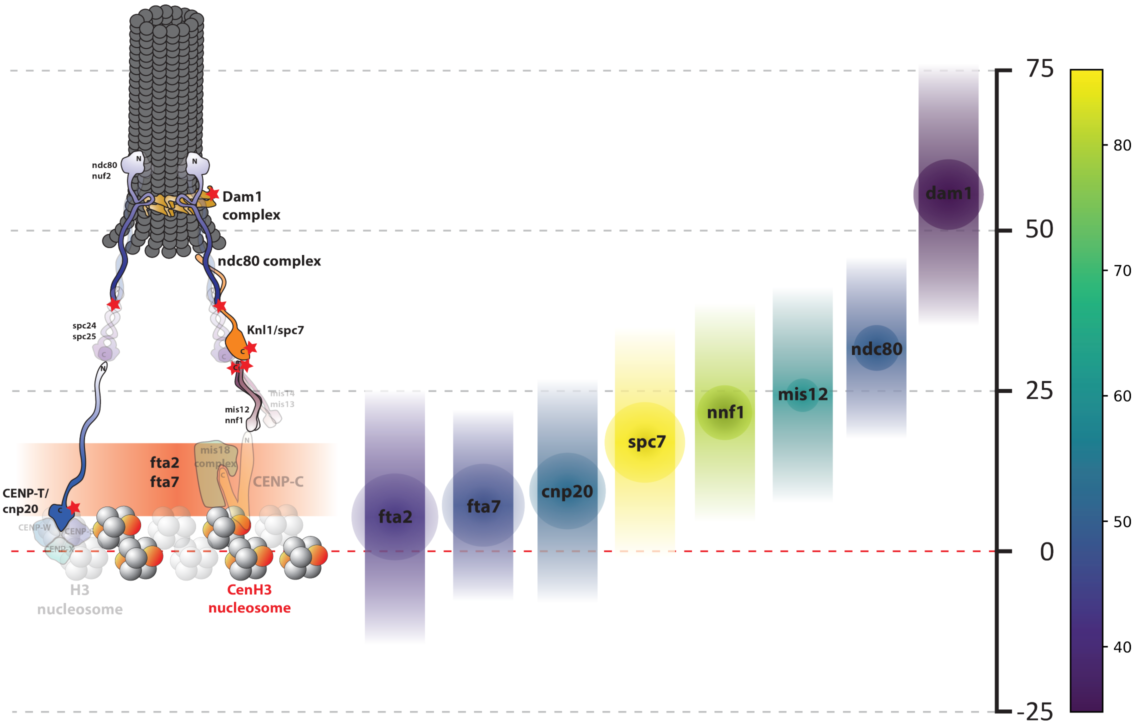

**Figure 7.4:** Results of SMLM imaging of the *S. pombe* kinetochore. A schematic representation of the kinetochore based on protein-protein interaction, crystallography and electron microscopy data. Proteins that were imaged in the context of this thesis are represented as solid, while proteins that were not imaged in the context of this work are faded out. All imaged POIs were tagged on their C-termini. The predicted locations of the fluorescent tag are represented as stars. On the right, vertical bars represent the cnp1-POI distance distributions, with the centers of the bars marking the expected distance and the lengths of the bars representing the standard deviations of the distributions. Diameters of circles in the middle of the bars represent the uncertainty of the expected value, obtained by calculating the standard deviation of the distribution of all the means obtained from the several thousand bootstrapping runs. Numbers on the first axis are in nanometers and the colormap on the right codes for the mean of the distribution of the number of blinking events recorded for each protein cluster - see color of protein distribution bars. All numerical values are specified in Table 7.1.

In SMLM, images are only used for graphical representation, not data anylsis. Actual analysis is performed on the localization files, lists of coordinates where each point represents a single fluorophore in a single frame of the movie. These are extracted with specialized fitting algorithms. In this work, two such programs were used; RapidStorm [87] and ThunderStorm [88]. Since the amount of data generated was too large to process manually, the localization files were analyzed by custom scripts written in the Python 3 programming language, described in more detail in **Appendix B, section 9.3**. In short, localization files were aligned based on the coordinates of fiducial markers added to the samples. Localizations of each channel were run through a clustering routine based on the Ordering Points To Identify the Cluster Structure (OPTICS) algorithm. Each such cluster represented the cnp1 or POI population of a single kinetochore. The number of localizations in these clusters directly represented the number of blinking events recorded, and is proportional to the total number of proteins in the population. Though this is not an absolute number without careful control experiments, it can already be used as a relative reference to the

**Table 7.1:** Results of kinetochore POI SMLM imaging

| | **fta2** | **fta7** | **cnp20** | **spc7** | **nnf1** | **mis12** | **ndc80** | **dam1** |
|---|---|---|---|---|---|---|---|---|
| **distance mean** | 5.3 | 7.2 | 9.3 | 17 | 21.6 | 24.3 | 31.7 | 55.6 |
| **distribution sigma** | 20 | 14.9 | 17.4 | 18 | 17 | 16.8 | 14.1 | 20.4 |
| **experimental precision** | 6.7 | 6.5 | 6 | 6.3 | 4 | 3.6 | 3.6 | 5.5 |
| **POI count** | 49 | 54.4 | 60.8 | 100 | 93 | 70 | 57.8 | 40.5 |
| **N kinetochores analyzed** | 28 | 20 | 35 | 37 | 39 | 57 | 16 | 10 |

abundance of each protein. At every step of the analysis, the data was visualized with a custom visualization software written in the C++ programming language. The visualized localization clusters were manually assigned to kinetochores, pairing up cnp1 and POI clusters. Localizations of each cluster pair were then projected onto the mitotic spindle axis, defined by the centers of the two SPB fluorescent spots. This collapsed the complex shapes into a simple 1-dimensional normal distribution, allowing the protein-protein distances to be determined by measuring the distance between the centers of the two distributions. The measurement produced a distribution of these projection distances for each analyzed protein. To improve the accuracy of the measurement, a custom bootstrapping algorithm was employed, in which the mean and standard deviation of the distance distribution was calculated several thousand times, on re-sampled subsets of the data. The calculated mean was taken as the expected distance of the analyzed protein from cnp1 (represented by centers of the vertical bars in Figure 7.4), while the calculated standard deviation was interpreted as the natural spread of the protein along the kinetochore axis (length of the bars in Figure 7.4). The uncertainty of this expected distance was determined by calculating the standard deviation of the distribution of the means generated by the bootstrapping (diameter of the diffuse circles in Figure 7.4). This process was carried out for several kinetochore proteins and the results obtained are summed up in Figure 7.4.

While these results are preliminary and significantly more imaging and control experiments must be carried out in the future, some interesting conclusions can already be drawn from them. Overall, results of the distance measurements fit well with what is known from the literature. Three of the eight imaged proteins, cnp20, fta7 and fta2, belong to the CCAN network, which is known to be closely associated with the centromere. Indeed, the three proteins were measured to be the closest to cnp1 at 9.3, 7.2 and 5.3 nanometers, respectively. While the data shows a high amount of variation, both in terms of the width of the distribution of the protein distances as well as in the accuracy of the measurement, this is likely caused by an inherent limitation of the distance calculation (discussed in more detail in **Appendix B, section 9.3**) and can probably only be improved by modification of the imaging strategy. To gain more accurate measurements on these centromere-associated proteins, a protein from the outer kinetochore (such as ndc80, mis12 or spc7) should replace cnp1 as the reference point. Such a modification would not only improve the quality of data on proteins close to the chromatin but also serve as a control; if the distances between cnp1 and an outer kinetochore reference to a POI add up to the same number as the distance between the two reference proteins themselves, this would be a good indication that the measurements are accurate. This strategy will definitely be implemented in the near future. Results obtained for mis12, nnf1 and ndc80 are also in accordance with the literature, with expected distances from cnp1 of 24.3, 21.6 and 31.7 nanometers, respectively. As discussed in **section 7.2.2**, mis12 and nnf1 are known to be parts of the same complex and should have the same orientation in terms of their C- and N-termini. In agreement with this,the distance distributions of these two proteins in the measured data overlap almost perfectly. Interestingly, the localization counts of mis12 and nnf1 differ with 60 and 80 blinking events, respectively. This is in conflict with crystallographic data and at this stage, it is impossible to conclude whether this difference is an artefact of the imaging procedure (due to chromophore maturation and other such effects), data analysis due to low statistics and lack of control experiments, or a real property of a kinetochore studied in its natural environment. Overall, analysis of protein counts is currently in a rudimentary state at best and very few conclusions can be drawn from it. In the future, the relative counts will be converted into absolute protein counts through the use of tagged protein-complex standards with known stoichiometries, such as ferritins [22] or nuclear pore complexes [89]. The distance of ndc80 from cnp1 of 31.7 nanometers is also in agreement with what is expected from the literature. As measured here, the distance between the C-termini of nnf1 and mis12 to ndc80 are 10.1 and 7.4 nanometers. Judging by the crystal structure of the entire ndc80 complex (spc24 and spc25 included), these numbers appear to be in the correct range — though it is difficult to judge where exactly on the complex the FP tag is located. Finally, the spc7 result is surprising. As discussed above, spc7 (knl1) interacts with the mis12 complex with its C-terminl domain. In the presented data, it seems closer to cnp1 than either mis12 or nnf1, at an expected distance of 17 nanometers. It is possible that the C-terminus, where the FP is located, extends further past the mis12 complex, explaining this shorter distance. In any case, while the data is very promising, much more of it must be acquired, both in the case of the proteins already imaged, as well as the plethora of the ones that have not yet been imaged. Higher statistics, the discussed flipped-reference control and a quantitative standard for protein counting would greatly improve the quality of the current model. This two-dimensional model is not the final goal, though. Once sufficient numbers of imaged kinetochores are reached, the approach could easily be extended with particle averaging. Using the reference proteins and mitotic spindle angles to anchor and orientate each kinetochore, particle averaging is within reach. Such an approach could be improved upon even further by the implementation of 3-dimensional imaging and finally computer simulations of the entire complex, based on data known from the literature and measured using this approach. Either way, the presented data shows that the tools developed in the scope of this thesis can indeed be effectively applied to study large multi-protein complexes such as the kinetochore. While not all of them were employed in the final imaging strategy, that was more due to the specific properties of the studied model organism, rather than the tools themselves.

# 8 | Appendix A: Other published work

## 8.1 A transient pool of nuclear F-actin at mitotic exit controls chromatin organization

# A transient pool of nuclear F-actin at mitotic exit controls chromatin organization

Christian Baarlink, Matthias Plessner, Alice Sherrard, KohtaroMorita, ShinjiMisu, David Virant, Eva-Maria Kleinschnitz, Robert Harniman, Dominic Alibhai, Stefan Baumeister, Kei Miyamoto, Ulrike Endesfelder, Abderrahmane Kaidi and Robert Grosse

This part of the thesis is written in the style of a manuscript and was published in Nature Cell Biology. While not directly related to the main project, it was a technically challenging project that yielded interesting results. I contributed to this work by developing the optimized labelling and imaging procedure performing all the dSTORM imaging and data analysis, creating the related figures and writing that part of the materials and methods. [90]

nature
cell biology

# A transient pool of nuclear F-actin at mitotic exit controls chromatin organization

**Christian Baarlink[1,8], Matthias Plessner[1,8], Alice Sherrard[2,8], Kohtaro Morita[3], Shinji Misu[3], David Virant[4], Eva-Maria Kleinschnitz[1], Robert Harniman[5], Dominic Alibhai[6], Stefan Baumeister[7], Kei Miyamoto[3], Ulrike Endesfelder[4], Abderrahmane Kaidi[2] and Robert Grosse[1,9]**

**Re-establishment of nuclear structure and chromatin organization after cell division is integral for genome regulation or development and is frequently altered during cancer progression. The mechanisms underlying chromatin expansion in daughter cells remain largely unclear. Here, we describe the transient formation of nuclear actin filaments (F-actin) during mitotic exit. These nuclear F-actin structures assemble in daughter cell nuclei and undergo dynamic reorganization to promote nuclear protrusions and volume expansion throughout early G1 of the cell cycle. Specific inhibition of this nuclear F-actin assembly impaired nuclear expansion and chromatin decondensation after mitosis and during early mouse embryonic development. Biochemical screening for mitotic nuclear F-actin interactors identified the actin-disassembling factor cofilin-1. Optogenetic regulation of cofilin-1 revealed its critical role for controlling timing, turnover and dynamics of F-actin assembly inside daughter cell nuclei. Our findings identify a cell-cycle-specific and spatiotemporally controlled form of nuclear F-actin that reorganizes the mammalian nucleus after mitosis.**

Cytoplasmic actin polymerization at plasma membranes is an essential and versatile process that defines cellular shape, determines cell polarity, cell–cell and cell–matrix interactions, and drives cytokinesis[1]. In addition, it is well established that actin resides in the nuclear compartment of somatic cells[2,3]. For example, monomeric actin is stably assembled into chromatin-remodelling complexes[4,5], while a dynamic pool of actin appears to constantly shuttle between the nucleus and cytoplasm in an importin 9- and exportin 6-dependent manner[6]. Similarly, many actin-regulatory proteins have been described to enter the nuclear compartment[2]. More recently, using nuclear-targeted probes, the presence of F-actin structures was demonstrated in mammalian cell nuclei in response to serum, integrin signalling or DNA damage[7–9]. However, whether transient and dynamic nuclear actin filaments exert fundamental structural functions in somatic cells to spatially reorganize nuclear architecture has not been investigated[10].

Mitotic cell division relies on a complex cascade of mechanistic processes to precisely ensure maintenance of genomic organization and integrity in the emerging daughter cells. During mitotic exit, newly formed cells undergo a profound reorganization of their nuclear content to re-establish an interphase nucleus, which is accompanied by a striking expansion in nuclear size and volume[11,12]. Further key processes include the reformation of a nuclear envelope and lamina, assembly of nuclear pore complexes, and decondensation as well as reorganization of the highly condensed mitotic chromosomes[13,14]. Surprisingly, the cellular mechanisms, which drive nuclear expansion while reversing mitotic chromosomes into an interphase chromatin state, remain largely unexplored[11,15,16].

## RESULTS

### Transient nuclear F-actin assembly during mitotic exit

We recently reported an approach to monitor endogenous nuclear F-actin dynamics without detectable effects on nucleocytoplasmic shuttling or the polymerization state of actin[8]. Our live-cell-compatible approach relies on a transiently binding nanobody directed against actin fused to a nuclear localization signal (anti-actin-chromobody-GFP-NLS), herein referred to as nAC-GFP (nuclear actin-chromobody-GFP)[8]. While examining mouse fibroblasts stably

---

[1] Institute of Pharmacology, BPC Marburg, University of Marburg, Karl-von-Frisch-Str. 1, 35043 Marburg, Germany. [2] School of Cellular and Molecular Medicine, Biomedical Sciences, University of Bristol, University Walk, Bristol BS8 1TD, UK. [3] Faculty of Biology-Oriented Science and Technology, Kindai University, 930 Nishimitani, Wakayama 649-6493, Japan. [4] Department of Systems and Synthetic Microbiology, Max Planck Institute for Terrestrial Microbiology and LOEWE Center for Synthetic Microbiology (SYNMIKRO), Karl-von-Frisch-Str. 16, 35043 Marburg, Germany. [5] Electron Microscopy Unit, School of Chemistry, Biomedical Sciences, University of Bristol, Bristol BS8 1TS, UK. [6] Wolfson Bioimaging Facility, University of Bristol, Bristol BS8 1TD, UK. [7] Protein Analytics, Faculty of Biology, University of Marburg, Karl-von-Frisch-Str. 8, 35043 Marburg, Germany. [8] These authors contributed equally to this work.
[9] Correspondence should be addressed to R.G. (e-mail: robert.grosse@staff.uni-marburg.de)

Received 20 July 2017; accepted 5 October 2017; published online 13 November 2017; DOI: 10.1038/ncb3641

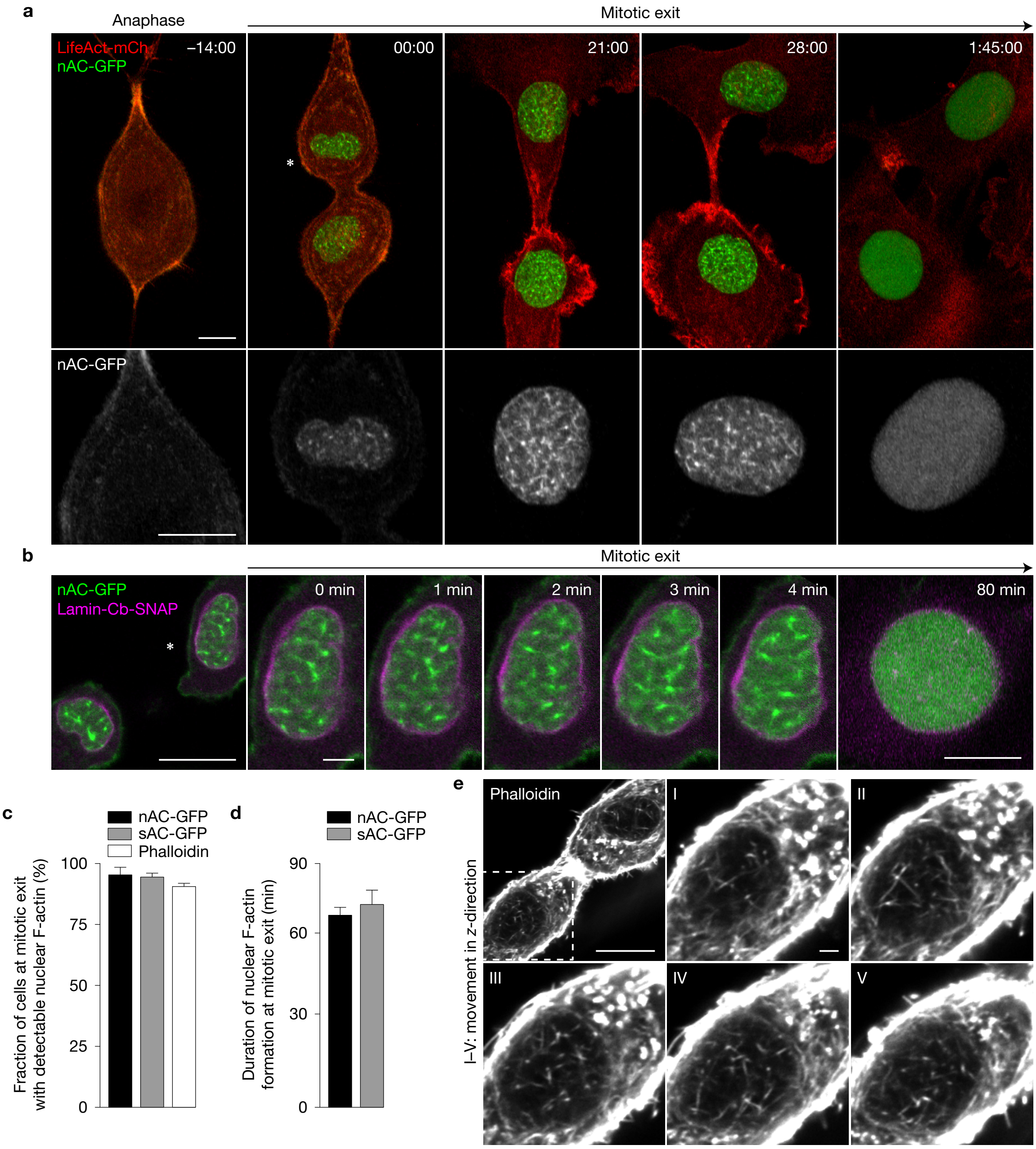

**Figure 1** Spatiotemporal features and dynamics of nuclear F-actin formation at mitotic exit. (**a**) Time-lapse imaging of NIH3T3 cells stably expressing nAC-GFP (nuclear actin-chromobody-GFP; anti-actin-chromobody-GFP-NLS, green, and grey in magnifications) together with LifeAct-mCherry (red) during anaphase and mitotic exit. The asterisk indicates a nucleus shown magnified in the lower panel. Images show maximum-intensity projections of confocal *z*-stacks. See also Supplementary Video 1. Scale bars, 10 μm; time stamp, h:min:s. (**b**) Live-cell imaging of NIH3T3 cells stably expressing nAC-GFP (green) together with lamin-Cb-SNAP (lamin-chromobody-SNAP, labelled by SiR-647, magenta) during mitotic exit. The nucleus indicated by an asterisk is shown magnified for individual time points. See also Supplementary Video 2. Scale bars, 10 μm (overview) and 1 μm (magnifications). (**c**,**d**) Quantification of incidence (**c**) and duration (**d**) of nuclear actin filament formation at mitotic exit using the indicated nuclear actin probes. Data are shown as mean + s.e.m. $n=60$ (nAC-GFP), $n=30$ (sAC-GFP, shuttling actin-chromobody-GFP), $n=60$ (phalloidin, formaldehyde fixation 70 min after mitotic shake-off) mitotic events, pooled from at least three independent experiments. (**e**) NIH3T3 cells at mitotic exit were fixed using glutaraldehyde and stained for actin filaments using phalloidin-Atto 488. The area indicated by a dashed square is shown magnified for individual confocal slices (I to V) in the *z*-direction with a step size of 0.37 μm. Scale bars, 10 μm (overview) and 1 μm (magnifications). Images in **a**,**b**,**e** are examples of at least five independent experiments.

expressing nAC-GFP together with LifeAct-mCherry to co-visualize cytoplasmic actin, we observed the striking and transient appearance of nuclear actin filament structures when daughter cell nuclei formed (Fig. 1a and Supplementary Video 1). These actin filaments were constantly and dynamically reorganized within the nuclear compartment (as visualized by a nanobody against lamin A/C), arguing for a spatiotemporal function during the final stages of cell division (Fig. 1b and Supplementary Video 2). Of note, nuclear actin concentrations appeared to be constant during exit from mitosis and were not affected by the presence of nAC (Supplementary Fig. 1a,b).

Cell-cycle-associated nuclear actin filaments could be detected and quantified using nAC-GFP or a shuttling actin-chromobody (sAC) with comparable frequencies (Figs 1c and 3a and Supplementary Video 3). Transient nuclear actin polymerization persisted for 60–70 min during early G1 phase, followed by filament disassembly during further progression into interphase (Fig. 1d and Supplementary Video 1). Importantly, we confirmed our observations by using the F-actin marker phalloidin in fixed, but otherwise native, untreated cells (Fig. 1e). Nuclear actin polymerization at mitotic exit could also be observed in MCF10A breast epithelial, RPE-1 retinal pigmented epithelial and HT1080 fibrosarcoma cells, arguing for a conserved feature among mammalian cell types (Supplementary Fig. 1c–e).

Mitotic nuclear actin filaments were not affected by silencing of the nucleoskeletal proteins emerin or lamin A/C (Supplementary Fig. 1f–h), or expression of a dominant-negative KASH (Klarsicht/ANC-1/Syne-1 homology) domain (Supplementary Fig. 1i), shown to disrupt the LINC (linker of nucleoskeleton and cytoskeleton) complex[17], suggesting that these filaments are different in origin and function from those forming during cell spreading and integrin-dependent signalling[8].

### Analysis of nuclear F-actin at mitotic exit using super-resolution microscopy

Next, cells stably expressing nAC fused to the photoconvertible fluorescent protein Dendra2 were imaged by photoactivated localization microscopy (PALM; Fig. 2a and Supplementary Fig. 2a). Under these conditions, 96% of all cells showed nuclear actin filaments at mitotic exit. Actin filaments were of several micrometre lengths with an apparent width of about 50–90 nm, which can be explained by single actin fibres stained with nAC-Dendra2 of about 10 nm width and thin bundles of about 2–5 fibre diameters convolved with the achieved PALM resolution of about 40 nm (Fig. 2b and Supplementary Fig. 2a,b).

To further investigate native cells, phalloidin staining was performed to confirm these findings using stochastic optical reconstruction microscopy (STORM) imaging on cells fixed at defined time points during mitotic exit (Supplementary Fig. 2c). This revealed nuclear actin fibres for up to 60 min after anaphase. The reduced background and improved resolution of 30 nm allowed us to detect a population of even thinner, 40-nm-wide nuclear actin filaments in addition to thicker, more bundled subsets of F-actin structures (Fig. 2c,d and Supplementary Fig. 2c).

### Postmitotic nuclear volume expansion requires nuclear actin polymerization

To gain insight into the functional role of nuclear F-actin formation in early G1, we visualized nuclear actin filaments together with a fluorescently labelled histone H2B to label the nuclear compartment. This revealed a substantial expansion of nuclear volume during the period of nuclear F-actin assembly as well as distinct nuclear protrusions associated with the emerging dynamic nuclear F-actin structures (Fig. 3a and Supplementary Video 4).

To assess a potential role of nuclear F-actin formation in reshaping the newly forming nuclei after cell division, we first tested for the effects of various pharmacological inhibitors of the actin cytoskeleton that were directly added under the microscope to cells exiting mitosis. The actin-depolymerizing agents cytochalasin D or latrunculin B robustly impaired nuclear volume expansion, while the Arp2/3 inhibitor CK-666 had no effect (Supplementary Fig. 3a,b).

As pharmacological agents interfere globally with actin dynamics, we aimed to directly assess the impact of nuclear actin by expression of its specific nuclear export factor exportin 6 to enhance nuclear export of actin monomers (Supplementary Fig. 1b)[15]. This resulted not only in a strongly reduced number of cells displaying nuclear F-actin during mitotic exit (Fig. 3b), but also in a significantly impaired volume expansion of daughter nuclei (Fig. 3c,d).

To more specifically address the role of polymerized nuclear actin, we generated cell lines stably expressing a doxycycline-inducible, nuclear-targeted version of the polymerization-deficient actin mutant actin$^{R62D}$ (NLS-BFP-actin$^{R62D}$)[8,18], to dilute the amount of polymerization-competent actin monomers within the nuclear compartment. Similarly to expression of exportin 6, this approach resulted in a strong reduction of nuclear actin filaments as well as impaired nuclear expansion compared with control cells expressing only BFP-NLS (Fig. 3e–g). To control for any effects potentially arising from an increased concentration of nuclear actin monomers, we additionally compared the effects of actin$^{R62D}$ with wild-type actin (actin$^{WT}$) instead of BFP. Given the potential limitations of fluorophore-tagged actin[19], we generated doxycycline-inducible Flag-NLS-actin constructs fused to a self-cleavable SNAP-tag, which allowed us to indirectly identify expression of these Flag-actin derivatives in live dividing cells (Supplementary Fig. 3c–f). Importantly, this experimental set-up confirmed our results (Fig. 3g); clearly demonstrating the critical need for a polymerization-competent pool of nuclear actin required for nuclear volume expansion.

Notably, the effects of nuclear F-actin on nuclear volume expansion were specific for cells at the mitotic exit, as no differences in nuclear volume could be detected among nuclei of cells arrested in interphase during induction of actin$^{R62D}$ expression (Supplementary Fig. 3g). Furthermore, global transcriptional inhibition by the CDK inhibitory drug flavopiridol during cell division did not affect the rate of daughter nuclei expansion (Supplementary Fig. 3h,i), excluding altered transcription as a cause of the observed phenotype.

Using atomic force microscopy (AFM) on isolated nuclei from synchronized live cells enabled us to visualize the structure of the nuclear surface in early G1 as well as interphase (Fig. 3h). This revealed a remarkably rough nuclear surface indicative of nuclear protrusions in postmitotic control cells expressing Flag-NLS-actin$^{WT}$, which were absent in Flag-NLS-actin$^{R62D}$-expressing nuclei displaying an overall much flatter nuclear surface (Fig. 3h,i). Similar nuclear protrusions were observed on postmitotic nuclei from untransfected cells. Of note, induction of chromatin decompaction by trichostatin A (TSA)-treatment of interphase nuclei[20] did not result in an increased nuclear surface roughness (Fig. 3h,j), arguing for a cell-cycle-specific phenomenon that critically depends on the involvement of nuclear F-actin formation in early G1.

### Nuclear actin assembly affects early G1 chromatin reorganization

While visualizing nuclear actin dynamics together with the histone H2B, we found nuclear F-actin to reside within interchromatin spaces

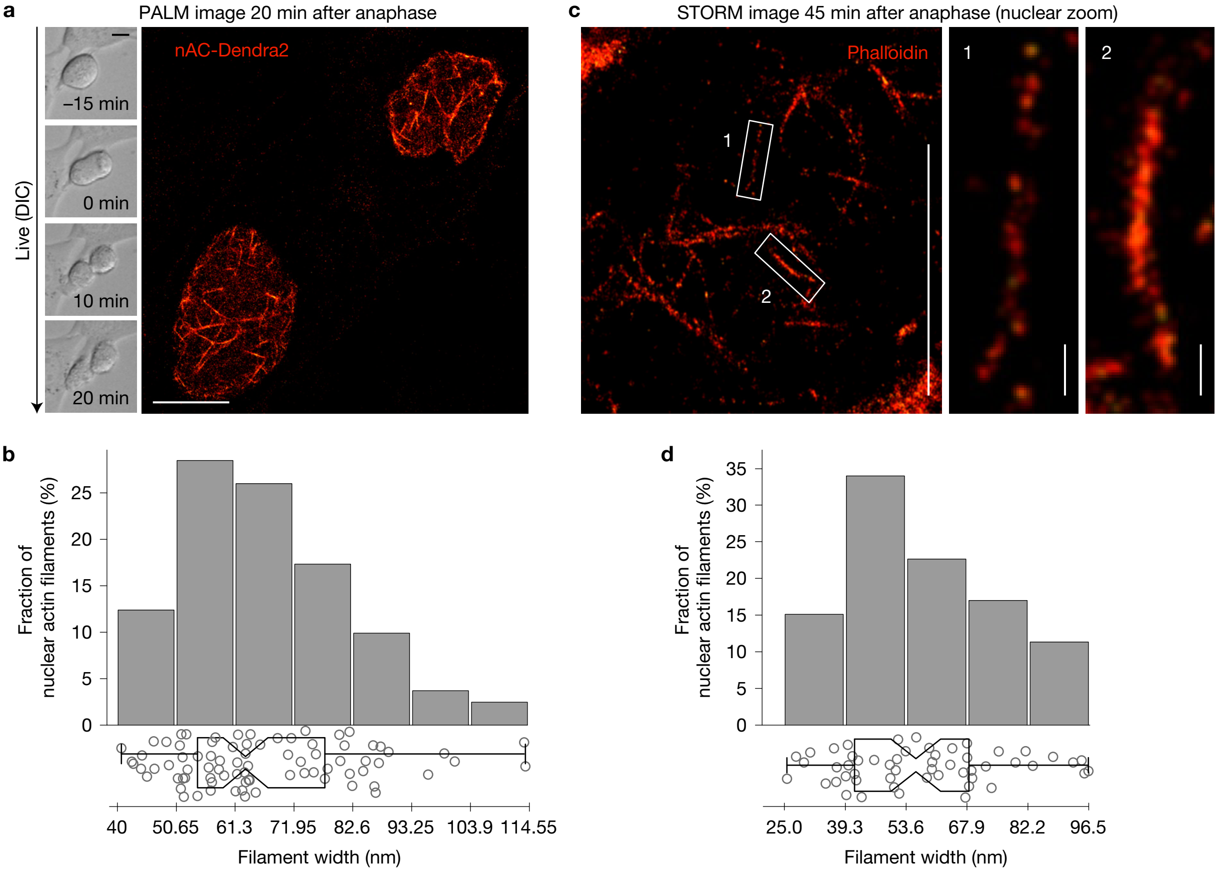

**Figure 2** Super-resolution microscopy reveals structural features of nuclear F-actin at mitotic exit. (**a**) Photoactivated localization microscopy (PALM) of nuclear actin filaments in fixed NIH3T3 cells stably expressing nAC-Dendra2 (anti-actin-chromobody-Dendra2-NLS, orange) at mitotic exit. DIC (differential interference contrast) images were acquired over time to monitor mitotic progression and to allow for time-defined fixation 20 min after anaphase. Experimental resolution after drift correction is 33 ± 1 nm. Scale bars, 5 μm. (**b**) Filament widths of nAC-Dendra2-labelled nuclear actin filaments ($n = 81$ filaments, data were pooled from at least three independent experiments) as histograms (top) with a bin size of 10.65 nm (*x* axis) plotted against frequency (*y* axis). Full data are represented underneath the histograms as box and scatter plots with the same *x* axis. The box marks the first and third quartiles and the indent represents the median. Whiskers mark minimal and maximal values. (**c**) Stochastic optical reconstruction microscopy (STORM) of phalloidin-stained nuclear actin filaments in native NIH3T3 cells at mitotic exit. The overview image focuses on a nucleus 45 min after anaphase (see also Supplementary Fig. 2c). The magnifications show representative thin (1) and thick (2) filaments with different labelling densities. Scale bars, 5 μm (overview) and 200 nm (magnifications). (**d**) Filament widths of phalloidin-labelled nuclear actin filaments ($n = 53$ filaments, data were collected from one experiment) as histograms (top) with a bin size of 14.3 nm (*x* axis) plotted against frequency (*y* axis). Full data are represented underneath the histograms as box + scatter plots with the same *x* axis. The box marks the first and third quartiles and the indent represents the median. Whiskers mark minimal and maximal values.

in the emerging daughter cell nuclei (Fig. 4a and Supplementary Video 3). This observation as well as the time period of nuclear actin polymerization during which chromatin decondensation takes place[12] prompted us to further investigate a potential role for F-actin in this process.

Quantifications of chromatin density assessed by three-dimensional (3D) H2B-mCherry fluorescence intensities revealed a significantly higher degree of chromatin compaction in postmitotic nuclei impaired for the assembly of nuclear F-actin either by expression of exportin 6 or nuclear-targeted actin$^{\mathrm{R62D}}$ (Fig. 4b–e).

To more directly measure the degree of chromatin compaction, we established a fluorescent lifetime imaging microscopy (FLIM) assay to determine fluorescence energy transfer (FRET) between GFP- and mCherry-tagged histone H2B (Supplementary Fig. 4a,b)[21]. Consistent with a role of nuclear F-actin in postmitotic chromatin dynamics, we found that induced expression of Flag-NLS-actin$^{\mathrm{R62D}}$ but not Flag-NLS-actin$^{\mathrm{WT}}$ (Fig. 4f,g), as well as expression of exportin 6 (Fig. 4h,i) resulted in a significantly reduced fluorescence lifetime of GFP-H2B in synchronized early G1 cells (Fig. 4f–i).

Given the conserved roles of increased histone H3 Ser10 phosphorylation (H3S10ph) and decreased histone H4 Lys16 acetylation (H4K16ac) in mitotic chromatin condensation[22], we confirmed the effects of altered nuclear F-actin assembly on chromatin reorganization by analysing these histone modifications in cells synchronized by mitotic shake-off. While control cells (BFP-NLS) re-established lower levels of H3S10ph and higher levels of H4K16ac within 90 min, cells expressing NLS-BFP-actin$^{\mathrm{R62D}}$ sustained mitotic levels of these histone modifications (Supplementary Fig. 4c). In addition, we found higher nuclear levels of Aurora B, a kinase responsible for H3S10 phosphorylation[23], as well as a lower levels of KAT5, known to mediate H4K16 acetylation[24], in cells expressing Flag-NLS-actin$^{\mathrm{R62D}}$ (Supplementary Fig. 4d,e). Consistently, chromatin obtained from cells exiting mitosis

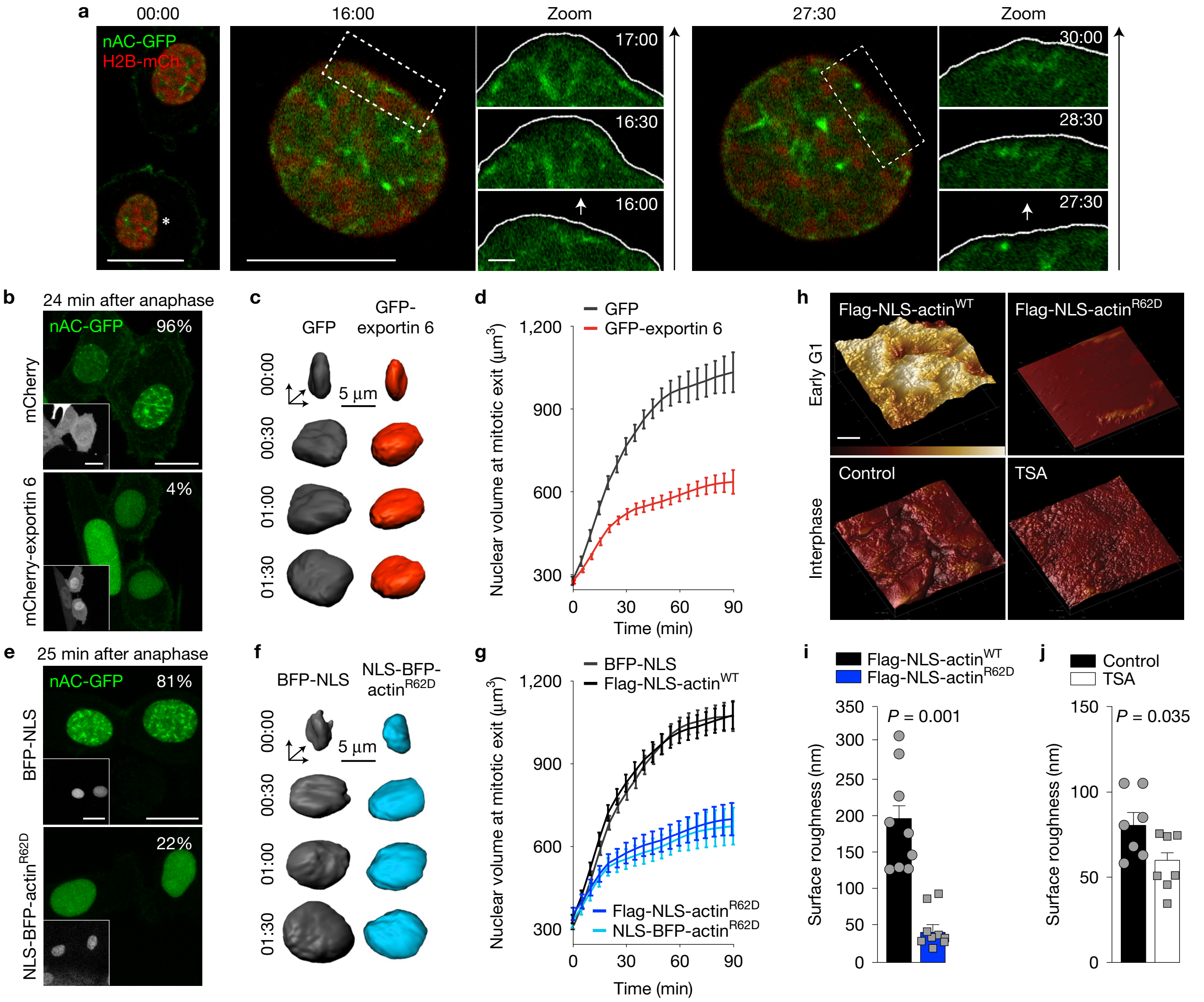

**Figure 3** Nuclear F-actin reshapes nuclei, and promotes nuclear volume expansion after mitotic cell division. (**a**) NIH3T3 cells stably expressing nAC-GFP and H2B-mCherry during mitotic exit. The asterisk indicates the nucleus shown for the additional time points. The dashed rectangles indicate areas of dynamic nuclear protrusions, shown magnified over time. The arrows indicate the direction of protrusions. See also Supplementary Video 4. Time stamp, min:s. (**b**) NIH3T3 cells expressing nAC-GFP, and mCherry or mCherry-exportin 6 (insets) after anaphase. The figures give the proportion of cells showing nuclear F-actin in the presence ($n = 15$) or absence ($n = 17$ mitotic events) of GFP-exportin 6, visualized by nAC-mCherry. (**c**) Nuclear expansion after anaphase (00:00), visualized by H2B-mCherry in NIH3T3 cells expressing GFP or GFP-exportin 6. Images are examples of quantifications in **d**, showing 3D surface reconstructions of daughter nuclei. Time stamp, h:min. (**d**) Quantification of nuclear volume during mitotic exit in NIH3T3 cells expressing either GFP or GFP-exportin 6. Data are shown as mean ± s.e.m. ($n = 30$ nuclei, pooled from four independent experiments). (**e**) NIH3T3 cells stably expressing nAC-GFP and doxycycline-induced BFP-NLS or NLS-BFP-actin$^{R62D}$ (insets) at mitotic exit. The figures give the proportion of cells showing nuclear F-actin ($n = 22$ (BFP-NLS), $n = 18$ (NLS-BFP-actin$^{R62D}$) mitotic events). (**f**) Visualization of nuclear expansion in NIH3T3 cells expressing doxycycline-induced BFP-NLS or NLS-BFP-actin$^{R62D}$ similar to **c**. Images are examples of quantifications in **g**. (**g**) Quantification of nuclear volume during mitotic exit in NIH3T3 cells expressing doxycycline-induced BFP-NLS or actin derivatives, as indicated. Data are shown as mean ± s.e.m. ($n = 60$ (BFP-NLS, NLS-BFP-actin$^{R62D}$), $n = 50$ (Flag-NLS-actin$^{WT}$, Flag-NLS-actin$^{R62D}$) nuclei, pooled from three independent experiments). (**h**) AFM images are examples of quantifications in **i** and **j**, showing nuclear surface morphology of isolated NIH3T3 nuclei. Early G1 nuclei were obtained from cells expressing Flag-NLS-actin$^{WT}$ or Flag-NLS-actin$^{R62D}$, whereas interphase nuclei were treated with or without TSA to induce chromatin decondensation. (**i**) Quantification of surface roughness of early G1 nuclei expressing Flag-NLS-actin$^{WT}$ or Flag-NLS-actin$^{R62D}$. Data are shown as mean ± s.e.m. ($n = 9$ nuclei per condition, pooled from two independent experiments). $P$ values were calculated by $t$-test. (**j**) Quantification of surface roughness of control or TSA-treated interphase nuclei. Data are shown as mean ± s.e.m. ($n = 7$ nuclei per condition, pooled from two independent experiments). $P$ values were calculated by $t$-test. Scale bars, 10 µm (**a**,**b**,**e**) or 1 µm (**h**, magnifications in **a**). Images in **a**,**b**,**e** are examples of at least three independent experiments.

and expressing NLS-BFP-actin$^{R62D}$ appeared more resistant to MNase digestion (Supplementary Fig. 4f), arguing for reduced chromatin accessibility.

Furthermore, electron microscopy of cryopreserved samples allowed us to directly quantify the amount of condensed chromatin, which appears as an electron-dense structure in unlabelled samples (Fig. 4j and Supplementary Fig. 4g). This approach confirmed a highly significant increase in the proportion of condensed chromatin at mitotic exit in cells expressing either nuclear-targeted actin$^{R62D}$ (Fig. 4j,k) or exportin 6 (Fig. 4l and Supplementary Fig. 4h) compared

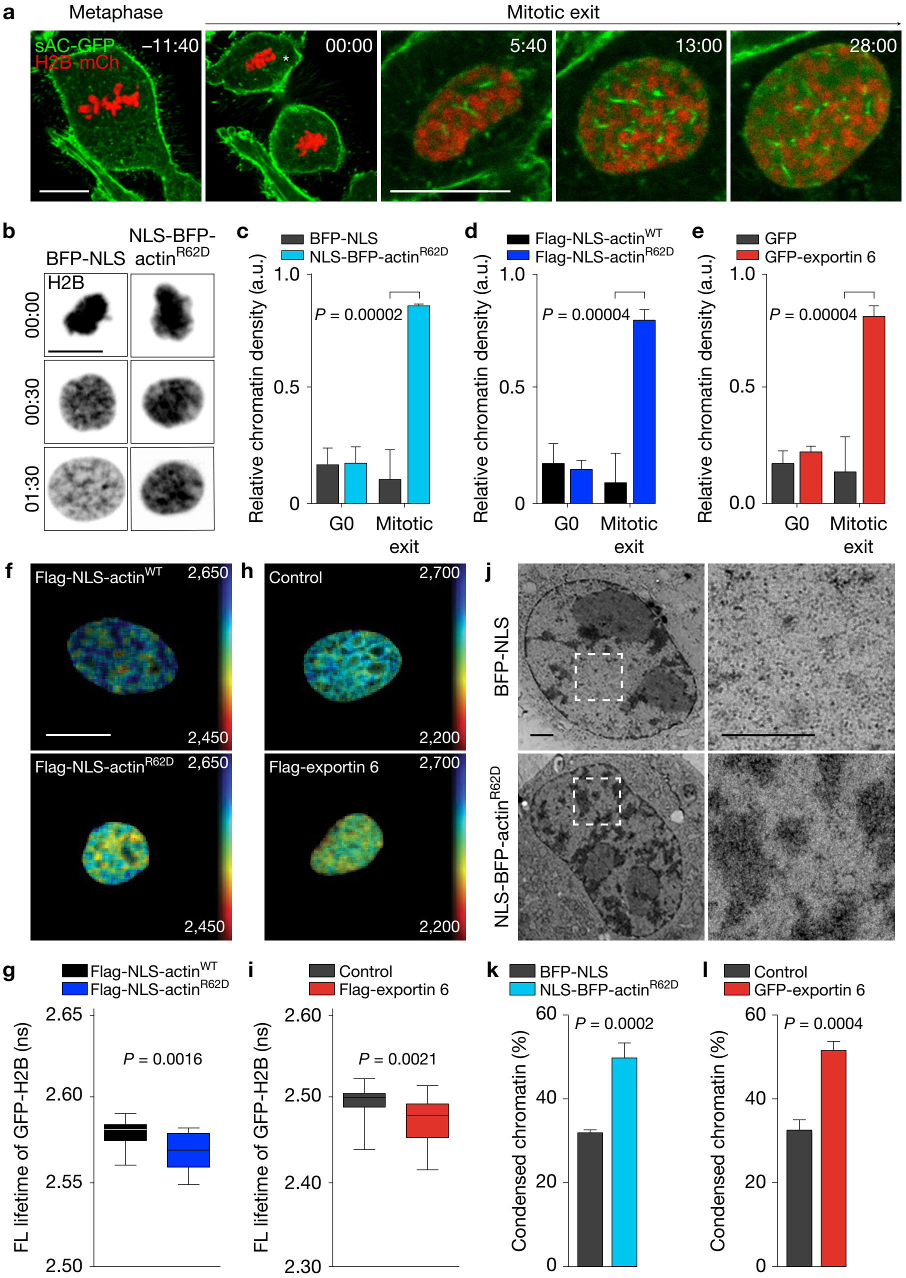

**Figure 4** Nuclear actin dynamics promote chromatin decondensation at mitotic exit. (**a**) NIH3T3 cells stably expressing a shuttling actin-chromobody (sAC-GFP, green) together with H2B-mCherry. The asterisk indicates the nucleus shown magnified for the additional time points to visualize nuclear F-actin within interchromatin spaces. The image series is one example of at least three independent experiments. See also Supplementary Video 3. Scale bars, 10 μm; time stamp, min:s. (**b**) Maximum-intensity projections of confocal *z*-stacks are examples of the quantifications in **c**, illustrating H2B-mCherry fluorescence densities (grey) during mitotic exit in NIH3T3 cells co-expressing BFP-NLS or NLS-BFP-actin$^{R62D}$. Scale bar, 10 μm; time stamp, h:min. (**c**–**e**) Chromatin densities of NIH3T3 cells were assessed in G0 or 90 min after anaphase (mitotic exit) and compared between expression of BFP-NLS and NLS-BFP-actin$^{R62D}$ (each $n = 60$ nuclei) (**c**), expression of Flag-NLS-actin$^{WT}$ and Flag-NLS-actin$^{R62D}$ (each $n = 50$ nuclei) (**d**) or expression of GFP and GFP-exportin 6 (each $n = 30$ nuclei) (**e**). In each panel, data are shown as mean + s.e.m. pooled from three independent experiments. *P* values were calculated by two-way ANOVA. (**f**–**i**) FLIM of FRET between GFP- and H2B-mCherry NIH3T3 cells at mitotic exit. Images in **f** and **h** are examples of quantifications in **g** and **i**. The colour code indicates fluorescence lifetime of GFP-H2B. Scale bar, 10 μm. (**g**,**i**) Quantifications of GFP-H2B fluorescence lifetime (Tau) in early G1 NIH3T3 cells expressing either Flag-NLS-actin$^{WT}$ or Flag-NLS-actin$^{R62D}$ (each $n = 20$) (**g**) or Flag-exportin 6 (each $n = 30$) (**i**). Data are shown as boxplot, pooled from three independent experiments. The box marks the first and third quartiles and the indent represents the median. Whiskers mark minimal and maximal values. *P* values were calculated by *t*-test. See also Supplementary Fig. 4a,b. (**j**) Electron microscopy images are examples of quantifications in **k**, showing cryopreserved, synchronized early G1 NIH3T3 cells induced to express BFP-NLS or NLS-BFP-actin$^{R62D}$. The areas indicated by a dashed square are shown magnified. Scale bar, 2 μm. (**k**,**l**) Quantifications of condensed chromatin based on EM images. Chromatin condensation was compared between control conditions and expression of either NLS-BFP-actin$^{R62D}$ (each $n = 30$) (**k**) or expression of GFP-exportin 6 ($n = 15$ (control), $n = 23$ (GFP-exportin 6)) (**l**). In each panel, data are shown as mean + s.e.m., pooled from two independent experiments. *P* values were calculated by *t*-test.

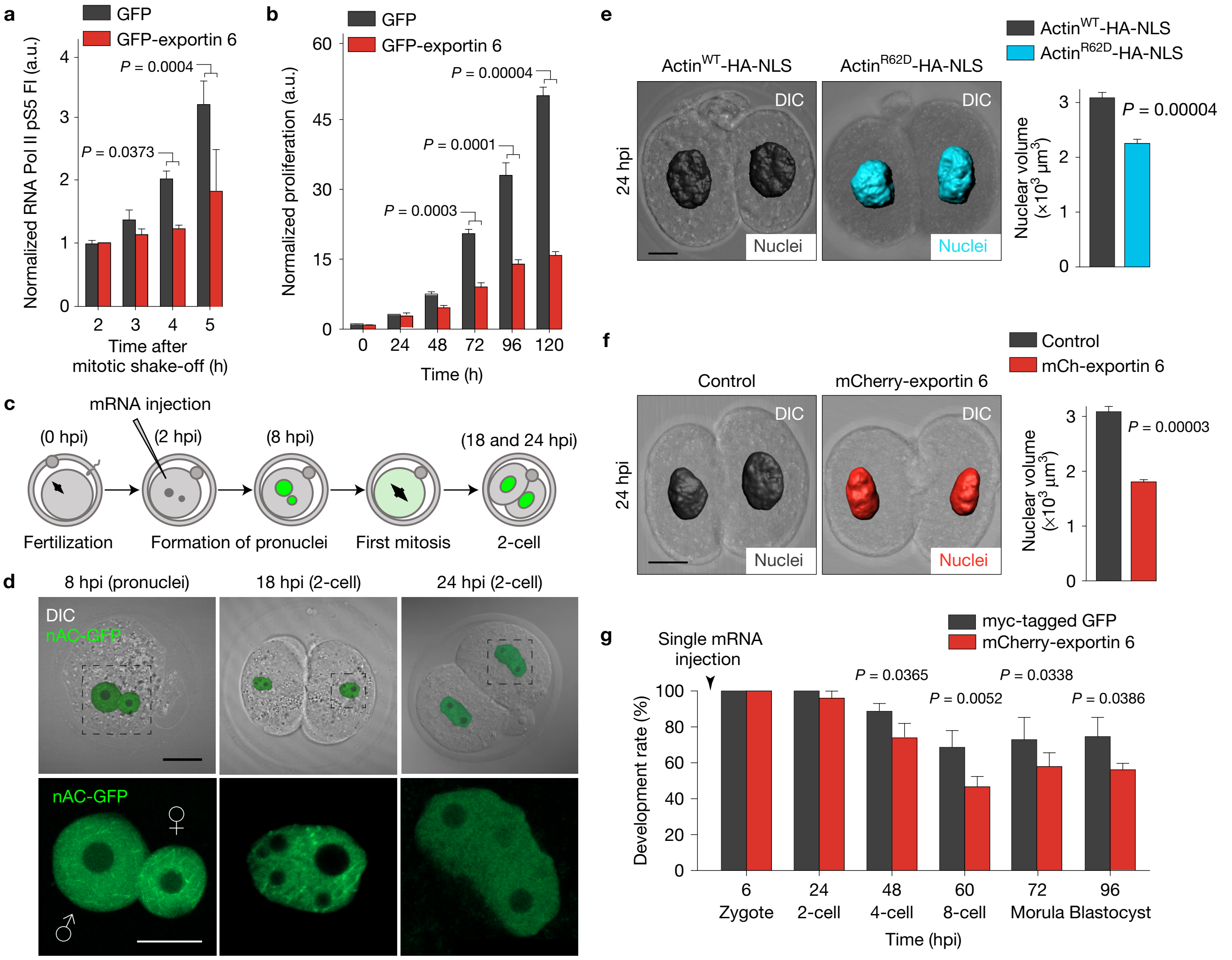

**Figure 5** Inhibition of nuclear F-actin formation impairs transcription, proliferation and early embryonic development. (**a**) 3D quantification of nuclear RNA Pol II pS5 fluorescence intensities in NIH3T3 cells expressing either GFP ($n=14$) or GFP-exportin 6 ($n=18$) at the indicated time points after mitotic shake-off. See also Supplementary Fig. 5a. Data are shown as mean + s.d. (pooled from two independent experiments). *P* values were calculated by two-way ANOVA. (**b**) Proliferation of NIH3T3 cells expressing either GFP or GFP-exportin 6 was measured using WST-1. Data were normalized to values of control cells at time 0 h and are shown as mean + s.e.m. from $n=3$ independent experiments. *P* values were calculated by two-way ANOVA. (**c**) Experimental scheme for studying nuclear F-actin in fertilized mouse embryos. At 2 hpi (hours post insemination) mRNA encoding for the indicated proteins was injected into fertilized embryos to either visualize or manipulate nuclear actin dynamics. (**d**) Image examples showing early embryo development at 8 hpi (pronuclei), 18 hpi and 24 hpi (2-cell). DIC, differential interference contrast. Nuclear F-actin corresponding to dashed squares is shown magnified below (nAC-GFP, green). Scale bars, 20 μm (overview) and 10 μm (magnifications). (**e**,**f**) Image examples and quantitative analysis of nuclear volume in two-cell embryos expressing either actin$^{\mathrm{R62D}}$-HA-NLS ($n=82$) or actin$^{\mathrm{WT}}$-HA-NLS ($n=54$) (**e**) or mCherry-exportin 6 ($n=84$, $n=118$ (control)) (**f**). Scale bars, 20 μm. Quantitative data are shown as mean + s.d. (pooled from three independent experiments). *P* values were calculated by *t*-test. (**g**) Preimplantation development of embryos after a single injection of mCherry-exportin 6 mRNA. Note the significant developmental delay at 48 hpi, 60 hpi, 72 hpi and 96 hpi compared with injection of mRNA encoding myc-tagged GFP. Data are shown as mean + s.e.m. from $n=3$ independent experiments. *P* values were calculated by chi-squared test. See also Supplementary Fig. 5b.

with control. Altogether, these data support a requirement for polymerization-competent nuclear actin to achieve proper chromatin organization after mitosis.

## Nuclear F-actin is formed and required for nuclear volume expansion in early mouse embryos

To gain insight into the biological consequences of impaired mitotic nuclear actin assembly, we determined general transcriptional activity by quantifying nuclear 3D RNA polymerase II phospho-Ser5 (pS5) fluorescence. This revealed strongly reduced transcriptional activity in cells expressing GFP-exportin 6 (Fig. 5a and Supplementary Fig. 5a) as well as significantly lower proliferation rates (Fig. 5b).

Next, we asked whether similar functions of nuclear F-actin are exerted during development. For this, we investigated fertilized mouse embryos, which rely on substantial chromatin decondensation of sperm and oocyte nuclei. Mouse fertilized embryos were injected with 150 ng nAC-GFP mRNA and analysed at the indicated time points post insemination (hpi) (Fig. 5c). Notably, nuclear actin filaments were readily detected in pronuclei, as well as in the early G1 phase after the first mitotic division (71.43%, 18 hpi) and disassembled following

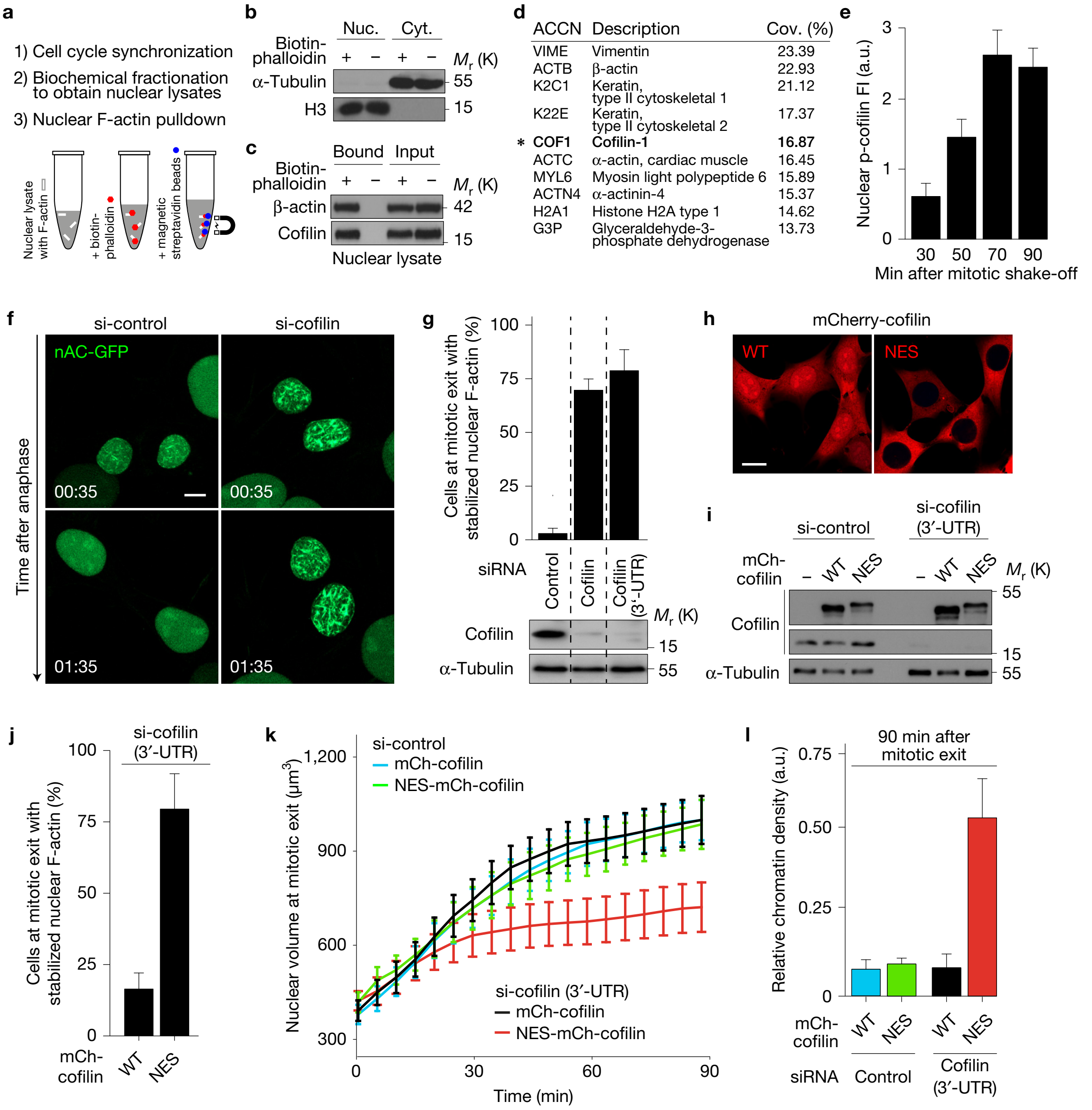

**Figure 6** Nuclear cofilin-1 regulates nuclear F-actin during mitotic exit. (**a**) Schematic diagram illustrating nuclear F-actin pulldown at mitotic exit. (**b**,**c**) Immunoblots on samples analysed by mass spectrometry. (**b**) Detection of α-tubulin and histone 3 (H3) confirms successful fractionation. (**c**) Detection of β-actin and cofilin-1 validates efficient F-actin pulldown and co-precipitation of cofilin-1. (**d**) Table listing nuclear F-actin-binding proteins as identified by mass spectrometry (cov., coverage). (**e**) 3D quantitative immunofluorescence analysis of nuclear p-cofilin at the indicated times after mitotic shake-off. Data are shown as mean + s.d. from $n = 30$ mitotic events for each time point. See also Supplementary Fig. 6a,b. (**f**) Time-lapse imaging shows nAC-GFP-expressing NIH3T3 cells transfected with si-control or si-cofilin at the indicated times after anaphase. See also Supplementary Video 5. Scale bar, 5 μm; time stamp, h:min. (**g**) Quantifications of stabilized nuclear F-actin (present for $\geq$2 h after anaphase) in NIH3T3 cells treated with the indicated siRNAs. Data are shown as mean + s.d. ($n = 49$ (si-control), $n = 58$ (si-cofilin), $n = 59$(si-cofilin (3′-UTR)) mitotic events, pooled from three independent experiments). Immunoblot confirms efficient silencing of cofilin-1. (**h**) Confocal images of fixed NIH3T3 cells stably expressing WT- or NES-mCherry-cofilin. Scale bar, 10 μm. (**i**) Immunoblot of NIH3T3 cells stably expressing WT- or NES-mCherry-cofilin confirms siRNA (si-cofilin (3′ UTR)) -resistant expression of mCherry-cofilin derivatives. (**j**) Quantifications of stabilized nuclear F-actin (present for $\geq$2.5 h after anaphase) in NIH3T3 cells treated with si-cofilin (3′-UTR) in the presence of either WT- or NES-mCherry-cofilin. Data are shown as mean + s.d. ($n = 30$ (WT), $n = 38$ (NES) mitotic events, pooled from three independent experiments). (**k**) Quantifications of nuclear volume during mitotic exit in NIH3T3 cells treated with si-control or si-cofilin (3′-UTR) in the presence of either WT- or NES-mCherry-cofilin. Data are shown as mean + s.d. ($n = 50$ nuclei per condition, pooled from three independent experiments). (**l**) NIH3T3 cells expressing WT- or NES-mCherry-cofilin were treated with si-control or si-cofilin (3′-UTR) and chromatin densities were assessed 90 min after anaphase. Data are shown as mean + s.e.m. ($n = 50$ nuclei per condition, pooled from three independent experiments). Unprocessed original scans of blots are shown in Supplementary Fig. 7. All immunoblots were performed once.

further cell-cycle progression of the two-cell embryos (25%, 24 hpi) (Fig. 5d). Of note, expression of actin$^{R62D}$-HA-NLS or exportin 6 inhibited nuclear volume expansion after the first mitotic division (Fig. 5e,f), consistent with our findings in mammalian somatic cells. Furthermore, a significant developmental delay was observed in exportin 6 mRNA-injected embryos (Fig. 5g and Supplementary

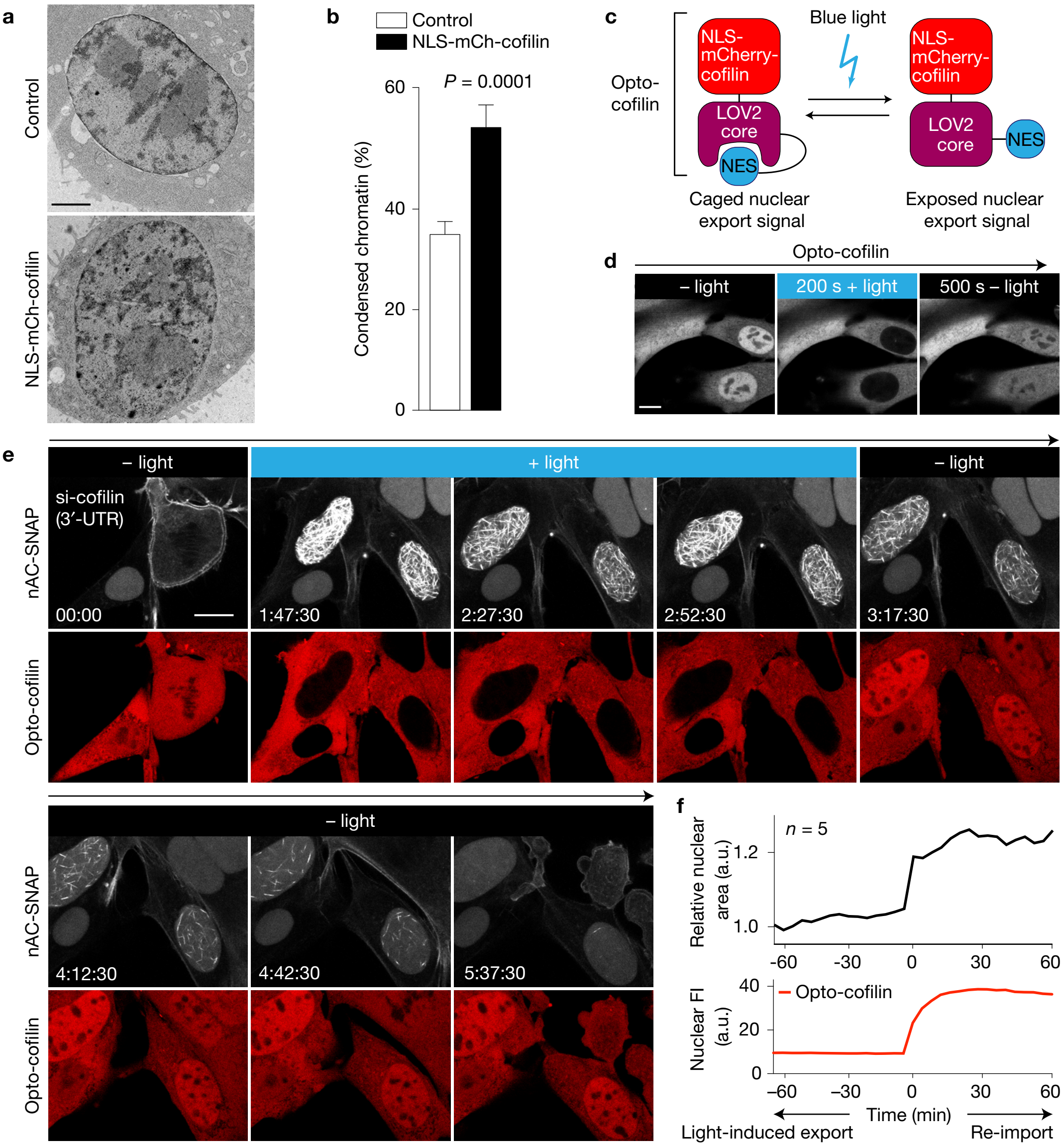

**Figure 7** Nuclear cofilin-1 affects chromatin organization and its optogenetic control reveals critical functions in nuclear F-actin disassembly at mitotic exit. (**a**) Electron microscopy images are examples of quantifications in **b**, showing cryopreserved NIH3T3 cells at mitotic exit in the absence or presence of NLS-mCherry-cofilin. Scale bar, 2 μm. (**b**) Quantifications of condensed chromatin based on EM images. Data are shown as mean + s.e.m., pooled from two independent experiments ($n=15$ (control), $n=21$ (NLS-mCherry-cofilin)). $P$ values were calculated by $t$-test. (**c**) Schematic diagram illustrating the design and photoconvertibility of opto-cofilin. Blue light induces exposure of a photocaged NES (nuclear export sequence), thereby promoting its nuclear export. (**d**) Time-lapse imaging of NIH3T3 cells demonstrates light-regulated control of opto-cofilin subcellular localization. NIH3T3 cells stably expressing opto-cofilin (grey) were imaged at 10 s intervals either with (+ light) or without (– light) additional irradiation by blue laser light (488 nm). See also Supplementary Video 6. Scale bar, 10 μm. (**e**) Image examples of quantifications in **f**. NIH3T3 cells stably expressing nAC-SNAP (labelled by SiR-647, grey) and opto-cofilin (red) were treated with si-cofilin (3′-UTR) and imaged during and after mitosis. To promote nuclear export of opto-cofilin, cells were exposed to blue laser light (488 nm) at 2.5 min intervals (+ light). Note the excessive formation of stabilized nuclear F-actin in the absence of nuclear cofilin as well as the onset of filament disassembly coinciding with controlled nuclear re-import of opto-cofilin (– light). See also Supplementary Video 8. Scale bar, 10 μm. (**f**) Nuclear fluorescence intensities of opto-cofilin (red line) and relative nuclear area (black line) were quantified before and during light-regulated re-import of opto-cofilin. Nuclear re-import of opto-cofilin is accompanied by nuclear shape changes and overall nuclear expansion. Data are shown as mean from $n=5$ nuclei.

Fig. 5b), providing further evidence for a physiological role of nuclear F-actin assembly in the early steps of mouse embryo development.

### Cofilin-1 controls nuclear F-actin assembly, volume expansion and chromatin organization in daughter cell nuclei

As short interfering RNA (siRNA) against several known actin assembly factors had no obvious effect on nuclear F-actin formation (Supplementary Table 1) and to gain further mechanistic insight, we performed a proteomic screen using biotin-phalloidin to identify potential nuclear F-actin-binding proteins from nuclear fractions of cells released from a mitotic nocodazole arrest (Fig. 6a,b). Hereby, we identified the F-actin disassembly factor cofilin-1 as a candidate interactor (Fig. 6c,d and Supplementary Table 1). Since cofilin-1 is inactivated by phosphorylation on Ser3 (p-cofilin)[25], we analysed nuclear p-cofilin levels by measuring 3D nuclear fluorescence intensities in synchronized NIH3T3 cells and observed a pronounced increase in nuclear p-cofilin levels during mitotic exit, revealing cofilin-1 as a cell-cycle-controlled nuclear actin regulator (Fig. 6e and Supplementary Fig. 6a–d). Indeed, and consistent with the role of cofilin-1 in F-actin disassembly, siRNA against cofilin-1 resulted in a pronounced stabilization of nuclear F-actin during mitotic exit (Fig. 6f,g and Supplementary Video 5).

To specifically address the nuclear function of cofilin-1 during this cell-cycle phase, we generated cells expressing either wild-type (WT-cofilin) or cytoplasm-targeted cofilin-1 (NES-cofilin; NES, nuclear export signal) resistant to siRNA targeting (Fig. 6h,i). Imaging mitotic cells revealed that after silencing of endogenous cofilin-1, cells devoid of its nuclear localization failed to prevent extensive nuclear F-actin stabilization during mitotic exit (Fig. 6j and Supplementary Fig. 6e), similarly to depletion of total cofilin-1 (Fig. 6g). Consistent with deregulated actin filament dynamics and turnover, this resulted in defective nuclear volume expansion (Fig. 6k) and chromatin decompaction (Fig. 6l), underscoring the critical importance of dynamic F-actin reorganization for the processes of nuclear volume expansion and chromatin reorganization.

### Optogenetic control of cofilin-1 establishes its role in reorganizing daughter cell nuclei after mitosis

To corroborate our findings that nuclear cofilin-1 controls chromatin dynamics, we expressed a nuclear-targeted version of cofilin-1 (NLS-cofilin) to inhibit nuclear F-actin formation in early G1 (Supplementary Fig. 6f), and observed a striking defect in establishing open chromatin in cryopreserved electron microscopy (EM) samples (Fig. 7a,b).

To directly and reversibly control cofilin-1 function within the nucleus in real time, we generated an optogenetic cofilin-1 (opto-cofilin) (Fig. 7c) based on a previously described light-inducible nuclear export system[26]. Under control conditions, opto-cofilin exhibited a subcellular distribution similar to that of WT-cofilin, but allowed for rapid and efficient light-induced nuclear export within 200 s, which could be reverted within 500 s after illumination was switched off (Fig. 7d and Supplementary Video 6).

In cells silenced for endogenous cofilin-1 (Supplementary Fig. 6g), light-induced nuclear export of opto-cofilin resulted in extensive stabilization of nuclear F-actin during mitotic exit (Fig. 7e and Supplementary Videos 7 and 8), while its timely controlled nuclear re-accumulation, by switching off illumination, triggered rapid reorganization and successive disassembly of nuclear F-actin (Fig. 7e and Supplementary Video 8). Notably, light-controlled export of opto-cofilin during mitotic exit also resulted in arrested growth of daughter cell nuclei, while nuclear re-import of opto-cofilin promoted their further volume expansion (Fig. 7f).

Together, these results uncover a critical nuclear-specific function of cofilin-1 in spatiotemporally controlling actin dynamics for nuclear reorganization in the early phases after mitotic cell division.

## DISCUSSION

Here, we discovered dynamic and transient F-actin assembly in the growing nuclei of daughter cells exiting mitosis. The mechanisms and cellular factors that determine nuclear volume regulation are poorly understood[11]. Our data reveal a key function for nuclear actin filaments in nuclear volume and chromatin expansion during mitotic exit as well as a critical nuclear function of cofilin-1 in tightly controlling the spatiotemporal turnover of these actin filaments. As such, nuclear reorganization during mitotic exit is impaired by loss of polymerization-competent nuclear actin as well as excessive nuclear F-actin formation, illustrating that the dynamic interplay between polymerization and depolymerization of nuclear F-actin appears to be critical during this cell-cycle-specific process. Accordingly, it is tempting to speculate that additional actin-regulatory factors as well as actin bundling proteins are involved in nuclear actin assembly during early G1.

Since cytoskeletal actin dynamics are well known to exert contractile and mechanical forces to shape or move a variety of cellular components[27] and in light of our observation of F-actin-dependent nuclear protrusions, one may envisage similar functions for nuclear F-actin during mitotic exit in rearranging the chromatin and nuclear content of mammalian cells. Thus, future work will be directed to dissect whether the role for nuclear actin in promoting efficient reorganization of chromatin is primarily exerted through direct effects of F-actin on chromatin, or more indirectly through expanding and reshaping the nuclear compartment, or both.

Our findings thus open a perspective to gain a better understanding of nuclear actin filament dynamics and its role in regulating spatiotemporal chromatin organization and maintenance of a defined nuclear architecture, all of which have profound implications for genome stability and regulation in health and disease. □

## METHODS

Methods, including statements of data availability and any associated accession codes and references, are available in the online version of this paper.

*Note: Supplementary Information is available in the online version of the paper*

ACKNOWLEDGEMENTS

We thank members of our laboratory for discussions, P. Chinchilla, G. Pathria, M. Losekam, A. Takasu, H. Hatano, K. Matsumoto and K. Yamagata for technical assistance, A. Herman and L. S. Ballesteros for cell sorting and B. Di Ventura for critical reading of the manuscript. This work was funded by an HFSP collaborator programme grant RGP0021/2016-GROSSE to K.M., A.K. and R.G. Work in the R.G. laboratory is supported by the Deutsche Forschungsgemeinschaft (DFG) (GR 2111/7-1), and the Wilhelm-Sander-Stiftung 2013.149.1. A.K. is funded by a MRC New Investigator Award (MR/N000013/1) and a Wellcome Trust Seed Awards in Science (WT107789AIA). K.M. is funded by JSPS KAKENHI grants (JP16H01321, JP16H01222). AFM was carried out in the Chemical Imaging Facility, University of Bristol, funded by EPSRC (EP/K035746/1), and FLIM was carried out at the Wolfson Bioimaging Facility, University of Bristol, a BBSRC/EPSRC-funded Synthetic Biology Research Centre (L01386X).

AUTHOR CONTRIBUTIONS

C.B., M.P. and R.G. conceived the study. C.B., M.P. and A.S. performed and analysed most of the experiments with help from R.G. and A.K.; R.H. assisted in AFM, D.A. in FLIM data fitting; K.Morita, S.M. and K.Miyamoto performed experiments on fertilized mouse embryos; E.M.K., D.V. and U.E. performed PALM/STORM, and S.B. mass spectrometry. R.G. and C.B. wrote the manuscript.

COMPETING FINANCIAL INTERESTS

The authors declare no competing financial interests.

1. Bezanilla, M., Gladfelter, A. S., Kovar, D. R. & Lee, W.-L. Cytoskeletal dynamics: a view from the membrane. *J. Cell Biol.* **209,** 329–337 (2015).
2. Grosse, R. & Vartiainen, M. K. To be or not to be assembled: progressing into nuclear actin filaments. *Nat. Rev. Mol. Cell Biol.* **14,** 693–697 (2013).
3. Belin, B. J. & Mullins, R. D. What we talk about when we talk about nuclear actin. *Nucleus* **4,** 291–297 (2013).
4. Kapoor, P., Chen, M., Winkler, D. D., Luger, K. & Shen, X. Evidence for monomeric actin function in INO80 chromatin remodeling. *Nat. Struct. Mol. Biol.* **20,** 426–432 (2013).
5. Cao, T. *et al.* Crystal structure of a nuclear actin ternary complex. *Proc. Natl Acad. Sci. USA* **113,** 8985–8990 (2016).
6. Virtanen, J. A. & Vartiainen, M. K. Diverse functions for different forms of nuclear actin. *Curr. Opin. Cell Biol.* **46,** 33–38 (2017).
7. Baarlink, C., Wang, H. & Grosse, R. Nuclear actin network assembly by formins regulates the SRF coactivator MAL. *Science* **340,** 864–867 (2013).
8. Plessner, M., Melak, M., Chinchilla, P., Baarlink, C. & Grosse, R. Nuclear F-actin formation and reorganization upon cell spreading. *J. Biol. Chem.* **290,** 11209–11216 (2015).
9. Belin, B. J., Lee, T. & Mullins, R. D. DNA damage induces nuclear actin filament assembly by Formin -2 and Spire-1/2 that promotes efficient DNA repair. [corrected]. *Elife* **4,** e07735 (2015).
10. Plessner, M. & Grosse, R. Extracellular signaling cues for nuclear actin polymerization. *Eur. J. Cell Biol.* **94,** 359–362 (2015).
11. Webster, M. *et al.* Sizing up the nucleus: nuclear shape, size and nuclear-envelope assembly. *J. Cell Sci.* **122,** 1477–1486 (2009).
12. Gerlich, D., Beaudouin, J., Gebhard, M., Ellenberg, J. & Eils, R. Four-dimensional imaging and quantitative reconstruction to analyse complex spatiotemporal processes in live cells. *Nat. Cell Biol.* **3,** 852–855 (2001).
13. Schooley, A., Vollmer, B. & Antonin, W. Building a nuclear envelope at the end of mitosis: coordinating membrane reorganization, nuclear pore complex assembly, and chromatin de-condensation. *Chromosoma* **121,** 539–554 (2012).
14. Burke, B. & Ellenberg, J. Remodelling the walls of the nucleus. *Nat. Rev. Mol. Cell Biol.* **3,** 487–497 (2002).
15. Strzelecka, M. & Heald, R. RUVs drive chromosome decondensation after mitosis. *Dev. Cell* **31,** 259–260 (2014).
16. Magalska, A. *et al.* RuvB-like ATPases function in chromatin decondensation at the end of mitosis. *Dev. Cell* **31,** 305–318 (2014).
17. Lombardi, M. L. *et al.* The interaction between nesprins and sun proteins at the nuclear envelope is critical for force transmission between the nucleus and cytoskeleton. *J. Biol. Chem.* **286,** 26743–26753 (2011).
18. Posern, G., Sotiropoulos, A. & Treisman, R. Mutant actins demonstrate a role for unpolymerized actin in control of transcription by serum response factor. *Mol. Biol. Cell* **13,** 4167–4178 (2002).
19. Chen, Q., Nag, S. & Pollard, T. D. Formins filter modified actin subunits during processive elongation. *J. Struct. Biol.* **177,** 32–39 (2012).
20. Kaidi, A. & Jackson, S. P. KAT5 tyrosine phosphorylation couples chromatin sensing to ATM signalling. *Nature* **498,** 70–74 (2013).
21. Llères, D., James, J., Swift, S., Norman, D. G. & Lamond, A. I. Quantitative analysis of chromatin compaction in living cells using FLIM–FRET. *J. Cell Biol.* **187,** 481–496 (2009).
22. Wilkins, B. J. *et al.* A cascade of histone modifications induces chromatin condensation in mitosis. *Science* **343,** 77–80 (2014).
23. Wei, Y., Yu, L., Bowen, J., Gorovsky, M. A. & Allis, C. D. D. Phosphorylation of histone H3 is required for proper chromosome condensation and segregation. *Cell* **97,** 99–109 (1999).
24. Kimura, A. & Horikoshi, M. Tip60 acetylates six lysines of a specific class in core histones *in vitro*. *Genes Cells* **3,** 789–800 (1998).
25. Mizuno, K. Signaling mechanisms and functional roles of cofilin phosphorylation and dephosphorylation. *Cell. Signal.* **25,** 457–469 (2013).
26. Niopek, D., Wehler, P., Roensch, J., Eils, R. & Di Ventura, B. Optogenetic control of nuclear protein export. *Nat. Commun.* **7,** 10624 (2016).
27. Blanchoin, L., Boujemaa-Paterski, R., Sykes, C. & Plastino, J. Actin dynamics, architecture, and mechanics in cell motility. *Physiol. Rev.* **94,** 235–263 (2014).

DOI: 10.1038/ncb3641

## METHODS

**Antibodies and reagents.** Cell culture and transfection reagents (Lipofectamine 2000 and RNAiMax) were obtained from Invitrogen.

Rhodamine-phalloidin, biotin-phalloidin, phalloidin-AF647 and phalloidin-Atto 488 were purchased from Life Technologies. SNAP-Cell 647-SiR was obtained from NEB. SiR-DNA was from Spirochrome. CK-666, cytochalasin D, dimethylsulfoxide, doxycycline, latrunculin B and nocodazole were from Sigma-Aldrich and used at the indicated concentrations. Flavopiridol was obtained from Santa Cruz and used at a final concentration of 1 μM.

Information on the antibodies used is listed in Supplementary Table 3.

**Plasmids and constructs.** The generation of nuclear actin-chromobody-GFP (nAC-GFP, anti-actin-chromobody-GFP-NLS) and sAC was described previously[8]. The nuclear actin-chromobody is a genetically encoded, NLS-tagged nanobody against the actin protein. Due to its NLS-fusion, the nuclear actin-chromobody is enriched in the nuclei of interphasic cells. Nuclear envelope breakdown in prophase is accompanied by a temporary loss of its specific nuclear localization, which re-establishes during mitotic exit and daughter nuclei assembly.

nAC-Dendra2, nAC-mCherry and nAC-SNAP were generated by replacing the GFP of pWPXL-nAC-GFP by either pDendra2 (Clontech Laboratories), mCherry or the SNAP-tag (New England Biolabs).

To obtain a lamin-nanobody fused to the SNAP-tag, the tagRFP2 of pLC-TagRFP2 (ChromoTek) was replaced by a cDNA encoding the SNAP-tag. For stable expression of lamin-nanobody-SNAP, the corresponding cDNA was subcloned into pWPXL using the MluI/SpeI restriction sites.

For stable expression of H2B-mCherry, the GFP of pWPXL was replaced by mCherry, before insertion of a cDNA encoding human H2B via the BamHI/MluI restriction sites.

For generation of tagRFP-KASH, the cDNA of murine Nesprin-1α was amplified as described previously[17]. KASH was expressed from the EFpLink plasmid carrying an N-terminal tagRFP.

The cDNA of human exportin 6 was obtained by reverse transcription of total mRNA obtained from HeLa cells. Exportin 6 was expressed from the EFpLink plasmid carrying an N-terminal Flag-, Flag-GFP- or mCherry-tag.

To obtain mCherry-cofilin plasmids for lentiviral transductions, the cDNA of mouse cofilin-1 (kindly provided by M. Rust, University of Marburg, Germany) was N-terminally fused to mCherry and cloned into pWPXL via MluI/SpeI. For NES-mCherry-cofilin the NES (nuclear export signal) of HIV1-Rev (LPPLERLTL) was fused to the N terminus of mCherry. Opto-cofilin was generated by addition of the cMyc$^{P1A}$ NLS (AAAKRVKLD) to the N terminus of mCherry-cofilin and a C-terminal fusion to the LEXY module[26]. Opto-cofilin was inserted into pWPXL via MluI/SpeI to allow for production of lentiviral particles.

To obtain NLS-BFP-actin$^{R62D}$, the SV40 large T antigen NLS (PPKKKRKV) was N-terminally fused to tagBFP2 (separated by one linking glycine), which was further fused to the N terminus of actin$^{R62D}$ (ref. 18), separated by a SGLRSRA linker. For BFP-NLS, the cDNA encoding tagBFP2 was C-terminally fused to the SV40 large T antigen NLS, separated by a GDPPVAT linker. To obtain Flag-NLS-actin-T2A-SNAP derivatives, a cDNA encoding human β-actin (either wild-type or containing the point mutation R62D) was N-terminally fused to a Flag-tag and the SV40 large T antigen NLS (separated by a BamH1 restriction site) and C-terminally linked to a SNAP-tag by a self-cleaving T2A peptide (GSGEGRGSLLTCGDVEENPGP). To allow for stable doxycycline-inducible expression of NLS-BFP-actin$^{R62D}$, BFP-NLS or Flag-NLS-actin-T2A derivatives, the corresponding cDNAs were inserted into the pInducer20 plasmid[28] by homologous recombination using the Gateway technology (Invitrogen). LifeAct-mCherry lentiviral particles were a gift from O. Fackler (University of Heidelberg, Germany).

**Cell culture, viral transductions, transfections and treatments.** NIH3T3, HT1080, RPE-1 cells and all of their derivatives were grown in DMEM supplemented with 10% FCS (fetal calf serum), 100 U ml$^{-1}$ penicillin and 100 mg ml$^{-1}$ streptomycin at 37 °C in a 5% $CO_2$ atmosphere. MCF10A cells and derivatives were cultured as described previously[29]. The original source of each cell line was ATCC. None of the cell lines used are listed in the ICLAC database. Cell lines were not authenticated on a molecular level. Cells were tested monthly and controlled for mycoplasma contamination throughout the course of the study.

Lentiviral transductions were performed as previously described[8].

Transient transfections of exportin 6 or tagRFP-KASH were carried out using Lipofectamine LTX&PLUS Reagent according to the manufacturer's instructions. Transfection of siRNAs and sequences for si-emerin and si-lamin A/C have been described previously[8]. In addition, the following siRNAs were obtained from Qiagen: 3′-CCGCTGCACCCTGGCAGAGAA-5′ (si-cofilin), 3′-TGCCAACTTC TAACCACAATA-5′ (si-cofilin (3′-UTR)) and TTGGACTATCTGACAAGTAAA (si-exportin 6). Sequences of siRNAs used to obtain the data presented in Supplementary Table 1 are shown within the table.

SNAP-Cell 647-SiR and SiR-DNA were used according to the manufacturer's instructions.

Induction of BFP-NLS, NLS-BFP-actin$^{R62D}$ or Flag-NLS-actin-T2A-SNAP derivatives was achieved by addition of 0.5 μg ml$^{-1}$ doxycycline for 16 h to the cell culture medium. NIH3T3 cells were arrested in G0 phase by serum starvation (growth medium without FCS) for at least 16 h.

**Immunofluorescence and phalloidin staining.** For immunofluorescence stainings, cells were grown on coverslips, before fixation using 4% formaldehyde (15 min at room temperature). Immunolabelling was performed as described previously[29].

For phalloidin staining in Fig. 1e, cells were fixed using glutaraldehyde according to ref. 7. Phalloidin staining for the quantification shown in Fig. 1c and for super-resolution microscopy (Fig. 2c,d and Supplementary Fig. 2c) was performed on formaldehyde-fixed samples (4% for 15 min at room temperature). After washing with PBS, samples were incubated with phalloidin-AF647 or phalloidin-Atto 488 at 4 °C for 96 h. For super-resolution microscopy, samples were post-fixed using 1% formaldehyde for 10 min at room temperature.

**Image acquisition and live-cell imaging.** All confocal image acquisitions were performed on an LSM 700 or LSM 800 confocal laser scanning microscope (Zeiss) equipped with a 63×/1.4 NA oil objective. For live-cell imaging, cells were cultured in μ-slides (ibidi) at 37 °C in a 5% $CO_2$ atmosphere using a humidified incubation chamber (Pecon).

Experiments with opto-cofilin were carried out using the LSM 800 microscope. To induce nuclear export of opto-cofilin, the excitation of mCherry (555 nm) was combined with 488 nm irradiation at 1% laser power and a pixel dwell of 2.06 μs.

**Image processing and quantification of nuclear volumes, chromatin densities and 3D fluorescence intensities.** Image processing was performed with IMARIS (Bitplane), FIJI (NIH) and Photoshop CS6 (Adobe).

For quantification of nuclear volume in living NIH3T3 cells, images were acquired every 2.5 or 5 min over an interval of 90 min. Complete $z$-stacks of the signal obtained by either H2B-mCherry (Fig. 3c,d,f,g) or SiR-DNA (Fig. 6k and Supplementary Fig. 3a,b) were analysed with IMARIS. 3D surfaces based on the nuclear-specific signal were generated, and their respective volumes were measured over time. Chromatin density was calculated by dividing the sum of H2B or SiR-DNA fluorescence intensities by total nuclear volume.

To measure nuclear fluorescence intensities in three dimensions, nuclear staining (that is, DAPI) was used to threshold a nuclear region of interest (with FIJI for 2D data, and IMARIS for 3D data), from which the respective pixel intensities were calculated.

**PALM and measurement of nuclear actin filament width.** For super-resolution imaging of nAC-Dendra2, NIH3T3 cells were washed and fixed in 3.7% formaldehyde, for 20 min at room temperature. For all super-resolution imaging, a 1:5,000 dilution of fluorescent beads (TetraSpeck Microspheres, 0.1 μm, Life Sciences T7279 or FluoSpheres 715/755, Life Sciences F8799) was sonicated to break up clumps of beads. About five microlitres of the beads were added to the sample and allowed to settle and adhere for 15 min, to serve as fiducial markers for drift correction. Super-resolution imaging was performed as described in detail elsewhere[30]. Briefly, a customized and automated Nikon Eclipse Ti microscope was equipped with 405 nm, 488 nm, 561 and 640 nm lasers (all OBIS, Coherent). Laser intensities were controlled by an acousto-optical tunable filter (Acal BFi Germany GmbH) to illuminate the sample using the quad-colour dichroic zt405/488/561/640rpc. The illumination could be switched from epifluorescence to total internal reflection fluorescence (TIRF) mode by a motorized TIRF mirror (Thorlabs). Fluorescence signals were collected by a quad-line laser rejection filter ZET405/488/561/640 and the band-pass filters ET 525/50, ET 610/75 or HC 689/23 dependent on the imaging channel (all filters AHF). The detection of the single-fluorophore emissions was performed using an electron-multiplying charge-coupled device (emCCD iXon 888, Andor).

For PALM imaging of Dendra2, the sample was irradiated by about 1–2 kW cm$^{-2}$ (561 nm) and $<$0.5 kW cm$^{-2}$ (405 nm) and imaged at an acquisition frame rate of 60 ms. Cells were imaged until all Dendra2 fluorophores were read-out. For STORM imaging of Phalloidin-Alexa 647, the sample was imaged in 100 mM methyl diethanolamine (MEA) with a glucose oxidase oxygen scavenger system[31] illuminated with about 2–4 kW cm$^{-2}$ (640 nm) and recorded at an acquisition frame rate of 70 ms.

Super-resolution videos were analysed by the RapidSTORM software[32] and post-processed by customized scripts written in Python programming language (Python Software Foundation, https://www.python.org) to correct for sample drift during the image acquisition. From the post-processed data, the experimental nearest-neighbour-approach resolution[33] was calculated and super-resolution images were reconstructed according to their individual resolution.

Filament widths were analysed by a self-written, customized script for the FIJI software[34]. Briefly, the filaments were selected by a segmented line profile covering the filament width and length. To minimize the selection and pixelation error, selections were shifted by 0.5 pixels (5 nm) in all directions to obtain five measures in total for each filament. These selected ROIs were straightened to remove the individual curvatures of the filaments and projected along their long axis. Each obtained profile was fitted by a Gaussian that yields the filament width by its full-width at half-maximum value. The optimal histogram bin size was calculated using the Freedman–Diaconis rule[35].

**Fluorescent lifetime imaging microscopy (FLIM) of fluorescence resonance energy transfer (FRET).** For FLIM/FRET, NIH3T3 cells were transduced with lentiviruses encoding PGK-H2B-mCherry and PGK-GFP-H2B, and sorted for homogeneous expression. For experiments involving expression of exportin 6, cells were seeded and synchronized by a single thymidine block, 24 h after transfection of Flag-exportin 6. After this, cells were washed three times in PBS and cultured in normal media for 10 h. Cells were then fixed (2% PFA in PBS, 10 min), permeabilized (0.1% Triton in PBS, 10 min) and blocked (2% BSA in PBS, 30 min), before incubation with anti-Flag antibodies for 2 h. Cells were washed three times in PBS, and incubated with secondary Alexa Fluor 405-conjugated antibodies for 45 min. Cells were then washed again in PBS. Postmitotic, Flag-exportin 6-overexpressing-cells were identified using 405 nm excitation.

In the case of Flag-WT/R62D mutant actin, transfected cells expressing Flag-WT/R62D-NLS-actin were sorted through SNAP-mediated tagging. Following this, cells were transduced to express GFP-H2B and mCherry-H2B, and sorted by FACS. For these experiments, cells were synchronized at G1/S transition using thymidine (2 mM for 20 h). Cells were then washed three times in PBS, and returned to normal media containing 500 ng ml$^{-1}$ doxycycline to induce expression of Flag-actin derivatives. After 4 h, 1 μM of CDK1i (RO-3306, Sigma) was added to the medium for a subsequent period of 4 h. Cells were washed three times in PBS, and then returned to normal media containing 500 ng ml$^{-1}$ doxycycline. Thirty minutes, mitotic cells were isolated by mitotic shake-off, centrifuged at 1,500*g* for 5 min and plated onto poly-L-lysine (PLL)-coated 35 mm dishes. After 1 h, cells were pre-extracted with CSK buffer for 5 min, washed three times in PBS and fixed with 2% PFA.

Lifetime measurements were taken on a Leica TCS SP8 system, using a white light laser with a repetition rate of 20 MHz and an excitation wavelength of 488 nm. GFP-H2B emission was detected over an emission range of 495–530 nm. Data were fitted using FLIMfit software[36]. Temporal binning of the fluorescence decays was performed prior to fitting, resulting in 256 time bins per decay. Tail-fitting of the fluorescence images was performed pixel-wise with a single exponential model on all pixels above an intensity threshold of 175 photons, allowing spatial variations in fluorescence lifetime to be visualized.

**Nuclear F-actin pulldown at mitotic exit.** For nuclear F-actin pulldowns, RPE-1 cells were mitotically blocked by nocodazole (100 nM for 24 h), before washout with growth medium. Four hours after washout, cells were lysed and subjected to subcellular fractionation as described previously[8]. The purity of subcellular fractionations was controlled by immunoblotting for α-tubulin and histone H3. The obtained nuclear lysates were incubated with 5 μg biotin-phalloidin at 4 °C and constant rotation for 2 h. Then, pre-washed magnetic streptavidin Dynabeads (Thermo Fisher) were added, followed by incubation at 4 °C and constant rotation for 2 h. After washing, the magnetic beads were collected and boiled in 2× Laemmli buffer for 10 min. The supernatant containing lysed nuclear F-actin and associated proteins was used for further analyses.

**Mass spectrometry-based protein identification.** Samples were loaded on an SDS gel and immediately after they had entered the separation gel, electrophoresis was stopped and the protein bands were excised and subjected to in-gel digest using trypsin[37].

For mass spectrometric analysis, an Orbitrap Velos Pro mass spectrometer (ThermoScientific) was used that was connected online with an Ultimate nanoRSLC-HPLC system (Dionex), equipped with a nano C18 RP column. Ten microlitres of the tryptic digest was usually injected onto a C18 pre-concentration column and automated trapping and desalting of the sample was performed at a flow rate of 6 μl min$^{-1}$ using water/0.05% formic acid as the solvent.

Tryptic peptides were separated with water/0.045% formic acid (solvent A) and 80% acetonitrile/0.05% formic acid (solvent B) at a flow rate of 300 nl min$^{-1}$: holding 4% B for 5 min, followed by a linear gradient to 45% B within 30 min and linear increase to 95% solvent B for 5 min. The column was connected to a stainless-steel nanoemitter (Proxeon) and the eluent sprayed directly towards the heated capillary of the mass spectrometer using a potential of 2,300 V. A survey scan with a resolution of 60,000 within the Orbitrap mass analyser was combined with at least three data-dependent MS/MS scans with dynamic exclusion for 30 s either using CID with the linear ion-trap or using HCD and Orbitrap detection at a resolution of 7,500.

Data analysis was performed using Proteome Discoverer (v4.0; ThermoScientific) with SEQUEST and MASCOT (v2.4; Matrix Science) search engines using either SwissProt or NCBI databases.

**Mitotic shake-off.** For the indicated immunoblot analyses, immunofluorescence staining and MNase assays, cells were seeded at 40% confluency and allowed to adhere for 8 h. Cells were then serum-starved for 24 h, followed by addition of growth media, containing 0.33 μg ml$^{-1}$ doxycycline for experiments involving doxycycline-inducible protein expression. After 16 h, nocodazole (100 nM) was added for a further 3 h. Mitotic cells were collected by mitotic shake-off and washed three times in growth media. These mitotic cells were then reseeded and further processed for subsequent analyses.

**Micrococcal nuclease (MNase) digestion assay.** One million cells were harvested, and washed once with 1 ml of 1× RSB buffer (10 mM Tris, pH 7.6, 15 mM NaCl and 1.5 mM $MgCl_2$). After centrifugation (3,000*g*), the cell pellet was resuspended in 1 ml of 1× RSB buffer with 1% Triton-X 100 and homogenized. Nuclei were collected by centrifugation (13,000*g*) and washed twice with 1 ml of buffer A (15 mM Tris, pH 7.5, 15 mM NaCl, 60 mM KCl, 0.34 M sucrose, 0.1% β-mercaptoethanol, and EDTA-free protease inhibitor cocktail). Nuclei were resuspended in 500 μl MNase reaction buffer (from NEB, 50 mM Tris-HCl, 5 mM $CaCl_2$ pH 7.9) and aliquoted into 100 μl aliquots. MNase digestion was performed in 100 μl reactions by addition of 50 kunitz units of MNase (NEB) at 37 °C for 5 min. Reactions were terminated by adding 25 mM EDTA. DNA was purified using a PCR purification kit and 1,000 ng of DNA was analysed on a 1.5% agarose gel.

**Animals.** ICR mice were obtained from Kiwa Experimental Animals (Wakayama). This study conformed to the Guide for the Care and Use of Laboratory Animals. All animal experiments were approved and performed under the guidelines of the Animal Research Committee of Kindai University.

***In vitro* fertilization of mouse oocytes and mRNA injection.** Female ICR mice (or ICR × ICR), aged 8–13 weeks, were superovulated with pregnant mare serum gonadotropin (PMSG; Novartis Animal Health), followed 48 h later with human chorionic gonadotropin (hCG; ASKA Pharmaceutical). Cumulus–oocyte complexes were collected from the oviducts in HTF medium. The sperm suspension was added to the oocyte cultures, and morphologically normal fertilized oocytes were collected 1–1.5 h after insemination at 37 °C under 5% $CO_2$ in air. Fertilized oocytes were transferred to HEPES–CZB medium. mRNAs for nAC-GFP, actin$^{R62D}$-HA-NLS, actin$^{WT}$-HA-NLS, mCherry-exportin 6 and myc-GFP were injected using a piezo manipulator (Prime Tech). mRNAs were prepared from pCS2 (ref. 38) or pcDNA3.1 vectors[39]. In the case of pCS2 vectors, mRNAs produced from the SP6 promoter were subjected to the addition of polyA tails while pcDNA3.1 vectors were transcribed from the T7 promoter. Since the translation efficiency is different between mRNAs produced from pCS2 vectors and those from pcDNA3.1 vectors, different concentrations of mRNA were injected: nAC-GFP (150 ng μl$^{-1}$), HA-NLS-actin$^{R62D}$(650 ng μl$^{-1}$), HA-NLS-actin$^{WT}$(650 ng μl$^{-1}$), mCherry-exportin 6 (1,000 ng μl$^{-1}$), myc-GFP (1,000 ng μl$^{-1}$) and histone H2B-mCherry (5 ng μl$^{-1}$). After mRNA injections, the fertilized embryos were cultured in KSOM medium at 37 °C in a 5% $CO_2$ atmosphere. mCherry-exportin 6 mRNA or control myc-tagged GFP mRNA was injected into oocytes denuded by 0.1% hyaluronidase before subsequent *in vitro* fertilization.

**Confocal microscopy of oocytes.** mRNA-injected embryos were fixed in 4% formaldehyde for 10 min and washed three times in PBS containing 0.01% PVA. Then, fixed embryos were incubated in PBS–BSA with 0.2% Triton-X for 60 min, followed by three washes with PBS–BSA. Washed embryos were stained with 5 μg ml$^{-1}$ DAPI for 15 min, followed by three washes using PBS–BSA. Embryos were mounted and observed under a confocal microscope (LSM800, ZEISS). Images were analysed using the ZEN software (ZEISS).

**Electron microscopy (EM).** For EM-based analysis of chromatin compaction at mitotic exit, NIH3T3 cells (either stably expressing BFP-NLS, NLS-BFP-actin$^{R62D}$ or transfected with GFP-exportin 6 or NLS-mCherry-cofilin) were synchronized at G1/S transition using thymidine (2 mM for 20 h). Expression of GFP-exportin 6 and NLS-mCherry-cofilin was ensured by FACS-based cell sorting prior to sample preparation. Cells were washed three times in PBS, and then returned to normal media containing 500 ng ml$^{-1}$ doxycycline. After 4 h, analysis of flow cytometry data, using the Watson (Pragmatic) model, determined that 40% of cells had completed S phase. This time point was therefore chosen to add 1 μM of CDK1i (RO-3306, Sigma), for a period of 4 h. Cells were washed three times in PBS, and then returned to normal media containing 500 ng ml$^{-1}$ doxycycline. Thirty minutes later, mitotic cells were isolated by mitotic shake-off. Cells were centrifuged at 1,500*g* for 5 min, and plated onto PLL-coated 35 mm dishes.

After 1 h, cells were trypsinized and centrifuged at 1,500*g* for 5 min. Pellets were resuspended in complete media containing 10% BSA, and centrifuged at 1,500*g* for 5 min. One microlitre of this cell pellet was then put into a 0.1 mm gold membrane carrier and high-pressure frozen (Leica EM PACT2). Samples were then freeze-substituted in a freeze-substitution acetone mix, containing 0.1% uranyl acetate and 1% osmium tetroxide. During this procedure, samples were first held at −90 °C, and then brought to 0 °C, over a period of 18 h. These samples were then embedded in EPON, and baked at 60 °C for 48 h. Sections (70 nm) were cut using an ultratome, and these were stained with uranyl acetate and lead citrate and images were taken at 2,900× magnification on a FEI Tecnai 12 TEM, operated at 120 kV.

For analysis, nuclei and nucleoli were manually segmented in 2D slice images across the cell using the freehand selection tool of ImageJ/Fiji to generate a binary mask of the nucleoplasm. Condensed chromatin was then semi-automatically segmented across the nucleoplasmic region using the WEKA Trainable Segmentation plugin for ImageJ/Fiji[40]. Classification was based on the Gaussian blur, Sobel filter, Hessian, Difference of Gaussians and membrane projections metrics using the built-in fast random forest algorithm. Due to the variability in chromatin staining, it was necessary to train a new classification model for each image. Condensed chromatin distribution was subsequently analysed in the segmented images using a custom ImageJ/Fiji macro, which measured the total condensed chromatin area and perimeter, as well as the area fraction of condensed chromatin, as a proportion of the total nucleoplasmic area.

**Atomic force microscopy.** To obtain early G1 or interphase NIH3T3 nuclei, cells were collected 60 min or 7 h after mitotic shake-off, respectively. To induce chromatin decondensation, cells were treated with 1 μM trichostatin A (TSA) for 5 h. Nuclei were isolated as described previously[41]. AFM measurements were conducted in aqueous solution utilizing a Multi-mode VIII microscope with Nanoscope V controller and a PeakForce feedback control mechanism with an enclosed liquid cell. Isolated live nuclei were bound to a PLL-coated glass coverslip and remained hydrated in this buffer (20 mM HEPES at pH 7.8, 25 mM KCl, 5 mM $MgCl_2$, 0.25 M sucrose and 1 mM ATP) to increase the longevity of the nuclei for investigation. The surface morphologies of nuclei were observed to remain unchanged under these conditions, allowing multiple nuclei to be tested in each sample and an average surface roughness and associated error to be calculated for each nucleus type. Using SCANASYST-FLUID cantilevers (Bruker) of nominal spring constant 0.7 N $m^{-1}$ and nominal tip radius 2 nm, the force applied to the plane of the sample by the AFM tip was kept below 1 nN; thus, imaging stability was maintained whilst avoiding tip-induced deformation of the sample. Images were collected at a scan rate of 0.404 Hz and 500 × 500 pixels giving a digital resolution of ∼10 nm per pixel. Nuclear height and roughness were calculated and quantified for the corresponding nuclei. Surface roughness was defined as the root-mean-square average of height deviations.

**Statistics and reproducibility.** For each experiment, sample sizes were chosen on the basis of initial pilot experiments. Similar experiments reported in previous publications were further used to direct sample sizes. No data were excluded from the analysis. No blinding or randomization was used in the course of the experiments. All attempts of replication were successful. In most cases, three independent experiments were performed to collect sample sizes allowing for quantitative comparisons, and representative images from these experiments are shown. Exact numbers of sample sizes and independent experiments are stated in the corresponding figure legends. Statistical analyses were performed with Prism 7 (GraphPad). Data are presented as stated in the respective figure legends. All *t*-tests were performed as unpaired, two-sided *t*-tests.

**Code availability.** Computer code is available from the authors on request.

**Data availability.** Mass spectrometry data have been deposited in ProteomeXchange with the primary accession code PXD213854. All other data supporting the findings of this study are available from the corresponding author on reasonable request.

28. Meerbrey, K. L. *et al.* The pINDUCER lentiviral toolkit for inducible RNA interference *in vitro* and *in vivo*. *Proc. Natl Acad. Sci. USA* **108,** 3665–3670 (2011).
29. Grikscheit, K., Frank, T., Wang, Y. & Grosse, R. Junctional actin assembly is mediated by Formin-like 2 downstream of Rac1. *J. Cell Biol.* **209,** 367–376 (2015).
30. Endesfelder, U. & Heilemann, M. Direct stochastic optical reconstruction microscopy (dSTORM). *Methods Mol. Biol.* **1251,** 263–276 (2015).
31. van de Linde, S. *et al.* Direct stochastic optical reconstruction microscopy with standard fluorescent probes. *Nat. Protoc.* **6,** 991–1009 (2011).
32. Wolter, S. *et al.* rapidSTORM: accurate, fast open-source software for localization microscopy. *Nat. Methods* **9,** 1040–1041 (2012).
33. Endesfelder, U., Malkusch, S., Fricke, F. & Heilemann, M. A simple method to estimate the average localization precision of a single-molecule localization microscopy experiment. *Histochem. Cell Biol.* **141,** 629–638 (2014).
34. Schindelin, J. *et al.* Fiji: an open-source platform for biological-image analysis. *Nat. Methods* **9,** 676–682 (2012).
35. Freedman, D. & Diaconis, P. On the histogram as a density estimator: L2 theory. *Z. Wahrscheinlichkeitstheor. Verwandte Geb.* **57,** 453–476 (1981).
36. Warren, S. C. *et al.* Rapid global fitting of large fluorescence lifetime imaging microscopy datasets. *PLoS ONE* **8,** e70687 (2013).
37. Hellman, U., Wernstedt, C., Góñez, J. & Heldin, C. H. Improvement of an "In-Gel" digestion procedure for the micropreparation of internal protein fragments for amino acid sequencing. *Anal. Biochem.* **224,** 451–455 (1995).
38. Miyamoto, K., Pasque, V., Jullien, J. & Gurdon, J. B. Nuclear actin polymerization is required for transcriptional reprogramming of Oct4 by oocytes. *Genes Dev.* **25,** 946–958 (2011).
39. Yamagata, K. & Ueda, J. Long-term live-cell imaging of mammalian preimplantation development and derivation process of pluripotent stem cells from the embryos. *Dev. Growth Differ.* **55,** 378–389 (2013).
40. Arganda-Carreras, I. *et al.* *Trainable_Segmentation: Release v3.1.2.* Zenodo http://dx.doi.org/10.5281/zenodo.59290 (2016).
41. Guilluy, C. *et al.* Isolated nuclei adapt to force and reveal a mechanotransduction pathway in the nucleus. *Nat. Cell Biol.* **16,** 376–381 (2014).

# 9 | Appendix B

## 9.1 Supplemental information: A peptide tag-specific nanobody enables high-quality labeling for dSTORM imaging

## Supplementary Note 1

As an additional, independent measure, we applied Fourier-Ring Correlation (FRC)[1]. The Fourier Image Resolution (FIRE) value is determined by the highest spatial frequencies which still positively correlate with each other above a chosen threshold. Thus, in the case of highly blinking dyes like AF647, the FIRE value mainly correlates with the optical resolution. Only when using a blinking correction factor or in the case of seldom-blinking fluorophores like PAmCherry it also takes the structural resolution into account[1]. Since all nanobodies were coupled to AF647, their stainings yielded highly similar FIRE values of 40 to 50 nm. These values correlate with the 9 to 12 nm NeNA localization precisions, which also mainly rely on the optical properties of the fluorophore (**Supplementary Fig. 6**). Notably, the labeling coverages of the individual fibers do not correlate with their NeNA and FIRE values which illustrates why the optical resolution should not be mistaken as an overall resolution. In the case of PAmCherry, a relatively seldom-blinking fluorophore, blinking events have a much smaller impact on the calculation of the FIRE value. Consequently, FIRE values for PAmCherry are closer to the actual overall resolution as the structural resolution is taken into account. As PAmCherry has low coverages of 35% for the thinnest fibers and up to 75% for the thickest fibers, the high FIRE values of 120 nm clearly illustrates that the limiting factor for the overall resolution is not the optical resolution (NeNA 17 nm) but rather the low coverage (**Supplementary Fig. 6**). The contribution of the linkage error to overall resolution is shown by comparing the sizes of the thinnest filaments stained with either nanobodies or conventional antibodies (**Supplementary Fig. 7**). The differences cannot be differentiated using the FIRE value since both approaches use AF647 as the readout (**Supplementary Fig. 7**). The bias in FIRE values is also visible in the structural analysis of $_{\text{BC2T}}$actin filaments (**Supplementary Fig. 9b**).

# Supplementary Table 1

Primer sequences

| **primer name** | **Sequence (5´- 3´)** |
|---|---|
| PAmCherry-F | ATATATACCGGTGCCACCATGGTGAGCAAGGGCGAGG |
| PAmCherry-R | ATATATAGATCTGCTTGTACAGCTCGTCCATGCC |
| VIM-BC2T-for | ATATATGCTAGCGCCACCATGTCCACCAGGTCCGTGTCCTCGTCC |
| VIM-BC2T-rev | GATCCGGTGGATCCCGGGCCC |
| VIM-for | AGTGAACCGTCAGATCCGCTA |
| VIM-rev | TCCACCTAAGCTTGAGCTCGAGATCTGTTCAAGGTCATCGTGATGCT |
| PAmCherry/eGFP-for | TCGAGCTCAAGCTTAGGTGGAGGAGGTTCTGTGAGCAAGGGCGAGGA |
| PAmCherry/eGFP-rev | ATCTAGAGTCGCGGCCGCTTACTTGTACAGCTCGTCCATGC |
| BC2TActb(1)-for | AAGCGCGCTGTTAGTCACTGGCAGCAAGATGATGATATCGCCGCGCT |
| BC2TActb(1)-rev | GACTTTCCACACCTGGTTGCTGA |
| BC2TActb(2)-for | TCAGCAACCAGGTGTGGAAAGTC |
| BC2TActb(2)-rev* | CGGCGCGCTTTCTGTCTGGCATGGTGGCGACCGGTAGC |
| BC2TLamin-for | GGACTCGAGATGCCAGACAGAAAGGCGGCTGTTAGTCACTGGCAGCAAGCGACTGCGACCCCCGT |
| BC2TLamin-rev | GGAGCTAGCATTACATAATTGCACAGCTTCTATTGGAT |
| laminBC2T-for | AAAGCTAGCGCCACCATGGCGACTGCGACC |
| laminBC2T-rev* | AAAGCGCGCTTGCGATCAGGCATAATTGCACAGCTTCTA |
| tubulinBC2T-for | AAAGCTAGCGCTACCGGTCGCCACCATGCGTGAGTGCATCTCCAT |
| tubulinBC2T-rev* | AAAGCGCGCTTGCGATCAGGGTATTCCTCTCCTTCTTCCTCACCCTC |
| BC2Ttubulin-for* | AATGCGCGCCGTGAGCCATTGGCAGCAGCGTGAGTGCATCTCCATCC |
| BC2Ttubulin-rev | ATTGGATCCCTAGTATTCCTCTCCTTCTTCCTCA |
| BC2TLC3B-for* | GTAGCGCGCCGTGAGCCATTGGCAGCAGCCGTCGGAGAAGACCTTCAA |
| BC2TLC3B-rev | GGTGGATCCTTACACTGACAATTTCATCCCGA |
| BC2TYpet-for* | AAAGCGCGCTTGCGATCAGGCATGGTGGCGACCGGTG |
| BC2TYpet-rev* | AAAGCGCGCCGTCTCTCATTGGCAGCAGGTGAGCAAAGGCGAAGAGCTG |
| SorTag Ins_for | TTACCGGTCACCACCATCACCATCACTAAG |
| SorTag Ins_rev | TTACCGGTTTCCGGCAGGCTACCTGAGGAGACGGTGACCTGG |
| F_KanR_BC2 | AAGGCCGCAGTTTCACATTGGCAACAATAAGGCGCGCCAGATCTACTT |
| R_KanR | GACAGCAGTATAGCGACCAGC |
| F1_cbp1 | ATCAAATTGCTTCGCAGTACATGG |
| cbp1_BC2_R1 | CAATGTGAAACTGCGGCCTTTCTGTCAGGGGTGCTTCTCAAACGAGAAAGATTC |
| F2_cbp1 | AATGCTGGTCGCTATACTGCTGTCTGTCTGTATTCGTTGTGCATATTTGAC |
| R2_cbp1 | GCTCGTATAGCGATTTTGCGTT |
| ACTB_sgRNA | CTTGTGGAAAGGACGAAACACCCGAGAATAGCCGGGCGCGCTGTTTGGGTCTTCGAGAAGACCTCACCGCCGTTGTCGACGACGAGCGGTTTTAGAGCTAGAAATAGC |
| ACTB_HDR | GAAGTGGCCAGGGCGGGGGCGACCTCGGCTCACAGCGCGCCCGGCTATTCTCGCAACTCACCATGCCTGATCGGAAGGCCGCCGTGAGCCATTGGCAGCAGGATGATGATATCGCCGCGCTCGTCGTCGACAACGGGTCCGGCATGTGCAAGGCCGGCTTCGCGGGCGACGATGCCCCCC |
| sgRNA_fw | TTTCTTGGCTTTATATATCTTGTGGAAAGGACGAAAC |
| sgRNA_rev primer | GACTAGCCTTATTTTAACTTGCTATTTCTAGCTCTAAAAC |
| ACTB_fw | GGGGCTGGGAATTGGCGCTAATTG |
| BC2_rev | TGCTGCCAATGGCTCACGGCG |

* to facilitate cloning, primer sequence encodes an amino acid substitution A>R at position 5 of BC2-tag. This substitution does not affect binding properties of BC2-Nb as shown previously.[2]

# Supplementary Figures

## Supplementary Figure 1

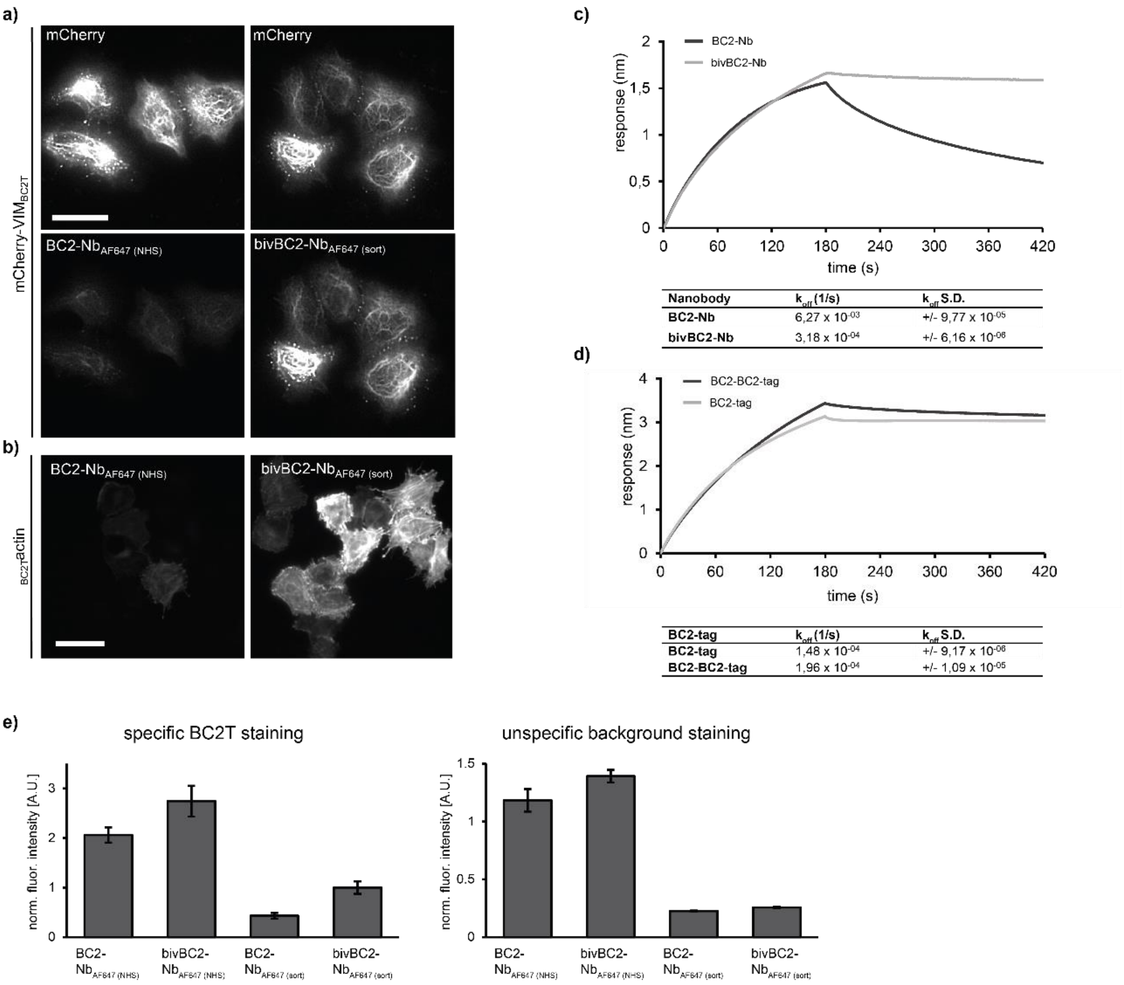

| Nanobody | $k_{off}$ (1/s) | $k_{off}$ S.D. |
|---|---|---|
| **BC2-Nb** | $6,27 \times 10^{-03}$ | +/- $9,77 \times 10^{-05}$ |
| **bivBC2-Nb** | $3,18 \times 10^{-04}$ | +/- $6,16 \times 10^{-06}$ |

| BC2-tag | $k_{off}$ (1/s) | $k_{off}$ S.D. |
|---|---|---|
| **BC2-tag** | $1,48 \times 10^{-04}$ | +/- $9,17 \times 10^{-06}$ |
| **BC2-BC2-tag** | $1,96 \times 10^{-04}$ | +/- $1,09 \times 10^{-05}$ |

Characterization of binding properties and labeling intensities of monovalent vs. bivalent BC2-Nb. (**a**) Comparison of labeling intensities of mono- and bivalent BC2 nanobodies either labeled via NHS conjugation to Alexa Fluor 647 (BC2-Nb$_{AF647 (NHS)}$) or sortase-mediated coupling (bivBC2-Nb$_{AF647 (sort)}$). HeLa cells transiently expressing a C-terminally BC2-tagged mCherry-vimentin construct (mCherry-VIM$_{BC2T}$, upper row) were fixed and stained with either BC2-Nb$_{AF647 (NHS)}$ (lower row, left panel) or bivBC2-Nb$_{AF647 (sort)}$ (lower row, right panel). Scale bar, 50 µm. (**b**) Comparison of labeling intensities of BC2-Nb$_{AF647 (NHS)}$ and bivBC2-Nb$_{AF647 (sort)}$ on BC2-tagged actin ($_{BC2T}$actin). HeLa cells transiently expressing $_{BC2T}$actin were fixed and stained with either BC2-Nb$_{AF647 (NHS)}$ (left panel) or bivBC2-Nb$_{AF647 (sort)}$ (right panel). Scale bar, 50 µm. (**c**) Determination of nanobody binding kinetics by bio-layer interferometry. Exemplary sensograms of BC2-Nb (240 nM) and bivBC2-Nb (120 nM) are shown. The table summarizes the dissociation rate ($k_{\text{off}}$) and standard deviation (S.D.) of BC2-Nb and bivBC2-Nb derived from the analysis of three concentrations (120 nM, 240 nM, 480 nM). (**d**) Determination of bivBC2-Nb$_{\text{AF647 (sort)}}$ binding kinetics on mono or tandem BC2-tag (BC2-BC2-tag). Exemplary sensograms of bivBC2-Nb$_{\text{AF647 (sort)}}$ (120 nM) are shown. The table summarizes the dissociation rate ($k_{\text{off}}$) and standard deviation (S.D.) of bivBC2-Nb$_{\text{AF647 (sort)}}$ derived from the analysis of three concentrations (120 nM, 240nM, 480nM). (**e**) Assessment of staining quality. Labeling of the different nanobody formats was quantified by measuring the signal intensity of mCherry-VIM$_{\text{BC2T}}$ expressing cells (left) and non-transfected cells (background, right), (BC2-Nb$_{\text{AF647 (NHS)}}$: n=115; bivBC2-Nb$_{\text{AF647 (NHS)}}$: n=134; BC2-Nb$_{\text{AF647 (sort)}}$: n=150; bivBC2-Nb$_{\text{AF647 (NHS)}}$: n=195). Calculated ratio is shown in **Fig 1c**.

## Supplementary Figure 2

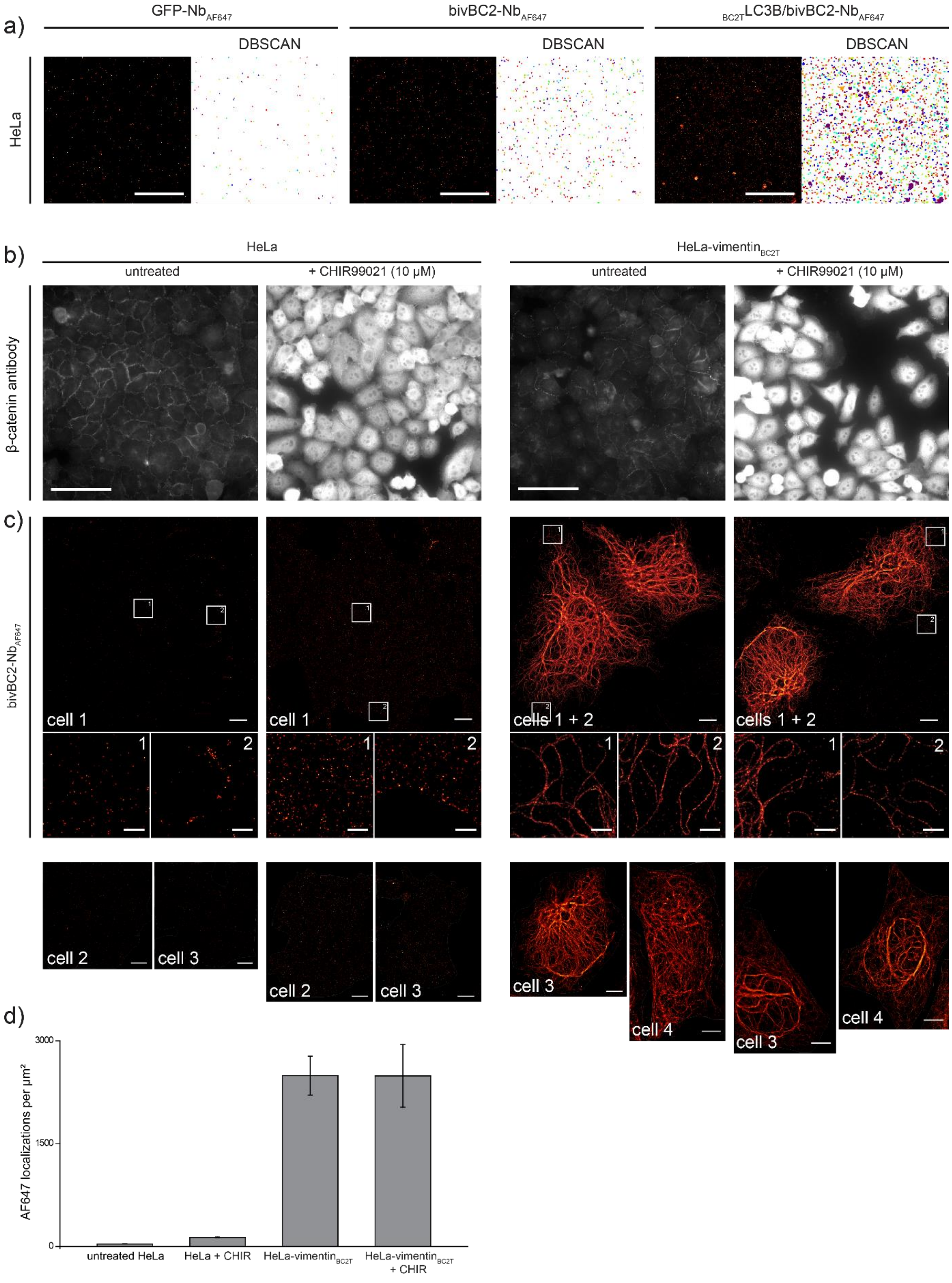

Assessment of bivBC2-Nb$_{AF647}$ staining of endogenous β-catenin (**a**) dSTORM images and corresponding DBSCAN plots, showing only clustered localizations of untransfected chemically fixed HeLa cells stained with GFP-$\mathrm{Nb}_{\mathrm{AF647}}$ and bivBC2-$\mathrm{Nb}_{\mathrm{AF647}}$ , as well chemically fixed HeLa cells transiently expressing $_{\mathrm{BC2T}}$LC3B stained with bivBC2-$\mathrm{Nb}_{\mathrm{AF647}}$ . Scale bars 5 µm. N = 3 cells for each condition. Bar chart summarizing all three conditions is shown in **Fig. 1c**. (**b**) Untransfected HeLa cells (left panel) or HeLa cells expressing C-terminally BC2-tagged vimentin ($\mathrm{vimentin}_{\mathrm{BC2T}}$) were left untreated or incubated with CHIR99021. Cells were chemically fixed and stained with a conventional anti-β-catenin antibody. Scale bar, 100 µm. (**c**) dSTORM images of cells as described in (**b**) stained with bivBC2-$\mathrm{Nb}_{\mathrm{AF647}}$. Scale bars in images 5 µm and 1 µm in insets. Additional dSTORM images used in localization counting analysis (lower panel). (**d**) Localization counts per µm$^2$ plotted as bar charts for all four conditions. Errors are given as standard deviation (S.D.). Image reconstruction details are given in the **Methods** section.

## Supplementary Figure 3

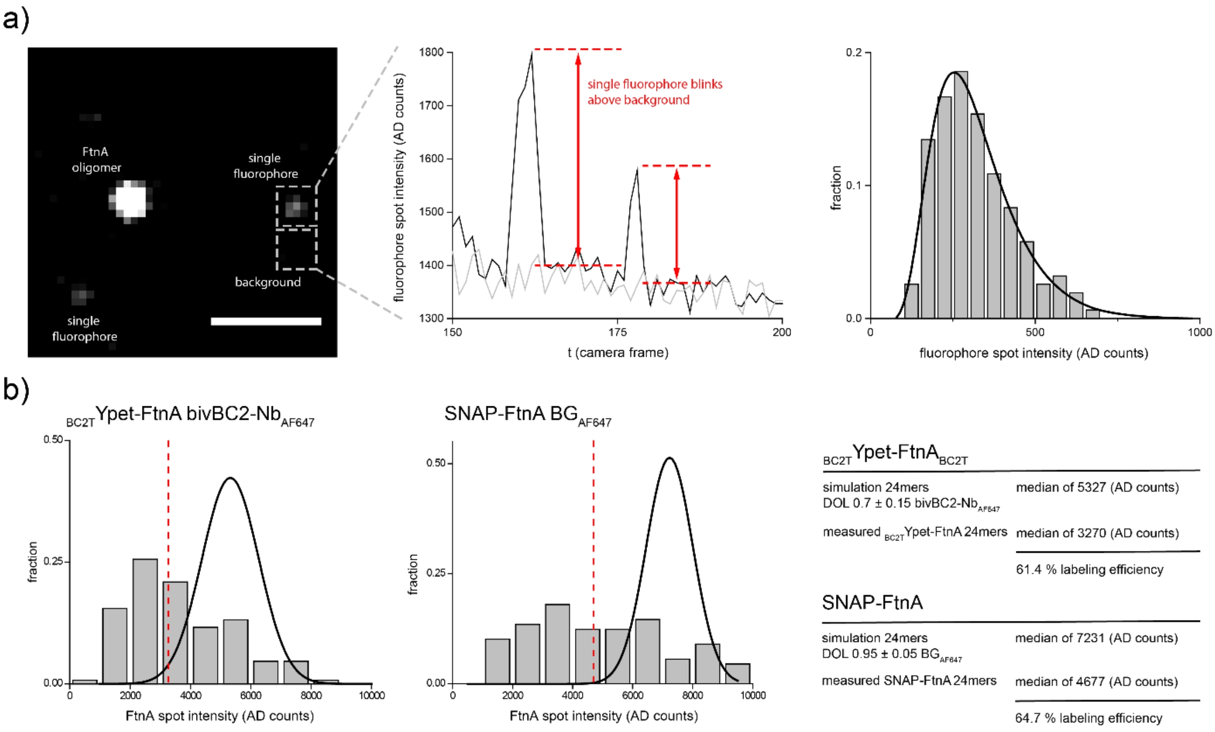

$_{BC2T}$Ypet-FtnA$_{BC2T}$

| | |
|---|---|
| simulation 24mers<br>DOL 0.7 ± 0.15 bivBC2-Nb$_{AF647}$ | median of 5327 (AD counts) |
| measured $_{BC2T}$Ypet-FtnA 24mers | median of 3270 (AD counts) |
| | 61.4 % labeling efficiency |

SNAP-FtnA

| | |
|---|---|
| simulation 24mers<br>DOL 0.95 ± 0.05 BG$_{AF647}$ | median of 7231 (AD counts) |
| measured SNAP-FtnA 24mers | median of 4677 (AD counts) |
| | 64.7 % labeling efficiency |

Quantification of completeness of labeling of FtnA oligomers tagged with the BC2- or SNAP-tag. (**a**) Wide-field fluorescence image of a $_{BC2T}$YPET-FtnA oligomer stained with the bivBC2-Nb$_{AF647}$ and single AF647 molecules bound to the slide surface (dashed line). Scale bar 1 µm. Single AF647 molecule intensity trace plotted in integrated intensity AD counts (y axis) over time in frame number (x axis). Blinking events are visible as clear jumps in fluorescence over the background (marker with red arrows and dashed lines). Right panel shows distribution of AF647 single molecule intensities plotted as a relative fraction histogram of integrated intensities with a bin size of 100 AD counts, fitted with a log-normal distribution function. (**b**) Distribution of bivBC2-Nb$_{AF647}$ and AF647-BG stained $_{BC2T}$Ypet-FtnA and SNAP-FtnA spot intensities (in the red channel) plotted as relative fraction histograms of integrated intensity AD counts with a bin size of 1000 AD counts is shown. Red lines represent the median value of both populations and the black curves represent the intensity distribution of simulated theoretical staining maximum. Table summarizes median values of simulations and measured distributions of FtnA oligomers which yields the completeness of labeling for both labeling systems. Corresponding summarizing bar chart is shown in **Fig. 1c**.

## Supplementary Figure 4

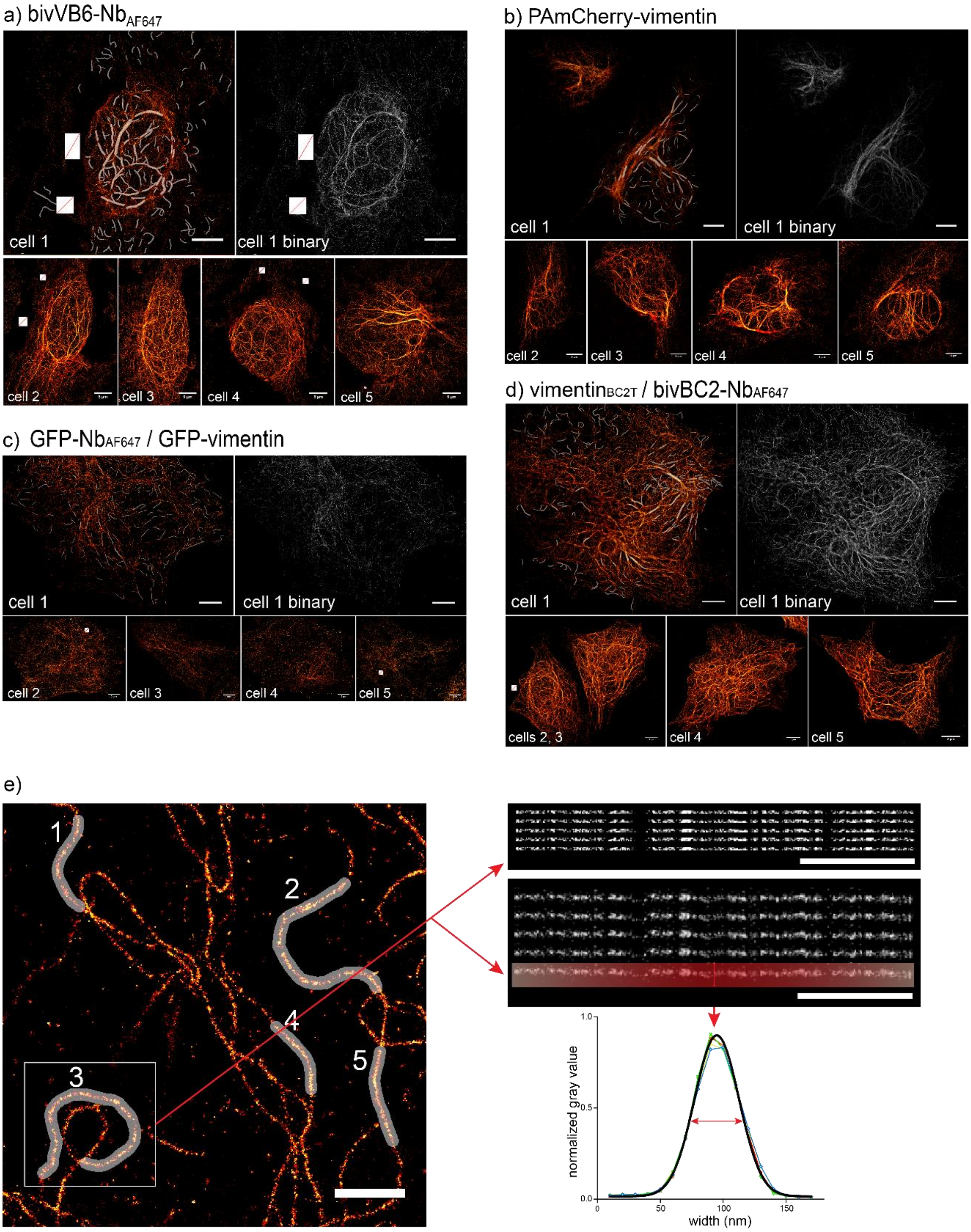

Analysis of PALM/dSTORM images of vimentin filaments in chemically fixed HeLa cells. (**a**) dSTORM images of five cells with native vimentin labeled with bivVB6-Nb$_{AF647}$. (**b**) dSTORM images of five cells expressing GFP-vimentin labeled with GFP-Nb$_{AF647}$. (**c**) dSTORM images of five cells expressing vimentin$_{BC2T}$ labeled with bivBC2-Nb$_{AF647}$. (**d**) PALM images of five cells expressing PAmCherry-vimentin. Scale bars, 5 µm.

Cells were analyzed with a custom-written ImageJ script. Each image was divided into 10 µm x 10 µm sections and 15 filaments per section were analyzed. First images include overlays for all analyzed filaments. All images are calculated corresponding to their individual experimental spatial resolution using the NeNA value. A binary version of each image was used to calculate filament coverages. The workflow is summarized in (**e**); first, lines were drawn along filaments. To minimize the selection and pixilation error, selections were shifted by 0.5 pixels (5 nm) in all directions to obtain five measures in total for each filament by straightening all selections. The middle 3 pixels filaments were taken from the binary image to calculate lengthwise coverage. The coverage of each filament was obtained from averaging the five measurements. To determine the filament width, lengthwise intensity profiles of the five filament selections were fitted with Gaussian curves. The average full width at half maximum (FWHM) of the five selections yields the average filament width. Width and lengthwise fluorophore coverage were analyzed for a total of 676 (bivVB6-Nb$_{AF647}$), 295 (PAmCherry), 724 (GFP-Nb$_{AF647}$) and 620 (bivBC2-Nb$_{AF647}$) filaments as shown in **Fig. 2**. Scale bars, 1 µm. Image reconstruction details are given in the **Methods** section

## Supplementary Figure 5

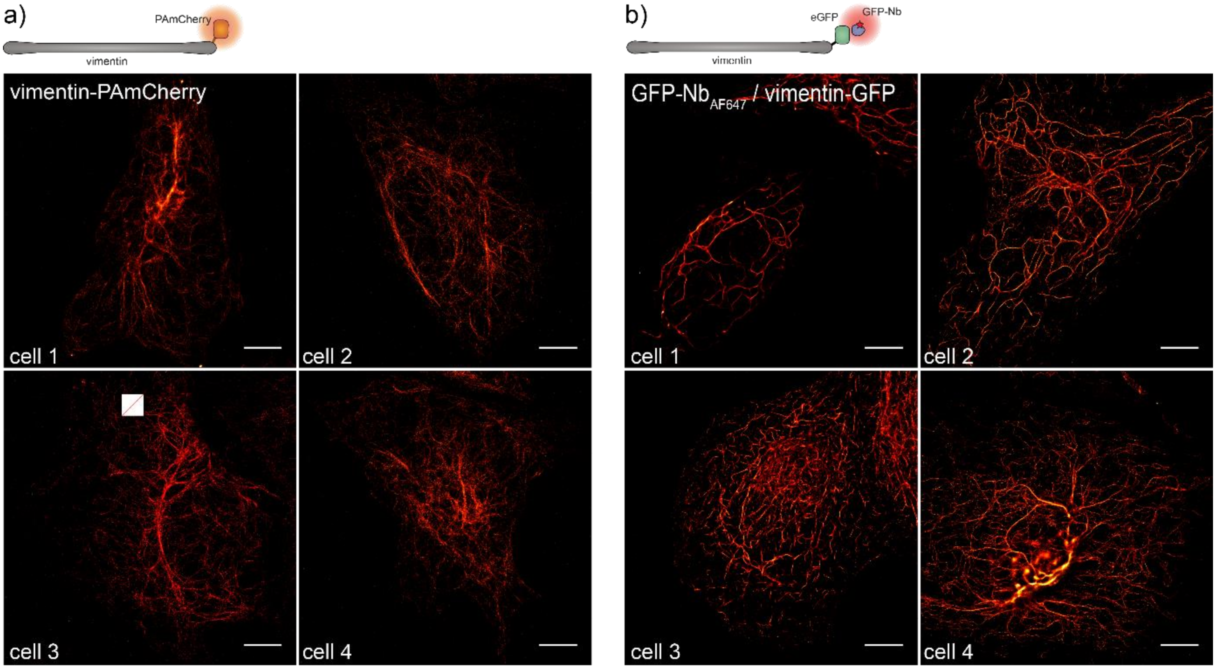

Representative PALM images of chemically fixed HeLa cells transiently expressing (**a**) vimentin C-terminally tagged with photoactivatable mCherry (vimentin-PAmCherry) and (**b**) dSTORM images of chemically fixed HeLa cells transiently expressing vimentin C-terminally with eGFP followed by staining with GFP-Nb$_{AF647}$ are shown. While vimentin-PAmCherry expressing cells are small and show thick vimentin bundles and few thin filaments (cell 1 - 4), vimentin-GFP expressing cells display different phenotypes, from only a few thick filaments (cell 1), networks of uniform medium-thick filaments (cell 2), fragmented filaments (cell 3) and very few cells that appear physiological (cell 4). Scale bars, 5 µm. Image reconstruction details are given in the **Methods** section.

**Supplementary Figure 6**

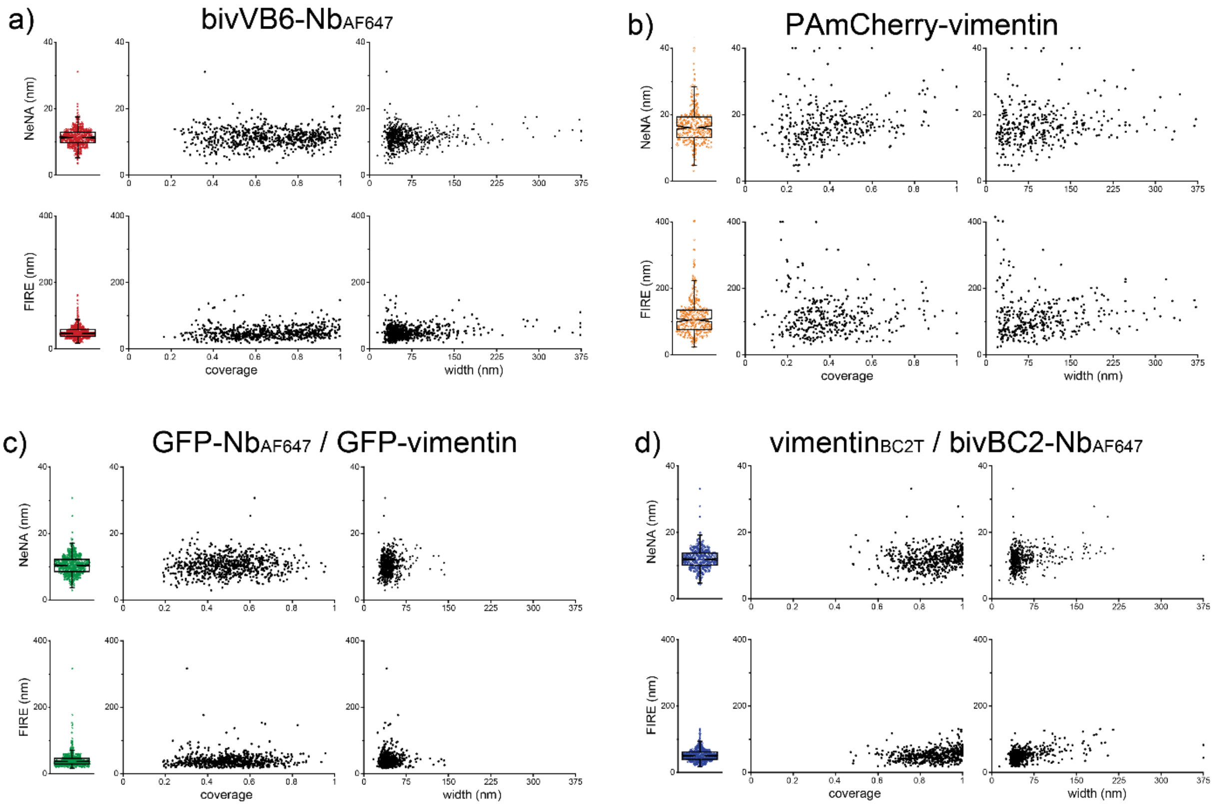

Plots of NeNA and FIRE image resolution analysis for PALM/dSTORM images. Graphs are shown for (**a**) native vimentin labeled with bivVB6-Nb$_{AF647}$, (**b**) GFP-vimentin labeled with GFP-Nb$_{AF647}$ (**c**) vimentin$_{BC2T}$ labeled with bivBC2-Nb$_{AF647}$ (**d**) PAmCherry-vimentin. Scatter + box plots (the box marks the 3 quartiles and the whiskers mark 95% of all the data) of all calculated NeNA (upper) and FIRE (lower) values as individual filament measurements. Individual NeNA and FIRE values were also plotted against filament coverage (middle, in fraction) and filament width (left, in nm) for each condition. The total number of filament ROIs was 636 (NeNA bivVB6$_{AF647}$), 644 (FIRE bivVB6$_{AF647}$), 347 (NeNA PAmCherry), 353 (FIRE pPAmCherry), 714 (NeNA bivVB6$_{AF647}$), 682 (FIRE bivVB6$_{AF647}$), 514 (NeNA bivBC2-Nb$_{AF647}$) and 519 (FIRE bivBC2-Nb$_{AF647}$). Numbers differ slightly from the total n of chosen ROIs as for some ROIs no NeNA or FIRE value could be calculated.

**Supplementary Figure 7**

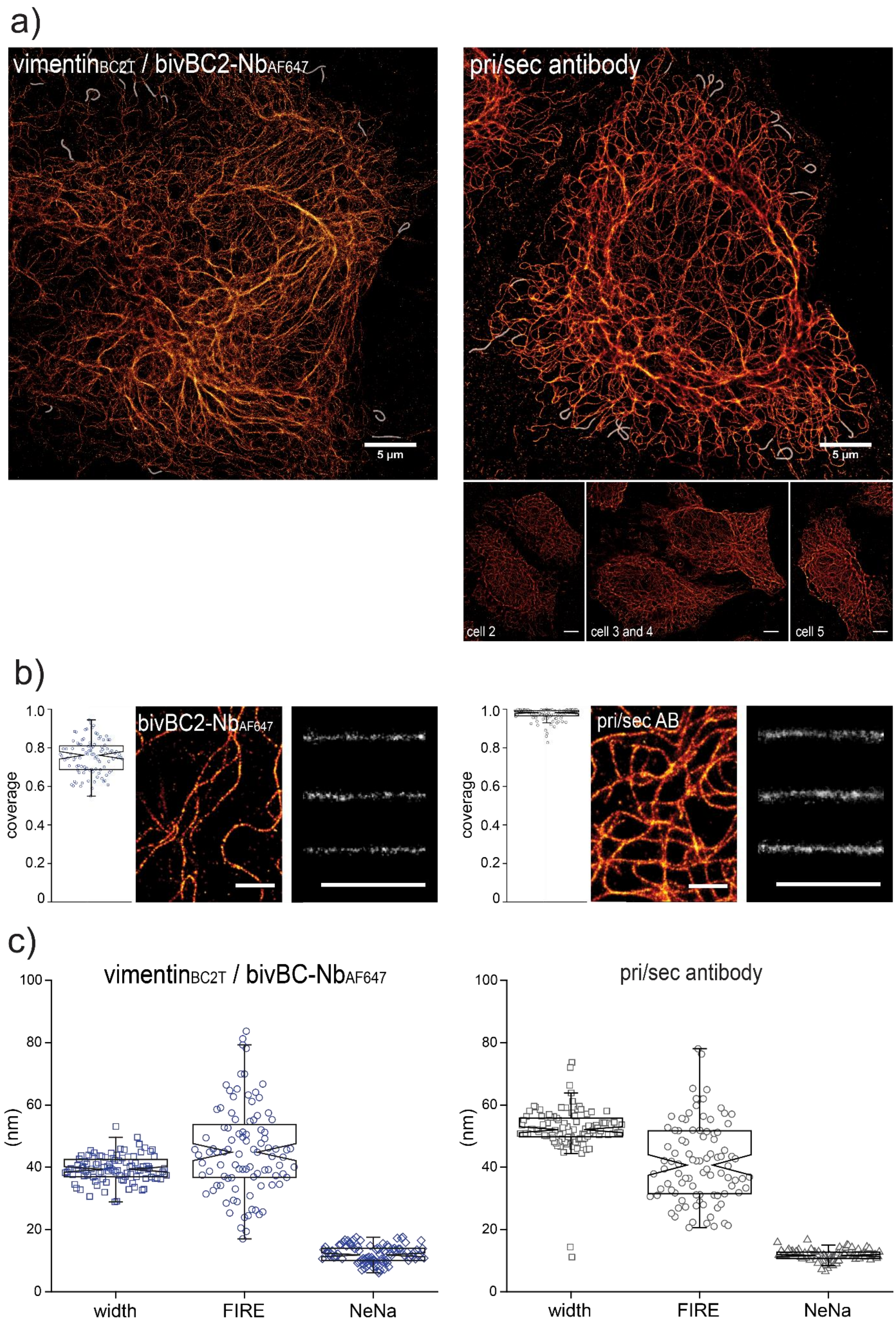

bivBC2-Nb labeling of BC2-tagged vimentin compared to conventional antibody labeling of native vimentin. (**a**) Representative dSTORM images of chemically fixed HeLa cells expressing vimentin$_{BC2T}$ stained with bivBC2-Nb$_{AF647}$ or chemically fixed HeLa cells where native vimentin was stained with a conventional primary antibody followed by staining with a secondary antibody coupled to AF647. Scale bars, 5 µm. 100 peripheral (single) filaments were analyzed per labeling strategy. (**b**) Coverage analyses of affinity tags. Scatter + box plots (the box marks the 3 quartiles and the whiskers mark 95% of all the data.) of thin filament coverages for bivBC2-Nb$_{AF647}$ and pri/sec antibody staining plotted as individual filament statistics of fluorophore covered fractions and representative peripheral filaments, before analysis and straightened. Scale bars, 1 µm. 100 filaments were analyzed per method. (**c**) Scatter + box plots (descriptive statistics same as (**b**) of thin filament widths, FIRE values and NeNA values for all conditions. Image reconstruction details are given in the **Methods** section.

**Supplementary Figure 8**

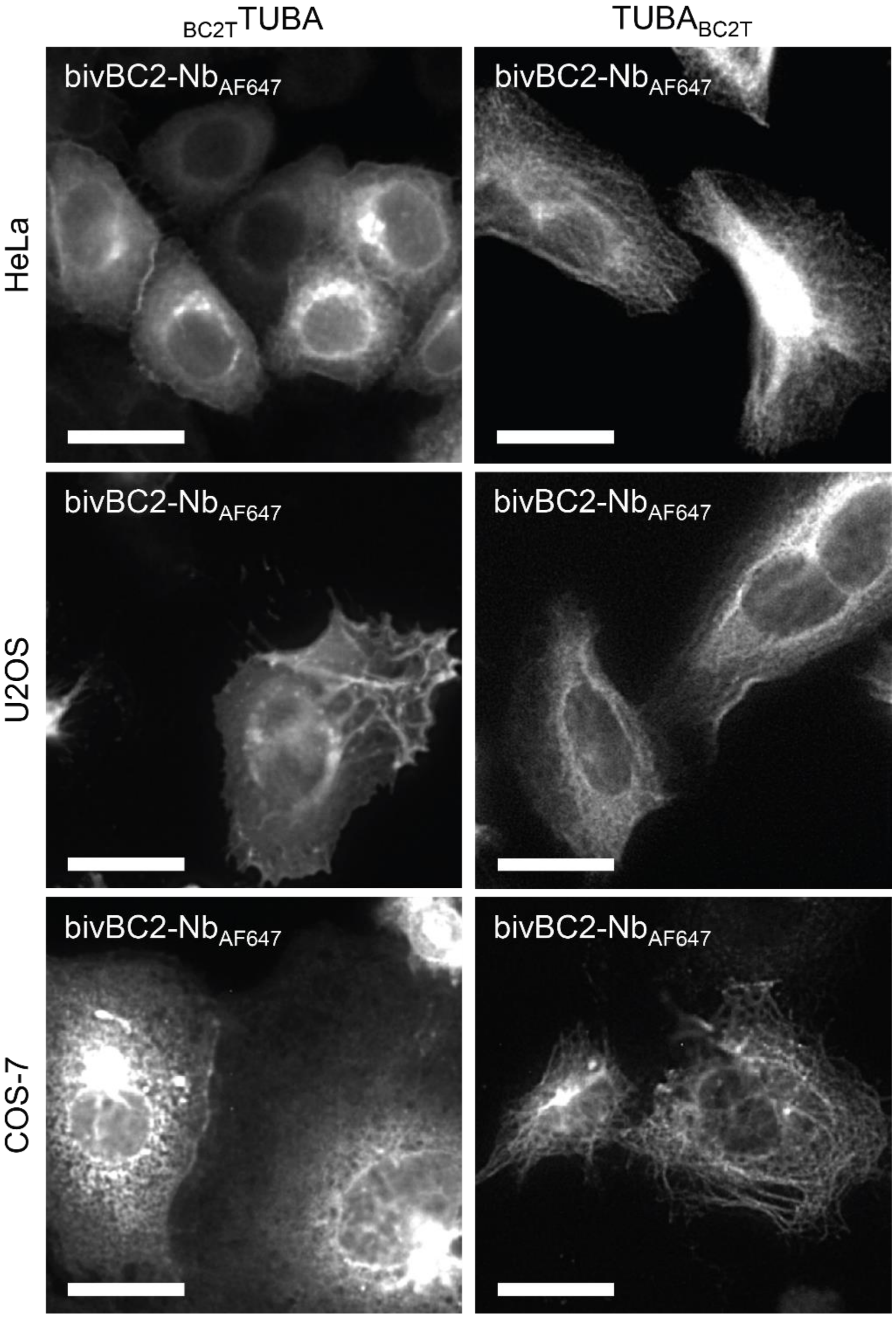

Visualization of N- or C-terminally BC2-tagged tubulin-alpha-1B chain (*TUBA*) in human cells. Immunofluorescence images of chemically fixed HeLa, U2OS and COS-7 cells transiently expressing N- or C-terminally BC2-tagged tubulin ($_{\mathrm{BC2T}}$TUBA, TUBA$_{\mathrm{BC2T}}$). Cells were stained with the bivBC2-Nb$_{\mathrm{AF647}}$. Scale bars, 25 µM.

## Supplementary Figure 9

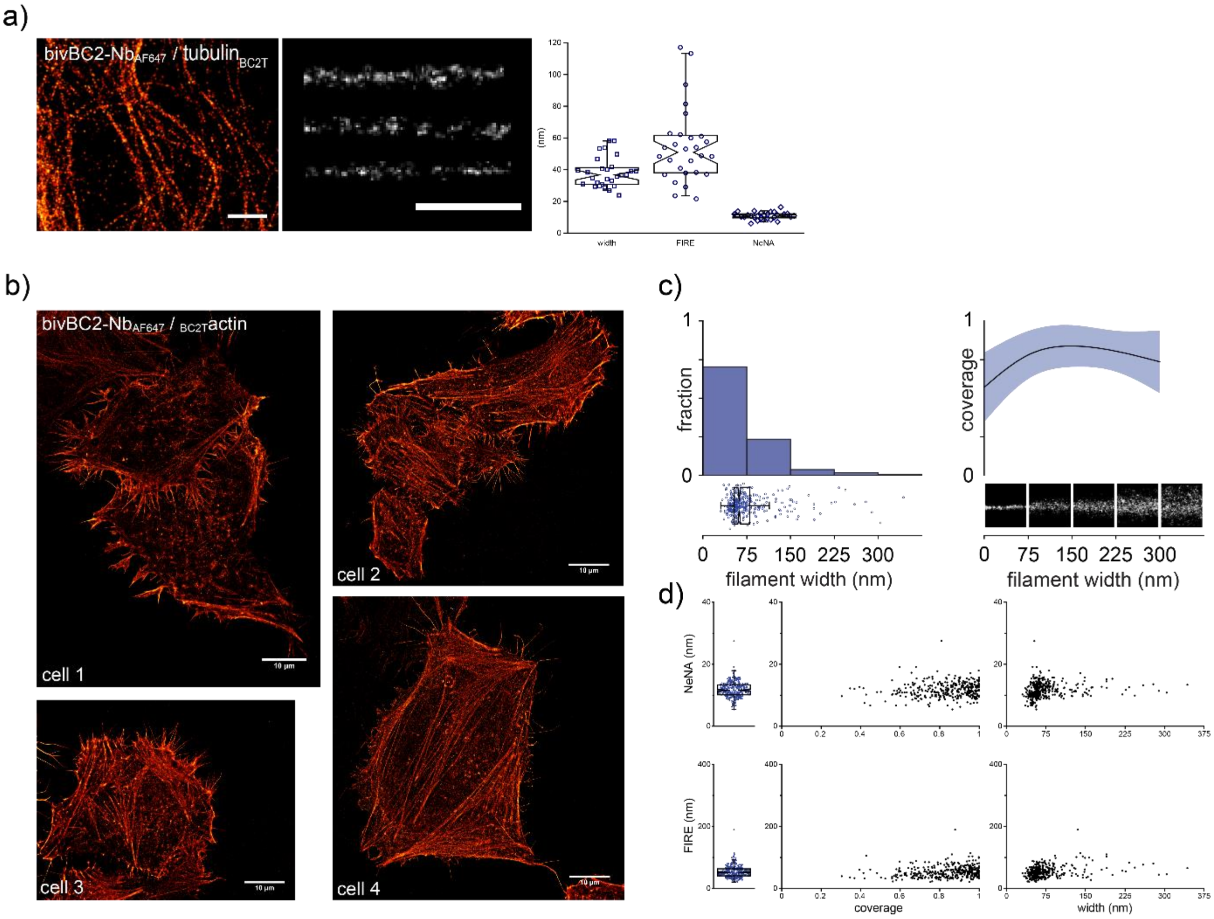

Image resolution measures for tubulin and actin visualized by tubulin$_{BC2T}$ or $_{BC2T}$actin respectively. (**a**) Tubulin fibers of an exemplary HeLa cell expressing tubulin$_{BC2T}$ are straightened like for vimentin in **Supplementary Fig. 4** and **6** and analyzed for filament width yielding a FWHM of 38.2 ± 9.2 nm. (n = 29 fibers). (**b**) dSTORM images of five chemically fixed cells expressing $_{BC2T}$actin labeled with bivBC2-Nb$_{AF647}$. Scale bars, 10 µm. (**c**) Actin filament widths as histograms (left) with a bin size of 75 nm (x axis) plotted against relative fraction (y axis). Full data is represented underneath the histograms as box + scatter plots with the same x axis. The box marks the 3 quartiles and the whiskers mark 95% of all the data. The average lengthwise fluorophore coverage was calculated for each bin and plotted (right) as mean filament width (black line) and standard deviation (colored area) against relative fraction covered by fluorophores (y axis). A total of 351 filaments were analyzed for width and lengthwise fluorophore coverage. (**d**) Scatter + box plots of all calculated NeNA (upper) and FIRE (lower) as individual filament measurements. Individual NeNA and FIRE values were also plotted against filament coverage (middle, in fraction) and filament width (left, in nm). (Sample size same as in (**c**)). Image reconstruction details are given in the **Methods** section.

## Supplementary Figure 10

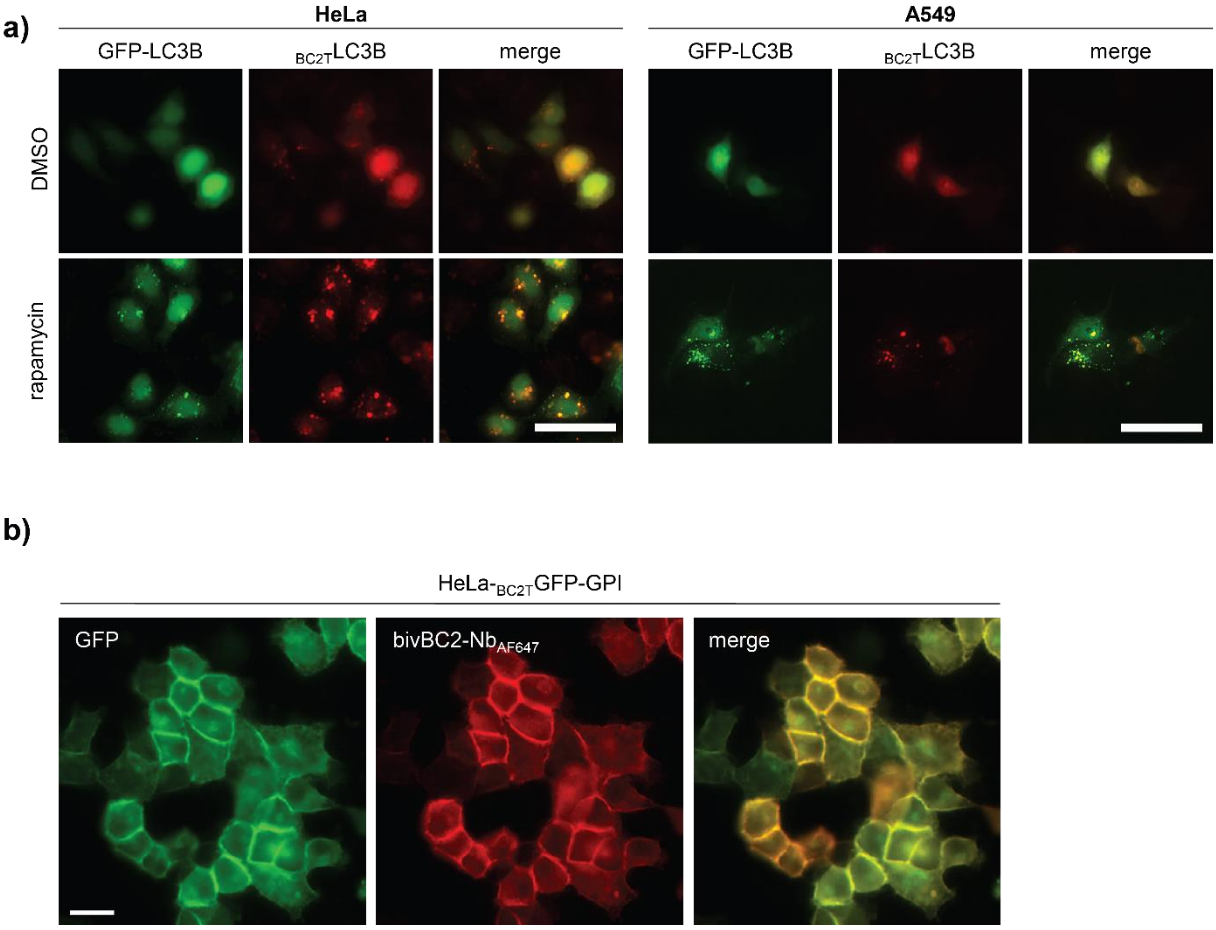

Detection of non-structural proteins with the BC2-tag/bivBC2-Nb system. (**a**) HeLa cells or A549 cells transiently coexpressing GFP-LC3B and $_{\mathrm{BC2T}}$LC3B were incubated with 0.5 µM rapamycin to induce autophagy or control treated with 0.1 % DMSO. Shown are images of chemically fixed cells displaying the co-localizing GFP- and bivBC2-Nb$_{\mathrm{AF647}}$ signal after 20 h incubation with rapamycin. (**b**) HeLa cells expressing $_{\mathrm{BC2T}}$GFP-GPI were chemically fixed and stained with the bivBC2-Nb$_{\mathrm{AF647}}$. Shown are representative images displaying co-localizing GFP- and bivBC2-Nb$_{\mathrm{AF647}}$ signals at the plasma membrane. Scale bars, 25 µm.

## Supplementary Figure 11

a) $_{\mathrm{BC2T}}$LC3B

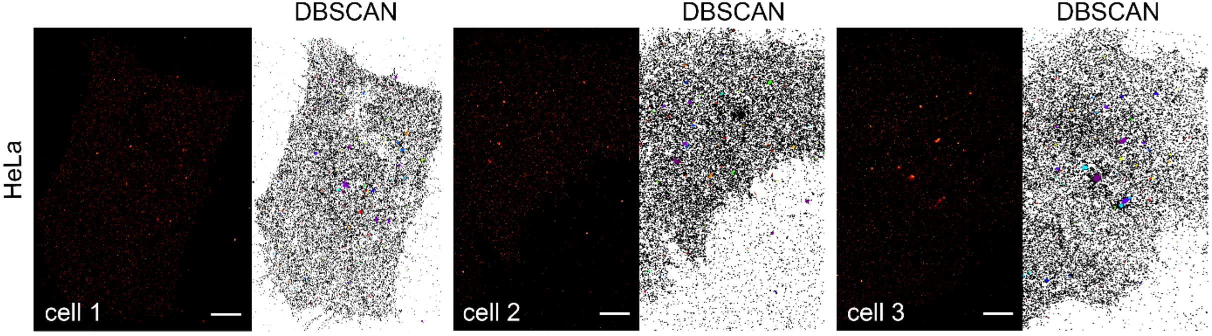

b) $_{\mathrm{BC2T}}$LC3B + rapamycin

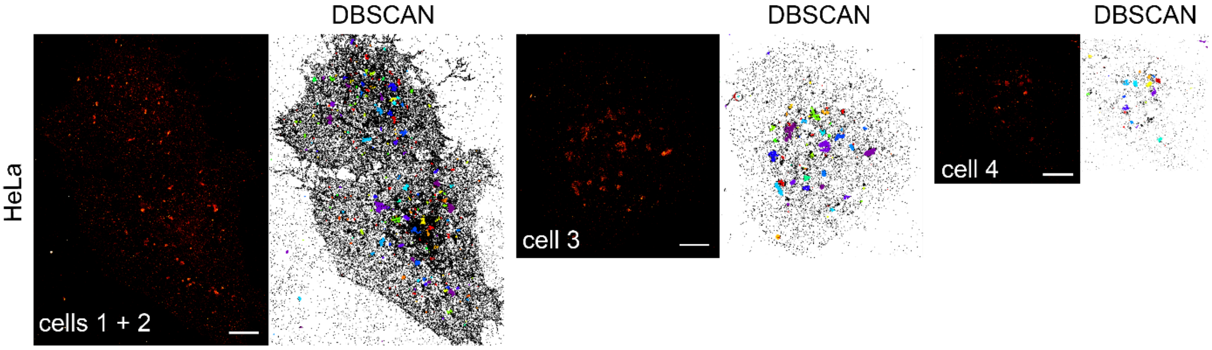

dSTORM images (left) and corresponding DBSCAN plots (right) of all the chemically fixed HeLa cells transiently expressing $_{\mathrm{BC2T}}$LC3B that were used for analysis shown in **Fig. 3d**. (**a**) non-treated cells, n = 120 clusters for cell 1, 76 clusters for cell 2 and 146 clusters for cell 3. (**b**) cells treated with rapamycin, n = 203 clusters for cell 1, 74 for cell 2, 85 for cell 2 and 43 for cell 4. Image reconstruction details are given in the **Methods** section. Summarizing bar charts are shown in **Fig. 3d**.

**Supplementary Figure 12**

a)

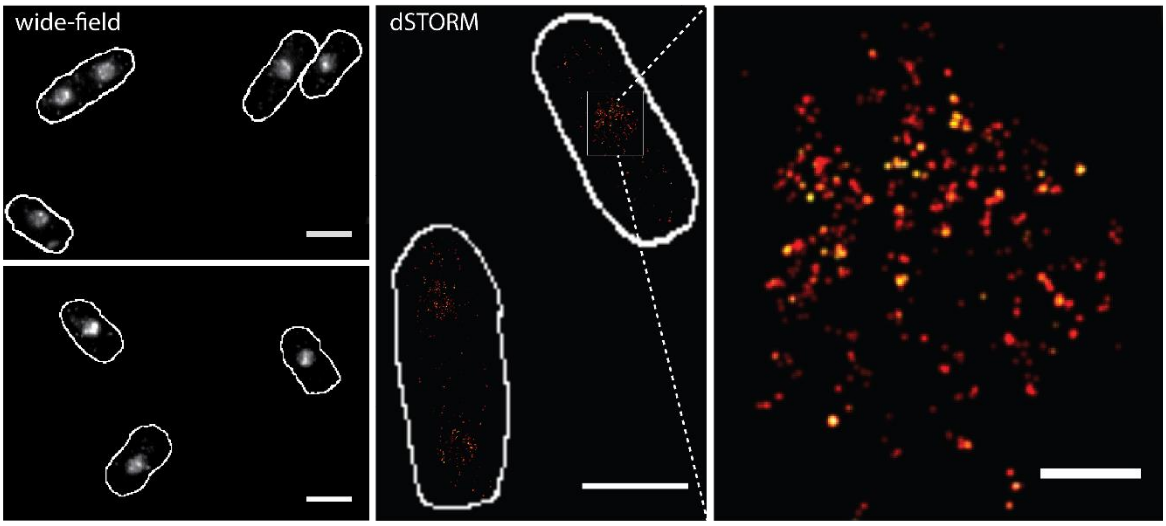

b)

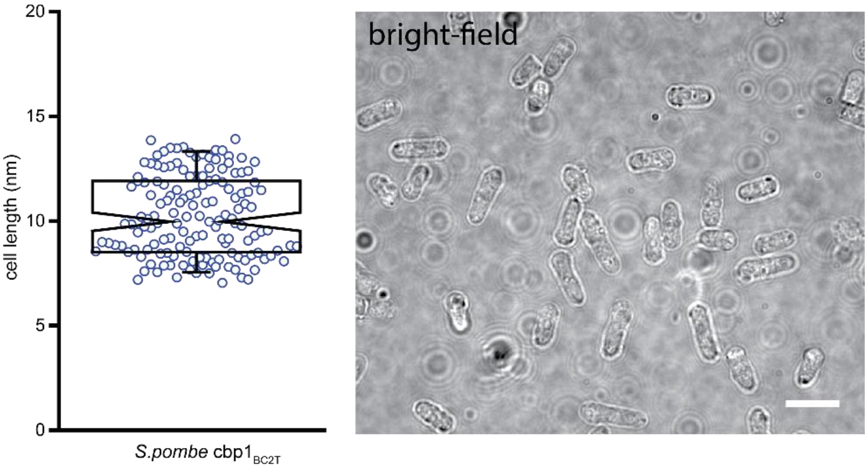

Labeling of the endogenously tagged DNA-binding protein cbp1 in *S. pombe.* (**a**) Shown are exemplary wide-field images of C-terminally tagged cbp1 (cbp1$_{BC2T}$) in chemically fixed *S. pombe* cells, scale bar, 10 µm (left panel). The nuclear cbp1$_{BC2T}$ was then imaged by dSTORM to resolve the distribution of individual proteins within the nucleus, scale bar, 5 µm (inset, scale bar, 0.5 µm). (**b**) The *S. pombe* strain encoding cbp1$_{BC2T}$ at the endogenous locus does not show any growth defects when analyzing the cell length distribution, n = 100 cells, nor abnormalities in the phenotype. Scale bar, 10 µm. Image reconstruction details are given in the **Methods** section.

## Supplementary Figure 13

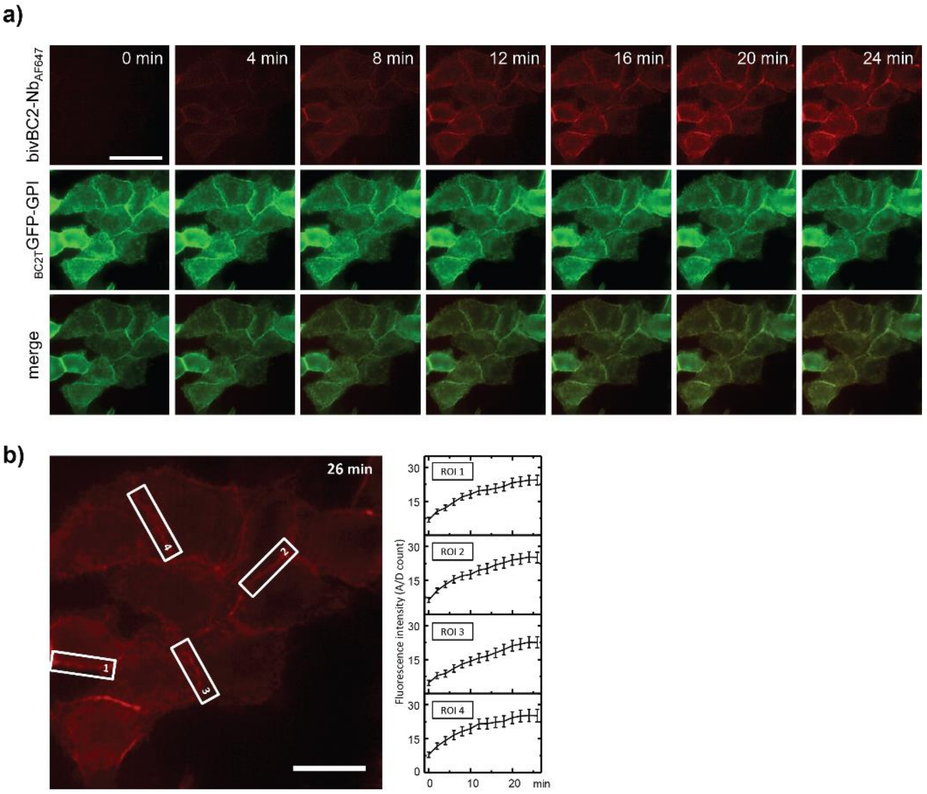

Imaging of BC2-tagged membrane protein in living cells. (**a**) HeLa cells expressing $_{BC2T}$GFP-GPI were subjected to live cell imaging 72 h after transfection. Shown are images displaying the nanobody signal (upper row) and GFP-signal (mid-row) derived from time lapse acquisition starting with the addition of bivBC2-Nb$_{AF647}$. Scale bar, 50 µm. (**b**) The fluorescence staining process was assessed by quantifying the fluorescence intensity increase over time for four different regions of interest (ROI 1 - 4, left) of cellular contact zones. Plotted (right) are the mean intensity values of each ROI and s.e.m. error bars. Scale bar 25 µm.

**Supplementary Figure 14**

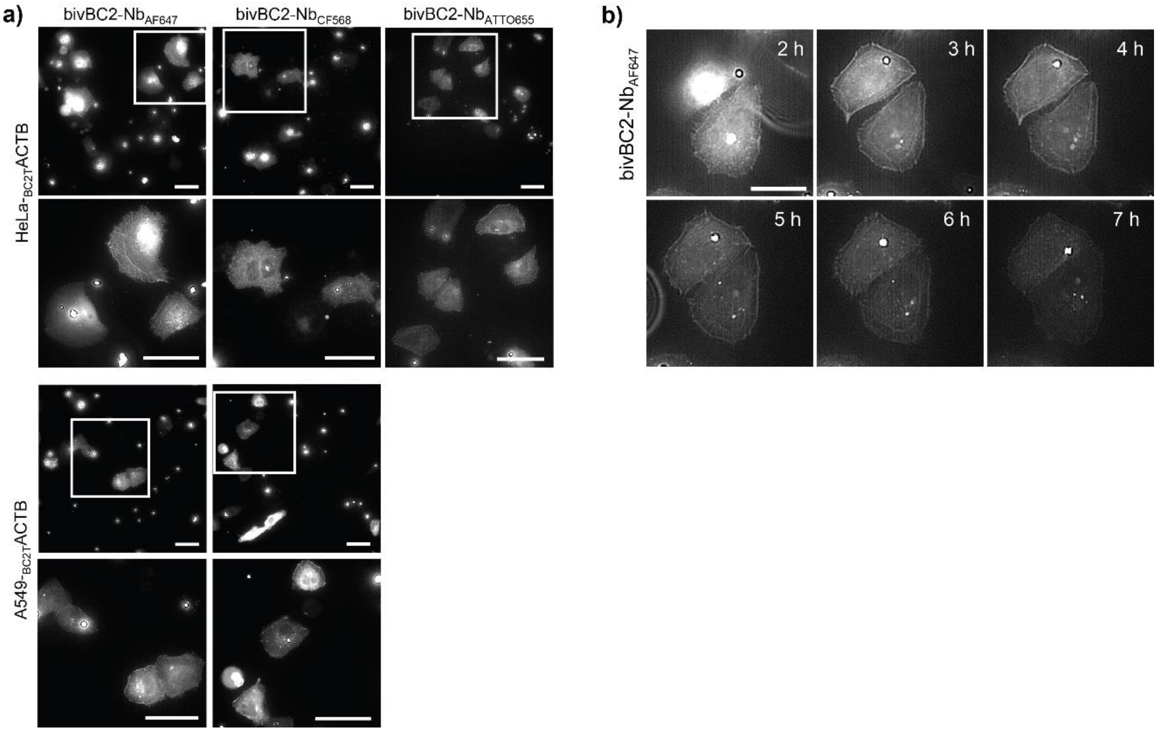

(**a**) Labeling of endogenous BC2-tagged actin upon transduction of bivBC2-Nb conjugated to different fluorescent dyes. Shown are representative images of living HeLa-$_{BC2T}$ACTB cells labeled either with bivBC2-Nb$_{AF647}$, bivBC2-Nb$_{CF568}$ or bivBC2-Nb$_{ATTO655}$ (upper panel) and A549-$_{BC2T}$ACTB cells labeled with either bivBC2-Nb$_{AF647}$ or bivBC2-Nb$_{CF568}$ (lower panel). Selected areas of transduced cells (indicated by white squares) are depicted as enlarged images. Scale bars, 50 µM. (**b**) Time lapse imaging of HeLa-$_{BCT2}$ACTB upon transduction of the bivBC2-Nb$_{AF647}$. Shown are representative images of two nanobody-transduced cells. Scale bar, 25 µm.

**Supplementary Figure 15**

a) chemically fixed HeLa-$_{\mathrm{BC2T}}$ACTB/bivBC2-Nb$_{\mathrm{AF647}}$

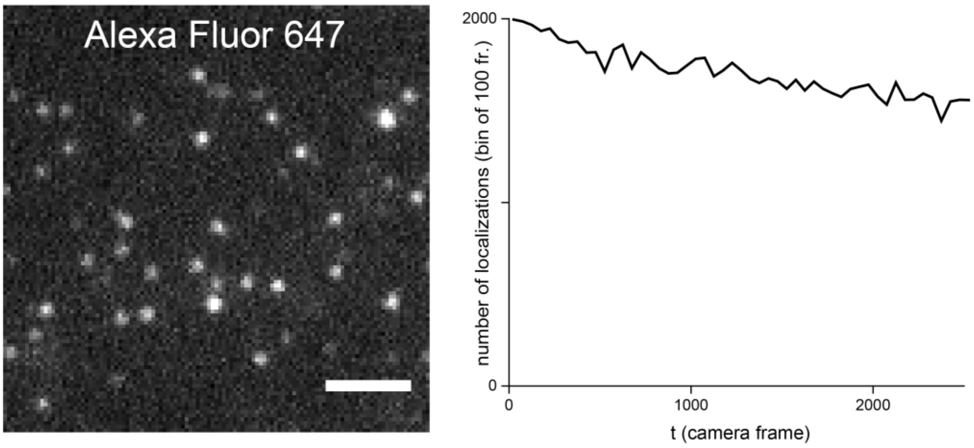

b) living HeLa-$_{\mathrm{BC2T}}$ACTB/bivBC2-Nb$_{\mathrm{ATTO655}}$

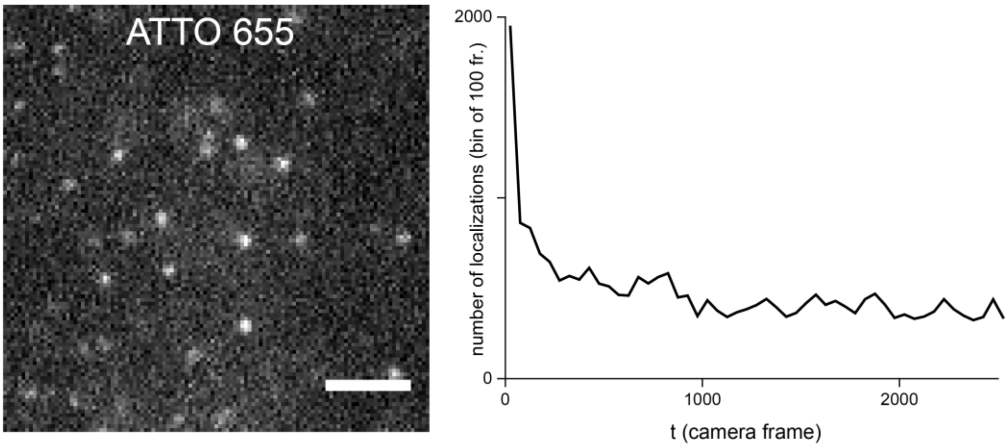

Comparison of ATTO655 and AF647 photophysics under dSTORM imaging conditions in living and chemically fixed cells. (**a**) Representative single imaging frame, extracted from a dSTORM movie of chemically fixed HeLa-$_{\mathrm{BC2T}}$ACTB stained with the bivBC2-Nb$_{\mathrm{AF647}}$, under standard dSTORM conditions (**Methods**). Line graph representing the absolute frequency count of localizations (y axis) at a bin size of 100 over the first 2500 frames of a 15 x 15 µm ROI of the movie (x axis). (**b**) Representative single imaging frame, extracted from a dSTORM movie of live HeLa-$_{\mathrm{BC2T}}$ACTB stained with the bivBC2-Nb$_{\mathrm{ATTO655}}$. Line graph representing the absolute frequency count of localizations (y axis) at a bin size of 100 over the first 2500 frames of a 15 x 15 µm ROI of the movie (x axis). Imaging sequences taken from raw data acquisitions of both conditions can be found in **Supplementary Movies 5 and 6.**

## References

1. Nieuwenhuizen, R.P. et al. Measuring image resolution in optical nanoscopy. *Nature methods* **10**, 557-562 (2013).
2. Braun, M.B. et al. Peptides in headlock–a novel high-affinity and versatile peptide-binding nanobody for proteomics and microscopy. *Scientific reports* **6** (2016).

## 9.2 Supplemental information: A General Mechanism of Photoconversion of Green-to-Red Fluorescent Proteins Based on Blue and Infrared Light Reduces Phototoxicity in Live-Cell Single-Molecule Imaging

Angewandte Chemie
Eine Zeitschrift der Gesellschaft Deutscher Chemiker

Supporting Information

# A General Mechanism of Photoconversion of Green-to-Red Fluorescent Proteins Based on Blue and Infrared Light Reduces Phototoxicity in Live-Cell Single-Molecule Imaging

*Bartosz Turkowyd[+], Alexander Balinovic[+], David Virant, Haruko G. Gölz Carnero, Fabienne Caldana, Marc Endesfelder, Dominique Bourgeois, and Ulrike Endesfelder 0000-0002-7801-6278**

anie_201702870_sm_miscellaneous_information.pdf
anie_201702870_sm_SM_1.gif
anie_201702870_sm_SM_2.gif
anie_201702870_sm_SM_3.gif
anie_201702870_sm_SM_4.gif
anie_201702870_sm_SM_5.gif
anie_201702870_sm_SM_6.gif

## Materials and Methods

### Fluorescent protein plasmids

Plasmids carrying the sequences of the fluorescent proteins (FPs) were obtained from different sources or constructed as listed in **Table S1**. All plasmids were checked by sequencing (Eurofins Genomics, Germany) and heat-shock-transformed into expression-optimized BL21-AI (Thermo Fischer, Germany).

### Plasmid construction

pRSETa-mMaple, pRSETa-mMaple3, pRSETa-mEos3.2 and pRSETa-mKikGR were generated by a customized CPEC protocol [1]. In short, the pRSETa backbone (from pRSETa-mEos2, addgene #20341) and the FP sequences (pBAD18 templates [2]) were amplified by PCR (Phusion, NEB) using the corresponding primers (**Table S3**). Purified PCR products were mixed in 1:10 molar ratio and ligated. CPEC reaction mixes were used for bacterial transformation directly after ligation.

pRSETb-pcDronpa-A69T, pRSETb-pcDronpa2-A69T, pRSETa-mEos3.2-A69T, pRSETa-mEos4b-A69T, pRSETa-mKikGR-V69T, pRSETa-mMaple3-V157I(V166I) were generated by site-directed mutagenesis PCR using the corresponding primers (**Table S3**). PCR reaction mixes were digested by DpnI (NEB, Germany) to remove residual template plasmids (2 h, 37°C) prior to the transformation. All primer were designed in Benchling (Benchling Inc.) and synthesized by Eurofins Genomics.

### MG1655 rpoC-Dendra2 strain

MG1655 incorporating rpoC-Dendra2 was generated by homologous recombination using a modified lambda red recombination pKD46 protocol [3]. In short, the PCR-amplified Dendra2-sequence followed by the frt flanked chloramphenicol resistance gene from the codon-optimized Dendra2 pBAD18 template[2] with auxiliary homologous overhang sequences was electroporated (5ms, 1.8 kV) into MG1655 cells.

### Samples with transiently expressed FPs in BL21ai cells

Strains from -80°C stocks were cultured overnight at 37°C, 210 rpm, LB with 100 µg/mL ampicillin, reinoculated, grown to OD 0.2 and induced by 0.5% w/v arabinose (Sigma-Aldrich, Germany). After 2 hours, cells were fixed for 15 minutes with 2% paraformaldehyde (Sigma-Aldrich, Germany) and washed twice in 100 mM PBS (*pH* 7.4). Samples were stored in 100 mM PBS (*pH* 7.4)/0.1% sodium azide at 4°C or immediately immobilized on 8-well slides (Ibidi, Germany) previously cleaned with 2% Hellmanex (Hellma, Germany) and coated with 0.05% poly-L-lysine (Sigma-Aldrich, Germany).

### Live cell samples with MG1655 rpoC-Dendra2

Strains from -80°C stocks were cultured overnight at 37°C, 210 rpm, LB with 34 µg/mL chloramphenicol, reinoculated into 2% glucose EZ Rich Defined Medium (Teknova, USA) and grown at 32°C, 210 rpm to OD 0.2. Bacteria were placed on fresh agarose pads (1% low melting agarose (Sigma-Aldrich, USA) with EZRDM).

### Purification of fluorescent proteins

Pellets of cultures overexpressing FPs from pRSET plasmids were suspended in 10 mM PBS (*pH* 7.4) with lysozyme (0.5 mg/mL) for 2h, homogenized by ultrasound (UP100H, Hielscher, Germany) and centrifuged for 15 minutes (17000 x g, 4°C). FPs were purified from the supernatant by Ni-NTA spin columns (Thermo Fischer, Germany) followed by a buffer exchange to 10 mM PBS (*pH* 7.4) (Nanosep columns, VWR, Germany).

### Microscope Setup

Imaging was performed on a custom build setup based on an automated Nikon Ti Eclipse microscope equipped with appropriate dichroic and filters (ET dapi/Fitc/cy3 dichroic, ZT405/488/561rpc rejection filter, ET525/50 or ET610/75 bandpass, all AHF Analysentechnik, Germany), and a CFI Apo TIRF 100x oil objective

(NA 1.49, Nikon). For PC using 640 nm laser illumination, a zt405/488/561/640rpc dichroic and a ZET405/488/561/640 rejection filter were used (both AHF Analysentechnik, Germany). All lasers (405 nm OBIS, 561 nm OBIS, 640 nm OBIS, 730 nm OBIS, 488 nm Sapphire; all Coherent Inc. USA) except 730 nm were modulated via an acousto-optical tunable filter (AOTF) (Gooch and Housego, USA). Fluorescence was detected by an emCCD (iXON Ultra 888; Andor, UK). The z-focus was controlled by a commercial perfect focus system (Nikon, Germany). Acquisitions were controlled by µManager [4]. Live cell experiments were performed on a customized heating stage at 32°C.

### Spectroscopy

Absorption spectra and fluorescence spectra (**Fig. S2**) were measured in V-750 and FP-8500 instruments (Jasco, Germany), respectively, using a 50µl UV-transparent quartz cuvette. Molar extinction coefficients (**Table 1 and Table S2**) were calculated as described [5]. $pK_a$ values (**Fig. S2**) were determined as per previous description [6].

### Photoconversion experiments

Photoconversion of the pcFPs variants by 405 nm and 488/ 730 nm illumination was measured in fixed BL21ai cells immobilized on 8-well slides (Ibidi, Germany) in 100 mM PBS equilibrated to different *pH* values (**Fig. S3 (c)**). In 405 nm-mediated photoconversion experiments, immobilized fixed cells were continuously illuminated by 2.5 W*cm$^{-2}$ 405 nm light; in the PC experiments, cells were continuously illuminated by 450 W*cm$^{-2}$ of 730 nm light and 488 nm laser pulses of 4 W*cm$^{-2}$ were synchronized with every fifth imaging frame. In both modes, the fluorescence was read-out by a continuous illumination of 200 W*cm$^{-2}$ of 561 nm laser irradiation. All regions of interests were imaged for 30 s with 30 ms exposure time making use of the frame transfer mode of the camera. For experiments measuring the PC efficiency for Dendra2 at different 488 and 730 nm light intensities, 100 mM PBS (*pH* 7.4) was used (**Fig. S3 (b)**). For PC experiments with 488 and 640 nm light, cells were imaged in 100 mM PBS (*pH* 8.5) and laser intensities were adjusted to 4 W*cm$^{-2}$ of 488 nm light pulsed every fifth frame and 400 W*cm$^{-2}$ of continuous 640 nm light (**Fig. S3 (e)**).

### Experiments on the stability of fluorescence signals

Fluorescence of the green and red chromophore form of the photoconvertible FPs was measured in fixed BL21ai cells immobilized on 8-well slides (Ibidi, Germany) in 100 mM PBS (*pH* 7.5). For fluorescence intensity measurements in the green chromophore form, samples were illuminated by 3 W*cm$^{-2}$ of 488 nm light. The red chromophore form was imaged after photoconverting the ROIs by illumination of 2.5 W*cm$^{-2}$ 405 nm laser light for 15 seconds. ROIs were then illuminated by 200 W*cm$^{-2}$ of 561 nm laser light. Intensity traces for both channels were recorded for 90 s with 30 ms exposure time in the frame transfer mode of the camera (**Fig. S3 (d)**).

### Intermediate state lifetime measurements

Intermediate state half-life measurements were performed in fixed BL21ai cells immobilized on 8-well slides (Ibidi, Germany) in 100 mM PBS (*pH 7.5*). Samples were illuminated by alternating between 30 ms irradiation by 4 W*cm$^{-2}$ of 488 nm light and 30 ms irradiation by 200 W*cm$^{-2}$ of 561 nm and 2 kW*cm$^{-2}$ of 640 nm light. Both channels were rapidly switched by an AOTF controller (ESTechnical, Kent, UK) with in between delays set from 0 to 30 ms (**Fig. S4 a (i)**). 640 nm light instead of 730 nm light had to be used due to the technical limitation of the AOTF, necessary for fast modulation, of only accepting wavelengths from 400 - 650 nm only. Intensity traces were measured over 1000 frames for each channel. Additionally, a UV photoconversion control was performed by illuminating the samples with alternations of 30 ms long irradiations of 2.5 W*cm$^{-2}$ of 405 nm light and 200 W*cm$^{-2}$ of 561 nm light (**Fig. S4 b (i)**).

### Reversible photoswitching experiments of the green fluorophores

Fluorescence decay under 488 nm illumination and recovery upon 405 nm light were measured in fixed BL21ai cells immobilized on 8-well slides (Ibidi, Germany) in 100 mM PBS (*pH 7.5*). For fluorescence decrease measurements, samples were continuously illuminated by 4 W*cm$^{-2}$ of 488 nm light. For fluorescence recovery, measurements samples were continuously illuminated by 2.5 W*cm$^{-2}$ of 405 nm light and 488 nm laser pulses of 4 W*cm$^{-2}$ were synchronized with every 20th imaging frame. Six cycles were recorded on the same ROI, both for 60 s with an exposure time of 30 ms exposure time (**Fig. S5 (a)**).

### Post-processing and data analysis of ensemble measurements

All image stacks were post-processed by scripts in Fiji [7] as illustrated in **Fig. S3 (a)**. In short, ROIs were extracted by identifying individual bacterial shapes from fluorescence averages excluding overlapping or out-of-focus cells. The mean fluorescence intensity per pixel was measured as a function of time. For primed conversion experiments, frames including 488 nm illumination pulses were excluded from the analysis due to increased background of channel-leaking green fluorescence. For photoconversion efficiency experiments (**Fig. S3 (b,c)**), extracted data was fitted by equation (1).

$$I(t) = BG - Ae^{-kt} \tag{1}$$

Fitted conversion rates *k* and amplitudes *A* were taken only from fits of R-squared values of 0.95 or higher. For non-converting settings, where no curve could be fitted, the difference of the average intensity prior to the photoconversion and the maximum value reached during the illumination was plotted instead. To measure the photostability of the green fluorescence signal (**Fig. S3 (d)**), extracted data was fitted by equation (2).

$$I(t) = BG + Ae^{-kt} \tag{2}$$

Fitted conversion rates *k* were taken only from fits with R-squared values of 0.95 or higher, and their reciprocal multiplied by *ln(2)* yielded the fluorescence decrease time $t_{0.5}$. The red fluorescence decay cannot be fitted by a single exponential decay; instead $t_{0.5}$ was directly measured at the moment it reached 50% of intensity $I_0$.

### Single-molecule experiments

Purified protein solutions were placed on 8-well slides (Ibidi, Germany) previously cleaned with 2% Hellmanex (Hellma, Germany) and rinsed twice with 100 mM PBS (*pH* 7.4) after 15 minutes. Surfaces were imaged under 405 nm and 488/730 nm photoconversion conditions in highly inclined and laminated optical sheet (HILO) illumination [8]. Additionally, a cleaned surface without single molecules was recorded as a purity control. Applied laser intensities were: 5 W*cm$^{-2}$ of 405 nm, 4 W*cm$^{-2}$ of 488 nm, 1 kW*cm$^{-2}$ of 561 nm and 450 W*cm$^{-2}$ of 730 nm. 405 nm and 488 nm lasers were pulsed every 25th frame. Movies were recorded at 33 Hz image acquisition rate for two minutes. Localizations of the fitted single fluorescent spots were obtained by the open source software rapidSTORM [9] and tracked with the help of customized tracking software written in C++. For analysis, only trajectories that started after 405 or 488 nm pulse frames and were visible for at least two frames were used (**Fig. S8 (a)**). Analysis was performed by using OriginPro software (Origin LAB Corporation). AD counts were converted to photon counts according to the emCCD camera sensitivity.

### Single-particle-tracking PALM experiments followed by cell growth quantification

Living rpoC-Dendra2 MG1655 *E.coli* cells were imaged under 405 nm and 488/730 nm photoconversion sptPALM conditions for 2, 4, 6 and 8 minutes in HILO illumination mode. Additionally, two controls were recorded: cells not illuminated by any laser light and cells illuminated for 6 minutes by the 561 nm read-out laser only. Applied laser intensities were: 690 mW*cm$^{-2}$ of 405 nm, 400 mW*cm$^{-2}$ of 488 nm, 450 W*cm$^{-2}$ of 730 nm and 600 W*cm$^{-2}$ of 561 nm. 405 nm and 488 nm lasers were pulsed every 12th frame. Movies were recorded at 77 Hz image acquisition rate to follow the diffusing RNA polymerase. After sptPALM imaging all illuminated regions and controls were imaged under bright light for 8 hours at 2 min intervals to quantify the cellular growth after the experiments. During sptPALM and overnight imaging, cells were incubated in 32°C. Localizations of the fitted single fluorescent spots were obtained by rapidSTORM [9], tracked with the help of customized tracking software written in C++ and visualized by customized software written in C++, to filter and group single molecule localizations or trajectories by their characteristics. The mean squared displacement (*MSD*) was calculated for all trajectories of at least four steps as per previous description [10]. (**Fig. 2** and **Fig. S7**)

**Visualization software** 3D protein structures taken from the Protein Data Bank (PDB) were visualized by Chimera (**Fig. S1 c**) [11]. All figures were prepared in Abobe Illustrator (Adobe Systems Inc.).

**Table S1.** Bacterial plasmids used for transient expression of fluorescent proteins.

| **FP** | **Backbone** | **Source** |
|---|---|---|
| Dendra2 | pRSETb | gift from Bourgeois lab, Grenoble, France[12] |
| Dendra2-T69A | pRSETb | gift from Bourgeois lab, Grenoble, France[12] |
| Dendra2-M159A | pRSETb | this work, created by David Virant using the pRSETb Dendra2 template |
| Dendra2-Q116N | pRSETb | this work, created by David Virant using the pRSETb Dendra2 template |
| Dendra2-Q116Y | pRSETb | this work, created by David Virant using the pRSETb Dendra2 template |
| Dendra2-S105N-Q116N | pRSETb | this work,created by David Virant using the pRSETb Dendra2 template |
| Dendra2-T104N-S105N-Q116N | pRSETb | this work,created by David Virant using the pRSETb Dendra2 template |
| IrisFP | pRSETa | gift from Bourgeois lab, Grenoble, France[5] |
| mEos2 | pRSETa | Addgene #20341 |
| mEos2-A69T | pRSETa | gift from Bourgeois lab, Grenoble, France[12] |
| mEos3.2 | pRSETa | this work, created by Haruko Gölz using codon-optimized mEos3.2 [2] |
| mEos3.2-A69T | pRSETa | this work, created by Haruko Gölz using the pRSETa mEos3.2 template |
| mEos4b | pRSETa | Addgene #51073 |
| mEos4b-V69T | pRSETa | this work, created by David Virant using the pRSETa mEos4b template |
| mKikGR | pRSETa | this work, created by Haruko Gölz using codon-optimized mKikGR [2] |
| mKikGR-V69T | pRSETa | this work, created by David Virant using the pRSETa mKikGR template |
| mMaple | pRSETa | this work, created by David Virant using codon-optimized mMaple[2] |
| mMaple3 | pRSETa | this work, created by Alexander Balinovic using codon-optimized mMaple3[2] |
| mMaple3-V157I | pRSETa | this work, created by David Virant using the pRSETa mMaple3 template |
| NijiFP | pRSETb | gift from Bourgeois lab, Grenoble, France[13] |
| pcDronpa | pRSETb | gift from Dedecker lab, Leuven, Belgium[14] |
| pcDronpa-A69T | pRSETb | gift from Dedecker lab, Leuven, Belgium[14] |
| pcDronpa2 | pRSETb | Addgene #78184 |
| pcDronpa2-A69T | pRSETb | this work, created by Alexander Balinovic using the pRSETb pcDronpa2 template |

**Table S2.** Properties of non-PC-converting green-to-red pcFPs

| **Name** | **Genetic background** | $\lambda_{exc}$ **(nm)** | $\lambda_{em}$ **(nm)** | **oligomeric state** | $\varepsilon$ **(M$^{-1}$ * cm$^{-1}$)** | $\Phi$ | ***pKa*** | $t_{0.5*int}$ **(s)** | **opt. pH$_{405}$** | **Refs** |
|---|---|---|---|---|---|---|---|---|---|---|
| Dendra2-T69A | Dendra2 T69A | 502[a]/563[a] | 518[a]/578[a] | m | 42000[a]/35400[a] | 0.56[a]/0.64[a] | 6.0[a]/7.0[a] | 0.4/0.8 | 6-7.5 | **a** [12] |
| Dendra2-M159A | Dendra2 M159A | 471[b]/528[b] | 504[b]/562[b] | m | 51100[b]/42000[b] | 0.55[b]/0.65[b] | 6.5[b]/7.3[b] | ND/ND | ND | **b** [13] |
| NijiFP | Dendra2 F173S | 469[b]/526[b] | 507[b]/569[b] | m | 41100[b]/42000[b] | 0.64[b]/0.65[b] | 7.0[b]/7.3[b] | ND/ND | 6-7.5 | **b** [13] |
| mEos2 | EosFP N11K E70K H74N H121Y | 508[a]/573[a] | 519[a]/584[a] | m | 79000[a]/34300[a] | 0.66[a]/0.65[a] | 5.0[a]/6.6[a] | 0.8/0.1 | 5.5-7 | **a** [12] |
| mEos3.2 | mEos2 I102N H158E Y189A | 507[c]/572[c] | 516[c]/580[c] | m | 63400[c]/32200[c] | 0.84[c]/0.55[c] | 6.5[c]/5.8[c] | 1.1/0.1 | 6-7.5 | **c** [6] |
| mEos4b | mEos3.2 K9R F34Y S39T A69V C195A | 505[d]/570[d] | 516[d]/580[d] | m | 78200[d]/55500[d] | 0.84[d]/0.71[d] | ND/ND | 1.2/0.1 | 6-7.5 | **d** [15] |
| IrisFP | EosFP F173S | 488[b]/551[b] | 516[b]/580[b] | t | 57800[b]/27000[b] | 0.48[b]/0.50[b] | 5.7[b]/6.8[b] | ND/ND | 5.5-7.5 | **b** [13] |
| pcDronpa | Dronpa V60A C62H N94S N102I E218G | 505[e]/569[e] | 517[e]/581[e] | t | 115000[e]/75000[e] | 0.85[e]/0.68[e] | 5.5[e]/6.3[e] | 1.1/3.1 | 6.5-7.5 | **e** [14] |
| pcDronpa2 | pcDronpa Y116N | 504[e]/569[e] | 515[e]/583[e] | t | 100000[e]/105000[e] | 0.83[e]/0.68[e] | 5.8[e]/6.1[e] | 0.6/0.2 | 6.5-7.5 | **e** [14] |
| mKikGR | KikGR A17S Q32R F34Y I37T N39T C116T V126T N161E Q167E F193Y L212A H219Y L222T P223Y L225G +228Y 229E 230F 231E 232A | 505[f]/580[f] | 515[f]/591[f] | m | 49000[f]/28000[f] | 0.69[f]/0.63[f] | 6.6[f]/5.2[f] | 0.6/0.3 | 5.5-6.5 | **f** [16] |

Table summarizing the properties of green-to-red pcFPs used in this study which can be photoconverted by 405 nm illumination but not by PC. Listed are their key photophysical properties with $\lambda_{exc}$ – excitation wavelength; $\lambda_{em}$ – emission wavelength; ε – molar extinction coefficient at pH 7.5; Φ – fluorescence quantum yield; $t_{0.5*int}$ – time of 50% intensity loss when irradiated by 488 nm or 561 nm light respectively at pH 7.5 in relation to Dendra2 (**Fig. S3e)**. Furthermore, their genetic background, oligomeric state (m – monomeric; t – tetrameric), the pKa values of the chromophores (**Fig. S2**) as well as the optimal pH for 405 nm light-mediated photoconversion are given (**Fig. S3**). Values are either from the literature as labeled or were measured in this study. ND - not determined.

**Table S3**. List of primers.

| **lambda red recombination primers (MG1655 rpoC-Dendra2)** | |
|---|---|
| rpoC_Dendra2_FP | CCAGCCTGGCAGAACTGCTGAACGCAGGTCTGGGCGGTTCTGATAACGAGtctggtggcggcggttcta |
| rpoC_Dendra2_RP | CCCCCCATAAAAAAACCCGCCGAAGCGGGTTTTTACGTTATTTGCGGActagagaataggaacttcctgccactcatc |
| rpoc_FP_seq | CGTACCACCAGGATCGTATGCG |
| Dendra2_RP_seq | GGTGAAAGTTGGAACCTCTTACGTGC |
| **CPEC primers** | |
| F_mEos3.2-CPEC | GGATCGATGGGGATCCATGTCTGCCATTAAACCGGATATGAA |
| R_mEos3.2-CPEC | CCGGATCAAGCTTCGAATTCTTATTAGCGACGCGCATTATCC |
| F_mKikGR_CPEC | ATAAGGATCGATGGGGATCCATGAGCGTTATCACCAGCGAGATGA |
| R_mKikGR_CPEC | CCGGATCAAGCTTCGAATTCTTATTAGGCCTCGAATTCGTACTTGG |
| F_mMaple-CPEC | AGGATCGATGGGGATCCATGGTTAGCAAGGGCGAGGAGACC |
| R_mMaple-CPEC | CCGGATCAAGCTTCGAATTCTTATTTGTACAGCTCATCCATGCTGTC |
| F_mMaple3-CPEC | CGATAAGGATCGATGGGGATCCATGGTTAGCAAGGGCGAAGAAACCAT |
| R_mMaple3-CPEC | GCCGGATCAAGCTTCGAATTCTTATTATTTGTACAGCTCATCCATGCTGTC |
| F_pRSETa_CPEC | TAAGAATTCGAAGCTTGATCCG |
| R_pRSETa_CPEC | CATGGATCCCCATCGATCCTTAT |
| **Site-directed mutagenesis primers** | |
| F_Dendra2-M159A | CATCAACGCAGCCCTGCTGCTGGAGGGCGGC |
| R_Dendra2-M159A | AGGGCTGCGTTGATGTTGCCCACCAGCAGGCC |
| F_Dendra2-Q116N | CTTCTTCAACAACGTGCGCTTCAAGGGCACCAACTTCCC |
| R_Dendra2-Q116N | GCACGTTGTTGAAGAAGCAGTCGCCCTCCAGGCTGAT |
| F_Dendra2-Q116Y | TGCTTCTTCTATAACGTGCGCTTCAAGGGCACCAACTTCCCC |
| R_Dendra2-Q116Y | CGCACGTTATAGAAGAAGCAGTCGCCCTCCAGGCTGATG |
| F_Dendra2-R104T | CACCATCACTAACGACATCAGCCTGGAGGGCGACTGCTTCTT |
| R_Dendra2-R104T | CTGATGTCGTTAGTGATGGTGCAGATGCCCTTGTCCTCGAAGGTC |
| F_Dendra2-S105N | ACCATCCGCAACGACATCAGCCTGGAGGGCGACTGC |
| R_Dendra2-S105N | GATGTCGTTGCGGATGGTGCAGATGCCCTTGTCCTCGAAGGT |
| F_mEos3.2-A69T | GCGTTTTCACTAAATATCCGGATAATATCCAGGATTACTTTAAA |
| R_mEos3.2-A69T | GATATTTAGTGAAAACGCGGTTACCATAATGAAACGCC |
| F_mEos4b-V69T | GGGTATTCACGAAATATCCAGACAACATACAAGACTATTTTAAGCA |
| R_mEos4b-V69T | GATATTTCGTGAATACCCTGTTGCCGTAATGGAATGC |
| F_mKikGR-V69T | GCGTGTTCACTGAGTACCCGGAGGAGATCGTGGACTACTTC |
| R_mKikGR-V69T | GGTACTCAGTGAACACGCGGTTACCGTAGTGGAAGGCGG |
| F_mMaple3-V157I | GGGCGACATTAAGATGAAGCTGCTGCTGAAGGGTGGCAG |
| R_mMaple3-V157I | CTTCATCTTAATGTCGCCCTTCAGCACACCGTCGCGC |
| F_pcDronpa2-A69T | GGTATTCACTAAATACCCAGAAAATATAGTAGACTATTTCAAGCA |
| R_pcDronpa2-A69T | GGGTATTTAGTGAATACCCTGTTGCCGTAATGGAA |

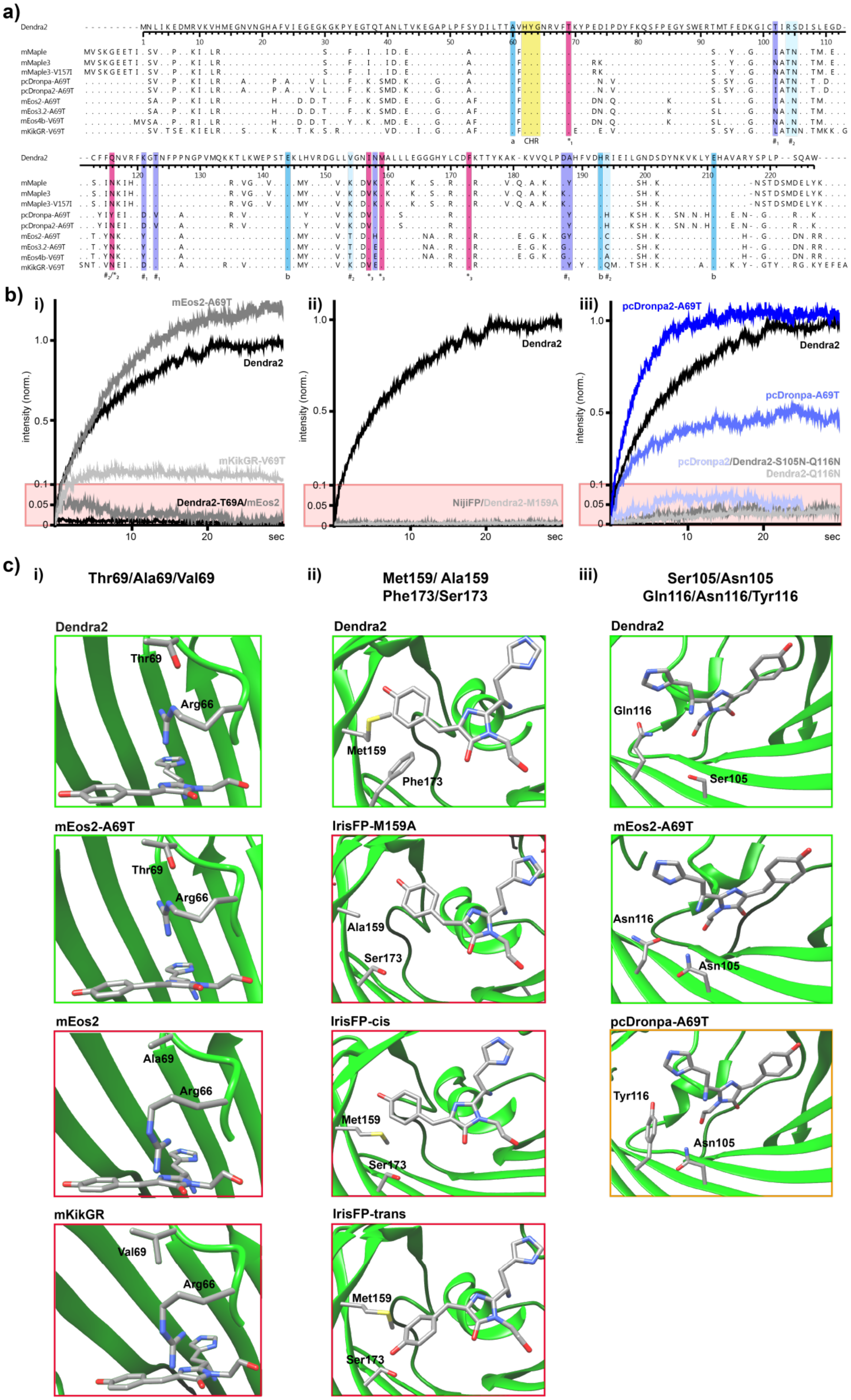
a)
Dendra2
mMaple
mMaple3
mMaple3-V157I
pcDronpa-A69T
pcDronpa2-A69T
mEos2-A69T
mEos3.2-A69T
mEos4b-V69T
mKikGR-V69T
CHR
b)
i)
intensity (norm.)
mEos2-A69T
Dendra2
mKikGR-V69T
Dendra2-T69A/mEos2
sec
ii)
Dendra2
NijiFP/Dendra2-M159A
iii)
pcDronpa2-A69T
pcDronpa-A69T
pcDronpa2/Dendra2-S105N-Q116N
Dendra2-Q116N
c)
i)
Thr69/Ala69/Val69
Dendra2
Thr69
Arg66
mEos2-A69T
mEos2
Ala69
mKikGR
Val69
ii)
Met159/ Ala159
Phe173/Ser173
Met159
Phe173
IrisFP-M159A
Ala159
Ser173
IrisFP-cis
IrisFP-trans
iii)
Ser105/Asn105
Gln116/Asn116/Tyr116
Gln116
Ser105
Asn116
Asn105
pcDronpa-A69T
Tyr116

**Figure S1. Influence of single amino-acid mutations on pcFP variants**

a) Sequences of pcFP variants capable of PC in alignment with Dendra2.

**a** V60A yields shortened maturation times; **CHR** chromophore sequence HYG. Deviation from His62 is common for several reversibly green switching FPs [14, 17].

**$*_1$** mEos2, mEos3.2, mEos4b, pcDronpa, pcDronpa2, mKikGR, Dendra2-T69A can be photoconverted by UV light but not by 488/730 nm illumination.

**$*_2$** pcDronpa-A69T, a predecessor of pcDronpa2 (=pcDronpa-Y116N) has a low 488/730 nm photoconversion efficiency. Dendra2-Q116N and Dendra2-Q116Y cannot be photoconverted. Dendra2-S105N-Q116N and Dendra2-R104T-S105N-Q116N regain their photoconversion ability but only at very low efficiency.

**$*_3$** Positions 157, 159 and 173 influence the photoswitching behavior of many pcFPs, e.g. NijiFP (=Dendra2-F173S) or Dendra2-M159A can be reversibly photoswitched [5, 13] but not converted by 488/730 nm light.

**b** amino acids critical for green GFP-like fluorescence [18].

**$\#_1$** amino acids influencing the oligomerization state [18].

**$\#_2$** amino acids critical for green-to-red pcFPs [18].

b) Exemplary photoconversion measurements for different pcFPs under PC conditions. All intensities were normalized to the intensity of red Dendra2 fluorescence. The y-axis within the red inset is stretched as indicated by the labels for better visibility.

c) Mutual organization of important amino acid residues in the chromophore environment. Colored boxes indicate the photoconversion characteristics of the different FPs: green, 405 & 488/730 nm converting; orange, moderately 488/730 nm converting but not 405 nm-converting and red, only UV converting.

(i) Residue 69 controls the orientation of the chromophore interacting residue Arg66. Only threonine variants can undergo PC.

(ii) Small residues at positions 159 (Ala159) and 173 (Ser173) increase the chromophore flexibilty and enable reversible conformation changes between *cis* and *trans* states which hinders PC.

(iii) Residues 105 and 116 are crucial for green-to-red photoconversion. Asn105/Tyr116 in pcDronpa-A69T prevents UV conversion, but allows for 488/730 nm conversion.

Structures were taken from the Protein Data Bank (PDB): Dendra2 (2VZX), mEos2 (3S05), mEos2-A69T (5DTL), mKikGR (4P76), IrisFP-M159A (4R6B), IrisFP-cis (2VVH), IrisFP-trans (2VVI), pcDronpa-A69T (4IZN).

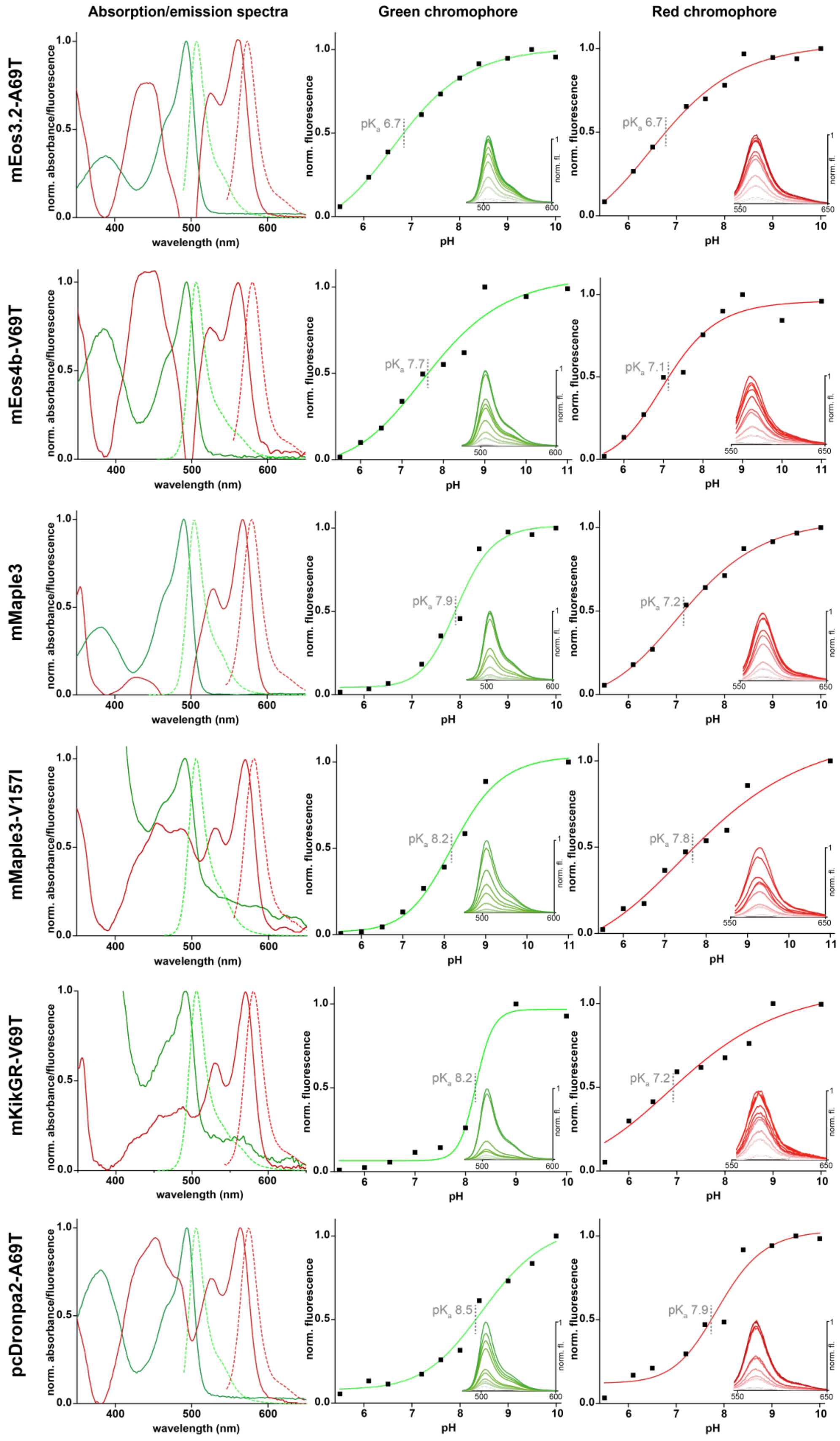

**Figure S2. Absorption, fluorescence spectra and pKa measurements of pcFPs in their green and red form.** Left: Absorption spectra (solid lines) and fluorescence spectra (dashed lines) of green and red chromophore forms. Middle and right: pH-dependency and fitted pK$_a$ values of the FPs measured for the green and red chromophore form, respectively.

a) Analysis procedure

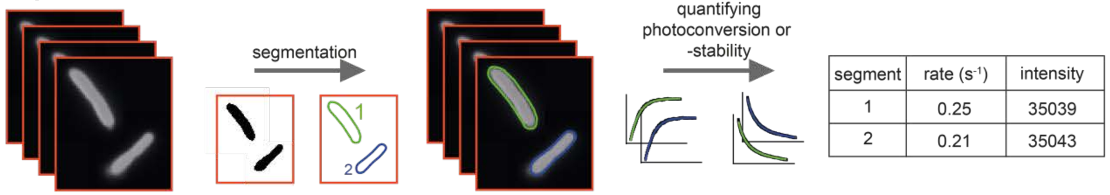

| segment | rate ($s^{-1}$) | intensity |
|---|---|---|
| 1 | 0.25 | 35039 |
| 2 | 0.21 | 35043 |

b) Efficiency of PC for Dendra2 in relation to 488 and 730 nm light intensity

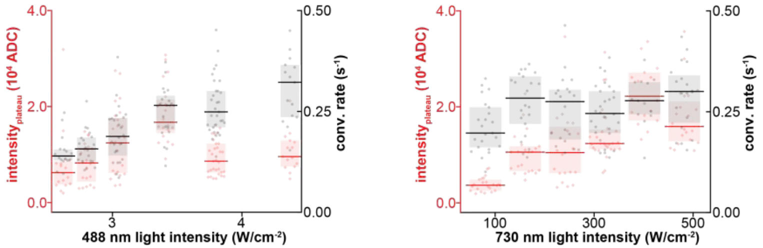

c) pH dependence of photoconversion mechanisms

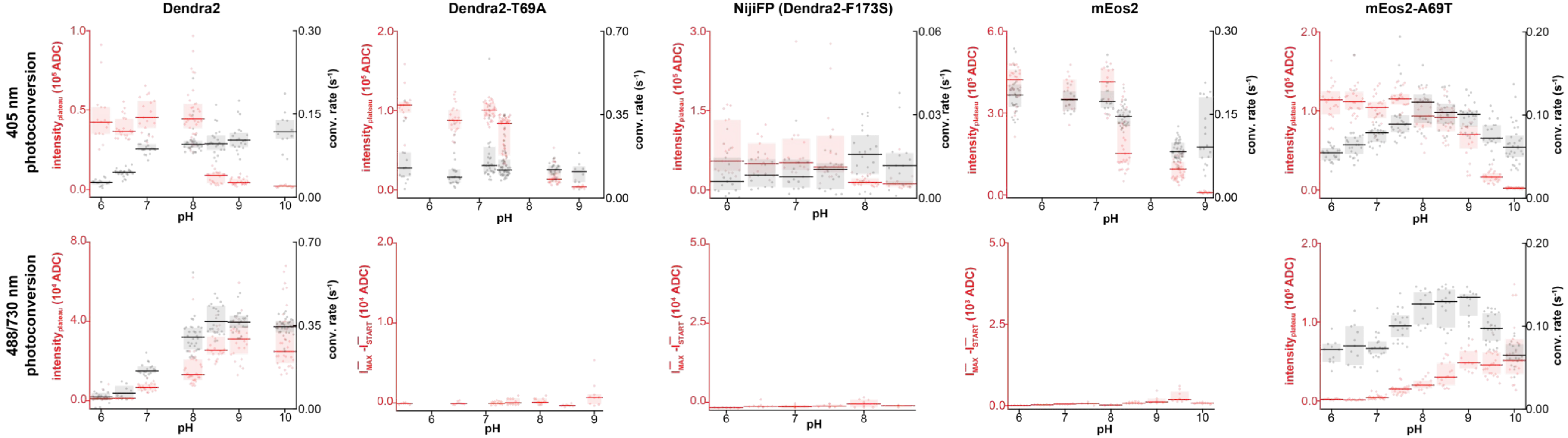
i) Dendra family

ii) mEos family

## c) pH dependence of photoconversion mechanisms- continuation

### ii) mEos family- continuation

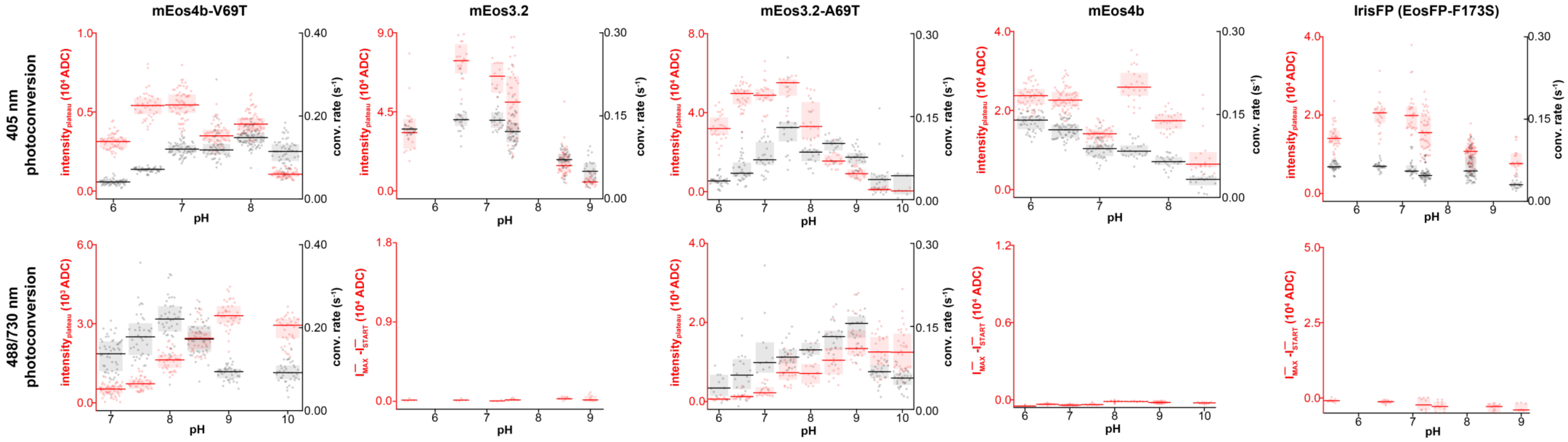

### iii) mMaple family

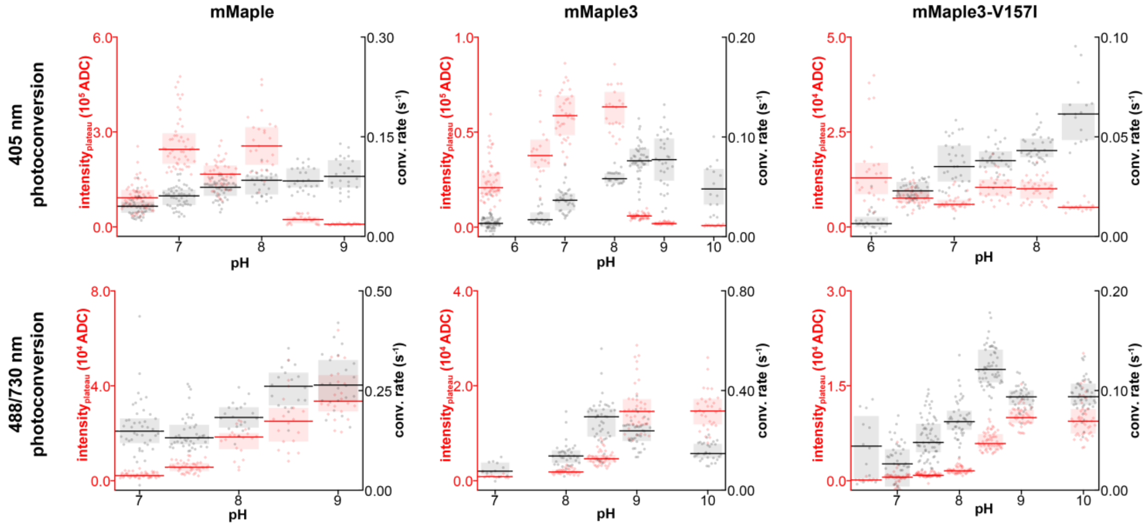

### iv) mKikGR family

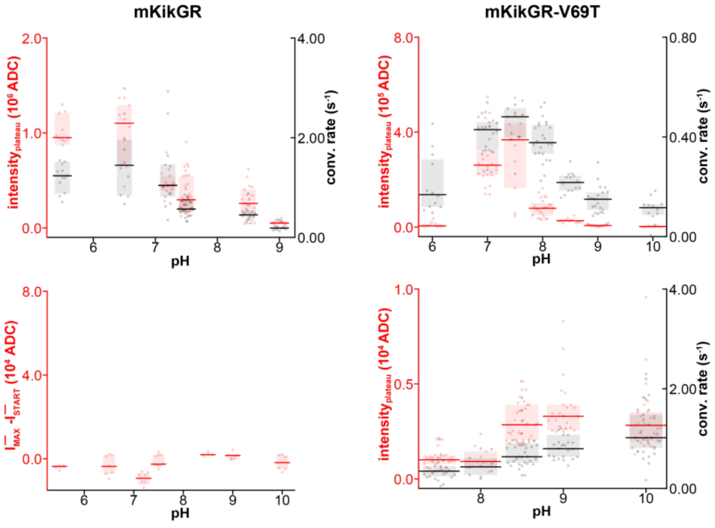

## c) pH dependence of photoconversion mechanisms- continuation

### v) pcDronpa family

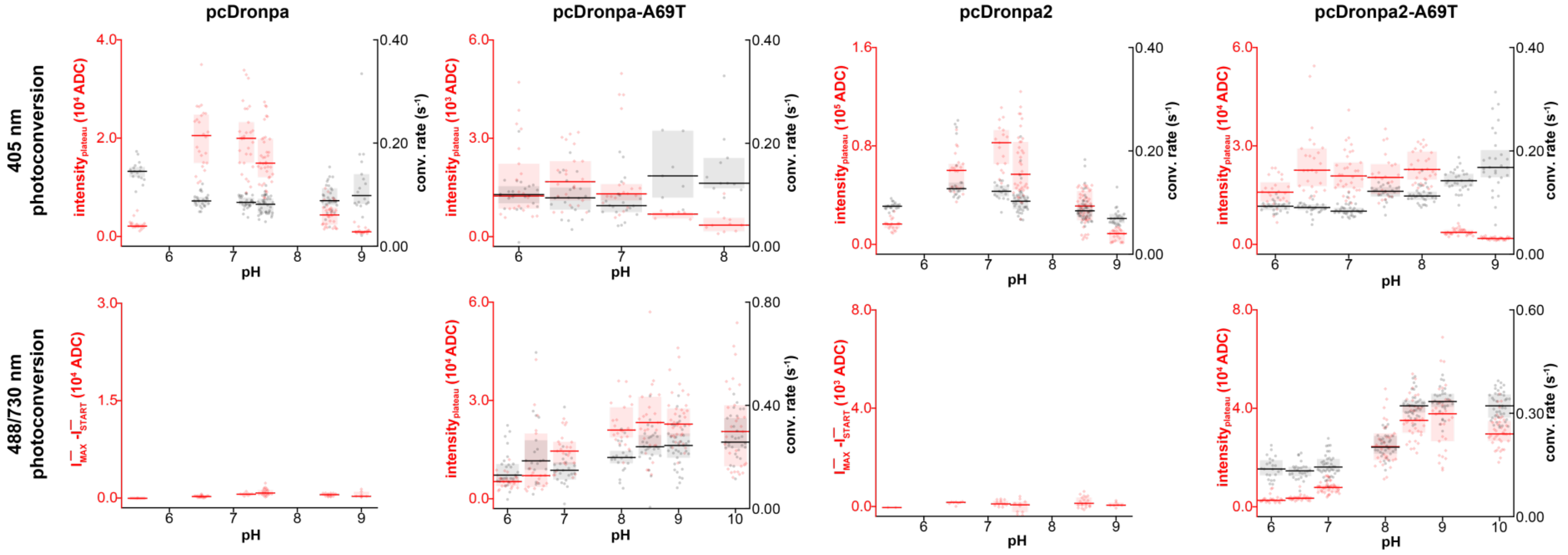

## d) Stability of fluorescence signal

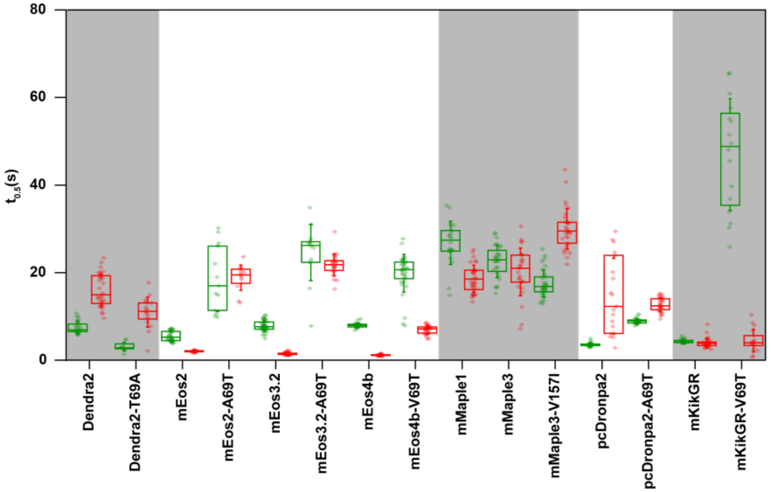

## e) Efficiency of 488 nm and 488/640 nm photoconversion ($PC_{488/730}$ = 100%)

| | $PC_{488}$ (%) | $PC_{488/640}$ (%) |
|---|---|---|
| **Dendra2** | 19 | 25 |
| **mEos2-A69T** | 13 | 31 |
| **mEos3.2-A69T** | 15 | 28 |
| **pcDronpa2-A69T** | 20 | 27 |
| **mMaple3** | 10 | 34 |
| **mKikGR-V69T** | 11 | 43 |

**Figure S3. Photoconversion rates, red fluorescence yield and photostability of the green and red form for pcFPs are dependent on applied laser wavelengths, laser intensities and pH.**

a) Analysis workflow for quantifying photoconversion and photostability of the pcFP variants as described in detail in the Materials and Methods section.

b) Impact of 488 nm and 730 nm light intensity on PC rate (grey) and red fluorescence intensity (red) measured for Dendra2. Increasing the 488 nm light intensity increases measured intensities (red bars and dots) as well as the conversion rate (gray bars and dots). For highest 488 nm laser intensities, the attained fluorescence intensity decreases, probably due to photobleaching of the green Dendra2 form. Increasing the 730 nm laser intensity increases the measured fluorescence intensities. The applied 730 nm light intensities do not alter the conversion rate significantly.

c) Green-to-red photoconversion efficiency and rates measured for pH values ranging from 6 to 10 by imaging overexpressed pcFPs in fixed *E.coli* cells and analyzed as depicted in a) and described in the Materials and Methods. 405 nm-mediated photoconversion and PC efficiencies were measured by the obtained red fluorescence intensities (red bars and dots) and photoconversion rates (gray bars and dots). Measurements were made for proteins from five different families: i) Dendra family; ii) mEos family; iii) mMaple family; iv) mKikGR family; v) pcDronpa family.

d) Stability of the fluorescence signal of the green and red chromophore forms for different proteins capable of 488/730 nm photoconversion and their non-PC-converting relatives. At time $t_{0.5I}$, the fluorescence intensity had decreased to 50% of the initial intensity. All threonine 69 variants show a slower decrease of the intensity in both the green and red channel.

e) Comparison of the photoconversion efficiency for different PC-converting pcFPs under illumination of only 488 nm light (4 $W*cm^{-2}$) and additional 640 nm light (400 $W*cm^{-2}$). Intensities in table are represented as a percentage of the intensity obtained by 488/730 nm illumination (4 $W*cm^{-2}$ and 400 $W*cm^{-2}$ for 488 and 730 nm, respectively) for each protein.

a) PC illumination with variable delay between 488 and 561/640 nm pulses

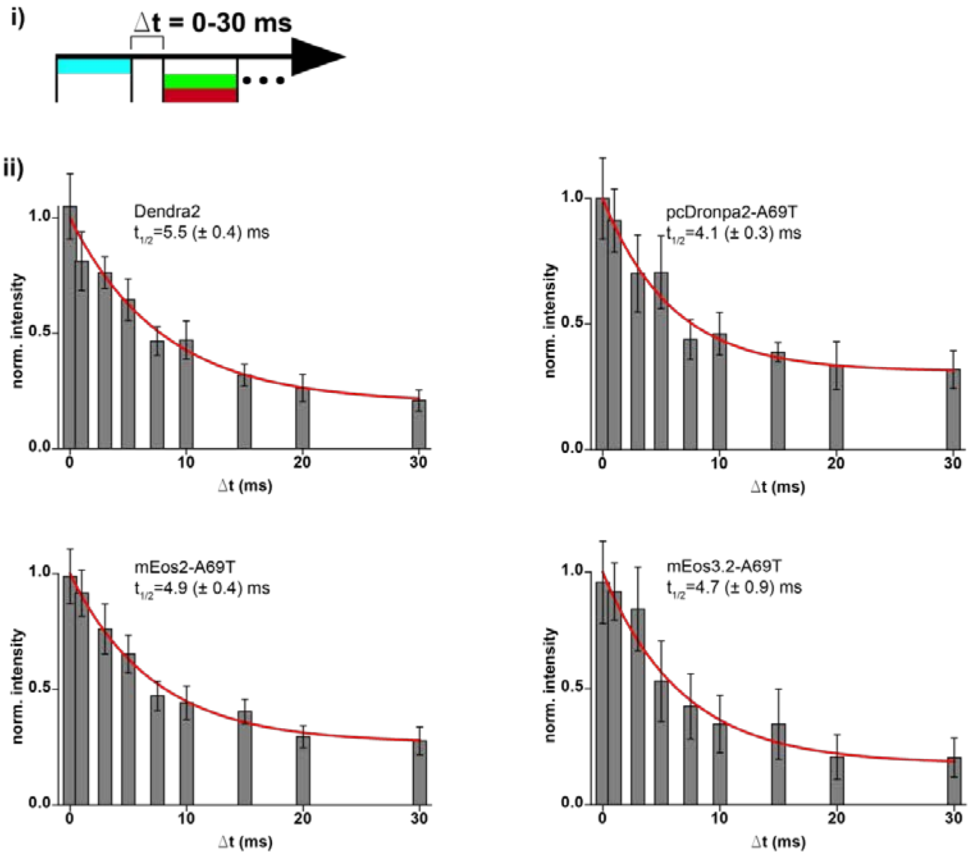

b) UV illumination with variable delay between 405 and 561 nm pulses

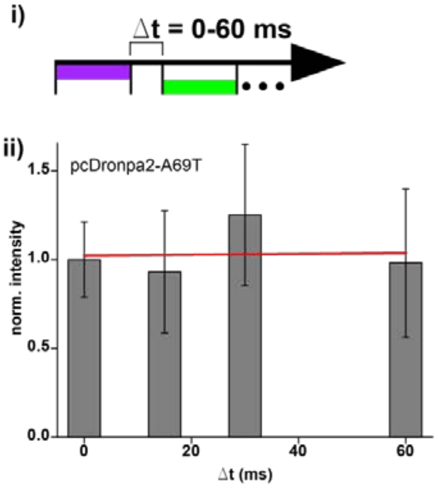

**Figure S4. Dependency of the PC efficiency on a delay of 0-30 ms between priming and conversion laser illumination.**

a) i) Scheme representing the applied illumination sequence with Δt being the delay between 488 laser pulses and 640 nm conversion/ 561 nm read-out. ii) The PC efficiency decreases exponentially for increasing delays between 488 and 640 nm light illuminations. Intensities, normalized to the intensity of Δt = 0 ms were fitted with a single exponential decay. Retrieved $t_{1/2}$ values represent the half-life of the presumed intermediate state, which is thought to be the entry state for PC by absorbing red/far red light.

b) i) Scheme representing illumination sequence for control experiments for 405 and 561 nm laser pulses. ii) Increasing the delay between 405 and 561 nm light does not affect the UV-photoconversion efficiency.

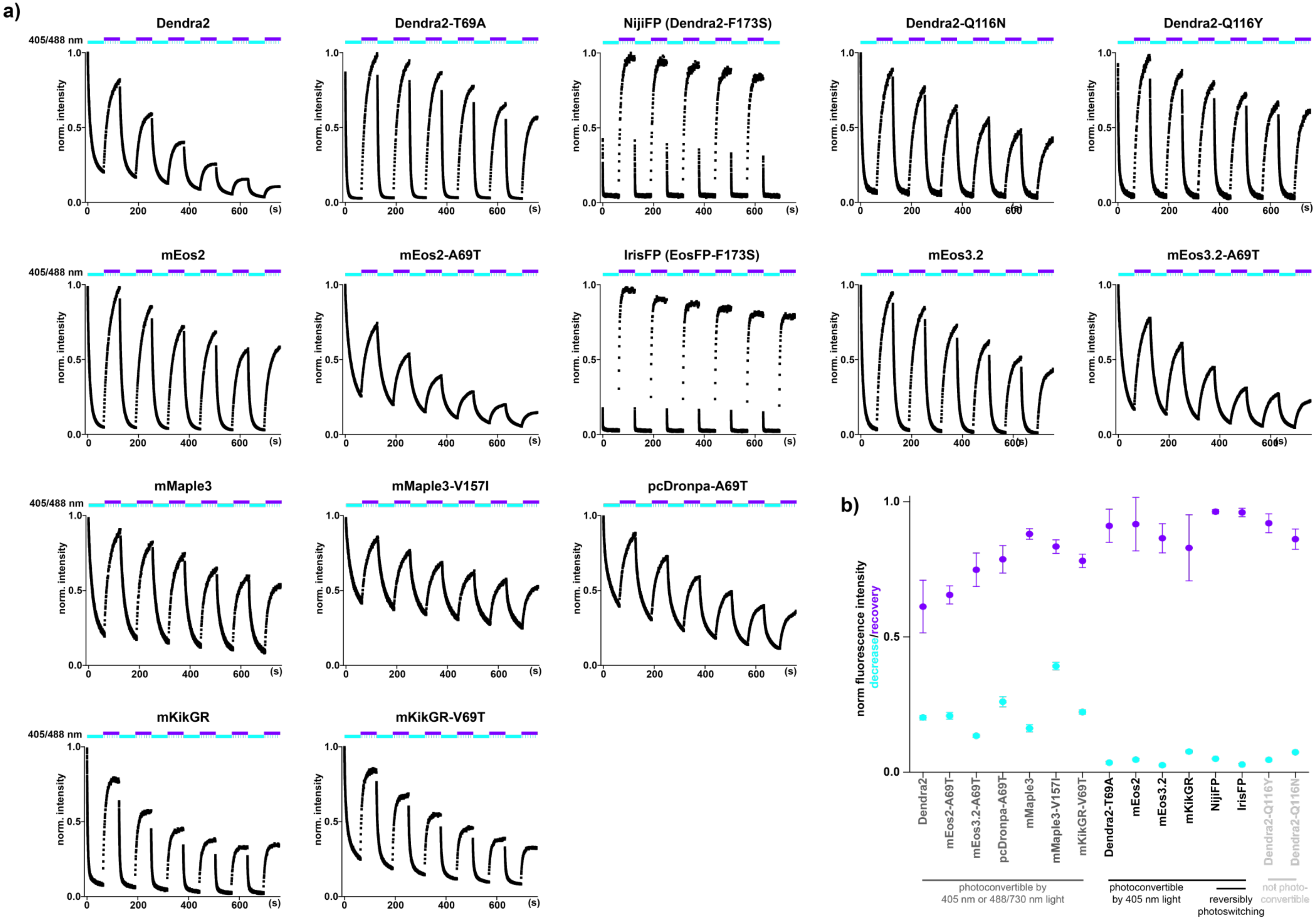
a)
405/488 nm
norm. intensity
(s)
0.0
0.5
1.0
0
200
400
600
Dendra2
Dendra2-T69A
NijiFP (Dendra2-F173S)
Dendra2-Q116N
Dendra2-Q116Y
mEos2
mEos2-A69T
IrisFP (EosFP-F173S)
mEos3.2
mEos3.2-A69T
mMaple3
mMaple3-V157I
pcDronpa-A69T
mKikGR
mKikGR-V69T
b)
norm fluorescence intensity
decrease/recovery
Dendra2
mEos2-A69T
mEos3.2-A69T
pcDronpa-A69T
mMaple3
mMaple3-V157I
mKikGR-V69T
Dendra2-T69A
mEos2
mEos3.2
mKikGR
NijiFP
IrisFP
Dendra2-Q116Y
Dendra2-Q116N
photoconvertible by 405 nm or 488/730 nm light
photoconvertible by 405 nm light
reversibly photoswitching
not photo-convertible

**Figure S5. Reversible photoswitching of the green form of pcFPs by 488 nm and 405 nm illumination**

a) Time traces of the green fluorescence intensity decrease under continuous 488 nm illumination for 60 s which is followed by continuous 405 nm illumination with probing 488 nm light pulses every 20th frame for another 60 s. This cycle was repeated six times on the same ROI. For all investigated proteins, recovery from non-fluorescent dark states was observed under 405 nm illumination. All pcFPs were overexpressed and measured in fixed E.coli cells as described in the Materials and Methods.

b) Evaluation of the green fluorescence intensity decrease levels (blue) and recovery levels (violet) of the pcFP-time traces in a): The fluorescence decrease level represents the fraction of FP molecules which remained fluorescent after one minute illumination by 488 nm light. The fluorescence recovery level shows the fraction of protein molecules which recovered their green fluorescent state after 60 s illumination with 405 nm light. All pcFPs capable of PC show a slower decrease in fluorescence under 488 nm illumination and thus a higher remaining fraction of molecules in their green fluorescent state after 60 s in comparison to the non-PC-converting FPs. Additionally, the fraction of molecules which recovers their green fluorescent state is lower in case of 488/730 nm photoconvertible proteins in comparison to proteins not capable of 488/730 nm photoconversion. NijiFP and IrisFP, which were designed for efficient reversible photoswitching show the highest contrast.

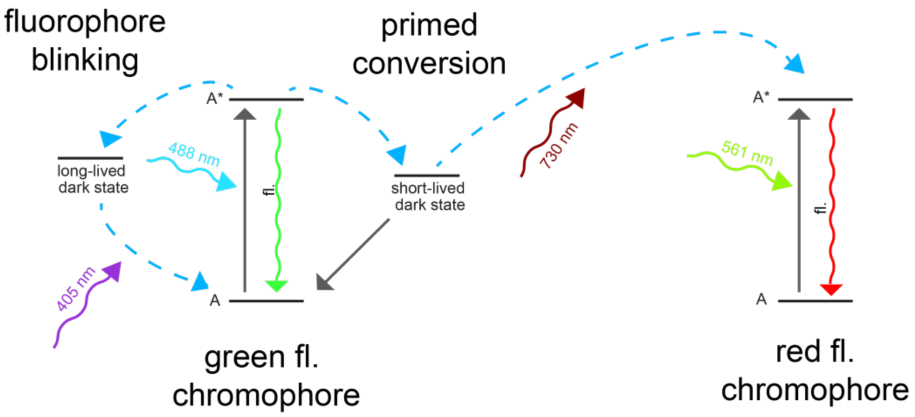

**Figure S6. Model of photoconversion**

Green-to-red pcFPs can populate different reversible dark states which might yield an explanation for the different PC efficiencies of different pcFPs. In this model, pcFPs which show strong blinking behavior and thus have a high tendency of populating long-lasting dark states, show only poor or non-detectable 488/730 nm photoconversion efficiency. Here, these dark states are thought to be directly competing with a short-lived intermediate state, which is suspected to be the entry point for PC by absorbing near-infra red light. Due to its estimated half-life, it is most likely a triplet or radical state. Both states are believed to be directly linked to the arginine 66 conformation and chromophore flexibility [12].

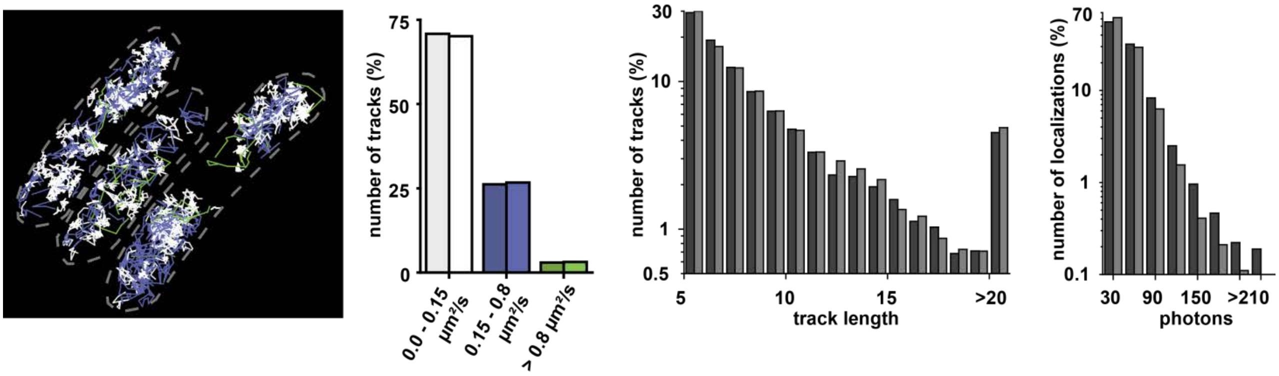

**Figure S7. RNA polymerase dynamics in living *E.coli* cells by UV and PC photoconversion.**
Examplary cells imaged by sptPALM using PC photoconversion (left) and diffusion coefficient distribution of RNA polymerase measured by 405 nm (left bars) and 488/730 nm (right bars) photoconversion. Trajectories are color coded by their apparent diffusion coefficient D: 0.0-0.15 µm²*s$^{-1}$ (white, ~ 70%), 0.15-0.8 µm²*s$^{-1}$ (blue, ~ 27%), faster than 0.8 µm²*s$^{-1}$ (green, ~3 %). PC was slightly more efficient and yielded more trajectories (with an average of 8 trajectories compared to 5 trajectories per µm² and minute) at lower conversion laser intensities (400 mW/cm² 488 nm in comparison to 690 mW/cm² 405 nm).

Statistics of single-particle track lengths (longer than 4 steps, middle right) obtained through 6 minute 405 nm or 488/730 nm-sptPALM imaging and statistics of single-molecule photon counts (right) of localizations in these trajectories are visualized by dark grey (UV-photoconversion: 5075 trajectories, 39913 localizations) and light grey (PC photoconversion: 7174 trajectories, 54127 localizations) histogram bars, bin size 1 (tracks) and 30 (photons). The average single-particle-trajectory lengths and spot intensities for both modes are comparable.

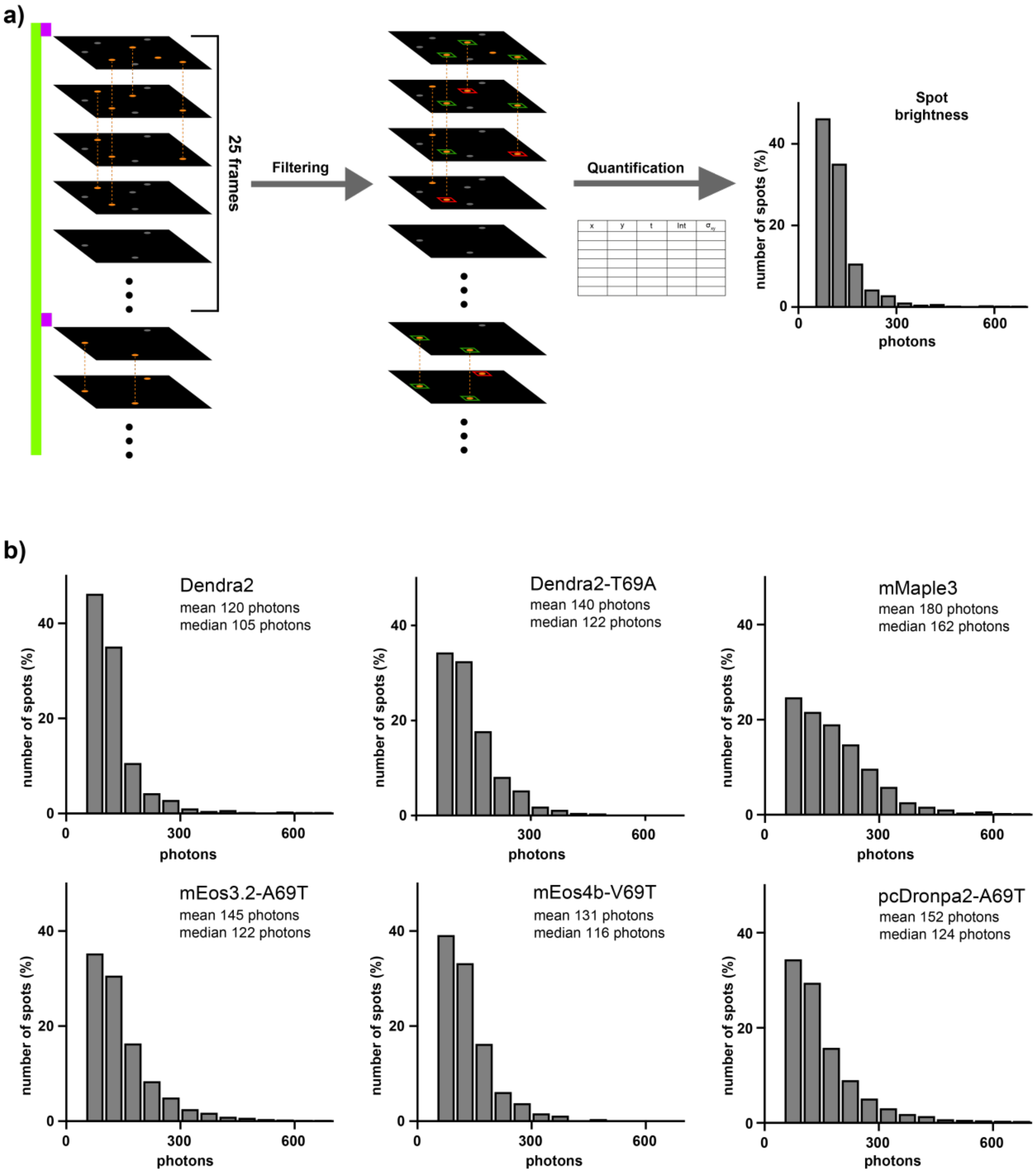

**Figure S8. Photon counts of single pcFP molecules recorded on single-molecule surfaces.**
a) Workflow of the single-molecule surfaces data analysis as described in the Materials and Methods section.
b) Photon counts of single fluorescent protein molecules recorded on single-molecule surfaces with 488/730 nm illumination at an imaging rate of 30 ms.

## References

[1] J. Quan, J. Tian, *Nat Protoc* **2011**, *6*, 242-251.

[2] S. Wang, J. R. Moffitt, G. T. Dempsey, X. S. Xie, X. Zhuang, *PNAS* **2014**, *111*, 8452-8457.

[3] K. A. Datsenko, B. L. Wanner, *Proc Natl Acad Sci U S A* **2000**, *97*, 6640-6645.

[4] A. Edelstein, N. Amodaj, K. Hoover, R. Vale, N. Stuurman, *Curr Protoc Mol Biol* **2010**, *Chapter 14*, Unit14 20.

[5] V. Adam, M. Lelimousin, S. Boehme, G. Desfonds, K. Nienhaus, M. J. Field, J. Wiedenmann, S. McSweeney, G. U. Nienhaus, D. Bourgeois, *PNAS* **2008**, *105*, 18343-18348.

[6] M. Zhang, H. Chang, Y. Zhang, J. Yu, L. Wu, W. Ji, J. Chen, B. Liu, J. Lu, Y. Liu, J. Zhang, P. Xu, T. Xu, *Nat Methods* **2012**, *9*, 727-729.

[7] J. Schindelin, I. Arganda-Carreras, E. Frise, V. Kaynig, M. Longair, T. Pietzsch, S. Preibisch, C. Rueden, S. Saalfeld, B. Schmid, J. Y. Tinevez, D. J. White, V. Hartenstein, K. Eliceiri, P. Tomancak, A. Cardona, *Nat Methods* **2012**, *9*, 676-682.

[8] M. Tokunaga, N. Imamoto, K. Sakata-Sogawa, *Nat Methods* **2008**, *5*, 159-161.

[9] S. Wolter, A. Loschberger, T. Holm, S. Aufmkolk, M. C. Dabauvalle, S. van de Linde, M. Sauer, *Nat Methods* **2012**, *9*, 1040-1041.

[10] S. Wieser, G. J. Schutz, *Methods* **2008**, *46*, 131-140.

[11] E. F. Pettersen, T. D. Goddard, C. C. Huang, G. S. Couch, D. M. Greenblatt, E. C. Meng, T. E. Ferrin, *J Comput Chem* **2004**, *25*, 1605-1612.

[12] R. Berardozzi, V. Adam, A. Martins, D. Bourgeois, *J Am Chem Soc* **2016**, *138*, 558-565.

[13] V. Adam, B. Moeyaert, C. C. David, H. Mizuno, M. Lelimousin, P. Dedecker, R. Ando, A. Miyawaki, J. Michiels, Y. Engelborghs, J. Hofkens, *Chem Biol* **2011**, *18*, 1241-1251.

[14] B. Moeyaert, N. Nguyen Bich, E. De Zitter, S. Rocha, K. Clays, H. Mizuno, L. van Meervelt, J. Hofkens, P. Dedecker, *ACS Nano* **2014**, *8*, 1664-1673.

[15] M. G. Paez-Segala, M. G. Sun, G. Shtengel, S. Viswanathan, M. A. Baird, J. J. Macklin, R. Patel, J. R. Allen, E. S. Howe, G. Piszczek, H. F. Hess, M. W. Davidson, Y. Wang, L. L. Looger, *Nat Methods* **2015**, *12*, 215-218.

[16] S. Habuchi, H. Tsutsui, A. B. Kochaniak, A. Miyawaki, A. M. van Oijen, *Plos One* **2008**, *3*.

[17] aA. C. Stiel, S. Trowitzsch, G. Weber, M. Andresen, C. Eggeling, S. W. Hell, S. Jakobs, M. C. Wahl, *Biochem J* **2007**, *402*, 35-42; bX. Zhang, M. Zhang, D. Li, W. He, J. Peng, E. Betzig, P. Xu, *PNAS* **2016**, *113*, 10364-10369; cH. Chang, M. Zhang, W. Ji, J. Chen, Y. Zhang, B. Liu, J. Lu, J. Zhang, P. Xu, T. Xu, *PNAS* **2012**, *109*, 4455-4460; dR. Ando, C. Flors, H. Mizuno, J. Hofkens, A. Miyawaki, *Biophys J* **2007**, *92*, L97-99.

[18] aS. F. Field, M. V. Matz, *Mol Biol Evol* **2010**, *27*, 225-233; bH. Kim, T. J. Grunkemeyer, C. Modi, L. Chen, R. Fromme, M. V. Matz, R. M. Wachter, *Biochemistry* **2013**, *52*, 8048-8059.

## 9.3 Aberration-Free, Live-Cell Compliant Multi-Color Single-Molecule Localization Microscopy Imaging

# Supplementary

# Combining Primed Photoconversion and UV-Photoactivation for Aberration-Free, Live-Cell Compliant Multi-Color Single-Molecule Localization Microscopy Imaging

**David Virant, Bartosz Turkowyd, Alexander Balinovic and Ulrike Endesfelder ***

Department of Systems and Synthetic Microbiology, Max Planck Institute for Terrestrial Microbiology
& LOEWE Center for Synthetic Microbiology (SYNMIKRO), Karl-von-Frisch-Str. 16, 35043 Marburg, Germany
* Correspondence: ulrike.endesfelder@synmikro.mpi-marburg.mpg.de; Tel.: +49-6421-28-21619

**Figure S1 –S4**

**Table S1**

**Supplementary Materials and Methods**

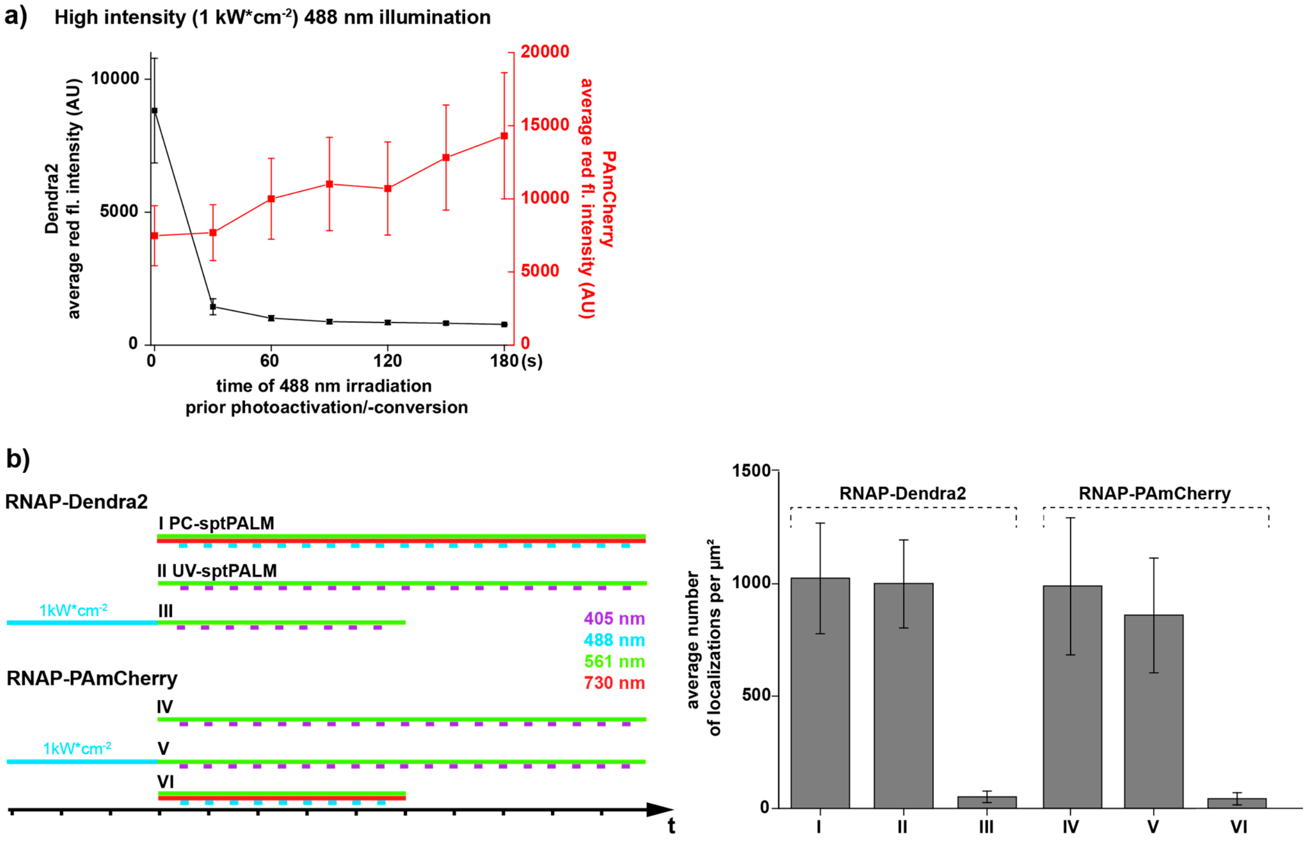

**Figure S1: (a)** Influence of high intensity (1 kW/cm²) 488 nm light illumination measured by the average red fluorescence intensity of PAmCherry and Dendra2 as a function of time of exposure by 488 nm light prior photoactivation/-conversion (for details, see materials and methods). Black graph: Dendra2 average fluorescence intensity; red graph: PAmCherry average fluorescence intensity. **(b) Left:** schemes representing illumination sequences for MG1655 RNAP-Dendra2 and MG1655 RNAP-PAmCherry samples serving as quantitative controls. Violet line: 405 nm light, blue line: 488 nm light, green line: 561 nm light, red line: 730 nm light. More details and laser intensities can be found in the materials and methods section. **Right:** average number of RNAP localizations per µm² identified during the imaging. **(I)** MG1655 RNAP-Dendra2 cells imaged with primed conversion-PALM. *n* = 13 cells; **(II)** MG1655 RNAP-Dendra2 cells imaged with UV-PALM. *n* = 21 cells; **(III)** MG1655 RNAP-Dendra2 cells illuminated with 488 nm light before imaging and imaged with UV-PALM. *n* = 21 cells; **(IV)** MG1655 RNAP-PAmCherry cells imaged with UV-PALM. *n* = 16 cells; **(V)** MG1655 RNAP-PAmCherry cells illuminated with 488 nm light before imaging and imaged with UV-PALM. *n* = 13 cells; **(VI)** MG1655 RNAP-PAmCherry cells imaged with primed conversion-PALM. *n* = 21 cells.

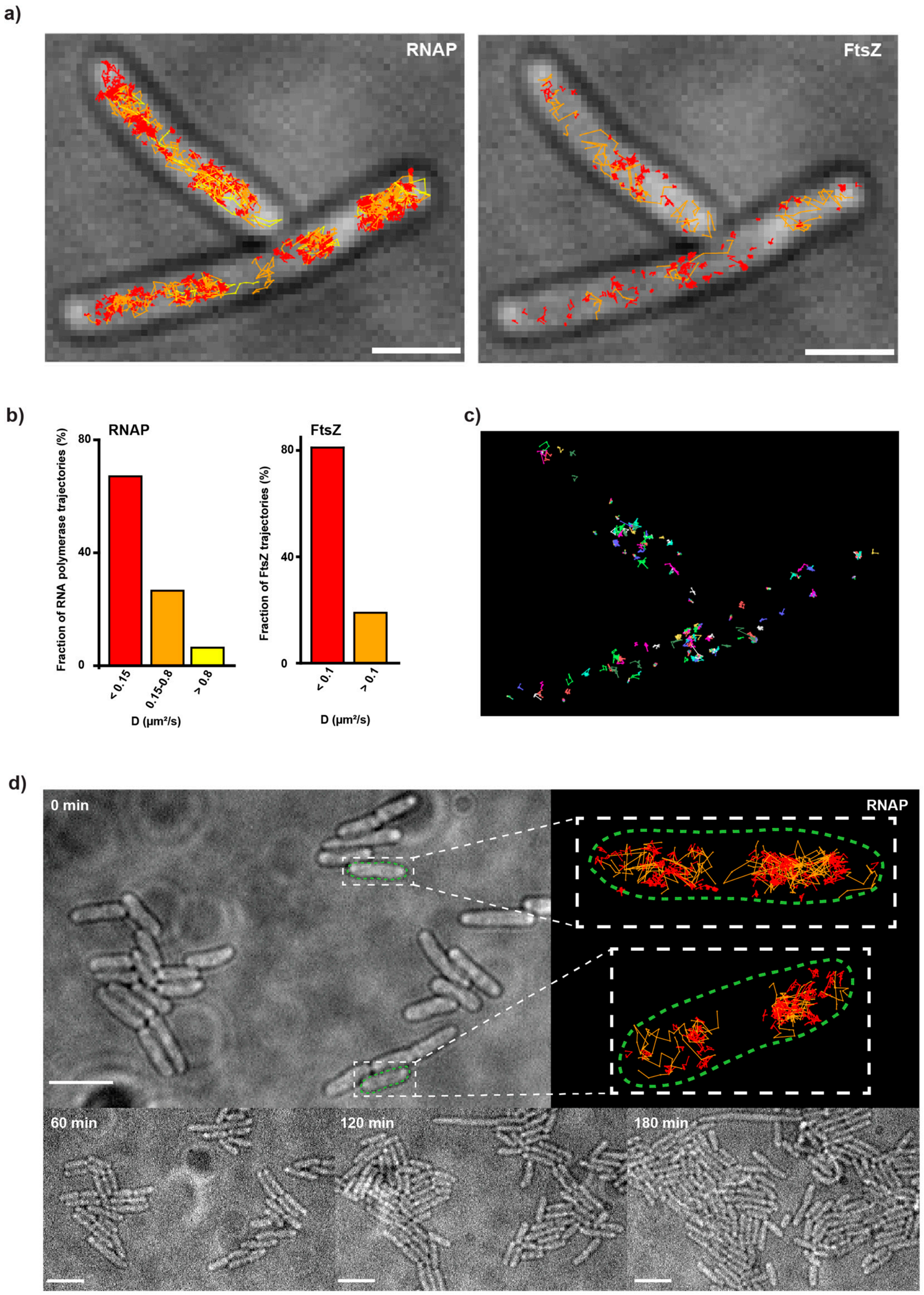

**Figure S2: Live-cell single-particle tracking PALM (sptPALM) in *E. coli* cells. (a)** Trajectories of RNAP molecules (left) and FtsZ (right). The individual trajectories are color coded by their apparent diffusion coefficient D and classified into categories. RNAP: 0.0–0.15 µm²/s (red), 0.15–0.8 µm²/s (orange), faster than 0.8 µm²/s (yellow) and FtsZ: 0.0–0.1 µm²/s (red), faster than 0.1 µm²/s (orange). This classification is based on recent literature on the protein dynamics [1,2] and chosen to be the same as in the histograms in **(b)**. Scale bar: 2 µm. **(b)** RNAP and FtsZ diffusion coefficient distribution histograms. RNAP molecules were classified by their diffusion coefficient as follows: slower than 0.15 µm²/s (67% of the whole population), faster than 0.15 and slower than 0.80 µm²/s (27%), and faster than 0.80 µm²/s (6%). $n = 471$ trajectories. This is in accordance with literature values [2,3]. FtsZ molecules were sorted into two classes: slower than 0.1 µm²/s (81% of the population- structural FtsZ) and faster than 0.1 µm²/s (19%). These values are also in accordance with literature values [1]. *n* = 174 trajectories. **(c)** FtsZ trajectories of the structural FtsZ molecules ($D < 0.1\ \mu m^2/s$) shown by distinct colors to visualize individual trajectories. **(d)** Cell growth after dual-color sptPALM imaging. Cells are not affected by the in total 9-minute-read-out (2 min for RNAP-mEos3.2-A69T, 2 minutes of 488 nm bleaching of unconverted mEos3.2-A69T and 5 min for FtsZ-PAmCherry (due to the slower frame rate of 30 ms to obtain the same number of images as for RNAP-mEos3.2-A69T imaged by 13 ms frames) imaging procedure. Big bright light image: cells at the beginning of the experiment. On the right, two examples of RNAP trajectories in single cells are shown; red trajectories are for slowly diffusing RNAPs with $D < 0.15\ \mu m^2/s$ and orange trajectories for RNAP with $0.15\ \mu m^2/s < D < 0.8\ \mu m^2/s$. Bottom bright light images: cells after one, two and 3 h of growth. Scale bars: 5 μm.

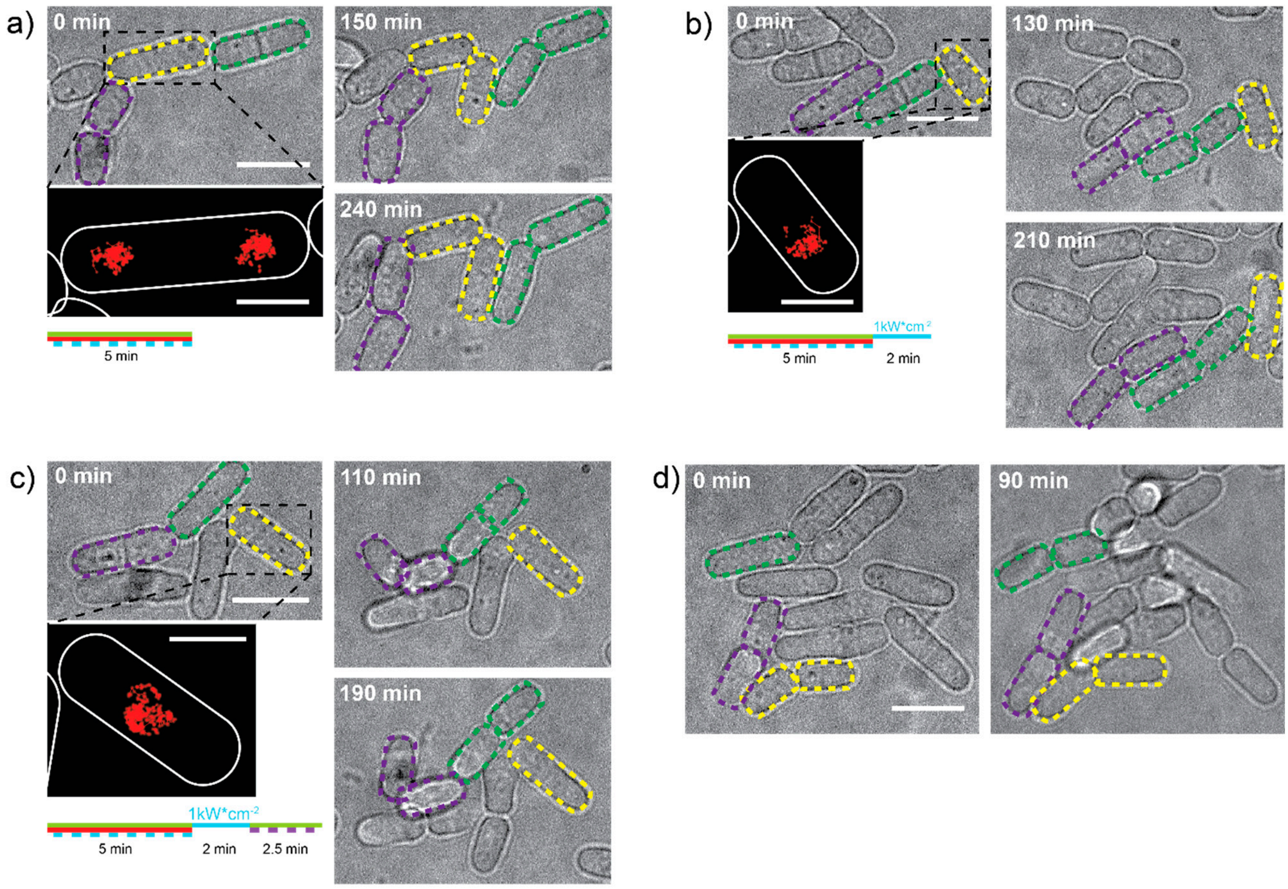

**Figure S3:** Comparison of *S. pombe* growth after different illumination schemes. Example cells are marked with dashed lines. Following the color-coded dashed lines, it is visible that the cells continue dividing and growing after imaging. Details experiment parameters are described in materials and methods. **(a)** Cell growth after 5 min of PC-PALM. **(b)** Cell growth after 5 min of PC-PALM and 2 min of 488 nm light post-bleaching. **(c)** Cell growth after 5 min of PC-PALM, 2 min of 488 nm light post-bleaching and 2.5 min of UV-PALM. The dose of UV light is not high enough to prevent cells from dividing/growing. **(d)** Control cells which were not illuminated by any laser light. Scale bars bright-field images 10 µm. Insets display examples of single-particle-trajectory data with a length >4 frames, obtained for cbp1-Dendra2, scale bars insets 4 µm. Colored lines beneath spt-PALM images represent the illumination scheme used in the experiment as described in **Figure S1**.

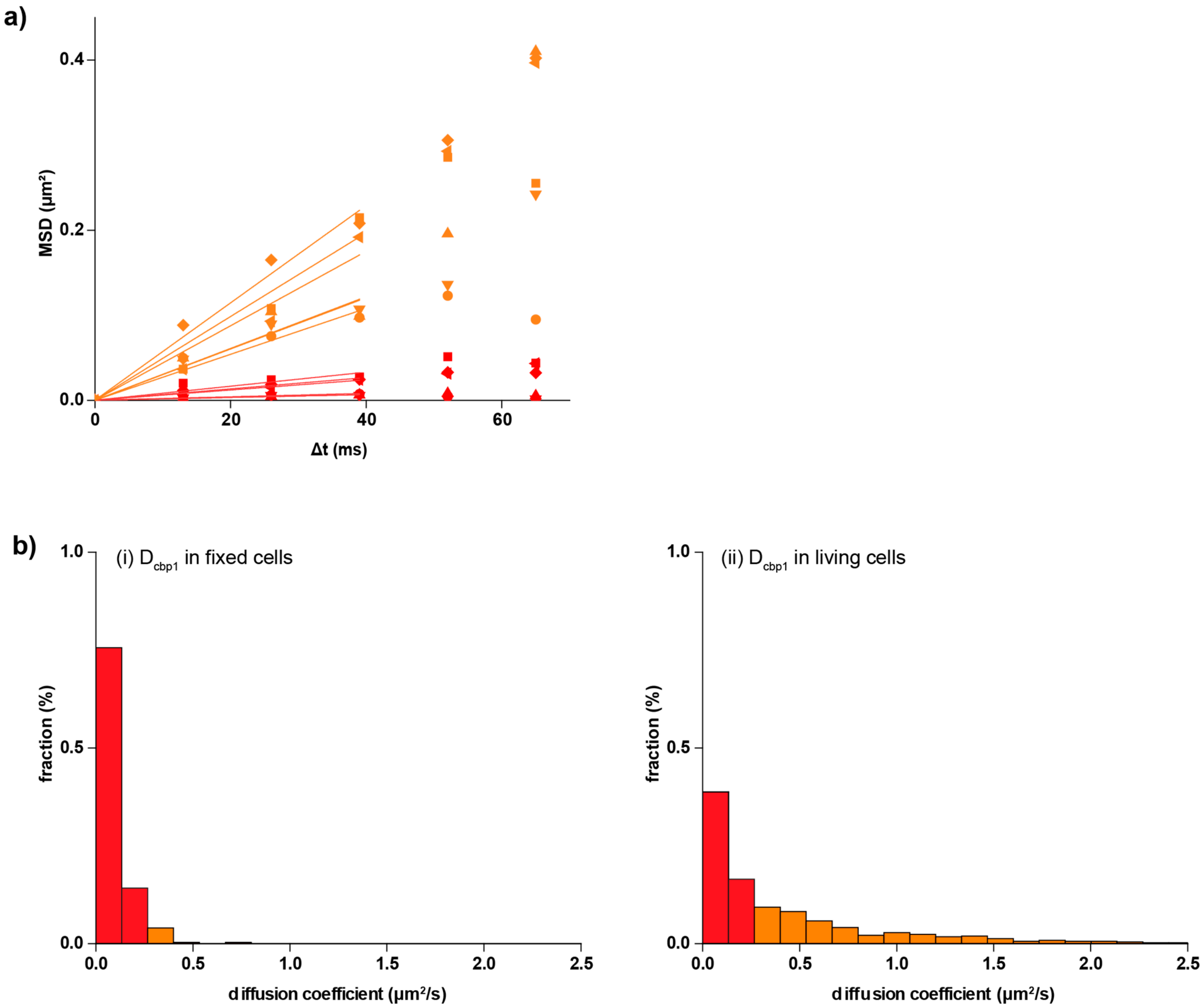

**Figure S4: (a)** Example fits of calculated MSD values, color coded red for MSDs corresponding to diffusion coefficients below 0.26 μm$^2$/s and orange for MSDs corresponding to diffusion coefficients above 0.26 μm$^2$/s. **(b)** Histograms of cbp1 diffusion coefficients in fixed **(i)** and living **(ii)** cells. Histogram bins are color coded as trajectories in **Figure 3b**, red for diffusion coefficients lower than 0.26 μm$^2$/s and orange for diffusion coefficients above 0.26 μm$^2$/s. **(i)** In fixed cells, the majority of analyzed trajectories displayed diffusion coefficients lower than 0.26 (~95%). All the present cbp1 molecules are expected to be immobilized by aldehyde fixation which results in a small, non-zero diffusion coefficient in agreement with the measurement error made within the localization precision. Some free-floating background may remain, resulting in a few detected mobile molecules with diffusion coefficients above 0.26 μm$^2$/s. **(ii)** In live cells, a significant fraction (~55%) of immobile, DNA-bound cbp1 is clearly visible, while the rest of the protein moves with varying velocity. Only trajectories with a length of >4 frames and MSD-curves fitted with an R-squared value >0.85 were used in the analysis. The bin size of 0.13 was calculated using the Freedman-Diaconis rule. Number of diffusion coefficients plotted is 275 for fixed cells and 462 for live cells.

## Table S1. Strains, plasmids and construction primers used in this study

| Strain | Description | Reference |
|---|---|---|
| *Escherichia coli* strains | | |
| **MG1655 rpoC_mEos3.2-A69T** | MG1655 RNAP-β′-mEos3.2-A69T, Cm$^{R}$ | This study |
| **MG1655 rpoC_mEos3.2-A69T+ pJB063** | MG1655 RNAP-β′-mEos3.2-A69T + pJB063-FtsZ-PAmCherry, Cm$^{R}$, Spect$^{R}$ | This study |
| **MG1655 rpoC_Dendra2** | MG1655 RNAP- β′-Dendra2, Cm$^{R}$ | [2] |
| **MG1655 rpoC_PAmCherry** | MG1655 RNAP- β′-PAmCherry, Amp$^{R}$ | [4] |
| **MG1655 pBAD/HisB_pamcherry1** | MG1655 pBAD/HisB_PAmCherry1, Amp$^{R}$ | This study |
| *Schizosaccharomyces pombe* strains | | |
| **cbp1_Dendra2** | C-terminal genomic integration, G418 resistance | This study |
| **cnp1_PAmCherry** | N-terminal genomic integration | [5] |
| **cnp1_PAmCherry + cbp1_Dendra2** | Combination of above strains | This study |
| Mammalian strains | | |
| **HeLa H2B-pDendra2(N)+ β-Actin-PAmCherry1** | Transient expression from plasmid | This study |
| **HeLa Dendra2-Keratin-17+ β-Actin-PAmCherry1** | Transient expression from plasmid | This study |

| Plasmids for transient expression | | | |
|---|---|---|---|
| **Plasmid** | **Expression organism** | **Description** | **Reference** |
| **H2B-pDendra2(N)** | mammalian | H2B-pDendra2(N), Kan$^{R}$ | Addgene 75283 |
| **Dendra2-Tubulin-6** | mammalian | Dendra2-Tubulin-6, Kan$^{R}$ | Addgene 57742 |
| **β-Actin-PAmCherry1** | mammalian | β-Actin-PAmCherry1, Kan$^{R}$, Neo$^{R}$ | [6] |
| **Dendra2-Keratin-17** | mammalian | KRT18-Dendra2, Kan$^{R}$ | Addgene 57726 |
| **pJB063** | bacteria | pBAD-FtsZ-pamcherry1, Spect$^{R}$ | Gift from the Xiao Lab, USA |
| **pBAD/HisB_PAmCherry** | bacteria | pBAD/HisB_PAmCherry1, Amp$^{R}$ | Addgene 31931 |

| Construction primers | |
|---|---|
| **Name** | **Sequence** |
| **rpoC_mEos3.2-A69T_F** | CCAGCCTGGCAGAACTGCTGAACGCAGGTCTGGGCGGTTCTGATAACGAGgccattaaaccggatatgaaaatcaaactgcg |
| **rpoC_mEos3.2-A69T_R** | CCCCCCATAAAAAAACCCGCCGAAGCGGGTTTTTACGTTATTTGCGGActagagaataggaacttcctgccactcatc |
| **F_KanR** | GGCGCGCCAGATCTACTT |
| **R_KanR** | GACAGCAGTATAGCGACCAGC |
| **F_Dendra2** | GCCGGAGGCAGTGGTATGAACACCCCGGGAATTAA |
| **R_Dendra2** | AGAAGTAGATCTGGCGCGCCTTACCACACCTGGCTGGG |
| **F1_cbp1** | CAGCCTTGTAGTGAGGGTGTG |
| **R1_cbp1** | ACCACTGCCTCCGGCGGTGCTTCTCAAACGAGAAAGATTC |

| | |
|---|---|
| **F2_cbp1** | AATGCTGGTCGCTATACTGCTGTCTGTCTGTATTCGTTGTGCATATTTGAC |
| **R2_cbp1** | ACGAAGCAGTTAGCAAAAGAGAAGTACA |

All primers were designed in Benchling (Benchling Inc.) and synthesized by Eurofins Genomics (Germany).

## Supplementary Material & Methods

### Strain constructions

***Escherichia coli* MG1655 rpoC-mEos3.2-A69T transformed with pJB063.** MG1655 expressing rpoC_mEos3.2-A69T was generated by homologous recombination using a modified lambda red recombination pKD46 protocol [7]. Briefly, the PCR-amplified (primers listed in **Table S1**) mEos3.2-A69T-sequence followed by the frt flanked chloramphenicol resistance gene from the codon-optimized mEos3.2-A69T pBAD18 plasmid [8] with auxiliary homologous overhang sequences was electroporated (5 ms, 1.8 kV) into MG1655 cells. After verifying the strain by sequencing (Eurofins, Ebersberg, Germany), the pJB063 plasmid (**Table S1**) containing an FtsZ sequence followed by the PAmCherry fluorescent protein and spectinomycin resistance gene sequences was introduced to MG1655 rpoC-mEos3.2-A69T via electroporation (5 ms, 1.8 kV). Transformed cells were selected under chloramphenicol and spectinomycin.

***Schizosaccharomyces pombe* cbp1-Dendra2**. The cloning strategy for tagging the C-terminus of the cbp1 was adapted from [9]. The *Saccharomyces cerevisiae* ADH1 terminator and kanamycin resistance gene were amplified from the PAW8 plasmid [10] using primers F_KanR and R_KanR. The Dendra2 fragment with the AGGSG linker was amplified from the pRSET-Dendra2 plasmid [11] using primers F_Dendra2 and R_Dendra2. The upstream (~600 bp) and downstream (~500 bp) *S. pombe* homologies were amplified from genomic DNA with the primer pairs F1_cbp1/ R1_cbp1 and F2_cbp1/ R2_cbp1 (all primers listed in **Table S1**). DNA fragments were assembled with overlap-extension PCR [12], using melting temperatures of the overlapping regions as the annealing temperature in the PCR. All PCRs were performed with Q5 High-Fidelity DNA polymerase (New England Biolabs, Frankfurt, Germany). 10 µL of the PCR product were transformed into wild type *S. pombe* using the Frozen-EZ Yeast Transformation II Kit (Zymo Research, Irvine, CA, USA), plated onto YES agar plates and incubated overnight at 30 °C, then replica plated onto 200 µg/mL G418 (Thermo Fisher Scientific, Darmstadt, Germany) YES agar plates and incubated at 30 °C until single colonies were visible. Genomic integration was confirmed by colony PCR and DNA sequencing.

***S. pombe* cnp1-PAmCherry1/cbp1-Dendra2.** The DNA fragment used for transformation was amplified from genomic DNA of the previously described cbp1-Dendra2 strain with the primer pair F1_cbp1/R2_cbp1 (**Table S1**). The fragment, containing upstream and downstream homologies, the Dendra2 sequence and the KanR gene was then transformed into an N-terminally tagged cnp1-PAmCherry *S. pombe* strain [5] as described earlier. Integration was confirmed by colony PCR and DNA sequencing.

### Sample preparations

***Escherichia coli*.** The strain MG1655 rpoC-mEos3.2-A69T+pJB063 was taken from a −80 °C stock and was cultured overnight at 37 °C, 210 rpm, LB with 34 µg/mL chloramphenicol and 100 µg/mL spectinomycin, reinoculated into fresh LB and grown to OD 0.1. Expression of FtsZ-PAmCherry from pJB063 plasmid was induced by arabinose (0.2% *w*/*v*). After 30 min of induction, the culture was centrifuged (2000× *g*, 3 min) to exchange the medium for fresh LB without inducer and again incubated in 37 °C, 210 rpm for two hours. Fixation was performed for 15 min with 1% paraformaldehyde (Sigma Aldrich, Munich, Germany) and cells were washed twice in 100 mM PBS (pH 7.4). Samples were stored in 100 mM PBS (pH 7.4) or immediately immobilized on 8-well slides (Ibidi, Munich, Germany) previously cleaned with 2% Hellmanex III (Hellma Analytivs, Muellheim, Germany) and coated with 0.05% poly-L-lysine.

MG1655 rpoC-Dendra2 and MG1655 rpoC-PAmCherry genomic strains were grown from −80 °C stocks overnight at 37 °C, 210 rpm in LB medium with appropriate antibiotic marker (**Table S1**), reinoculated and grown to OD 0.2. Fixation and cell immobilization were performed as above.

Prior to imaging, a 250 thousand fold dilution of FluoSphere dark red Carboxylate-Modified Microspheres (ThermoFisher, Munich, Germany) were added to the samples and allowed to settle for 5 min to serve as markers for drift correction.

For live-cell single-particle tracking of the strain MG1655 rpoC_mEos3.2A69T+pJB063, cells were inoculated into TB medium with chloramphenicol and spectinomycin (final concentration 34 and 100 µg/mL, respectively) and grown till OD 0.1. Then cells were induced for 45 min with 0.4% arabinose, washed with EZRDM medium (Teknova, Hollister, California, USA) and placed on 1% low melting agarose pads with EZRDM.

***Schizosaccharomyces pombe***. Yeast was grown in YES medium (5 g Yeast extract, 30 g glucose, 225 mg of each l-adenine, histidine, leucine, uracil, lysine-hydrochloride in 1 L of Milli-Q water) at 30 °C overnight, then inoculated into fresh YES to a starting OD of 0.1, grown to an OD of 1 and inoculated into EMM (Formedium, Hunstanton, UK) with 225 mg of each l-adenine, histidine, leucine, uracil, lysine-hydrochloride in 1 L of Milli-Q water to a starting OD of 0.1 and grown overnight at 30 °C. On the day of imaging, cells were inoculated into fresh EMM from the overnight culture to a starting OD of 0.1, grown at 30 °C until the cultures reached OD 0.4. For fixed cell experiments, yeast was fixed by adding 37% PFA to the growth medium to a final concentration of 1%, incubated for 10 min then washed three times with PBS. Cells were immobilized on poly-L-lysine coated Ibidi 8-well glass bottom slides, previously cleaned with a 2% solution of Hellmanex III , and then imaged at 30 °C.

**HeLa cells.** All cell culture reagents were obtained from ThermoFisher. HeLa cells were maintained in DMEM, supplemented with 10% fetal calf serum and 1% penicillin/streptomycin. Transfection of plasmid DNA was performed with FuGENE (Promega, Mannheim, Germany) according to the manufacturer's instruction. Two plasmid combinations were used, β-Actin-PAmCherry1 with Dendra2-Keratin-17 and β-Actin-PAmCherry1 with H2B-Dendra2 (**Table S1**). For each 6-well, 1 µg of plasmid DNA was diluted in 250 µL OptiMEM following addition of 4 µL FuGENE and incubation at room temperature for 30 min. 500 ng of each plasmid (250 ng in case of H2B-Dendra2) were used for co-transfections. Diluted plasmid DNA was then added to confluent Hela cells, and the culture medium was renewed after 3 h. Cells were subcultured in 8-well glass bottom slides (Ibidi, Germany) on the subsequent day. Fixation was performed with methanol (Carl Roth, Karlsruhe, Germany) at −20 °C for 15 min. Samples were washed with 1× PBS. Prior to imaging, a 250 thousand fold dilution of FluoSphere dark red Carboxylate-Modified Microspheres were added to the well and allowed to settle for 5 min to serve as markers for drift correction.

### Purification of fluorescent proteins

The pellet of a culture overexpressing PAmCherry from a pBAD plasmid (**Table S1**) was suspended in 10 mM PBS (pH 7.4) with lysozyme (0.5 mg/mL) for 2 h, homogenized by ultrasound (UP100H, Hielscher, Germany) and centrifuged for 15 min (17000×*g*, 4 °C). FPs were purified from the supernatant by Ni-NTA spin columns followed by a buffer exchange to 10 mM PBS (pH 7.4) (Nanosep columns, VWR, Germany).

### Microscope

Imaging was performed on a custom built setup based on an automated Nikon Ti Eclipse microscope, equipped with appropriate dichroic and filters (ET dapi/Fitc/cy3 dichroic, ZT405/488/561rpc rejection filter, ET525/50 or ET610/75 bandpass, all AHF Analysentechnik, Germany), and a CFI Apo TIRF 100× oil objective (NA 1.49, Nikon). All lasers (405 nm OBIS, 561 nm OBIS, 730 nm OBIS, 488 nm Sapphire; all Coherent Inc., Santa Clara, California USA) except 730 nm were modulated via an acousto-optical tunable filter (AOTF) (Gooch and Housego, Eching, Germany). Fluorescence was detected by an emCCD (iXON Ultra 888; Andor, UK). The z-focus was controlled by a commercial perfect focus system (Nikon, Duesseldorf, Germany). Acquisitions were controlled by µManager [13].

### Spectroscopy

Absorption spectra and fluorescence spectra (**Fig. 1a–d**) were measured in V-750 and FP-8500 instruments (Jasco, Gross-Umstadt, Germany), respectively, using purified PAmCherry protein with a final concentration 100 µM in 100 mM PBS (pH 7.5), NileRed diluted in acetone and Sytox Orange in ddH2O with final concentrations 1 µM for both in a 50µl UV-transparent quartz cuvette, except spectra of mEos3.2-A69T, which was taken from our previous work [2].

## References

1. Niu, L.; Yu, J. Investigating intracellular dynamics of ftsz cytoskeleton with photoactivation single-molecule tracking. *Biophysical journal* **2008**, *95*, 2009–2016.
2. Turkowyd, B.; Balinovic, A.; Virant, D.; Golz Carnero, H.G.; Caldana, F.; Endesfelder, M.; Bourgeois, D.; Endesfelder, U. A general mechanism of photoconversion of green-to-red fluorescent proteins based on blue and infrared light reduces phototoxicity in live-cell single-molecule imaging. *Angewandte Chemie* **2017**.
3. Stracy, M.; Lesterlin, C.; Garza de Leon, F.; Uphoff, S.; Zawadzki, P.; Kapanidis, A.N. Live-cell superresolution microscopy reveals the organization of rna polymerase in the bacterial nucleoid. *PNAS* **2015**, *112*, E4390-E4399.
4. Endesfelder, U.; Finan, K.; Holden, S.J.; Cook, P.R.; Kapanidis, A.N.; Heilemann, M. Multiscale spatial organization of rna polymerase in escherichia coli. *Biophysical journal* **2013**, *105*, 172–181.
5. Lando, D.; Endesfelder, U.; Berger, H.; Subramanian, L.; Dunne, P.D.; McColl, J.; Klenerman, D.; Carr, A.M.; Sauer, M.; Allshire, R.C., *et al.* Quantitative single-molecule microscopy reveals that cenp-a(cnp1) deposition occurs during g2 in fission yeast. *Open biology* **2012**, *2*, 120078.
6. Endesfelder, U.; Malkusch, S.; Flottmann, B.; Mondry, J.; Liguzinski, P.; Verveer, P.J.; Heilemann, M. Chemically induced photoswitching of fluorescent probes--a general concept for super-resolution microscopy. *Molecules* **2011**, *16*, 3106–3118.
7. Datsenko, K.A.; Wanner, B.L. One-step inactivation of chromosomal genes in escherichia coli k-12 using pcr products. *Proceedings of the National Academy of Sciences of the United States of America* **2000**, *97*, 6640–6645.
8. Wang, S.; Moffitt, J.R.; Dempsey, G.T.; Xie, X.S.; Zhuang, X. Characterization and development of photoactivatable fluorescent proteins for single-molecule–based superresolution imaging. *PNAS* **2014**, *111*, 8452–8457.
9. Hayashi, A.; Ding, D.Q.; Tsutsumi, C.; Chikashige, Y.; Masuda, H.; Haraguchi, T.; Hiraoka, Y. Localization of gene products using a chromosomally tagged gfp-fusion library in the fission yeast schizosaccharomyces pombe. *Genes to cells : devoted to molecular & cellular mechanisms* **2009**, *14*, 217–225.
10. Watson, A.T.; Garcia, V.; Bone, N.; Carr, A.M.; Armstrong, J. Gene tagging and gene replacement using recombinase-mediated cassette exchange in schizosaccharomyces pombe. *Gene* **2008**, *407*, 63–74.
11. Berardozzi, R.; Adam, V.; Martins, A.; Bourgeois, D. Arginine 66 controls dark-state formation in green-to-red photoconvertible fluorescent proteins. *Journal of the American Chemical Society* **2016**, *138*, 558–565.
12. Bryksin, A.V.; Matsumura, I. Overlap extension pcr cloning: A simple and reliable way to create recombinant plasmids. *BioTechniques* **2010**, *48*, 463–465.
13. Edelstein, A.; Amodaj, N.; Hoover, K.; Vale, R.; Stuurman, N. Computer control of microscopes using micromanager. *Current protocols in molecular biology / edited by Frederick M. Ausubel [et al.]* **2010**, *Chapter 14*, Unit14 20.

## 9.4 A transient pool of nuclear F-actin at mitotic exit controls chromatin organization

nature cell biology

DOI: 10.1038/ncb3641

In the format provided by the authors and unedited.

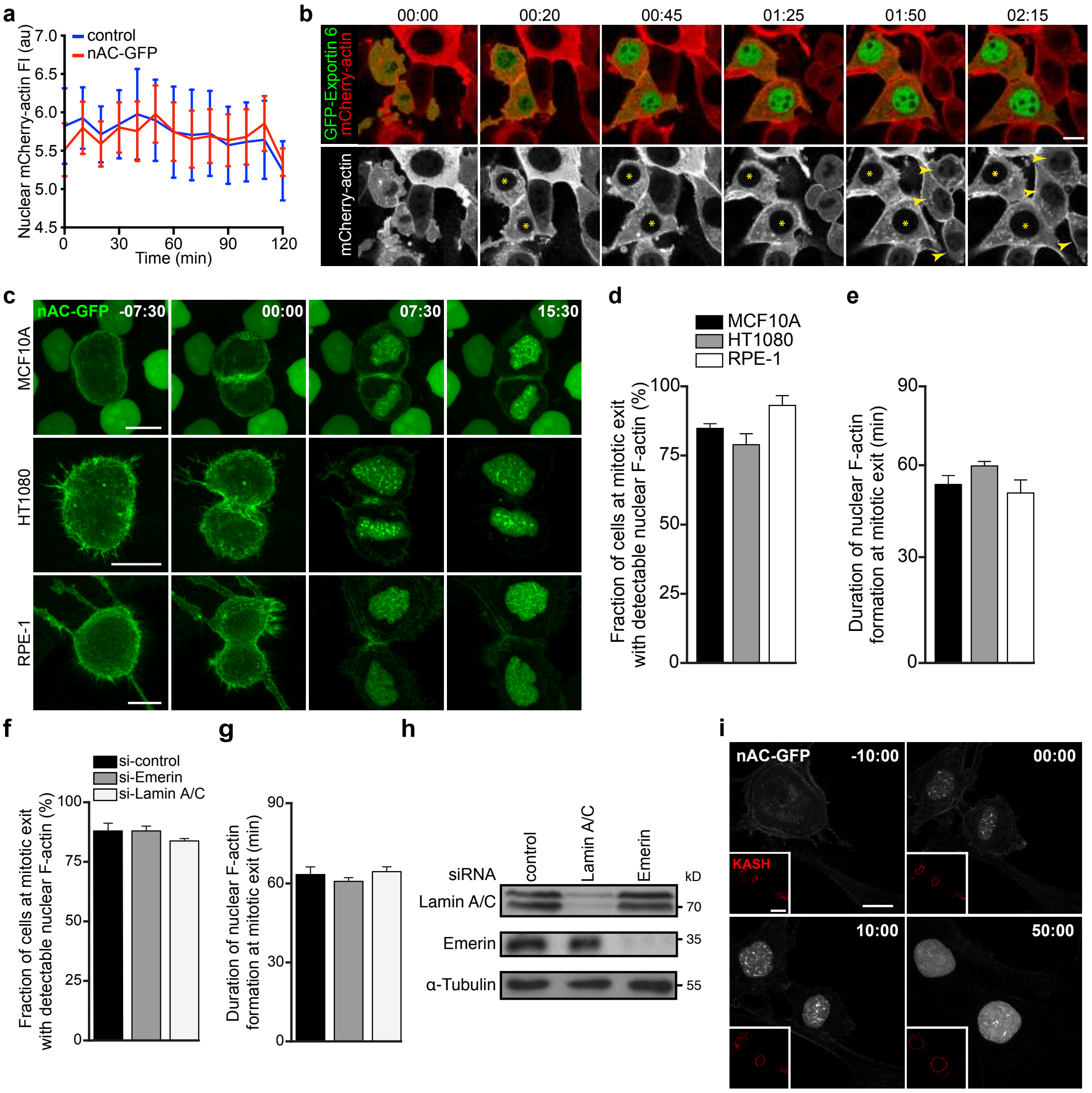

**Supplementary Figure 1** Nuclear actin levels during mitotic exit are not affected by expression of nAC-GFP. Nuclear actin filaments are a conserved feature among different mammalian cell lines and form independent of Emerin, Lamin A/C, and the LINC complex. **(a)** 3D nuclear fluorescence intensities (FI) of stably expressed mCherry-actin were measured at indicated times after cell division (0 min corresponds to anaphase) to compare its nuclear distribution in the absence or presence of co-expressed nAC-GFP. Nuclei were counterstained with SiR-DNA. Data are shown as mean ± SD (n=13 mitotic events per condition, pooled from several independent experiments). **(b)** NIH3T3 cells stably expressing mCherry-actin were transfected with GFP-Exportin 6 and followed during the time-course of mitotic cell division. Images show single confocal slices to illustrate nuclear distribution of mCherry-actin in postmitotic cells in either the presence (indicated by asterisks) or absence (arrowheads) of GFP-Exportin 6. Note the nuclear fluorescence signal produced by mCherry-actin in control daughter nuclei (indicated by arrowheads). The experiment was performed once. Time stamp, hours:min; scale bar, 10 μm. **(c)** Time-lapse imaging of stably nAC-GFP (green) expressing MCF10A, HT1080, and RPE-1 during cell division reveals nuclear F-actin formation at mitotic exit. Images show maximum intensity projections. Scale bar, 10 μm; time stamp, min:sec. **(d, e)** Quantification of incidence **(d)** and duration **(e)** of nuclear F-actin formation during mitotic exit in MCF10A, HT1080, and RPE-1 cells stably expressing nAC-GFP. Data are shown as mean + SEM (n=40 (MCF10A, HT1080), n=30 (RPE-1) mitotic events, pooled from several independent experiments). **(f, g)** Quantification of the incidence **(f)** and duration **(g)** of nuclear F-actin formation during mitotic exit in nAC-GFP expressing NIH3T3 cells, treated with indicated siRNAs. Data are shown as mean + SD (n=30 cells per condition, pooled from 2 independent experiments). **(h)** Immunoblot validating efficient siRNA-mediated knockdown of Lamin A/C and Emerin. The experiment was performed once. **(i)** Time-lapse imaging of NIH3T3 cells expressing nAC-GFP (grey) together with tagRFP-KASH (red, insets) to disrupt the LINC complex during and after mitotic division. The experiment was performed once. Scale bar, 10 μm; time stamp, min:sec. Unprocessed original scans of blots are shown in Supplementary Fig. 7.

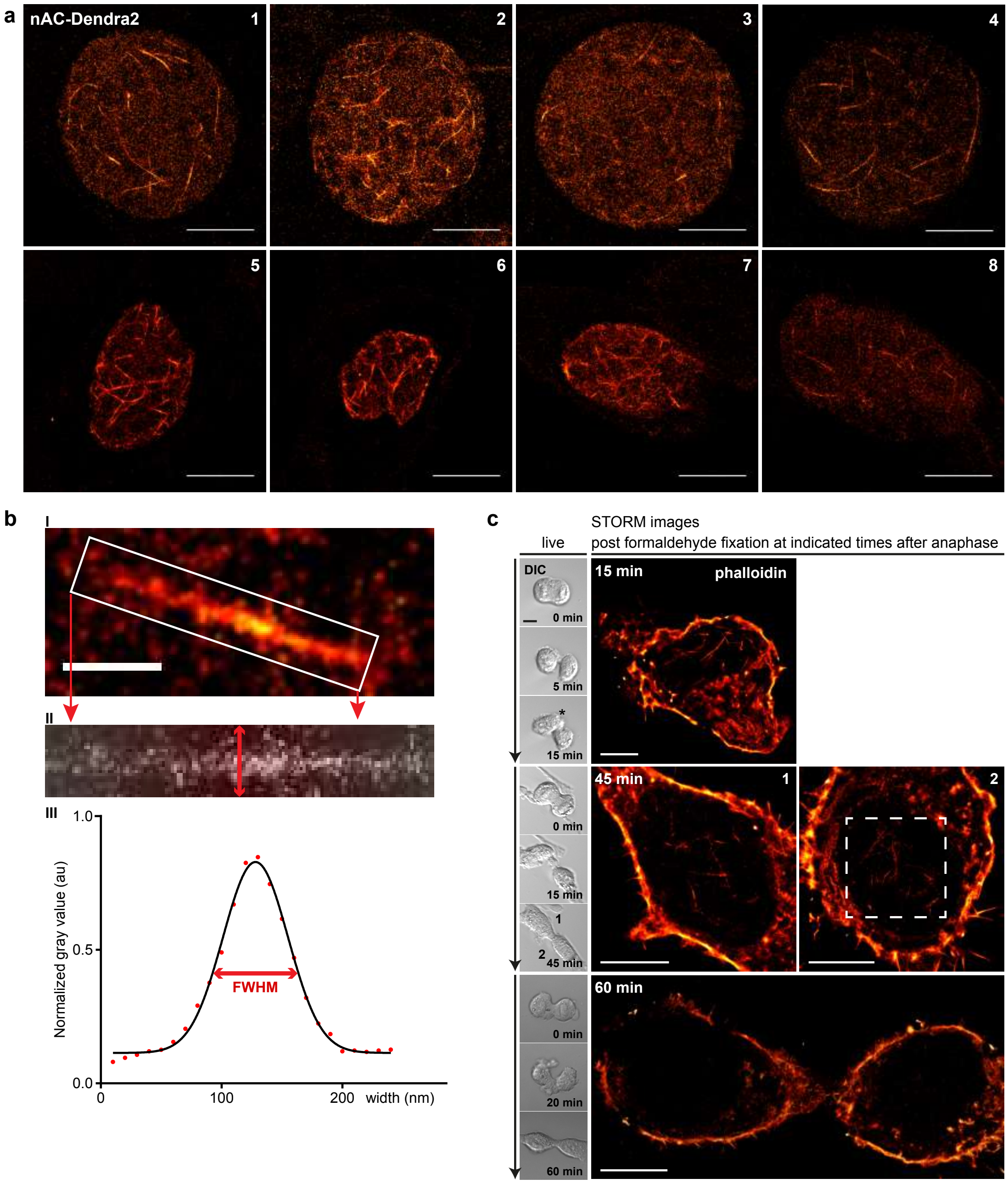

**Supplementary Figure 2** Super-resolution imaging of nuclear F-actin at mitotic exit. **(a)** PALM images of NIH3T3 cells stably expressing nAC-Dendra2 (orange) at mitotic exit used to calculate filament widths in Fig. 2b. Experimental resolutions after drift correction (see Methods) are 38 ± 1 nm (1, 2, 4), 39 ± 1 nm (3), 33 ± 1 nm (5, 6), 35 ± 1 nm (7,8). Cells 5 and 6 are shown in Fig. 2a. Scale bars, 5 µm. **(b)** Filaments were analysed by a self-written, customized script for FIJI. First, ROIs were drawn along filaments (I). To minimize the selection and pixelation error, selections were shifted by 0.5 pixels (5 nm) in all directions to obtain five measures in total for each filament by straightening all selections (II). To determine the filament width, lengthwise intensity profiles of the five filament selections were fitted with Gaussians (III). The average full width at half maximum (FWHM) of the five selections yields the average filament width. Scale bar, 0.5 µm. **(c)** Mitotic cell division of native NIH3T3 cells was monitored over time using DIC (Differential interference contrast) to allow for formaldehyde fixation at defined time points after anaphase, as indicated. Stochastic Optical Reconstruction Microscopy (STORM) images focus on the corresponding nuclei labelled by phalloidin (see Methods for details). The dashed rectangle is shown magnified in Fig. 2c. Experimental resolutions after drift correction are 40 ± 1 nm (15 min, 45 min-cell 1), 30 ± 1 nm (45 min-cell 2) and 34 ± 1 nm (60 min). Scale bars, 5 µm.

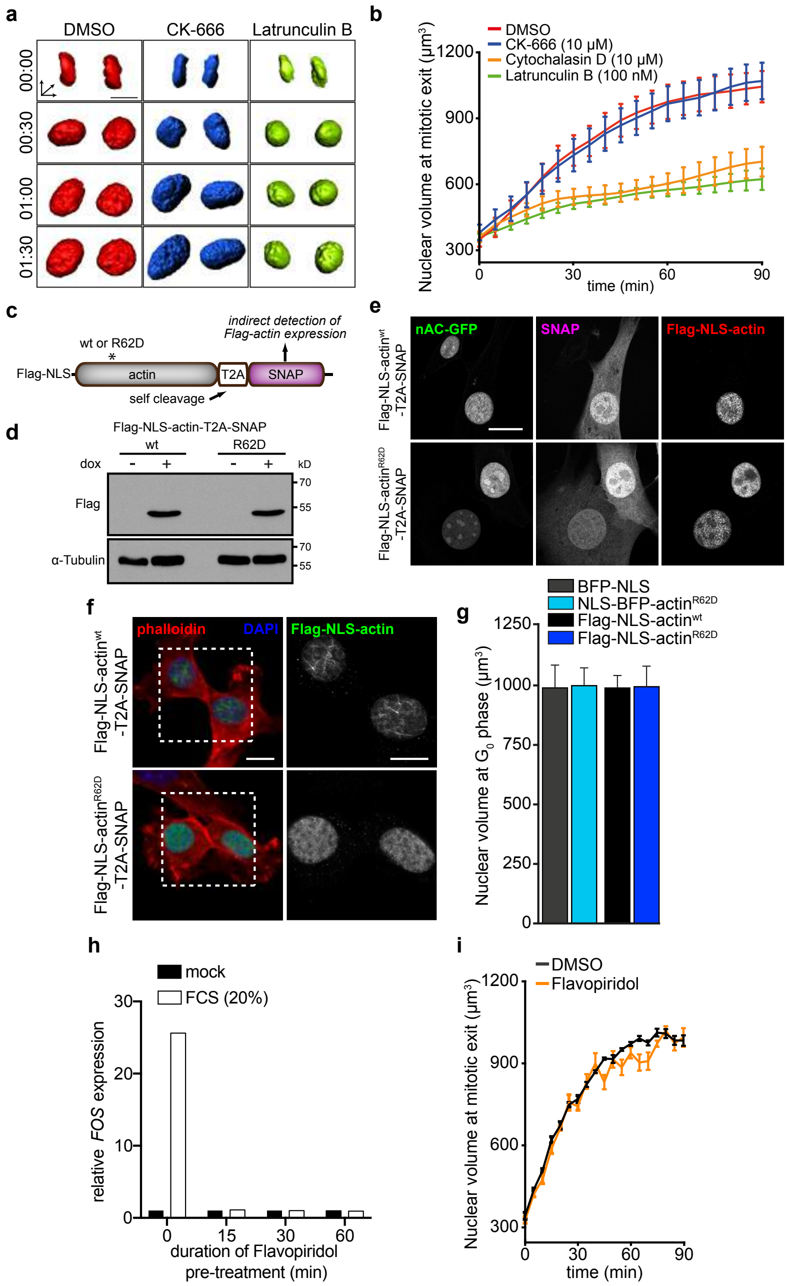

**Supplementary Figure 3** Actin dynamics but not transcriptional inhibition affect early G1 nuclear expansion. Detection of Flag-actin derivatives by doxycycline-inducible T2A-SNAP fusions. **(a)** 3D surface reconstructions of NIH3T3 nuclei (vizualized by SiR-DNA) at indicated times after drug treatment at mitotic exit. Scale bar, 10 µm; time stamp, hours:min. **(b)** Nuclear volume quantifications in cells treated similar to **a**. Data is shown as mean ± SD (n=50 nuclei per condition, pooled from at least 3 independent experiments). **(c)** Design of Flag-tagged nuclear actin derivatives linked to the SNAP-tag by a T2A peptide. Upon translation, the T2A peptide is cleaved resulting in equimolar expression of Flag-NLS-actin and the SNAP-tag. Accordingly, labelling of the SNAP-tag allows for indirect detection of Flag-NLS-actin in living cells. **(d)** Immunoblot confirms doxycycline-induced expression of Flag-NLS-actin-T2A-SNAP derivatives. A single band indicates efficient cleavage of Flag-NLS-actin-T2A-SNAP. **(e)** Confocal images of fixed NIH3T3 cells expressing nAC-GFP transfected with Flag-NLS-actin-T2A-SNAP derivatives. In contrast to Flag-NLS-actin the SNAP-tag (labelled by SiR-647) displays pancellular distribution. Scale bar, 10 µm. **(f)** Confocal images of fixed NIH3T3 cells at mitotic exit show expression of Flag-NLS-actin-T2A-SNAP derivatives, as indicated. Magnifications correspond to dashed rectangles and highlight Flag-actin. Scale bar, 10 µm. **(g)** Nuclear volume quantifications in live NIH3T3 cells stably expressing H2B-mCherry and doxycycline-induced BFP-NLS, NLS-BFP-actin$^{R62D}$ or Flag-NLS-actin-T2A-SNAP derivatives. Expression of the indicated constructs was induced during $G_0$. Data are mean + SD from n=30 nuclei per condition. **(h)** RT-qPCR analysis of *FOS* expression in serum-starved NIH3T3 cells, pre-treated with Flavopiridol (1 µM for indicated times) before stimulation with serum (20% FCS, fetal calf serum) for 30 minutes. Note that 15 min pre-treatment with Flavopiridol efficiently inhibits serum-induced transcriptional upregulation of *FOS* mRNA. Data are shown as mean from n=2 independent experiments. **(i)** Nuclear volume analysis in NIH3T3 cells stably expressing H2B-mCherry in the presence of Flavopiridol (1 µM) or DMSO (0.1%). Flavopiridol was added at metaphase prior to imaging the subsequent expansion of daughter nuclei. Data are shown as mean ± SD (n>14 nuclei [precise n?] per condition, pooled from 3 independent experiments). Unprocessed original scans of blots are shown in Supplementary Fig. 7.

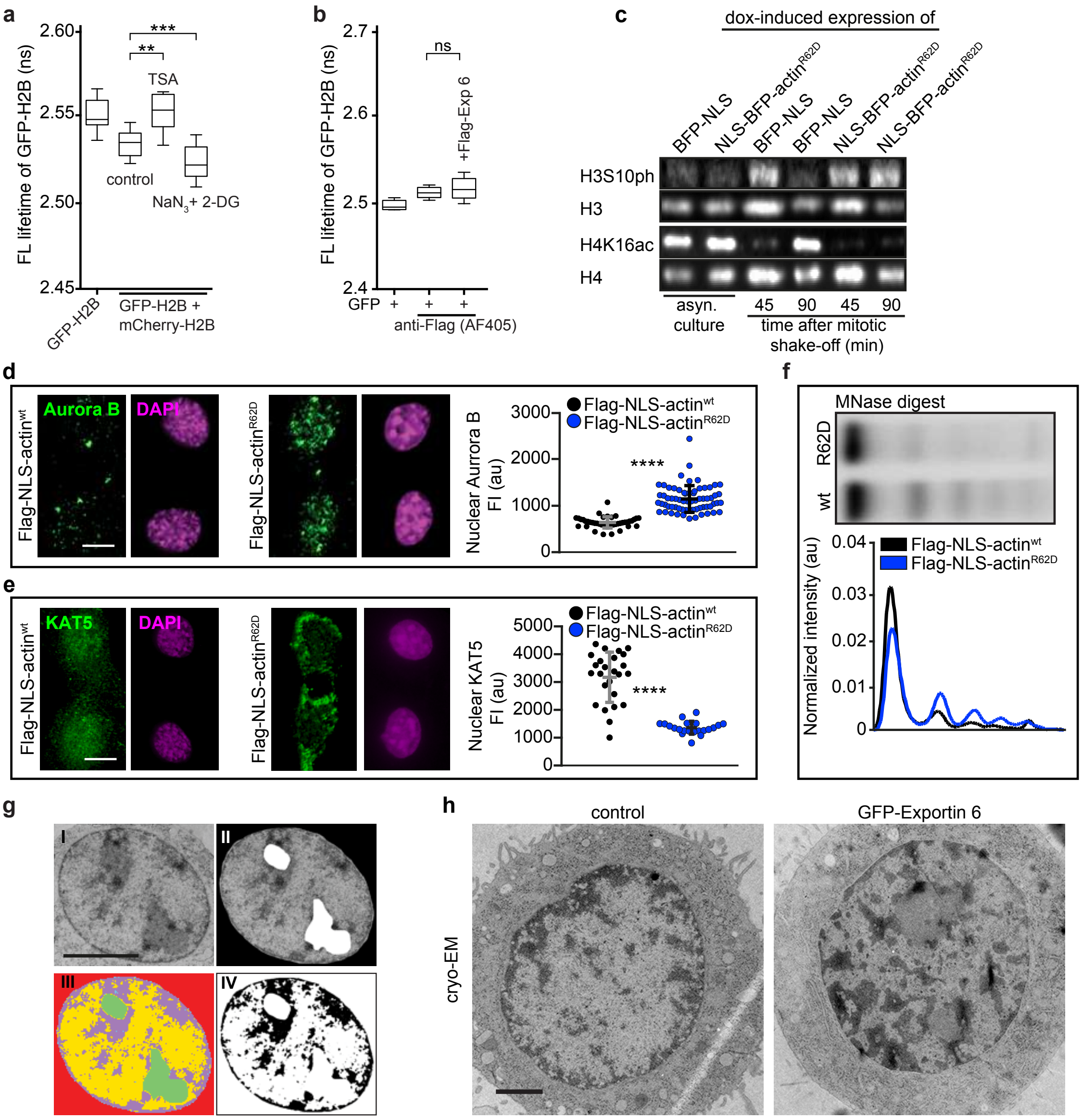

**Supplementary Figure 4** Inhibition of nuclear F-actin formation impairs chromatin decompaction at mitotic exit **(a)** Quantification of GFP-H2B fluorescence lifetime in cells expressing GFP-H2B alone, or in combination with mCherry-H2B and indicated treatments: trichostatin A (TSA), or sodium azide (NaN3) together with 2-deoxyglucose (2-DG). $^{**}P < 0.01$, $^{***}P < 0.001$ calculated by one-way ANOVA. **(b)** Quantification of fluorescence lifetime reveals no significant difference in GFP fluorescence lifetime upon expression of and staining for Flag-Exportin 6 using a Alexa Fluor 405-conjugated antibodies. ns, non-significant in one-way ANOVA. **(c)** Comparative immunoblot analysis of histone modifications (H3S10ph, H4K16ac) in NIH3T3 cells induced to express BFP-NLS or NLS-BFP-actin$^{R62D}$ and undergoing either asynchronous (asyn.) or synchronized (mitotic shake off) culture, as indicated. **(d, e)** Images and quantitative immunofluorescence analysis of nuclear Aurora B **(d)** and KAT5 **(e)** (both green; nuclei are stained with DAPI (magenta)) in NIH3T3 cells at mitotic exit expressing Flag-NLS-actin-T2A-SNAP derivatives, as indicated. Data are shown as mean ± SD (n=20 nuclei per condition, pooled from three independent experiments). Scale bar, 10 µm. $^{****}P < 0.0001$ calculated by *t*-test. **(f)** Analysis of chromatin compaction by an MNase accessibility assay 45 min after mitotic shake-off in NIH3T3 cells expressing either doxycycline-induced Flag-NLS-actin$^{wt}$ or -actin$^{R62D}$. Graph shows quantified pixel intensities corresponding to band intensities. **(g)** Example images illustrating the pipeline used for the quantification of condensed chromatin in cryo-electron microscopy images (for details see Methods). Based on raw images (I) nuclei and nucleoli were manually segmented (II). Condensed chromatin was semi-automatically segmented across the nucleoplasmic region and classified (III) allowing for an assessment of its distribution using a custom ImageJ/Fiji macro (IV). **(h)** Representative electron microscopy images of cryo-preserved, synchronized early $G_1$ NIH3T3 cells expressing GFP-Exportin 6 corresponding to Figure 4l. Scale bar, 2 µm. Unprocessed original scans of blots are shown in Supplementary Fig. 7. Immunoblot in c and MNase accessibility assay in f represent 1 out of 2 independent experiments.

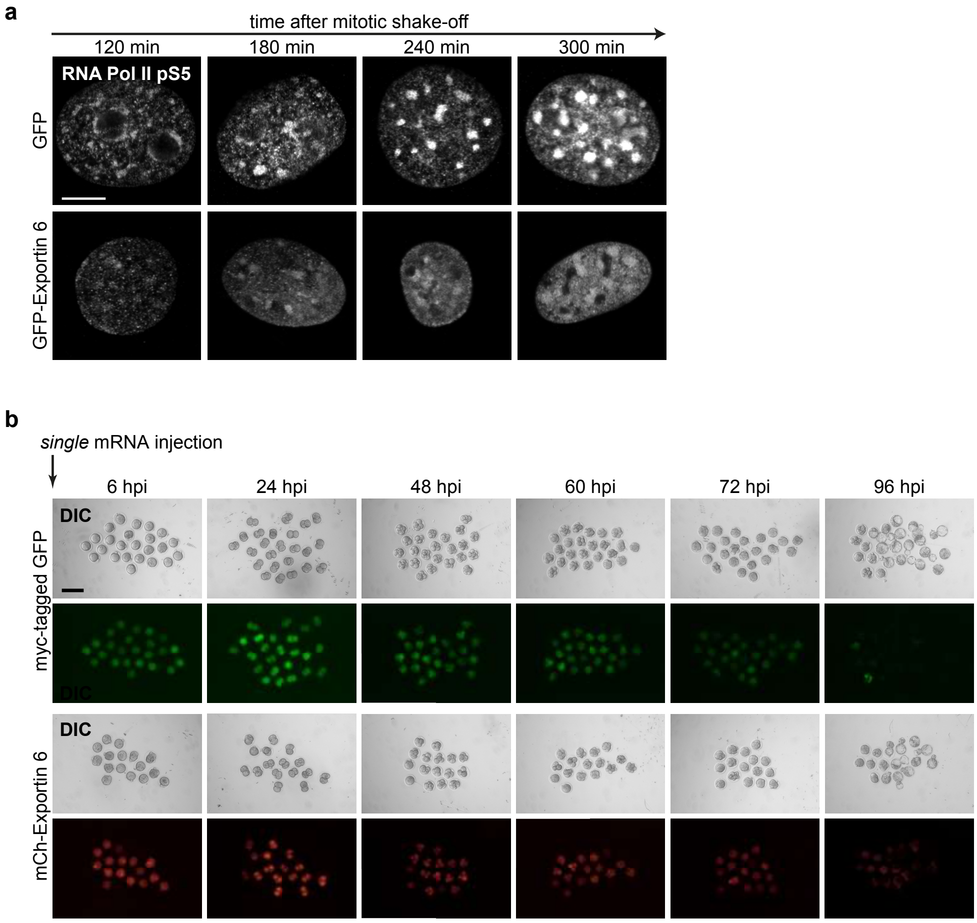

**Supplementary Figure 5** Inhibition of nuclear F-actin formation impairs Pol II-dependent transcription and preimplantation development of mouse embryos. **(a)** Images corresponding to Figure 5a showing RNA Pol II pS5 stainings (grey) in NIH3T3 cells expressing either GFP or GFP-Exportin 6 at indicated times after mitotic shake-off. Scale bar, 5 µm. **(b)** Images corresponding to Figure 5g showing preimplantation development of mouse embryos expressing either mCherry-Exportin 6 or myc-tagged GFP as a control. Similar amounts of mRNA were injected into oocytes at the metaphase II stage, followed by *in vitro* fertilization. Scale bar, 100 µm

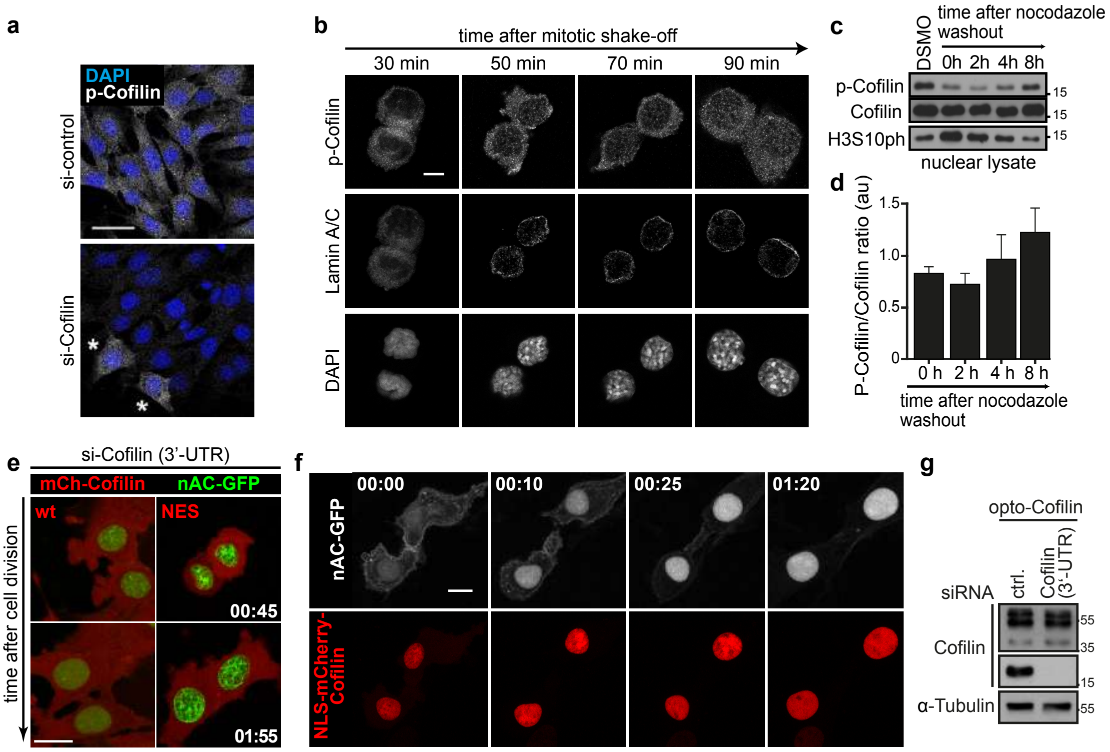

**Supplementary Figure 6** P-Cofilin levels change during mitotic exit and nuclear Cofilin-1 is essential for filament disassembly during mitotic exit. **(a)** Representative immunostaining of p-Cofilin (grey, DAPI (blue)) in NIH3T3 cells treated with si-Control or si-Cofilin to validate specificity of the obtained fluorescence signals. Asterisks indicate presumably non-silenced cells. Scale bar, 10 µm. The experiment was performed once. **(b)** Images corresponding to quantifications shown in Figure 6e. Confocal images show single slices at indicated time points after mitotic shake-off. Scale bar, 5 µm. **(c)** Immunoblot detecting p-Cofilin and Cofilin in RPE-1 cells after washout of nocodazole. Decreasing H3S10ph levels proof for successful release from the nocodazole-induced mitotic block. **(d)** P-Cofilin/Cofilin ratio was calculated by densitometric quantification of immunoblot intensities. Data are shown as mean + SD from n=3 independent experiments. **(e)** Time-lapse imaging of NIH3T3 cells during mitotic exit corresponding to Figure 6j. Cells stably express nAC-GFP (green) together with either WT- or NES-mCherry-Cofilin (red) and were treated with siRNA against the 3'-UTR of endogenous Cofilin-1. Scale bar, 10 µm. **(f)** Stably nAC-GFP expressing NIH3T3 cells were transfected with NLS-mCherry-Cofilin and followed during mitotic exit. Images show maximum intensity projections of confocal z-stacks and illustrate the absence of nuclear F-actin formation which was observed in 10 of 12 mitotic events. Time, hours:min; scale bar, 10 µm. **(g)** Immunoblot validating expression of opto-Cofilin in cells treated with either control siRNA or siRNA directed against the 3'-UTR of endogenous Cofilin-1. Unprocessed original scans of blots are shown in Supplementary Fig. 7.

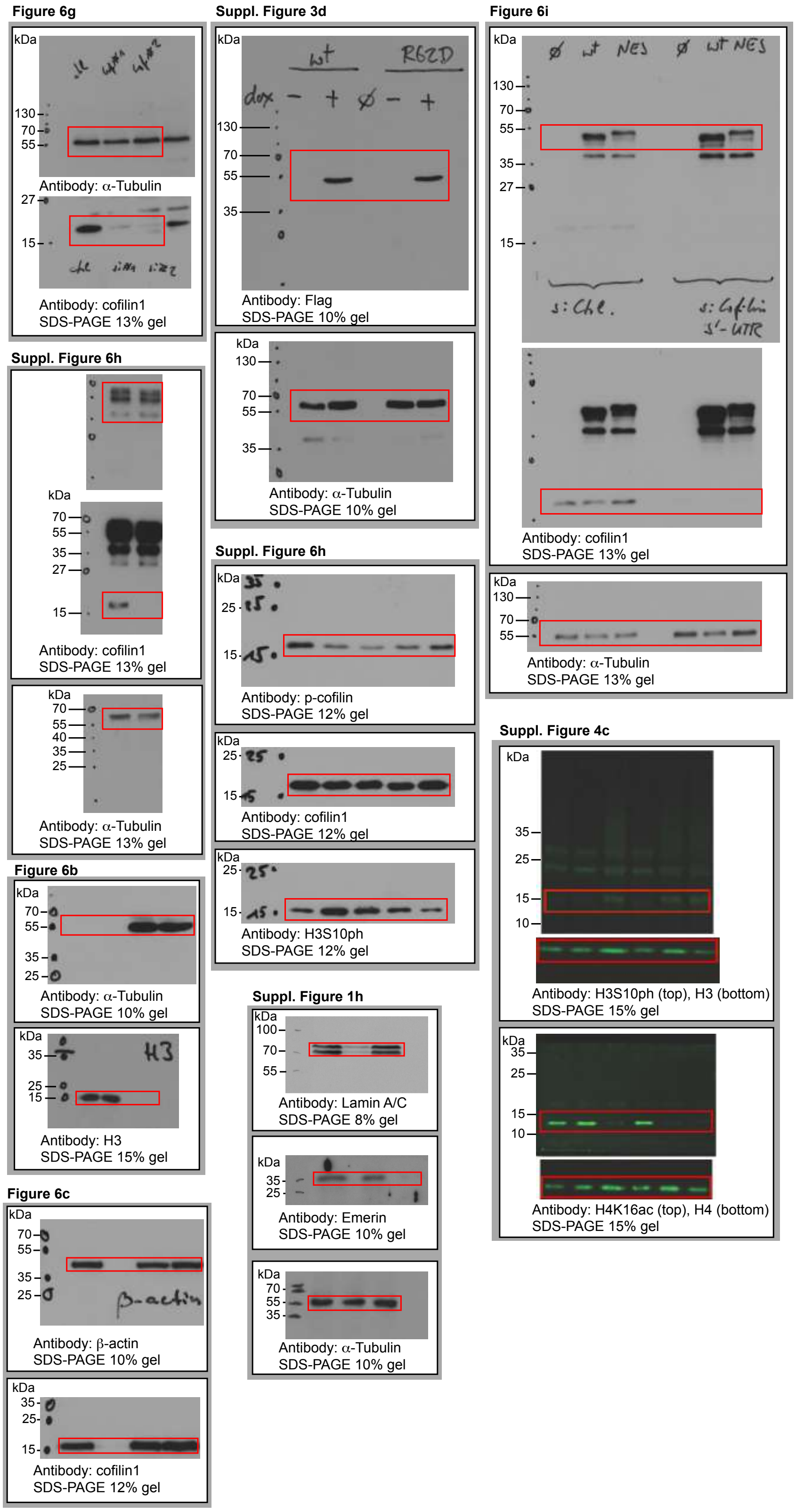

**Figure 6g**

Antibody: α-Tubulin

Antibody: cofilin1
SDS-PAGE 13% gel

**Suppl. Figure 6h**

Antibody: cofilin1
SDS-PAGE 13% gel

Antibody: α-Tubulin
SDS-PAGE 13% gel

**Figure 6b**

Antibody: α-Tubulin
SDS-PAGE 10% gel

Antibody: H3
SDS-PAGE 15% gel

**Figure 6c**

Antibody: β-actin
SDS-PAGE 10% gel

Antibody: cofilin1
SDS-PAGE 12% gel

**Suppl. Figure 3d**

Antibody: Flag
SDS-PAGE 10% gel

Antibody: α-Tubulin
SDS-PAGE 10% gel

**Suppl. Figure 6h**

Antibody: p-cofilin
SDS-PAGE 12% gel

Antibody: cofilin1
SDS-PAGE 12% gel

Antibody: H3S10ph
SDS-PAGE 12% gel

**Suppl. Figure 1h**

Antibody: Lamin A/C
SDS-PAGE 8% gel

Antibody: Emerin
SDS-PAGE 10% gel

Antibody: α-Tubulin
SDS-PAGE 10% gel

**Figure 6i**

Antibody: cofilin1
SDS-PAGE 13% gel

Antibody: α-Tubulin
SDS-PAGE 13% gel

**Suppl. Figure 4c**

Antibody: H3S10ph (top), H3 (bottom)
SDS-PAGE 15% gel

Antibody: H4K16ac (top), H4 (bottom)
SDS-PAGE 15% gel

**Supplementary Figure 7** Unprocessed original scans of Western blot analysis

## Supplementary Table Legends

**Supplementary Table 1** Table illustrating the incidence and duration of nuclear F-actin formation at mitotic exit upon siRNA-mediated knockdown of actin nucleators or regulators. All siRNA sequences used showed greater than 50% knockdown efficiency on mRNA level for the intended target, as determined by RT-qPCR (compared to control siRNA and normalized to expression of TBP). Statistical analysis did not show a significant difference for any condition compared to control cells, as determined by one-way ANOVA. n.d., not determined. Data are shown as mean +/- SEM, pooled from at least 2 independent experiments. Sample sizes (number of mitotic events) for each condition are shown within the table.

**Supplementary Table 2** Table summarizing the results of nuclear F-actin pulldown, as well as a control pulldown (without biotin-phalloidin), performed at mitotic exit and analysed by mass spectrometry (see Methods for details).

**Supplementary Table 3** Table listing the information of antibodies used in this study.

**Supplementary Video 1** Transient nuclear F-actin formation can be detected during mitotic exit. Video corresponding to Fig. 1a shows transient formation of nuclear F-actin during and after cell division in NIH3T3 cells as visualized by nAC-GFP (green). In addition, cells express LifeAct-mCherry (red). Scale bar, 10 μm.

**Supplementary Video 2** Nuclear F-actin shows dynamic turnover in cells at mitotic exit. Video corresponding to Fig. 1b shows dynamic reorganization of actin filaments after mitotic division in NIH3T3 cells as visualized by nAC-GFP (green). In addition, cells express Lamin-nanobody-SNAP, labelled by a SiR-647 dye (LaminCB-SNAP|SiR-647, magenta). Scale bar, 10 μm.

**Supplementary Video 3** Nuclear F-actin forms within interchromatin spaces. Video corresponding to Fig. 4a shows dynamic reorganization of actin filaments after mitotic division in NIH3T3 cells as visualized by sAC-GFP (green). In addition, cells express H2B-mCherry (red) to visualize chromatin content. Scale bar, 10 μm; time stamp, h:min:s.

**Supplementary Video 4** Nuclear actin filaments reshape newly assembled nuclei. Video corresponding to Fig. 3a shows NIH3T3 cells during mitotic exit, stably expressing nAC-GFP (green) and H2B-mCherry (red). Scale bar, 10 μm; time stamp, min:s.

**Supplementary Video 5** Knockdown of Cofilin affects nuclear actin dynamics during mitotic exit. Video corresponding to Fig. 6f, g. Time-lapse imaging of NIH3T3 cells stably expressing nAC-GFP (green), treated with si-control or si-Cofilin during mitotic exit. Video shows three representative examples for each condition. Note the appearance of excessive and stable nuclear actin filaments in si-Cofilin-treated cells. Scale bar, 10 μm.

**Supplementary Video 6** Light-regulated control of opto-Cofilin subcellular localization. Video corresponding to Fig. 7d shows NIH3T3 cells stably expressing opto-Cofilin (grey). Single confocal slices were acquired at 10 sec intervals, and cells were temporarily illuminated by additional blue laser light (488 nm, indicated by a green bar) to promote reversible nuclear export of opto-Cofilin.

**Supplementary Video 7** Formation of excessive, stable nuclear F-actin upon light-regulated nuclear exclusion of opto-Cofilin. NIH3T3 cells stably expressing nAC-SNAP (labelled by SiR-647, grey) and opto-Cofilin (red) were treated with si-Cofilin (3'-UTR) and imaged during and after mitosis. Cells were imaged either with (+ light, lower panel) or without (- light, upper panel) additional blue laser light (488 nm) to promote sustained nuclear export of opto-Cofilin.

**Supplementary Video 8** Reversible formation of excessive, stable nuclear F-actin by light-controlled subcellular shuttling of opto-Cofilin. Video corresponding to Fig. 7f shows NIH3T3 cells stably expressing nAC-SNAP (labelled by SiR-647, grey) and opto-Cofilin (red) during and after mitosis. Cells were treated with si-Cofilin (3'-UTR) and temporarily illuminated by blue laser light (488 nm) to promote nuclear export of opto-Cofilin for a defined period of time (indicated by a green bar).

## 9.5 *S. pombe* kinetochore protein imaging and data analysis

### 9.5.1 *S. pombe* strain construction

An *S. pombe* strain carrying the PAmCherry-cnp1 N-terminal fusion was obtained from the group of professor Ernest Laue, Department of Biochemistry, University of Cambridge. Construction of the strain is described in [91], strain DL70. The spindle pole body protein sad1 in the DL70 parent strain was then tagged with mScarlet-I [86] as described in [4]. In short, DL70 cells were transformed with a linear DNA fragment consisting of the sequence for mScarlet-I, followed by a hygromycin resistance cassette and flanked on both sides by 500-600 bp homology arms for homologous recombination into the genome downstream of the sad1 spindle-pole body protein, for a C-terminal sad1-mScarlet-I fusion. Transformants were selected for hygromycin resistance on solid YES medium (30g/L glucose, 5g/L yeast extract, 20g/L agar and 200mg/L each of adenine, uracil, histidine, leucine and lysine) and integration into the genome was confirmed by colony PCR and sequencing. The resulting strain was used as the parent for further transformations. The same procedure was repeated to tag each POI with the prime-convertible mEos3.2-A69T protein [3], but a kanamycin resistance cassette was used instead. Transformants were selected on solid YES medium containing geneticin. Resistance cassettes are described in [92]. All transformations were done using the Frozen-EZ Yeast Transformation II Kit (Zymo, USA, cat. T2001). Strains were cultured to early stationary phase in liquid YES medium, mixed 1:1 with sterile 87% glycerol and stored at -80 °C.

### 9.5.2 SMLM microscope slide preparation

8-well Ibidi $\mu$-Slides (Ibidi, Germany, cat. 80827) were cleaned by adding 400 $\mu$L of 1M KOH solution into each well and incubating for 40-60 minutes. After incubation, wells were thoroughly rinsed with distilled water. 200 $\mu$L of 0.1% poly-L-lysine (Sigma Aldrich, USA, cat. P8920) solution were added to each well and incubated until the slide was needed.

### 9.5.3 *S. pombe* SMLM sample preparation

A loopfull of *S. pombe* cryo-stock was spread on a YES plate containing the appropriate antibiotic to single colonies and incubated for 24-48h at 32 °C. A single colony was then inoculated into 10 mL of liquid YES medium and grown at 25 °C for 12-24h. Once the culture reached an OD600 of 1—2, it was used to inoculate 100 mL of freshly prepared EMM medium (Formedium, UK, cat. PMD0201) with 200mg/L each of adenine, histidine, uracil, leucine and lysine to a starting OD600 of 0.1. The culture was incubated at 25 °C for approximately 16h or until OD600 of 1-1.5. To enrich the fraction of cells in the desired cell-cycle stage (metaphase to early anaphase), the culture was synchronized using a lactose gradient as described in [93]. The 100 mL EMM culture was centrifuged in a standard tabletop centrifuge at 2000 rpm for 5 minutes. The supernatant was discarded and the pellet was resuspended in 500 $\mu$L of pre-warmed EMM. The cell slurry was carefully overlaid on top of a lactose gradient solution inside of a 50 mL falcon tube. The tube was centrifuged in a standard tabletop centrifuge at 1000 rpm for 8-10 minutes. During centrifugation, msot cells would pellet to the bottom of the tube, leaving a layer of G1 cells in suspension. The very top 1 mL of this layer was aspirated with a pipette and mixed with 1 mL of pre-warmed EMM in a 2 mL Eppendorf tube. The tube was centrifuged at 4000 G for 2 minutes and the supernatant was removed. Cells were resuspended in 1 mL EMM and the OD600 of this solution was measured. It was then used to inoculate a 10 mL EMM culture to a starting OD600 of 0.6. The culture was grown at 25 °C and 2 mL aliquots were fixed at 60, 70 and 80 minutes of incubation. Since such cell synchronization is not very tight, the fixation was staggered to capture the time when most cells are in metaphase or anaphase, which usually occured 60-80 minutes post synchronization. Fixation was done by adding 37% paraformaldehyde directly to the medium to a final concentration of 3.7%. Cells were incubated for 15 minutes, then centrifuged at 1000 G for 3 minutes and the supernatnat was removed. The pellet was resuspened in 1x phosphate buffered saline filtered through a 0.2 $\mu$m pore size syringe filter. The suspension was centrigued at 1000 G again and the supernatant removed. The pellet was then resuspended in 50 mM Tris-HCl in distilled water (also filtered). These alternating wash steps were repeated 2 more times. The changes in osmolarity between the two buffers assisted in washing free-floating fluorescent background fromt he cells. After the sixth wash,cells were resuspended in 400 $\mu$L of filtered Tris-HCl. A 1:500 solution of stock 660/680 red FluoSphere fluorescent beads (Thermo Fisher, USA, cat. F8807) was sonicated in a sonicator bath for 3 minutes, then added to the cell suspension in a ratio of 1:500. The fluorescent beads would attach to cell walls and serve as fiducial markers during the imaging process. The suspension was vortexed and incubated for 10 minutes. Poly-L-lysine was aspirated from an Ibidi well and replaced with 200 $\mu$L of the cell suspension, then incubated for 10 minutes. Meanwhile, 0.5% low-melting agarose was prepared in filtered Tris-HCl and kept at 32 °C. The microwell slide was placed on ice and the liquid was carefully aspirated, leaving a layer of cells attached to the slide. A few drops of the liquid agarose were carefully dripped onto the layer of cells, where the agarose promptly solidified due to the ice. The purpose of the agarose embedding was to keep the cells stable during imaging, while allowing diffusion of buffer through the porose agarose to the cells. The slide was incubated on ice for 5 minutes to ensure solidification, then the agarose was overlaid with 50 mM Tris-HCl to prevent drying and the sample was imaged.

### 9.5.4 SMLM imaging of *S. pombe*

The microscope setup was the same as described in [4], using an automated Nikon Ti Eclipse microscope, equipped with appropriate dichroic mirror and filters (ET dapi/Fitc/cy3 dichroic, ZT405/488/561rpc rejection filter, ET525/50 or ET610/75 bandpass, all AHF Analysentechnik, Germany), and a CFI Apo TIRF 100x oil objective (NA 1.49, Nikon). All lasers (405 nm OBIS, 561 nm OBIS, 730 nm OBIS, 488 nm Sapphire, all Coherent Inc., USA) except for the 730 nm were modulated by an acousto-optical tunable filter (AOTF) (Gooch and Housego, Germany). Fluorescence was detected by an emCCD (iXON Ultra 888, Andor, UK). The vertical focus was controlled by a commercial perfect focus system (Nikon, Germany). The acquisition was controlled by a customized version of the $\mu$Manager software [94].

The mScarlet-I was imaged first, excited with low intensity 561 nm illumination (0.1-1 W/cm2). The field of view was adjusted to contain the maximum amount of cells with two SPB spots (metaphase and anaphase cells) in focus, while keeping the illumination uniform. Intensity of the

561 laser was increased to 200 W/cm2 and 100 frames of the sad1-mScarlet-I were recorded at an exposure time of 60 ms for each field of view. The acquisition was stopped and the 561 laser intensity was increased to 500 W/cm2 for 60-120 seconds, to bleach away the mScarlet-I. The POI-mEos3.2-A69T was imaged next, activated with 450 W/cm2 of the 730 nm laser and 100-2500 mW/cm2 of the 488 nm laser (pulsed every 10th frame) with the intensity gradually increased to keep the number of localizations per frame constant. The mEos3.2-A69T was read out with the 561 (500 W/cm2) laser for 15-20 000 frames (or longer, if necessary for a full readout) at an exposure time of 60 ms per frame. When the acquisition was over, the sample was illuminated with 1 kW/cm2 of the 488 nm laser for 30 seconds, to bleach potential residual mEos3.2-A69T. Finally, the cnp1-PAmCherry was imaged by activation with the 405 laser, pulsed on every 10th frame, with the intensity gradually adjusted from 250-6500 mW/cm2 to keep the number of localizations per frame constant. The PAmCherry was read out with constant 561 illumination at 500 W/cm2 for 10-15 000 frames or as many as required for a full readout at 60 ms exposure per frame at an exposure time of 20 ms per frame.

### 9.5.5 SMLM data post-processing

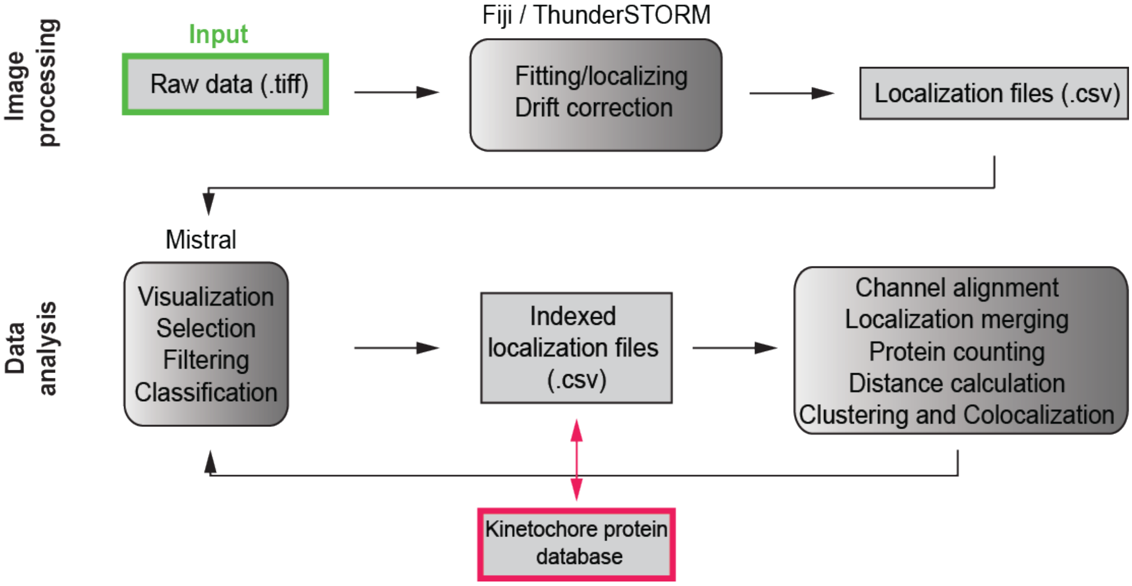

**Figure 9.1:** Flow chart of the data analysis workflow.

Localization files were generated from the SMLM movies using the ThunderSTORM [88] plugin for the open-source image analysis software FiJi [95], using an automated macro. Fit parameters used were the following: spot candidate identification in the tif-stack: B-spline wavelet filter with scale of 2.0 pixel and order of 3, local maximum detection in a 8 pixel neighborhood and threshold of 1.5*std(wavelet); Point Spread Function (PSF) model to fit spot candidates: integrated Gaussian, sigma 1.4 pixel, weighted least squares optimization with a fit radius of 4 pixel, no multi-emitter fit. Drift correction using fiducial markers was also performed in ThunderSTORM. Fiducial markers were identified by grouping localizations within 40 nm of each other in adjacent frames together. For the POI channel, traces that spanned at least 90% of the movie were used while for the cnp1 channel this was reduced to 70%. Though the mScarlet-I channel was not recorded as an SMLM movie, it still underwent the same fitting process. Instead of single molecules being fitted in each frame, the center of the entire SPB was fitted for each frame.

The drift corrected localization files were then ready to be processed by a semi-automated analysis suite written in the Python 3 programming langauge. The entire analysis pipeline is summarized in Figure 9.1. The workflow revolved around a single csv table for each field of view acquisition, where each line represented a single localization with a unique identifier number. Properties were attached to each localization after every analysis step (such as channel, whether the localization belongs to a fiducial marker or a protein population etc.), as described below.

Since the acquisition time of a single movie could take up to 30 minutes and the sample could have drifted significantly during that time, localization files of all three channels first had to be aligned. Each localization file was first run through a nearest neighbor tracking algorithm. Using the kd-tree class from the scipy Python module [96], the nearest neighboring localization in a radius of 150 nanometers of each localization was identified in the first subsequent frame. Neighbor identifiers were stored and used to connect localizations into tracks. Distance to the nearest neighbor were also stored for each localization. Tracks that spanned at least 90% of the movie in the POI channel or 70% of the movie in the cnp1 channel were classified as fiducial localizations. Al non-fiducial localization tracks were merged together by averaging the coordinates, intensity and PSF size of all localizations in a track. The tracked localization files were then merged into a single large file, in which each localization carried the information of its channel. Non-fiducial localizations were then filtered based on these averaged parameters to discard statistical outliers. Outlier thresholds were calculated using the standard statistical formula of Q1 - 1.5*IQR, Q3 + 1.5*IQR. The parameters used for filtering were intensity, chi-square goodness of fit and PSF width. For the PSF width, a set threshold of 70-200 nm was used instead of a dynamic outlier calculation. The filtered localization file was visualized using an unpublished visualization software written in the C++ programming language developed by the Endesfelder group. In this software, called Mistral, individual localizations could be selected and classified. Localizations in Mistral were color-coded by channel and localizations belonging to the same fiducial marker were grouped together manually. The data was then fed back into the Python analysis suite for channel alignment. Localizations belonging to the selected fiducial markers then underwent a quality check by fitting the distribution of localizations with a normal distribution in the x and y dimensions. A symmetry ratio was calculated by dividing the Full Width at Half Maximum of a normal distribution (FWHM) of the distributions in both dimensions. Fiducials where the symmetry factor fell outside the thresholds of 0.9 - 1.1 were discarded, if other fiducials were available. Using the distances obtained in the nearest-neighbor tracking step, the NeNA localization precision of each fiducial was calculated according to [97] and stored for later screening. Based on the selected fiducial markers, alignment correction values were calculated by measuring Euclidean distances between the centroids of the fiducial localization clusters in the different channels. Localization files of channels 2 and 3 were then aligned to channel 1 with a simple linear translation using the calculated correction factors. When multiple beads were present, the standard deviation of the correction factors was calculated and stored as a measure of channel alignment quality.

The aligned and merged localization files were again fed into Mistral for visualization. Yeast cells were visible due to the ever-present fluorescent background. This was taken advantage of to manually select cells for further analysis. Cells with kinetochore protein localization clusters in the focal plane were selected and classified, then exported with unique cell identification numbers and fed back into the Python script. To assign localizations to individual kinetochore protein clusters, a modified OPTICS clustering algorithm was then performed on just localizations belonging to the selected cells, to save on computation time. The OPTICS algorithm was run as described in [98] with a high distance threshold of 2000, assigning a reach distance and OPTICS order to each localization. Localizations of each cell were sorted according to the OPTICS order and a simple moving average with a variable window was calculated. The localizations were then iterated through and when the reach distance of a localization exceeded a certain threshold (termed "wiggle") above the simple moving average, the localization was classified as a separator point, while all other localizations were classified as potential cluster points. The list of localizations was then iterated through again to assign clusters. When a sufficient number of cluster points (minimum cluster size) was separated by a sufficient number of separator points (minimum separator points), the points were assigned to a unique cluster. To obtain the optimum moving average window, wiggle threshold, minimum cluster size and minimum required separator points, a grid search was performed on a learning data set. The learning dataset was generated by manual selection of clusters from filtered and merged localization files. The manual selection was done by at least two individuals separately, to avoid bias. The grid search then tested different combinations of all parameters, until a result that was the most similar to the learning dataset was achieved. These parameters were then used to run the clustering algorithm on all other movies from that particular imaging session. It was important to re-do the learning step for each session and protein separately, due to slightly different fluorescent backgrounds and different counts for each POI. Even though some clusters had to be classified manually, the clustering algorithm drastically increased the speed of data analysis compared to manual selection. This algorithm was only performed on localizations from channels 1 and 2. Since the mScarlet-I movies were not super-resolved and the localizations always represented the center of the ensemble sad1 spot, clusters were determined as localization tracks that spanned 100% of the movie.

Following the clustering algorithm, the data went through one last manual quality and classification check in Mistral. In this step, cnp1 clusters were manually paired together with POI clusters and assigned to individual kinetochores. Any residual noise points were also removed. This step was done by two individuals separately to avoid bias and the quality control was extremely strict. Whenever there was any doubt whether or not a two clusters belong to the same kientochore, the clusters were discarded. Each kinetochore was given a unique identification number, the data was exported and fed back into the Python routine.

The next step of analysis measured several different parameters, not all of which are relevant for this thesis. Since all cells had a significant amount of background localizations confined to the intracellular compartment, these could be used to calculated cell shapes and dimensions. This was done using all the localizations, even the ones that did not pass the quality filter steps. A convex hull (a shape connecting peripheral localizations that encompassess all other localizations) was drawn using the scipy [96] Python library and the hull area was extracted. Cell localizations were then rotated around the centroid of the cell until the cell was horizontal by finding the maximum difference between x min and x max and this distance was saved as the cell length. The same difference was calculated for the y axis. NeNA localization precision [97] was calculated for all the clustered localization in the cell and recorded.

The number of localizations in each cluster was checked and saved for later protein count analysis. The cluster centroid was calculated by averaging the x and y coordinates of all the localizations in the cluster. A convex hull was drawn for each cluster, used for area calculation and a similar rotating algorithm as for cells was employed to calculate the cluster width and length.

Each of the manually selected kinetochores, containing a cnp1 and a POI localization cluster was treated as a whole for several parameter calculations. The angle between the axis defined by the centroids of both kinetochore clusters and the axis defined by the POI cluster and the nearest SPB cluster was calculated and stored. The angle of the kinetochore (cnp1 through POI) relative to the mitotic spindle axis, defined by both SPBs was also calculated. Both kinetochore clusters were rotated around the centroid of the cnp1 cluster by both of these angles, adjusted so that the centroid of cnp1 was at 0 and stored as separate outputs, for future particle averaging.

Finally, the cnp1-POI distances were claculated by rotating the kinetochore by the mitotic spindle axis and collapsing all localizations of the two clusters onto that axis. This simplified the complex, 2-dimensional objects into simple 1-dimensional distributions. The absolute distance between the means of the two collapsed clusters was calculated. While it would have been ideal to take kinetochore orientation into account here, this was not possible due to the properties of the *S. pombe* mitotic spindle. The SPB closest to a kinetochore is not necessarily the SPB to which the kinetochore is attached (via a microtubule). This is caused by a phenomenon in fission yeast where kinetochores oscillate back and forth along the mitotic spindle until DNA segregation takes place [99]. Due to this, it was impossible to accurately determine the orientation of each kinetochore, hence the absolute distance was deemed as the safest measurement.

All of these measures were saved as extra columns in the localization table, where each localization had attached to it the parameters of the cell, cluster and kinetochore it belonged to. The tables could then be grouped, filtered and merged to extract any desired data.

### 9.5.6 Final distance and localization count extraction

To obtain the final distance and localization count numbers, the issue of the unknown kinetochore orientation had to be addressed. If the orientation of each kinetochore was n and the distance could be calculated with a direction, the distribution of such distances for any given protein would likely constitute a normal distribution. Some of the spread (standard deviation) of the distribution would be explained by the natural variation in the position of the protein, while experimental precision would contribute to the rest. As such, given the mean of the distribution was located close enough to zero and the standard deviation was high enough, the left tail of the distribution would extend past zero. When the orientation of the measurement is not known, such a distribution would be inherently biased. By taking the absolute value of all values in the distribution, this bias is avoided, but the distribution changes to where a simple arithmetic average no longer describes the actual expected value. The result is a distribution called the folded normal distribution [100], described by the following equation:

$$f_Y(x;\mu,\sigma^2) = \frac{1}{\sqrt{2\pi\sigma^2}}\, e^{-\frac{(x-\mu)^2}{2\sigma^2}} + \frac{1}{\sqrt{2\pi\sigma^2}}\, e^{-\frac{(x+\mu)^2}{2\sigma^2}}$$

The $\mu$ and $\sigma$ parameters in this equation represent the mean and standard deviation of the underlying normal distribution. Therefore, to obtain the expected value ($\mu$) and width ($\sigma$) of the distribution of cnp1-POI distances, the measured distances can be fitted with the folded normal equation. To increase the accuracy of this approach, a bootstrapping algorithm was used. The set of cnp1-POI distances for each POI was resampled 1000 times with replacement and a sample size equal to the length of the dataset. For each resample, Maximum Likelihood Estimation (MLE) of the parameters was performed using the Sympy Python library [101]. The MLE returned the $\mu$ and $\sigma$, as well as an objective score value of the quality of the fit for each of the 1000 resamples. The sympy approach was verified with a manually written gradient ascent script which produced the same results, but the sympy version was used do to faster performance. The objective scores were used as weights to calculate a weighted average of the $\mu$ and $\sigma$ values. The approach was also tested with extensive data simulations, simulating normally distributed data with known parameters, folding it and running the bootstrapping aproach to obtain the original input parameters. The method proved to be very robust as long as the mean of the unfolded normal distribution was more than 1 standard deviation away from zero. When the mean was closer to zero, the maximum likelihood estimation returned unreliable results. Due to this limitation, it would be necessary to change the reference protein for POIs close to the centromere, as discussed in **section 7.2.3**. The standard deviation of the distribution of the 1000 means is interpreted as a measure of precision, since this value decreases as the amount of data increases and the fits produced are more accurate. A similar, though simpler approach was taken for the localization counts. It has been discussed in the literature that fluorophore blinking behavior can be described by a lognormal distribution [102]. This means that to get the the expected value, the distribution of localization counts could be fitted with a lognormal function. However, matters can be further simplified by calculating the logarithm of the data, which converts the distribution into a normal distribution. Now, the expected value and distribution width can simply be calculated as the arithmetic and standard deviation. This was done with the bootstrapping (1000 resamples) approach for all POIs and the numbers generated by this are presented in **section 7.2.3**

# 10 | Bibliography

[1] B. Turkowyd, D. Virant, and U. Endesfelder, “From single molecules to life: microscopy at the nanoscale,” Analytical and Bioanalytical Chemistry, vol. 408, pp. 6885–6911, Oct 2016.

[2] D. Virant, B. Traenkle, J. Maier, P. D. Kaiser, M. Bodenhöfer, C. Schmees, I. Vojnovic, B. Pisak-Lukáts, U. Endesfelder, and U. Rothbauer, “A peptide tag-specific nanobody enables high-quality labeling for dstorm imaging,” Nature communications, vol. 9, no. 1, p. 930, 2018.

[3] B. Turkowyd, A. Balinovic, D. Virant, H. G. G. Carnero, F. Caldana, M. Endesfelder, D. Bourgeois, and U. Endesfelder, “A general mechanism of photoconversion of green-to-red fluorescent proteins based on blue and infrared light reduces phototoxicity in live-cell single-molecule imaging,” Angewandte Chemie International Edition, vol. 56, no. 38, pp. 11634–11639, 2017.

[4] D. Virant, B. Turkowyd, A. Balinovic, and U. Endesfelder, “Combining primed photoconversion and uv-photoactivation for aberration-free, live-cell compliant multi-color single-molecule localization microscopy imaging,” International Journal of Molecular Sciences, vol. 18, no. 7, 2017.

[5] S. H. Mueller, L. M. Spenkelink, and A. M. van Oijen, “When proteins play tag: the dynamic nature of the replisome,” Biophysical reviews, pp. 1–11, 2019.

[6] G. F. Schröder, “Hybrid methods for macromolecular structure determination: experiment with expectations,” Current opinion in structural biology, vol. 31, pp. 20–27, 2015.

[7] D. Marion, “An introduction to biological nmr spectroscopy,” Molecular & Cellular Proteomics, vol. 12, no. 11, pp. 3006–3025, 2013.

[8] A. Szymborska, A. De Marco, N. Daigle, V. C. Cordes, J. A. Briggs, and J. Ellenberg, “Nuclear pore scaffold structure analyzed by super-resolution microscopy and particle averaging,” Science, vol. 341, no. 6146, pp. 655–658, 2013.

[9] K. Schücker, T. Holm, C. Franke, M. Sauer, and R. Benavente, “Elucidation of synaptonemal complex organization by super-resolution imaging with isotropic resolution,” Proceedings of the National Academy of Sciences, vol. 112, no. 7, pp. 2029–2033, 2015.

[10] M. Mund, J. A. van der Beek, J. Deschamps, S. Dmitrieff, P. Hoess, J. L. Monster, A. Picco, F. Nédélec, M. Kaksonen, and J. Ries, “Systematic nanoscale analysis of endocytosis links efficient vesicle formation to patterned actin nucleation,” Cell, vol. 174, no. 4, pp. 884–896, 2018.

[11] X. Shi, G. Garcia III, J. C. Van De Weghe, R. McGorty, G. J. Pazour, D. Doherty, B. Huang, and J. F. Reiter, “Super-resolution microscopy reveals that disruption of ciliary transition-zone architecture causes joubert syndrome,” Nature cell biology, vol. 19, no. 10, p. 1178, 2017.

[12] C. Sieben, N. Banterle, K. M. Douglass, P. Gönczy, and S. Manley, “Multicolor single-particle reconstruction of protein complexes,” Nature methods, vol. 15, no. 10, p. 777, 2018.

[13] P. J. Cranfill, B. R. Sell, M. A. Baird, J. R. Allen, Z. Lavagnino, H. M. De Gruiter, G.-J. Kremers, M. W. Davidson, A. Ustione, and D. W. Piston, “Quantitative assessment of fluorescent proteins,” Nature methods, vol. 13, no. 7, p. 557, 2016.

[14] W. Margolin, “The price of tags in protein localization studies,” Journal of bacteriology, vol. 194, no. 23, pp. 6369–6371, 2012.

[15] F. O. Bendezú, C. A. Hale, T. G. Bernhardt, and P. A. De Boer, “Rodz (yfga) is required for proper assembly of the mreb actin cytoskeleton and cell shape in e. coli,” The EMBO journal, vol. 28, no. 3, pp. 193–204, 2009.

[16] M. B. Braun, B. Traenkle, P. A. Koch, F. Emele, F. Weiss, O. Poetz, T. Stehle, and U. Rothbauer, “Peptides in headlock–a novel high-affinity and versatile peptide-binding nanobody for proteomics and microscopy,” Scientific reports, vol. 6, p. 19211, 2016.

[17] J. Ries, C. Kaplan, E. Platonova, H. Eghlidi, and H. Ewers, “A simple, versatile method for gfp-based super-resolution microscopy via nanobodies,” Nature methods, vol. 9, no. 6, p. 582, 2012.

[18] D. Pérez-Sala, C. L. Oeste, A. E. Martínez, M. J. Carrasco, B. Garzón, and F. J. Canada, “Vimentin filament organization and stress sensing depend on its single cysteine residue and zinc binding,” Nature communications, vol. 6, p. 7287, 2015.

[19] H. Aizawa, M. Sameshima, and I. Yahara, “A green fluorescent protein-actin fusion protein dominantly inhibits cytokinesis, cell spreading, and locomotion in dictyostelium,” Cell structure and function, vol. 22, no. 3, pp. 335–345, 1997.

[20] M. Kimble, C. Kuzmiak, K. McGovern, and E. de Hostos, “Microtubule organization and the effects of gfp-tubulin expression in dictyostelium discoideum,” Cell motility and the cytoskeleton, vol. 47, no. 1, pp. 48–62, 2000.

[21] M. Mikhaylova, B. M. Cloin, K. Finan, R. Van Den Berg, J. Teeuw, M. M. Kijanka, M. Sokolowski, E. A. Katrukha, M. Maidorn, F. Opazo, et al., “Resolving bundled microtubules using anti-tubulin nanobodies,” Nature communications, vol. 6, p. 7933, 2015.

[22] K. Finan, A. Raulf, and M. Heilemann, “A set of homo-oligomeric standards allows accurate protein counting,” Angewandte Chemie International Edition, vol. 54, no. 41, pp. 12049–12052, 2015.

[23] E. Betzig, G. H. Patterson, R. Sougrat, O. W. Lindwasser, S. Olenych, J. S. Bonifacino, M. W. Davidson, J. Lippincott-Schwartz, and H. F. Hess, “Imaging intracellular fluorescent proteins at nanometer resolution,” Science, vol. 313, no. 5793, pp. 1642–1645, 2006.

[24] F. V. Subach, G. H. Patterson, S. Manley, J. M. Gillette, J. Lippincott-Schwartz, and V. V. Verkhusha, “Photoactivatable mcherry for high-resolution two-color fluorescence microscopy,” Nature methods, vol. 6, no. 2, p. 153, 2009.

[25] M. Andresen, A. C. Stiel, S. Trowitzsch, G. Weber, C. Eggeling, M. C. Wahl, S. W. Hell, and S. Jakobs, “Structural basis for reversible photoswitching in dronpa,” Proceedings of the National Academy of Sciences, vol. 104, no. 32, pp. 13005–13009, 2007.

[26] N. G. Gurskaya, V. V. Verkhusha, A. S. Shcheglov, D. B. Staroverov, T. V. Chepurnykh, A. F. Fradkov, S. Lukyanov, and K. A. Lukyanov, “Engineering of a monomeric green-to-red photoactivatable fluorescent protein induced by blue light,” Nature biotechnology, vol. 24, no. 4, p. 461, 2006.

[27] W. P. Dempsey, L. Georgieva, P. M. Helbling, A. Y. Sonay, T. V. Truong, M. Haffner, and P. Pantazis, “In vivo single-cell labeling by confined primed conversion,” Nature methods, vol. 12, no. 7, p. 645, 2015.

[28] M. J. Rust, M. Bates, and X. Zhuang, “Sub-diffraction-limit imaging by stochastic optical reconstruction microscopy (storm),” Nature methods, vol. 3, no. 10, p. 793, 2006.

[29] V. Adam, K. Nienhaus, D. Bourgeois, and G. U. Nienhaus, “Structural basis of enhanced photoconversion yield in green fluorescent protein-like protein dendra2,” Biochemistry, vol. 48, no. 22, pp. 4905–4915, 2009.

[30] N. Pavin and I. M. Tolić, “Self-organization and forces in the mitotic spindle,” Annual review of biophysics, vol. 45, pp. 279–298, 2016.

[31] L. Nezi and A. Musacchio, “Sister chromatid tension and the spindle assembly checkpoint,” Current opinion in cell biology, vol. 21, no. 6, pp. 785–795, 2009.

[32] S. Catania and R. C. Allshire, “Anarchic centromeres: deciphering order from apparent chaos,” Current opinion in cell biology, vol. 26, pp. 41–50, 2014.

[33] V. Wood, R. Gwilliam, M.-A. Rajandream, M. Lyne, R. Lyne, A. Stewart, J. Sgouros, N. Peat, J. Hayles, S. Baker, et al., “The genome sequence of schizosaccharomyces pombe,” Nature, vol. 415, no. 6874, p. 871, 2002.

[34] R. Wevrick and H. F. Willard, “Long-range organization of tandem arrays of alpha satellite dna at the centromeres of human chromosomes: high-frequency array-length polymorphism and meiotic stability,” Proceedings of the National Academy of Sciences, vol. 86, no. 23, pp. 9394–9398, 1989.

[35] R. Zinkowski, J. Meyne, and B. Brinkley, “The centromere-kinetochore complex: a repeat subunit model.,” The Journal of Cell Biology, vol. 113, no. 5, pp. 1091–1110, 1991.

[36] A. P. Joglekar, K. Bloom, and E. Salmon, “In vivo protein architecture of the eukaryotic kinetochore with nanometer scale accuracy,” Current Biology, vol. 19, no. 8, pp. 694–699, 2009.

[37] A. Musacchio and A. Desai, “A molecular view of kinetochore assembly and function,” Biology, vol. 6, no. 1, p. 5, 2017.

[38] R. C. Allshire and G. H. Karpen, “Epigenetic regulation of centromeric chromatin: old dogs, new tricks?,” Nature Reviews Genetics, vol. 9, no. 12, p. 923, 2008.

[39] B. Akiyoshi and K. Gull, “Evolutionary cell biology of chromosome segregation: insights from trypanosomes,” Open biology, vol. 3, no. 5, p. 130023, 2013.

[40] L. Clarke and J. Carbon, “Isolation of a yeast centromere and construction of functional small circular chromosomes,” Nature, vol. 287, no. 5782, p. 504, 1980.

[41] G. Cottarel, J. Shero, P. Hieter, and J. Hegemann, “A 125-base-pair cen6 dna fragment is sufficient for complete meiotic and mitotic centromere functions in saccharomyces cerevisiae.,” Molecular and cellular biology, vol. 9, no. 8, pp. 3342–3349, 1989.

[42] M. Winey, C. L. Mamay, E. T. O’toole, D. N. Mastronarde, T. H. Giddings, K. L. McDonald, and J. R. McIntosh, “Three-dimensional ultrastructural analysis of the saccharomyces cerevisiae mitotic spindle.,” The Journal of cell biology, vol. 129, no. 6, pp. 1601–1615, 1995.

[43] S. Hughes-Schrader and H. Ris, “The diffuse spindle attachment of coccids, verified by the mitotic behavior of induced chromosome fragments,” Journal of Experimental Zoology, vol. 87, no. 3, pp. 429–456, 1941.

[44] L. Sanchez-Pulido, A. L. Pidoux, C. P. Ponting, and R. C. Allshire, “Common ancestry of the cenp-a chaperones scm3 and hjurp,” Cell, vol. 137, no. 7, pp. 1173–1174, 2009.

[45] M. Nakano, S. Cardinale, V. N. Noskov, R. Gassmann, P. Vagnarelli, S. Kandels-Lewis, V. Larionov, W. C. Earnshaw, and H. Masumoto, “Inactivation of a human kinetochore by specific targeting of chromatin modifiers,” Developmental cell, vol. 14, no. 4, pp. 507–522, 2008.

[46] C. Obuse, H. Yang, N. Nozaki, S. Goto, T. Okazaki, and K. Yoda, “Proteomics analysis of the centromere complex from hela interphase cells: Uv-damaged dna binding protein 1 (ddb-1) is a component of the cen-complex, while bmi-1 is transiently co-localized with the centromeric region in interphase,” Genes to Cells, vol. 9, no. 2, pp. 105–120, 2004.

[47] D. R. Foltz, L. E. Jansen, B. E. Black, A. O. Bailey, J. R. Yates III, and D. W. Cleveland, “The human cenp-a centromeric nucleosome-associated complex,” Nature cell biology, vol. 8, no. 5, p. 458, 2006.

[48] M. Okada, I. M. Cheeseman, T. Hori, K. Okawa, I. X. McLeod, J. R. Yates III, A. Desai, and T. Fukagawa, “The cenp-h–i complex is required for the efficient incorporation of newly synthesized cenp-a into centromeres,” Nature cell biology, vol. 8, no. 5, p. 446, 2006.

[49] P. Hemmerich, S. Weidtkamp-Peters, C. Hoischen, L. Schmiedeberg, I. Erliandri, and S. Diekmann, “Dynamics of inner kinetochore assembly and maintenance in living cells,” The Journal of cell biology, vol. 180, no. 6, pp. 1101–1114, 2008.

[50] D. Hellwig, S. Emmerth, T. Ulbricht, V. Döring, C. Hoischen, R. Martin, C. P. Samora, A. D. McAinsh, C. W. Carroll, A. F. Straight, et al., “Dynamics of cenp-n kinetochore binding during the cell cycle,” J Cell Sci, vol. 124, no. 22, pp. 3871–3883, 2011.

[51] T. Hori, M. Okada, K. Maenaka, and T. Fukagawa, "Cenp-o class proteins form a stable complex and are required for proper kinetochore function," Molecular biology of the cell, vol. 19, no. 3, pp. 843–854, 2008.

[52] N. Kagawa, T. Hori, Y. Hoki, O. Hosoya, K. Tsutsui, Y. Saga, T. Sado, and T. Fukagawa, "The cenp-o complex requirement varies among different cell types," Chromosome research, vol. 22, no. 3, pp. 293–303, 2014.

[53] K. L. McKinley, N. Sekulic, L. Y. Guo, T. Tsinman, B. E. Black, and I. M. Cheeseman, "The cenp-ln complex forms a critical node in an integrated meshwork of interactions at the centromere-kinetochore interface," Molecular cell, vol. 60, no. 6, pp. 886–898, 2015.

[54] J. Bancroft, P. Auckland, C. P. Samora, and A. D. McAinsh, "Chromosome congression is promoted by cenp-q-and cenp-e-dependent pathways," J Cell Sci, vol. 128, no. 1, pp. 171–184, 2015.

[55] Y. H. Kang, C. H. Park, T.-S. Kim, N.-K. Soung, J. K. Bang, B. Y. Kim, J.-E. Park, and K. S. Lee, "Mammalian polo-like kinase 1-dependent regulation of the pbip1-cenp-q complex at kinetochores," Journal of Biological Chemistry, vol. 286, no. 22, pp. 19744–19757, 2011.

[56] A. Guse, C. W. Carroll, B. Moree, C. J. Fuller, and A. F. Straight, "In vitro centromere and kinetochore assembly on defined chromatin templates," Nature, vol. 477, no. 7364, p. 354, 2011.

[57] C. W. Carroll, K. J. Milks, and A. F. Straight, "Dual recognition of cenp-a nucleosomes is required for centromere assembly," The Journal of cell biology, vol. 189, no. 7, pp. 1143–1155, 2010.

[58] B. E. Black, L. E. Jansen, P. S. Maddox, D. R. Foltz, A. B. Desai, J. V. Shah, and D. W. Cleveland, "Centromere identity maintained by nucleosomes assembled with histone h3 containing the cenp-a targeting domain," Molecular cell, vol. 25, no. 2, pp. 309–322, 2007.

[59] C. W. Carroll, M. C. Silva, K. M. Godek, L. E. Jansen, and A. F. Straight, "Centromere assembly requires the direct recognition of cenp-a nucleosomes by cenp-n," Nature cell biology, vol. 11, no. 7, p. 896, 2009.

[60] E. M. Dunleavy, D. Roche, H. Tagami, N. Lacoste, D. Ray-Gallet, Y. Nakamura, Y. Daigo, Y. Nakatani, and G. Almouzni-Pettinotti, "Hjurp is a cell-cycle-dependent maintenance and deposition factor of cenp-a at centromeres," Cell, vol. 137, no. 3, pp. 485–497, 2009.

[61] K. J. Milks, B. Moree, and A. F. Straight, "Dissection of cenp-c–directed centromere and kinetochore assembly," Molecular biology of the cell, vol. 20, no. 19, pp. 4246–4255, 2009.

[62] A. Petrovic, S. Pasqualato, P. Dube, V. Krenn, S. Santaguida, D. Cittaro, S. Monzani, L. Massimiliano, J. Keller, A. Tarricone, et al., "The mis12 complex is a protein interaction hub for outer kinetochore assembly," The Journal of cell biology, vol. 190, no. 5, pp. 835–852, 2010.

[63] R. R. Wei, P. K. Sorger, and S. C. Harrison, "Molecular organization of the ndc80 complex, an essential kinetochore component," Proceedings of the National Academy of Sciences, vol. 102, no. 15, pp. 5363–5367, 2005.

[64] C. Ciferri, J. De Luca, S. Monzani, K. J. Ferrari, D. Ristic, C. Wyman, H. Stark, J. Kilmartin, E. D. Salmon, and A. Musacchio, "Architecture of the human ndc80-hec1 complex, a critical constituent of the outer kinetochore," Journal of Biological Chemistry, vol. 280, no. 32, pp. 29088–29095, 2005.

[65] R. R. Wei, J. R. Schnell, N. A. Larsen, P. K. Sorger, J. J. Chou, and S. C. Harrison, "Structure of a central component of the yeast kinetochore: the spc24p/spc25p globular domain," Structure, vol. 14, no. 6, pp. 1003–1009, 2006.

[66] C. Ciferri, S. Pasqualato, E. Screpanti, G. Varetti, S. Santaguida, G. Dos Reis, A. Maiolica, J. Polka, J. G. De Luca, P. De Wulf, et al., "Implications for kinetochore-microtubule attachment from the structure of an engineered ndc80 complex," Cell, vol. 133, no. 3, pp. 427–439, 2008.

[67] R. Valverde, J. Ingram, and S. C. Harrison, "Conserved tetramer junction in the kinetochore ndc80 complex," Cell reports, vol. 17, no. 8, pp. 1915–1922, 2016.

[68] G. M. Alushin, V. H. Ramey, S. Pasqualato, D. A. Ball, N. Grigorieff, A. Musacchio, and E. Nogales, "The ndc80 kinetochore complex forms oligomeric arrays along microtubules," Nature, vol. 467, no. 7317, p. 805, 2010.

[69] J. G. DeLuca and A. Musacchio, "Structural organization of the kinetochore–microtubule interface," Current opinion in cell biology, vol. 24, no. 1, pp. 48–56, 2012.

[70] E. Screpanti, A. De Antoni, G. M. Alushin, A. Petrovic, T. Melis, E. Nogales, and A. Musacchio, "Direct binding of cenp-c to the mis12 complex joins the inner and outer kinetochore," Current Biology, vol. 21, no. 5, pp. 391–398, 2011.

[71] Z. Yan, M. Delannoy, C. Ling, D. Daee, F. Osman, P. A. Muniandy, X. Shen, A. B. Oostra, H. Du, J. Steltenpool, et al., "A histone-fold complex and fancm form a conserved dna-remodeling complex to maintain genome stability," Molecular cell, vol. 37, no. 6, pp. 865–878, 2010.

[72] T. Nishino, K. Takeuchi, K. E. Gascoigne, A. Suzuki, T. Hori, T. Oyama, K. Morikawa, I. M. Cheeseman, and T. Fukagawa, "Cenp-twsx forms a unique centromeric chromatin structure with a histone-like fold," Cell, vol. 148, no. 3, pp. 487–501, 2012.

[73] T. Nishino, F. Rago, T. Hori, K. Tomii, I. M. Cheeseman, and T. Fukagawa, "Cenp-t provides a structural platform for outer kinetochore assembly," The EMBO journal, vol. 32, no. 3, pp. 424–436, 2013.

[74] F. Malvezzi, G. Litos, A. Schleiffer, A. Heuck, K. Mechtler, T. Clausen, and S. Westermann, "A structural basis for kinetochore recruitment of the ndc80 complex via two distinct centromere receptors," The EMBO journal, vol. 32, no. 3, pp. 409–423, 2013.

[75] T. Hori, M. Amano, A. Suzuki, C. B. Backer, J. P. Welburn, Y. Dong, B. F. McEwen, W.-H. Shang, E. Suzuki, K. Okawa, et al., "Ccan makes multiple contacts with centromeric dna to provide distinct pathways to the outer kinetochore," Cell, vol. 135, no. 6, pp. 1039–1052, 2008.

[76] T. Hori, W.-H. Shang, K. Takeuchi, and T. Fukagawa, “The ccan recruits cenp-a to the centromere and forms the structural core for kinetochore assembly,” J Cell Biol, vol. 200, no. 1, pp. 45–60, 2013.

[77] A. Schleiffer, M. Maier, G. Litos, F. Lampert, P. Hornung, K. Mechtler, and S. Westermann, “Cenp-t proteins are conserved centromere receptors of the ndc80 complex,” Nature cell biology, vol. 14, no. 6, p. 604, 2012.

[78] M. R. Przewloka, Z. Venkei, V. M. Bolanos-Garcia, J. Debski, M. Dadlez, and D. M. Glover, “Cenp-c is a structural platform for kinetochore assembly,” Current Biology, vol. 21, no. 5, pp. 399–405, 2011.

[79] A. Kerres, V. Jakopec, and U. Fleig, “The conserved spc7 protein is required for spindle integrity and links kinetochore complexes in fission yeast,” Molecular biology of the cell, vol. 18, no. 7, pp. 2441–2454, 2007.

[80] J. C. Meadows, L. A. Shepperd, V. Vanoosthuyse, T. C. Lancaster, A. M. Sochaj, G. J. Buttrick, K. G. Hardwick, and J. B. Millar, “Spindle checkpoint silencing requires association of pp1 to both spc7 and kinesin-8 motors,” Developmental cell, vol. 20, no. 6, pp. 739–750, 2011.

[81] J.-F. Maure, S. Komoto, Y. Oku, A. Mino, S. Pasqualato, K. Natsume, L. Clayton, A. Musacchio, and T. U. Tanaka, “The ndc80 loop region facilitates formation of kinetochore attachment to the dynamic microtubule plus end,” Current biology, vol. 21, no. 3, pp. 207–213, 2011.

[82] I. Sanchez-Perez, S. J. Renwick, K. Crawley, I. Karig, V. Buck, J. C. Meadows, A. Franco-Sanchez, U. Fleig, T. Toda, and J. B. Millar, “The dash complex and klp5/klp6 kinesin coordinate bipolar chromosome attachment in fission yeast,” The EMBO journal, vol. 24, no. 16, pp. 2931–2943, 2005.

[83] J. P. Welburn, E. L. Grishchuk, C. B. Backer, E. M. Wilson-Kubalek, J. R. Yates III, and I. M. Cheeseman, “The human kinetochore ska1 complex facilitates microtubule depolymerization-coupled motility,” Developmental cell, vol. 16, no. 3, pp. 374–385, 2009.

[84] B. Kniola, E. O’Toole, J. R. McIntosh, B. Mellone, R. Allshire, S. Mengarelli, K. Hultenby, and K. Ekwall, “The domain structure of centromeres is conserved from fission yeast to humans,” Molecular biology of the cell, vol. 12, no. 9, pp. 2767–2775, 2001.

[85] R. Ding, R. R. West, D. Morphew, B. R. Oakley, and J. R. McIntosh, “The spindle pole body of schizosaccharomyces pombe enters and leaves the nuclear envelope as the cell cycle proceeds.,” Molecular biology of the cell, vol. 8, no. 8, pp. 1461–1479, 1997.

[86] D. S. Bindels, L. Haarbosch, L. Van Weeren, M. Postma, K. E. Wiese, M. Mastop, S. Aumonier, G. Gotthard, A. Royant, M. A. Hink, et al., “mscarlet: a bright monomeric red fluorescent protein for cellular imaging,” Nature methods, vol. 14, no. 1, p. 53, 2017.

[87] S. Wolter, A. Löschberger, T. Holm, S. Aufmkolk, M.-C. Dabauvalle, S. Van De Linde, and M. Sauer, “rapidstorm: accurate, fast open-source software for localization microscopy,” Nature methods, vol. 9, no. 11, p. 1040, 2012.

[88] M. Ovesnỳ, P. Křížek, J. Borkovec, Z. Švindrych, and G. M. Hagen, "Thunderstorm: a comprehensive imagej plug-in for palm and storm data analysis and super-resolution imaging," Bioinformatics, vol. 30, no. 16, pp. 2389–2390, 2014.

[89] J. V. Thevathasan, U. Matti, M. Kahnwald, S. K. Peneti, B. Nijmeijer, M. Kueblbeck, J. Ellenberg, and J. Ries, "Nuclear pores as universal reference standards for quantitative microscopy," Biophysical Journal, vol. 116, no. 3, p. 137a, 2019.

[90] C. Baarlink, M. Plessner, A. Sherrard, K. Morita, S. Misu, D. Virant, E.-M. Kleinschnitz, R. Harniman, D. Alibhai, S. Baumeister, et al., "A transient pool of nuclear f-actin at mitotic exit controls chromatin organization," Nature cell biology, vol. 19, no. 12, p. 1389, 2017.

[91] D. Lando, U. Endesfelder, H. Berger, L. Subramanian, P. D. Dunne, J. McColl, D. Klenerman, A. M. Carr, M. Sauer, R. C. Allshire, et al., "Quantitative single-molecule microscopy reveals that cenp-acnp1 deposition occurs during g2 in fission yeast," Open biology, vol. 2, no. 7, p. 120078, 2012.

[92] H. Sato, F. Masuda, Y. Takayama, K. Takahashi, and S. Saitoh, "Epigenetic inactivation and subsequent heterochromatinization of a centromere stabilize dicentric chromosomes," Current Biology, vol. 22, no. 8, pp. 658–667, 2012.

[93] D. D. Luche and S. L. Forsburg, "Cell-cycle synchrony for analysis of s. pombe dna replication," in DNA Replication, pp. 437–448, Springer, 2009.

[94] A. Edelstein, N. Amodaj, K. Hoover, R. Vale, and N. Stuurman, "Computer control of microscopes using micromanager current protocols in molecular biology/edited by frederick m ausubel [et al]," Chapter, vol. 14, 2010.

[95] J. Schindelin, I. Arganda-Carreras, E. Frise, V. Kaynig, M. Longair, T. Pietzsch, S. Preibisch, C. Rueden, S. Saalfeld, B. Schmid, et al., "Fiji: an open-source platform for biological-image analysis," Nature methods, vol. 9, no. 7, p. 676, 2012.

[96] E. Jones, T. Oliphant, P. Peterson, et al., "SciPy: Open source scientific tools for Python," 2001–. [Online; accessed <today>].

[97] U. Endesfelder, S. Malkusch, F. Fricke, and M. Heilemann, "A simple method to estimate the average localization precision of a single-molecule localization microscopy experiment," Histochemistry and cell biology, vol. 141, no. 6, pp. 629–638, 2014.

[98] M. Ankerst, M. M. Breunig, H.-P. Kriegel, and J. Sander, "Optics: ordering points to identify the clustering structure," in ACM Sigmod record, vol. 28, pp. 49–60, ACM, 1999.

[99] C. L. Rieder, E. A. Davison, L. Jensen, L. Cassimeris, and E. D. Salmon, "Oscillatory movements of monooriented chromosomes and their position relative to the spindle pole result from the ejection properties of the aster and half-spindle.," The Journal of cell biology, vol. 103, no. 2, pp. 581–591, 1986.

[100] F. Leone, L. Nelson, and R. Nottingham, "The folded normal distribution," Technometrics, vol. 3, no. 4, pp. 543–550, 1961.

[101] A. Meurer, C. P. Smith, M. Paprocki, O. Čertík, S. B. Kirpichev, M. Rocklin, A. Kumar, S. Ivanov, J. K. Moore, S. Singh, T. Rathnayake, S. Vig, B. E. Granger, R. P. Muller, F. Bonazzi, H. Gupta, S. Vats, F. Johansson, F. Pedregosa, M. J. Curry, A. R. Terrel, v. Roučka, A. Saboo, I. Fernando, S. Kulal, R. Cimrman, and A. Scopatz, "Sympy: symbolic computing in python," PeerJ Computer Science, vol. 3, p. e103, Jan. 2017.

[102] N. Durisic, L. Laparra-Cuervo, Á. Sandoval-Álvarez, J. S. Borbely, and M. Lakadamyali, "Single-molecule evaluation of fluorescent protein photoactivation efficiency using an in vivo nanotemplate," Nature methods, vol. 11, no. 2, p. 156, 2014.

# 11 | List of Figures

# 12 | List of Tables

# 13 | Acknowledgments

First of all, I would like to thank Dr. Ulrike Endesfelder for giving me the chance to do all the work described in this thesis under her supervision. I want to thank her for putting faith into me as one of the first two members of the group. I thank her for the late night discussions, great ideas and true leadership by example which kept me motivated even when things were hard. It was truly a pleasure and I don't think I have ever learned as much as I have while working in her group in my entire life.

I would also like to thank members of my Thesis Advisory Comittee, Prof. Dr. Victor Sourjik, Prof. Dr. Knut Drescher and Dr. Simon Ringgaard for their critical input and for keeping me on track during my project work.

I want to thank Prof. Dr. Ulrich Rothbauer and Dr. Björn Tränkle for giving me the chance to work on the BC2 system with them. The project obviously would not have been possible without them, them having invented it in the first place. Special thanks for the discussions, the many hours of experiments and cloning it must have taken taken to produce the samples and the always punctual sample and nanobody shipments!

I also want to thank Prof. Dr. Ernest Laue for letting me stay in their group at the University of Cambridge for a month and to Dr. David Lando for actually teaching me how to work with *S. pombe* so I could bring the knowledge back to Marburg. Big thanks to Dr. Edward Taylor from the same group for acquainting me with his own PhD work, which resulted in some very interesting experimental work for me as well.

I am also grateful to Prof. Dr. Robert Grosse for giving me the opportunity to work on the exciting nuclear actin project with them and to the scientists in his group, Eva, Matthias and Sylvia for implementing my irritating (but necessary) adjustments to their protocols.

To Bartosz Turkowyd, thank you for being there from the start. It was a real pleasure setting the whole thing up with you. Thank you for the dumb jokes, the dank memes and the sometimes NSFW gifs, the early morning chats and the lone evenings in the lab (we NEVER mopped up an enzyme solution from a bench and used it anyway, it did not happen). Thank you for being an off-line version of Stack Overflow and thank you for the company when I was having my tires changed twice a year. That would really have been a boring experience otherwise.

To Ilijana and Jannik, who did a lot of the actual leg-work when it came to the fission yeast project.

Figure 7.4 would have been much, much smaller without them. To Ilijana and Alex, thank you for taking care of my cats while I was away on conferences and thanks to Jannik for being my mountain lake swimming buddy. And I would also like to extend this thanks to the entire Endesfelder group.

Getting to the end, I would like to thank my friend Matic for very frequent discussions and advice on just about everything, my friend Mihael for tearing down every idea I ever had and forcing me to make them better in the process. Thanks to Lipa, Kenda and Merko for the many hours of fun online that helped keep me sane. And thanks to Bani for a ton of help progamming.

Finally, a big thank you to my family who supported me through the entire thing. I want to thank my mom for her help at the very beginning, when my flat was nothing but an empty room with a mattress in the middle. Thanks to my dad for legal advice and thanks to my brother Benjamin for somehow knowing just about anything I ever asked. And thank you Fabienne, for putting up with me through the entire thing. Thank you for the caramelized almonds at 2 in the morning when you visited me all the way from Switzerland and I didn't even show up until you were asleep.